



TECHNISCHE UNIVERSITÄT MÜNCHEN

---

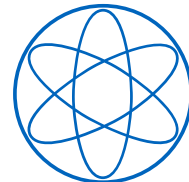
# Spectral Features from Dark Matter Annihilations and Decays in Indirect Searches

---

DISSERTATION

by

ANNA SOPHIA LAMPERSTORFER



PHYSIK DEPARTMENT T30D





TECHNISCHE UNIVERSITÄT MÜNCHEN

PHYSIK DEPARTMENT T30D

---

# Spectral Features from Dark Matter Annihilations and Decays in Indirect Searches

---

ANNA SOPHIA LAMPERSTORFER

Vollständiger Abdruck der von der Fakultät für Physik der Technischen Universität München  
zur Erlangung des akademischen Grades eines

**Doktors der Naturwissenschaften**

genehmigten Dissertation.

Vorsitzender: Univ.-Prof. Dr. Stefan Schönert

Prüfer der Dissertation: 1. Univ.-Prof. Dr. Alejandro Ibarra  
2. Univ.-Prof. Dr. Nora Brambilla

Die Dissertation wurde am 02.09.2015 bei der Technischen Universität München eingereicht und  
durch die Fakultät für Physik am 18.09.2015 angenommen.



## ABSTRACT

Although there is a plethora of gravitational evidence for the existence of dark matter, the nature of the dark matter particle remains one of the most intriguing open questions in high energy physics. A promising approach to identify the dark matter properties is the so-called indirect dark matter detection, in which a signature of the annihilation or decay of dark matter particles is searched for in the astrophysical gamma-ray, cosmic-ray and neutrino fluxes. Prime signals for dark matter identification are sharp spectral features in the GeV to TeV energy range because these cannot be mimicked by astrophysical sources.

In this thesis we study positron and gamma-ray spectral features from dark matter annihilations and decays. Using AMS-02 data we derive for the first time stringent and robust model-independent constraints on the dark matter parameters from the positron flux. Furthermore we consider three different types of gamma-ray spectral features: gamma-ray lines, internal bremsstrahlung and gamma-ray boxes. To this end we compute projected dark matter constraints for future experiments and make use of current measurements. Concretely, we study three different scenarios: First, a forecast for the detection of gamma-ray boxes is made for the future Cherenkov telescope CTA. As it turns out, heavy thermal dark matter candidates can be probed with this instrument. Second, we constrain minimal dark matter models, in particular extensions of the Standard Model with an extra  $SU(2)_L$  5-plet or 7-plet, with H.E.S.S. measurements and compute prospects for CTA. We demonstrate that the inclusion of internal bremsstrahlung and the Sommerfeld effect yields very strong limits and allows probing otherwise unconstrained mass regions. Third, the sensitivity of the future HERD instrument on gamma-ray lines is investigated. We show that a part of the supersymmetric dark matter parameter space can be ruled out with this experiment.

## ZUSAMMENFASSUNG

Obwohl es aufgrund ihrer Gravitationswechselwirkung eine überwältigende Zahl an Beweisen für die Existenz der Dunklen Materie gibt, bleiben ihre Teilcheneigenschaften eine der größten ungelösten Fragen der Hochenergiephysik. Eine vielversprechende Methode, dieses Rätsel zu lösen, ist der sogenannte indirekte Nachweis. Dabei wird eine Signatur von Annihilationen oder Zerfällen Dunkler Materie in den astrophysikalischen Flüssen von Gammastrahlung, kosmischer Strahlung und Neutrinos gesucht. Besonders gut geeignete Signale von Dunkler Materie sind scharfe spektrale Signaturen im GeV bis TeV Energiebereich, weil diese nicht aus astrophysikalischen Quellen stammen können.

In vorliegender Arbeit werden spektrale Merkmale von Positronen und Gammastrahlung aus Annihilationen und Zerfällen von Dunkler Materie untersucht. Zum einen leiten wir erstmalig starke Schranken für die Parameter Dunkler Materie aus den AMS-02 Messungen des Positronenflusses her, zum anderen betrachten wir drei verschiedene Gammastrahlungssignaturen: Linien, interne Bremsstrahlung und Boxen. Für diese Signaturen berechnen wir Schranken für die Parameter Dunkler Materie mit geplanten Experimenten, nutzen aber auch bestehende Messungen. Konkret untersuchen wir drei Szenarien: Erstens betrachten wir die Aussichten des künftigen Cherenkov Teleskops CTA, Gammastrahlungsboxen zu detektieren. Tatsächlich wird dieses Experiment thermisch produzierte Kandidaten Dunkler Materie ausschließen können. Zweitens schränken wir durch die H.E.S.S.-Messungen und CTA-Vorhersagen den Parameterraum minimaler Modelle Dunkler Materie ein, in denen das Standard Modell mit einem  $SU(2)_L$  5-plet oder 7-plet erweitert wird. Wir zeigen, dass man unter Berücksichtigung des Sommerfeld-Effekts und der internen Bremsstrahlung starke Schranken erhält und ansonsten unbeschränkte Massenbereiche ausschließen kann. Drittens bestimmen wir die Empfindlichkeit des geplanten HERD Experiments für Gammastrahlungslinien und zeigen, dass ein Teil des supersymmetrischen Parameterraums ausgeschlossen werden kann.

# Contents

<b>Introduction</b>	<b>13</b>
<b>I Dark matter preliminaries</b>	<b>17</b>
<b>1 Dark matter phenomenology</b>	<b>19</b>
1.1 Observational evidence for dark matter . . . . .	19
1.1.1 Dark matter in galaxies . . . . .	19
1.1.2 Dark matter in galaxy clusters . . . . .	21
1.1.3 Dark matter on cosmological scales . . . . .	24
1.2 Dark matter distribution in the Milky Way . . . . .	26
1.3 The dark matter particle . . . . .	30
1.3.1 Unstable dark matter . . . . .	32
1.3.2 Dark matter production . . . . .	32
1.4 Dark matter searches . . . . .	36
1.4.1 Direct searches . . . . .	36
1.4.2 Collider searches . . . . .	37
1.4.3 Indirect searches . . . . .	38
1.5 Relevance of spectral features . . . . .	40
<b>II Dark matter searches with positrons</b>	<b>41</b>
<b>2 Phenomenology of cosmic-ray electrons and positrons</b>	<b>43</b>
2.1 Astrophysical electron and positron background . . . . .	43
2.2 Positrons from dark matter . . . . .	47
2.2.1 Dark matter models with sharp positron features . . . . .	47
2.2.2 Spectra at production . . . . .	49
2.3 Propagation of electrons and positrons in the Milky Way . . . . .	50
2.3.1 The Milky Way . . . . .	52
2.3.2 The propagation equation . . . . .	54
2.3.3 Determination of the propagation parameters . . . . .	59
2.3.4 Solar modulation . . . . .	60

---

2.4	Positron experiments . . . . .	61
2.4.1	HEAT . . . . .	62
2.4.2	PAMELA . . . . .	62
2.4.3	AMS-02 . . . . .	63
<b>3</b>	<b>Limits from positrons</b>	<b>65</b>
3.1	Methodology . . . . .	65
3.1.1	Background model . . . . .	67
3.1.2	Statistical treatment . . . . .	70
3.2	Constraints on dark matter parameters . . . . .	71
3.2.1	Limits for different final states . . . . .	71
3.2.2	Dependence on the diffusion parameters and halo profile . . . . .	72
3.2.3	Comparison with limits from other experiments and messengers . . . . .	73
<b>III</b>	<b>Dark matter searches with gamma rays</b>	<b>77</b>
<b>4</b>	<b>Phenomenology of high-energy gamma rays</b>	<b>79</b>
4.1	The gamma-ray sky . . . . .	79
4.1.1	Astrophysical gamma-ray background . . . . .	79
4.1.2	Gamma rays from dark matter . . . . .	82
4.1.3	Optical depth in the Milky Way . . . . .	89
4.2	Gamma-ray experiments . . . . .	90
4.2.1	Fermi-LAT . . . . .	92
4.2.2	HERD . . . . .	93
4.2.3	H.E.S.S. . . . .	94
4.2.4	CTA . . . . .	94
<b>5</b>	<b>Limits from gamma rays</b>	<b>97</b>
5.1	Methodology . . . . .	97
5.1.1	Current experiment: H.E.S.S. . . . .	98
5.1.2	Future experiments: CTA and HERD . . . . .	101
5.2	Gamma-ray boxes . . . . .	113
5.2.1	Model-independent considerations . . . . .	113
5.2.2	Constraining benchmark models . . . . .	120
5.3	Minimal dark matter . . . . .	126
5.3.1	Model . . . . .	126
5.3.2	Sommerfeld enhancement . . . . .	129
5.3.3	Cross sections . . . . .	130
5.3.4	Constraints . . . . .	134

5.4 Gamma-ray lines . . . . .	141
5.4.1 Model-independent results . . . . .	142
5.4.2 Constraining the MSSM . . . . .	144
<b>Conclusions</b>	<b>149</b>
<b>A Statistical Methods</b>	<b>153</b>
A.1 $\chi^2$ -distribution and goodness-of-fit . . . . .	153
A.2 Parameter estimation . . . . .	154
A.3 Hypothesis tests . . . . .	156
<b>Acknowledgments</b>	<b>157</b>
<b>Bibliography</b>	<b>159</b>



# List of Figures

1.1	Flat rotation curves.	20
1.2	The Bullet Cluster.	24
1.3	Comparison of simulations and galaxy surveys.	27
1.4	Millennium dark matter simulation.	28
1.5	Dark matter density distributions.	29
1.6	Evolution of the comoving number density of dark matter particles.	34
2.1	Positron fraction measured by PAMELA.	45
2.2	Positron spectra at production.	51
2.3	Interstellar radiation field.	53
2.4	Positron spectra at Earth after propagation.	59
3.1	Positron fraction, electron and positron fluxes measured by HEAT, PAMELA and AMS-02.	66
3.2	Calculated secondary positron flux at Earth.	68
3.3	Limits from sampling over various energy windows together with the best limit.	70
3.4	Limits from the positron flux for annihilations and decays.	71
3.5	Limits from the positron fraction for annihilations and decays.	72
3.6	Limits from the positron flux for different propagation parameters.	73
3.7	Limits from the positron flux for different dark matter profiles.	73
3.8	Limits from the positron and gamma-ray measurements for $\mu^+\mu^-$ final states.	74
3.9	Limits from the positron and gamma-ray measurements for $b\bar{b}$ final states.	74
4.1	Fermi two-year all-sky map.	80
4.2	Fermi residual sky map.	81
4.3	Residual gamma-ray map showing the Fermi bubbles.	82
4.4	Annihilation processes leading to sharp spectral features.	84
4.5	Gamma-ray spectra from dark matter annihilations.	86
4.6	Simulated sky map of the gamma-ray emission from dark matter annihilations.	87
4.7	Energy dependent $J$ -factor.	91
4.8	HERD: effective area and energy resolution.	93
4.9	CTA: effective area and energy resolution.	95
5.1	Target regions for H.E.S.S. and CTA.	98

---

5.2	H.E.S.S. data from the central Galactic halo region. . . . .	99
5.3	Fluxes in the source and background regions measured by H.E.S.S. and the flux residua. . . . .	100
5.4	Cosmic-ray background rate for CTA. . . . .	106
5.5	Cosmic-ray and gamma-ray background for CTA. . . . .	107
5.6	Sliding energy window size for CTA. . . . .	108
5.7	Regions of interest for HERD. . . . .	109
5.8	Cosmic-ray and gamma-ray background for HERD. . . . .	112
5.9	Sliding energy window size for HERD. . . . .	113
5.10	Spectra of the three box sizes under consideration together with the CTA background. . . . .	115
5.11	95% CL upper limits on gamma-ray boxes in the baseline analysis. . . . .	116
5.12	Constraints on gamma-ray boxes for different widow sizes. . . . .	117
5.13	Gamma-ray box constraints for different dark matter profiles and including the optical depth. . . . .	118
5.14	Gamma-ray box constraints for different window positions. . . . .	119
5.15	Constraints on narrow gamma-ray boxes with systematic uncertainties. . . . .	120
5.16	Comparison of the projected CTA limits for gamma-ray boxes with constraints from other experiments. . . . .	121
5.17	Branching fractions for the decay of the intermediate pseudoscalar particle. . . . .	123
5.18	Gamma-ray box constraints for the benchmark models A and B. . . . .	125
5.19	Ratio of the 95% CL expected upper limit for CTA and the target cross sections of models A and B. . . . .	126
5.20	Ladder diagrams contributing to dark matter annihilations. . . . .	130
5.21	Sommerfeld enhancement factors for the 5-plet. . . . .	132
5.22	Sommerfeld enhancement factors for the 7-plet. . . . .	133
5.23	$W^+W^-$ and $\gamma\gamma$ annihilation cross section for the minimal dark matter 5-plet and the 7-plet. . . . .	135
5.24	Differential annihilation cross section into $\gamma\gamma$ , $\gamma Z$ , $W^+W^-$ and $ZZ$ . . . . .	136
5.25	Limits on the 5-plet dark matter fraction from H.E.S.S. measurements. . . . .	137
5.26	Limits on the 7-plet dark matter fraction from H.E.S.S. measurements. . . . .	138
5.27	Projected limits on the 5-plet dark matter fraction from CTA. . . . .	140
5.28	Projected limits on the 7-plet fraction dark matter from CTA. . . . .	141
5.29	Projected limits on dark matter annihilations and decays with HERD. . . . .	142
5.30	Comparison of the limits from HERD with other experiments and flux upper limits. . . . .	143
5.31	HERD constraints on the p7MSSM. . . . .	146
A.1	$\chi^2$ -distribution. . . . .	154

# Introduction

Today we know from a wide variety of observations that some kind of invisible matter exists in our Universe. This so-called dark matter is observed due to its gravitational interaction with ordinary matter on very different scales, ranging from galactic to cosmological distances as well as at very different times in the evolution of the Universe. Observations tell us that about 84% of the total matter content of the Universe is made up of dark matter and how the invisible matter is distributed. Dark matter is included in the Standard Model of cosmology ( $\Lambda$ CDM), which explains very successfully the evolution of our Universe.

The Standard Model of particle physics on the other hand has been confirmed to very high precision in collider experiments. In 2012 the last unobserved ingredient of the Standard Model of particle physics, the Higgs particle, was discovered at the LHC. However, the Standard Model does not feature any suitable dark matter candidate. How to extend it in order to include the dark matter particle remains one of the most intriguing open questions in high energy physics.

A great experimental effort is undertaken in order to observe the dark matter particle non-gravitationally and uncover its properties. Currently, many searches are conducted in order to observe dark matter particles with GeV to TeV masses. This mass range is theoretically well-motivated: Annihilations of massive particles featuring weak interactions with the Standard Model particles, so-called Weakly Interacting Massive Particles (WIMPs) naturally acquire the correct relic abundance in the early Universe through thermal freeze-out. We are currently living in an exciting era of dark matter searches since the experiments are starting to probe models with dark matter candidates that feature weak scale interactions. However, we do not restrict ourselves to the thermal freeze-out scenario in this thesis, but allow for alternative non-thermal production mechanisms.

Dark matter need not be absolutely stable, but its lifetime must be much longer than the age of the Universe. Interestingly, the same experiments that can probe the annihilations of WIMP dark matter allow constraining decaying dark matter candidates with lifetimes that originate from many well-motivated extensions of the Standard Model.

A promising method to reveal the particle physics properties of dark matter is the so-called indirect dark matter search. In this approach, one aims at observing signatures of annihilations or decays of dark matter particles. These signatures can be searched for using different messengers, for instance gamma-rays, anti-matter or neutrinos. From the non-observation of such signatures limits on the particle physics properties, the velocity-weighted dark matter annihilation cross section or the dark matter lifetime can be inferred. A particularly promising strategy is the search for spectral features, which can be very well discriminated against the smooth astrophysical

background and which provide a smoking gun for dark matter. In this thesis we focus on dark matter annihilations and decays that produce positrons and gamma-rays in the GeV to TeV energy range.

We argue that positrons are a prime tool to investigate annihilating or decaying dark matter. For the first time we search for a dark matter signal in the positron flux. In contrast to the previously used positron fraction, this does not require any knowledge about the electron flux, which is difficult to model. The exquisite measurements of the AMS-02 experiment allow deriving robust model-independent constraints on the dark matter annihilation cross section and lifetime, in particular for final states that produce a sharp positron spectrum. In contrast to the limits from other messengers, the positron limits do not suffer from large astrophysical uncertainties. Furthermore, we confront our results with limits from other experiments and other messengers and show that the positron limits provide the most stringent constraints for electron and muon final states.

While for positrons, due to their diffuse propagation, only a relatively small volume of the Milky Way halo can be probed, gamma-rays propagate almost freely and provide not only spectral but also directional information. Thus they allow investigating different target regions in the search for a dark matter signal. In this thesis we concentrate on the Galactic halo, with special focus on the center of the Galaxy since the largest dark matter signal is expected from this region. Dark matter annihilations can produce three different kinds of spectral features: a monochromatic line, an internal bremsstrahlung peak or a gamma-ray box. All three types of spectral features are considered in this thesis for the computation of constraints on the dark matter parameters from existing and future experiments.

In particular, we study the ability of the future Cherenkov Telescope Array (CTA) to constrain gamma-ray boxes using realistic projections for the instrument performance. To this end, we generate mock data for the astrophysical background and implement a profile likelihood analysis in combination with the sliding energy window technique. The derived constraints are applied to concrete particle physics models, for which, indeed, thermally produced dark matter candidates in the TeV range can be probed. We show that CTA will be able to probe thermal WIMPs in a mass range that is not accessible by any other search strategy.

The internal bremsstrahlung feature is investigated in minimal dark matter models. This class of models is theoretically very appealing because it only requires one new parameter and is thus very predictive. Concretely, we study the extension of the Standard Model with an  $SU(2)_L$  5-plet or 7-plet, which is automatically stable at the renormalizable level. In this framework, the Sommerfeld effect must be included for heavy dark matter particles since the multiple exchange of weak gauge bosons enhances the annihilation cross section. The sharp gamma-ray feature consists of the sum of monochromatic lines and internal bremsstrahlung. Using data from the High Energy Stereoscopic System (H.E.S.S.), we derive limits not only on this feature but also on the prompt gamma-ray continuum. We find that the inclusion of the internal bremsstrahlung allows setting stringent limits on otherwise unconstrained mass regions. In addition, we show

that CTA can improve the current H.E.S.S. limits and extend the constrained mass range. Even for cored dark matter profiles very strong constraints are obtained.

Lastly, the ability of the future High Energy cosmic-Radiation Detection facility (HERD) to constrain monochromatic gamma-ray lines is investigated. For the derivation of the constraints we employ the same methods as for CTA. We find that for dark matter candidates with a mass of 100 GeV HERD will deliver one of the most stringent limits compared to other existing and future experiments, namely Fermi-LAT, H.E.S.S., Gamma-400 and CTA. Applying our results to a scan of the MSSM parameter space, we demonstrate that HERD limits cut into the regions of the parameter space that are not constrained by other experiments.

This thesis consists of three parts. Part I reviews the basic concepts of dark matter phenomenology. In Chapter 1, the emphasis lies on the observational evidence for dark matter and its distribution in the Milky Way, the current knowledge of the particle nature of dark matter and its production mechanisms. In addition, the three main attempts to identify the dark matter particle are summarized: direct detection, indirect detection and production at particle colliders. Lastly, the importance of spectral features is discussed.

Part II of the thesis is dedicated to dark matter searches with positrons. In particular, Chapter 2 concentrates on the phenomenology of electron and positron cosmic rays. First, the cosmic-ray electron and positron background is discussed and concrete dark matter models that produce positron spectral features are presented. Afterwards, the positron spectra at production and at detection are reviewed for annihilations and decays into various final states, and the relevant propagation effects are described. Subsequently, the positron experiments considered in this work are introduced. Then, in Chapter 3, we describe our approach for the computation of the constraints and present robust and model-independent upper limits on the dark matter annihilation cross section and lifetime.

In Part III, we derive current constraints and projected limits on gamma-ray spectral features. The phenomenology of Galactic gamma-rays is presented in Chapter 4. First, the astrophysical gamma-ray flux and the gamma-ray flux from dark matter are presented, and interesting target regions are reviewed. Then, the ground and space based gamma-ray experiments under consideration in this thesis are introduced. Subsequently, in Chapter 5, our approach to derive limits with the current experiment H.E.S.S. and the future instruments CTA and HERD are explained. Lastly, the concrete particle physics models under consideration are introduced and the derived constraints on the different spectral features are presented.

Some parts of this work have been also discussed in separate articles:

- [1] **Dark matter annihilations and decays after the AMS-02 positron measurements,**  
A. Ibarra, A. S. Lamperstorfer, and J. Silk,  
Phys. Rev. D **89**, 063539 (2014),  
arXiv:1309.2570

- [2] **Limits on dark matter parameters after the AMS-02 positron measurements,**  
A. S. Lamperstorfer,  
Proceedings of the 26th Rencontres de Blois on Particle Physics and Cosmology Blois,  
Loire Valley, France, May 18-25, 2014
- [3] **On the sensitivity of CTA to gamma-ray boxes from multi-TeV dark matter,**  
A. Ibarra, A. S. Lamperstorfer, S. L. Gehler, M. Pato, and G. Bertone,  
JCAP 1509 (2015), no. 09 048,  
arXiv:1503.06797
- [4] **Gamma-rays from Heavy Minimal Dark Matter,**  
C. Garcia-Cely, A. Ibarra, A. S. Lamperstorfer, and M. H. G. Tytgat,  
arXiv:1507.05536,  
Accepted by JCAP
- [5] **Perspective of monochromatic gamma-ray line detection with the High Energy cosmic-Radiation Detection (HERD) facility onboard China's Space Station,**  
X. Huang, A. S. Lamperstorfer, Y. S. Tsai, M. Xu, Q. Yuan, J. Chang, Y. Dong, B. Hu,  
J. Lu, L. Wang, B. Wu and S. Zhang  
arXiv:1509.02672,  
Submitted to Astroparticle Physics

# **Part I**

## **Dark matter preliminaries**



# Chapter 1

## Dark matter phenomenology

The existence of dark matter has now become a widely accepted integral part of modern particle physics and astrophysics. This chapter introduces the ground work in this field of research. In Sec. 1.1, the various gravitational pieces of evidence for dark matter are reviewed. Subsequently, in Sec. 1.2, the current state of knowledge of the dark matter distribution in the Milky Way is recapped. Even though the evidence for dark matter is overwhelming, it has not yet been observed as a particle. However, many observations constrain the dark matter properties. In Sec 1.3, our insights about dark matter as an elementary particle are summarized, with special focus on  $\text{GeV} \sim \text{TeV}$  dark matter candidates, whereas in Sec. 1.4 the main attempts to discover dark matter as a particle and uncover its particle physics properties are explained. Lastly, as we study sharp dark matter signals, Sec. 1.5 discusses the relevance of spectral features for dark matter searches.

### 1.1 Observational evidence for dark matter

One of the first measurements that indicates the existence of dark matter dates back to 1933, when Fritz Zwicky observed a discrepancy in the visible and total matter in galaxy clusters. Subsequently, evidence for dark matter was found in many other observations, ranging from dwarf galaxies to the observable Universe (see e.g. Ref. [6] for a review). Within the last century our knowledge of dark matter has increased drastically. Nowadays the fraction of dark matter in the total energy budget of the Universe is measured with high precision. In this section, the main (but by no means exhaustive) pieces of evidence for dark matter will be discussed, ranging from small to large scales.

#### 1.1.1 Dark matter in galaxies

The puzzle of missing matter in galaxies was investigated by the American astronomer Vera Rubin and her collaborator Kent Ford. They studied rotation curves in the outer regions of spiral galaxies in the late 60s and early 70s. Galactic rotation curves show how the circular velocities of stars and interstellar gas depend on the radii of their orbits. With a new, very sensitive spectrograph it became feasible to accurately determine the circular velocity of interstellar gas from measurements of spectral emission lines of hydrogen. Under the assumption of spherical

symmetry, the velocity of an object orbiting the center of the Galaxy with a radius  $r$  can be calculated using Newtonian dynamics [6]:

$$v(r) = \sqrt{\frac{GM(r)}{r}}, \quad (1.1)$$

where  $G$  is Newton's constant and  $M(r)$  is the mass enclosed in a sphere of radius  $r$ . The measurements revealed that all the visible matter in the outer parts of galaxies orbits approximately at the same velocity around the center of the observed galaxy, independent of its orbit radius. If most of the matter was contained in the luminous disk, the rotational velocity is expected to decrease with radius,  $v(r) \propto 1/\sqrt{r}$ , because the enclosed visible mass is constant with increasing radii beyond the luminous part of the galaxy. The observation of flat rotation curves, however, lead to the conclusion that large portions of the mass of galaxies are not accounted for by luminous matter and that the mass extends well beyond the visible part of the galaxy. Starting with the Andromeda galaxy [7], flat rotation curves were subsequently observed in many other galaxies [8] by Vera Rubin and collaborators (Fig. 1.1).

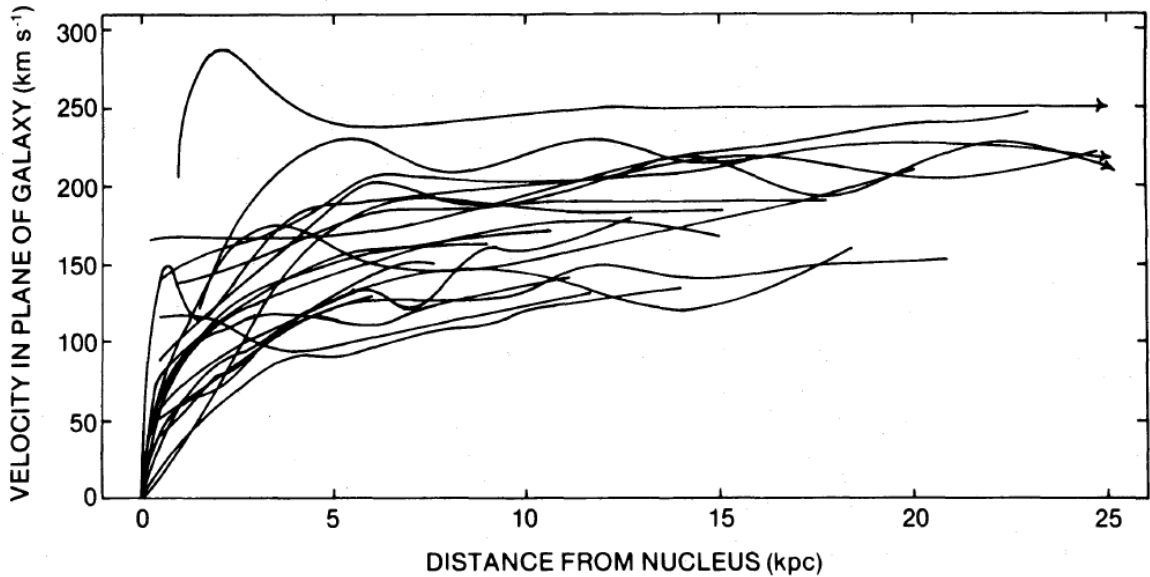


Figure 1.1: Compilation of flat rotation curves of 21 galaxies measured by Vera Rubin and collaborators. The figure is taken from Ref. [8].

Already in 1975 it was evident that beyond the visible part of a galaxy its mass has to grow linearly with the distance to the center. In fact, in order to get a flat rotation curve,  $M(r)$  has to be proportional to  $r$ . Now the radial dependence of the density profile  $\rho(r)$  can be inferred at large radii,  $\rho(r) \propto 1/r^2$ . While the density profile of the dark matter halo is well known in the outer parts of galaxies, its shape in the inner galaxy is still an open question (see Sec. 1.2).

Since the 80s, the number of flat rotation curves observed has increased dramatically. Today, there are databases containing data of millions of galaxies [9] and a flat rotation curve has also

been observed for our own Galaxy [10]. The determination of the dark matter profile of the Milky Way, however, is challenging due to our location inside the Galactic disk, which complicates the measurements, and the large uncertainties related to the distribution of baryons. Nevertheless, the value of the dark matter density of the Milky Way at the position of the Sun, the local dark matter density, has been determined in various studies (see Ref. [11] and Sec. 1.2), but the results comprise large uncertainties. Usually, the values found for the local dark matter density are compatible with zero at  $3\sigma$  when no assumption on the dark matter profile is made. In a recent work [12], a compilation of all rotation curve data of the Milky Way available in the literature is compared to a large set of baryonic mass distribution models. It was shown that the evidence for a dark matter component exceeds  $5\sigma$  for galactocentric radii within the solar circle for all considered baryonic models.

### 1.1.2 Dark matter in galaxy clusters

A cluster of galaxies is a group of several hundred galaxies that are gravitationally bound. Its mass can be determined in various ways, employing the virial theorem, by observing the X-ray radiation of hot gas and by gravitational lensing.

Historically, one of the first hints for the existence of dark matter was found by Fritz Zwicky. He measured the velocities of galaxies in the Coma Cluster (Abell 1656) and derived its mass using the virial theorem [13]. The theorem relates the kinetic energy  $T$  to the potential energy  $U$  in a stationary system by

$$\langle T \rangle = -\frac{1}{2} \langle U \rangle , \quad (1.2)$$

where the brackets denote the time average. Assuming that the galaxies are on average uniformly distributed in a sphere of radius  $R$ , the potential energy of the cluster is given by  $U = -\frac{3}{5} \frac{G}{R} M^2$ . As the velocity distribution is spherically symmetric as well,  $\langle v^2 \rangle = 3 \langle v_s^2 \rangle$ , the kinetic energy depends on  $v_s$ , the velocity along the line of sight. This quantity can be measured and the mass of the cluster can be inferred with the virial theorem. For about 1000 galaxies in the Coma Cluster, Zwicky obtains a conversion factor from luminosity to mass of  $\gamma = 500$ , which is a factor of more than 100 larger than what is observed in the solar neighborhood [14]. Commenting his findings, he was the first to use the term “dark matter” in a modern sense [13]. In more recent studies, mass-to-light ratios of  $M/L = 200 \sim 300 h M_\odot / L_\odot$  are found for various galaxy clusters [15], where  $h$  denotes the Hubble constant in units of  $100 \text{ km s}^{-1} \text{ Mpc}^{-1}$ ,  $M_\odot$  and  $L_\odot$  are the mass and luminosity of the Sun, respectively. Confirming Zwicky’s results, these ratios indicate that there must be some non-visible from of matter in galaxy clusters. If the clusters consisted mostly of stars, their mass-to-light ratios would be of order unity in solar units.

A matter component of galaxy clusters that is not accounted for in Zwicky’s work is hot gas, which fills the intergalactic space. The temperature of the gas is of the order of  $10^7 \sim 10^8 \text{ K}$  [16]. Thus X-rays are emitted by thermal bremsstrahlung radiation. As soon as it became experimentally feasible to measure the X-ray emission from galaxy clusters, these observations

were used to determine the total cluster masses. The measurements revealed that the mass of galaxy clusters is dominated by hot X-ray emitting gas. Assuming that the gas is in thermal equilibrium, which is justified for clusters that did not undergo any major collision, the radial distribution of mass can be calculated [6, 17, 18]. In hydrostatic equilibrium, the pressure  $p$  is related to the potential of the gas by

$$\frac{dp}{dr} = -\rho_g(r) \frac{d\phi(r)}{dr} = -\rho_g(r) \frac{GM_{\text{tot}}(r)}{r^2}. \quad (1.3)$$

The pressure of the baryonic gas with density  $\rho_g$  prevents the cluster from gravitational collapse caused by the gravitational potential  $\phi$  of total mass of the system  $M_{\text{tot}}(r)$  that is enclosed within a sphere of radius  $r$  [17]. This includes not only the baryonic gas, but also galaxies, dark matter and any other massive objects in the cluster. Using the perfect gas law to substitute the pressure in the equation above, one gets:

$$\frac{d \ln \rho_g}{d \ln r} + \frac{d \ln T}{d \ln r} = -\frac{GM_{\text{tot}}(r)}{r} \frac{\mu m_p}{kT(r)}, \quad (1.4)$$

where  $k$  is the Boltzmann constant,  $m_p$  the proton mass and  $\mu$  the average molecular weight, with  $\mu \approx 0.6$  for the intracluster gas [6]. The gas density  $\rho_g$  can be inferred from the X-ray luminosity per unit proper volume, which is proportional to the gas density squared,  $L_{\text{X-ray}} \propto \rho_g^2$  [15]. Neglecting the dark matter in the cluster the gas temperature can be estimated from Eq. (1.4). To this end the total cluster mass in Eq. (1.4) is substituted by the mass of the intracluster gas, which is the dominant contribution to the visible mass. This yields [6]

$$kT \approx (1.3 - 1.8) \text{keV} \left( \frac{M_g(r)}{10^{14} M_\odot} \right) \left( \frac{\text{Mpc}}{r} \right). \quad (1.5)$$

The result of  $kT = 1 \sim 2$  keV has to be compared to measured temperatures of about 10 keV [6, 17]. This discrepancy points to a substantial amount of dark matter in the clusters.

Using the measured temperature to calculate the total mass of the cluster, it is found that the hot gas and the visible galaxies together only amount to about one sixth of  $M_{\text{tot}}$ . The inconsistency between the visible mass and the dynamical mass of galaxy clusters is reduced from values of more than two orders of magnitude found by Zwicky to a factor of about 6, when X-ray observations are included, but a discrepancy remains nonetheless [19].

The third method to determine the mass of a cluster, gravitational lensing, does not rely on any assumptions but general relativity. Thus, it can also be employed for clusters that are not in equilibrium because they underwent a collision recently, such as the Bullet Cluster (see below). Gravitational lensing is the bending of light or distortion of an image of a luminous object, the source, through the gravitational potential of a very massive object in or close to the line of sight of the source [20]. The very massive object that distorts the image of the luminous object is called the lens. Through the observation of the lensed images of background galaxies or galaxy clusters for instance, the mass and mass distribution of the lens can be mapped. According to the degree of distortion or deflection of the image, one distinguishes three different variants of lensing: strong lensing, weak lensing and microlensing.

The most prominent example for lensing effects is strong lensing, the creation of multiple images of the source. As it was predicted by Einstein, its observation was an impressive confirmation of general relativity. In rare, extreme cases these images can form an arc or a ring, which is called Einstein ring, as observed for instance in Ref. [21]. In Ref. [22], strong gravitational lensing effects are used to reconstruct the mass profile of the lens. In that work, the observation of eight sub-images of a single background galaxy allows reconstructing the mass profile of the lensing galaxy cluster CL0024+1654.

Only in seldom cases the gravitational lensing effect is strong enough to create multiple images or an Einstein ring. However, light is bent by any mass distribution. In the majority of the cases, the massive objects between the observer and the source lead to two effects: Images of circular sources become elliptical and their luminosities are enhanced [20]. This is called weak lensing and can only be observed through statistical analyses, where a coherent distortion of the images of many background galaxies is analyzed [23]. Typically one finds an agreement within a factor of two from galaxy cluster mass determinations from lensing and X-ray observations [20].

For lenses of stellar and sub-stellar masses, the splitting of the images is too small to be observable by telescopes. Nevertheless, the focusing of the lens leads to an increase in luminosity of the source. This effect is called microlensing and is used, for instance, to search for so-called MACHOS (massive compact halo objects). These massive non-luminous astrophysical objects could account for (parts of) the dark matter because they do not radiate detectable electromagnetic radiation. Examples of such objects are faint stars, neutron stars, black holes, brown dwarfs and planets [20]. In order to detect passing MACHOS through an increase in luminosity, the light of millions of stars in the Milky Way is surveyed. The MACHO project revealed that the dark matter halo of the Milky Way cannot be fully composed of such objects [24].

The Bullet Cluster [25], as the cluster 1E0657-56 is commonly known, is actually the merger of two clusters of galaxies. Its name originates from the shock wave that the gas of the smaller subcluster exhibits as it passes through the larger subcluster and which can be observed in X-rays. The different components of the clusters, the gas and the member galaxies as well as the total mass can be inferred by using different observations and are shown in Fig. 1.2. The total mass distribution is mapped through weak lensing, the gas can be directly observed in X-rays, and the individual galaxies in the cluster are seen optically. Through the application and combination of all the methods on this cluster, it can be deduced that dark matter behaves collisionlessly: The halos of the two clusters pass through each other and through their baryonic components in a collisionless manner. It can be seen that the baryonic gas is displaced from the visible galaxies and is located between the two cluster centers. This happens because the gas clouds, which are smoothly distributed within the cluster, interact with each other electromagnetically and are thus retarded with respect to the visible galaxies. The latter can penetrate each other without interaction due to their large separations. The important observation here is that the dark matter, reconstructed from lensing, is distributed smoothly in the cluster, similar to the gas distribution, but is allocated with the visible galaxies. That indicates that the two dark halos

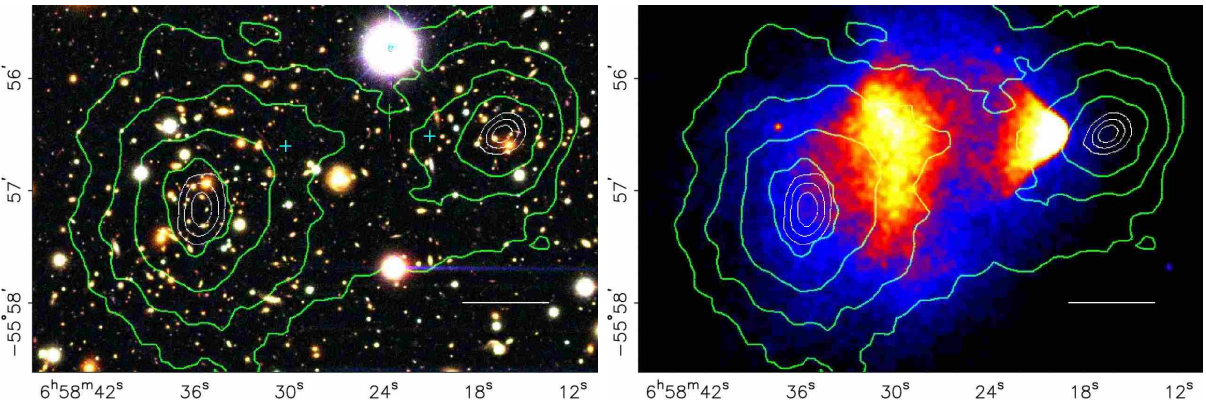


Figure 1.2: The left panel shows the optical image of the Bullet Cluster, where the green lines show contours of equal mass surface densities. In the right figure, the same contours are shown together with the Chandra image of the X-ray gas. The white line indicates 200 kpc at the distance of the merging cluster. The figures are taken from Ref. [26].

of the cluster pass through the baryonic components in a collisionless way. Thus dark matter cannot interact electromagnetically with baryonic matter. From this observation, an upper limit of  $\sigma/m < 1 \text{ cm}^2/\text{g}$  [27] can be inferred on the dark matter self-interaction. The displacement between the stellar and dark matter component in the Bullet Cluster cannot be explained solely with modified gravity [26], but requires that dark matter consists of particles.

### 1.1.3 Dark matter on cosmological scales

Dark matter not only enters in our description of astrophysical objects such as galaxies and clusters of galaxies, but it is also required in explaining the evolution of the Universe as a whole. Our standard cosmological model is the  $\Lambda$ CDM model that contains a cosmological constant ( $\Lambda$ ) and cold dark matter (CDM). It can be tested in many independent ways corresponding to probes that originate from very different stages in the evolution of the Universe. Examples of these probes are for instance the abundance of light elements, created a few minutes after the big bang in the big bang nucleosynthesis (BBN), and the cosmic microwave background, which was created when the Universe was 380000 years old. Other verifications of the  $\Lambda$ CDM model stem from the baryon acoustic oscillations (BAO) and from the simulation of the formation of observable structure in the Universe. Each of these points will be briefly discussed in the following.

Primordial nucleosynthesis explains the creation of the light elements in the early Universe and predicts their abundances, which can be measured today. The abundances of (different isotopes of) He, D, Li and Be are inferred from emission or absorption lines in extragalactic gas clouds, compact blue galaxies, atmospheres of Galactic halo stars or directly observed in the solar neighborhood [28]. Roughly speaking, about 75% of the mass fraction is made up by H and 25% by  ${}^4\text{He}$ , whereas the other isotopes and elements contribute at the sub-percent level.

Nowadays these values can be very precisely measured and calculated [15, 28]. The computed values depend strongly on the energy density of baryons at the time of BBN. Therefore, the baryon density can be determined to amount to  $\Omega_b h^2 = 0.021 - 0.025$ , where  $h$  denotes the Hubble constant in units of  $100 \text{ km s}^{-1} \text{ Mpc}^{-1}$  [29]. It is remarkable that the abundances of all light elements (except  $^7\text{Li}$ , see Ref. [30] for a review) can be explained with the same value of  $\Omega_b$ . Together with independent measurements of the total matter density, which is much larger than the baryon density, the light element abundances lead to the conclusion that the dark matter cannot be baryonic. Furthermore, the dark matter properties can be constrained through the impact of energy injection by dark matter annihilations and decays, which influences BBN [28].

One of the most powerful probes of the dark matter abundance in the Universe comes from the observation of the cosmic microwave background radiation (CMB). Its spectrum is very well described by a blackbody spectrum with a temperature of  $T = 2.7355 \text{ K}$  [29]. The CMB is a snapshot of the Universe as it became cold enough for electrons and nuclei to form neutral atoms. Due to the lack of free charges, the photons were not able to scatter any more, but they could free-stream. Many experiments have measured the CMB. Satellite missions opened up a new era of high precision cosmology with their long-term and full-sky surveys [31–33]. These instruments were able to measure and map temperature anisotropies at the level of  $10^{-5}$ . An expansion in spherical harmonics reveals several peaks in the power spectrum of temperature fluctuations, with the first peak at a characteristic scale of about  $1^\circ$  [29]. This is the so-called first acoustic peak. Its origin can be understood as follows: In the primordial plasma, before recombination, electrons and photons are coupled through Thomson scattering, and electrons and nuclei through Coulomb interactions. Initial density perturbations lead to oscillations in the plasma, which are driven by the pressure of the electron-baryon-photon fluid and the gravitational potential of the initial overdensity that acts on the fluid but also on the dark matter [34]. These different effects of baryons and dark matter leave an imprint in the oscillations and thus in the CMB. The density oscillations in the plasma translate into temperature perturbations of the photons. The physical length scale of these perturbations is the sound horizon at recombination, i.e. the distance an acoustic wave could have traveled in the primordial plasma before recombination. This length scale translates in turn into an angular scale in the CMB temperature map, visible in the measurements as peaks in the power spectrum. The peaks correspond to the different Fourier modes of the oscillations.

The heights and positions of the peaks depend on the cosmological parameters, in particular on the baryon and dark matter energy densities [34]. In fact, the exquisite data taken by the Planck satellite allows a very precise determination of these parameters. The baryon and dark matter abundance are measured to amount to  $\Omega_b h^2 = 0.02225 \pm 0.00023$  and  $\Omega_{\text{DM}} h^2 = 0.1194 \pm 0.0022$  [35].

After recombination, the radiation pressure on the baryons has almost vanished and the oscillations in the baryon fluid stalls. The overdense regions, separated by the size of the sound horizon, can attract more matter, grow and eventually collapse to form gravitationally bound objects [36]. Thus, it is expected to find a peak in the matter power spectrum at the length scale

of the sound horizon, which is about 150 Mpc today. In order to detect correlations in such large separations of galaxies and galaxy clusters, surveys that can detect objects in a large volume of the Universe are necessary [37]. With the measurement of thousands of galaxies out to redshift 0.47 in the Sloan Digital Sky Survey, the acoustic peak in the matter power spectrum, which constrains again the cosmological parameters [38], could be measured.

The same kind of surveys, together with observational data from galaxies and clusters of galaxies are tested against the results from numerical simulations of structure formation. The initial conditions for structure formation are reasonably well known [39]. They are given by the inhomogeneities as observed in the CMB at redshift  $\sim 1000$  and are evolved until structure formation starts at redshift  $\sim 100$  using a transfer function [34]. Given this input and fixing the background cosmology, it is then simulated how these density perturbations evolve in the nonlinear regime. This process depends of course on the underlying cosmology, the dark matter energy density and the dark matter properties, which are tested when the results from simulations are compared to observations. Cold, collisionless dark matter can successfully reproduce the large scale structure observed in galaxy surveys [40, 41]. Hot dark matter, on the other hand, yields too smooth distributions of matter that does not match observations and can be excluded as a dark matter candidate. The comparison of the results of simulations of galaxy formation using the Millennium Simulation [42] with observations of the Sloan Digital Sky survey is shown in Fig. 1.3.

In the cold dark matter simulations (see Fig. 1.4), self-similar structures are found. Large halos that could host galaxy clusters host smaller halos where galaxies could form that again contain a lot of substructure. It is remarkable that a universal density profile is found for these halos spanning a mass range of 20 decades [39]. The presence of substructure is very important for dark matter searches because they could lead to an enhancement of the dark matter signal. Many simulations are dark matter only simulations neglecting the baryons. With increasing computation power, the resolution of such simulations increases and the inclusion of baryons in the simulations becomes possible. Currently, the results of such simulation runs are investigated in the literature.

## 1.2 Dark matter distribution in the Milky Way

Although the dark matter profile in the outer parts of galaxies is well known, where  $\rho \propto r^{-2}$  (see Sec. 1.1.1), the dark matter density at the center of galaxies varies by orders of magnitudes between different parameterizations. For indirect dark matter searches, a precise knowledge of the dark matter density profile is crucial because, depending on the search strategy, the dark matter profile can be the main uncertainty. The different profiles are likewise motivated either by numerical simulations (see Sec. 1.1.3) or observations of galactic rotation curves. The former exhibit cusps in the center, which are in tension with the cored profiles inferred from rotation curves. This has been dubbed the cusp-to-core problem [44]. Observationally, the dark matter

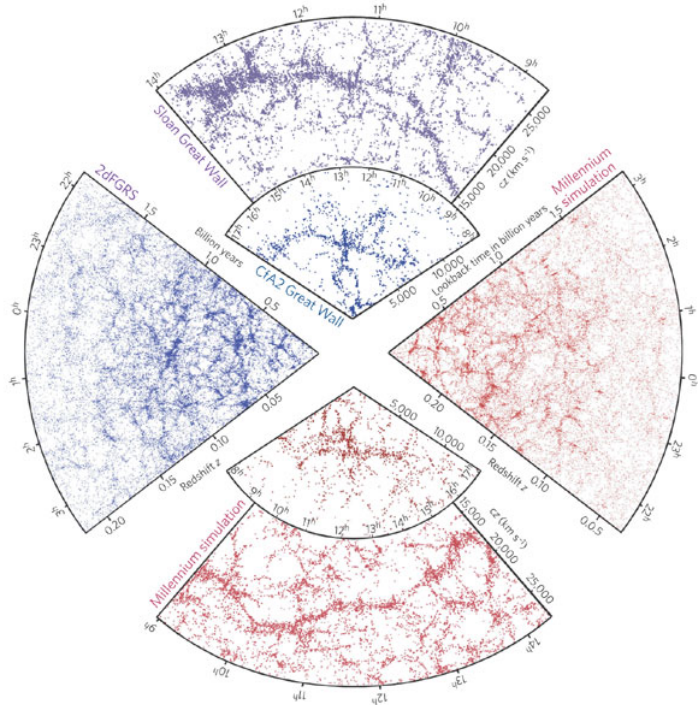


Figure 1.3: This figure, published in Ref. [41], shows the comparison of mock galaxy surveys obtained using the dark matter distribution from the Millennium Simulation. The small slice at the top shows the Great Wall as observed in the second CfA redshift survey, the larger slice at the top depicts a similar structure, the so-called Sloan Great Wall, in a small section of the Sloan Digital Sky Survey containing more than 10000 galaxies. It is one of the largest observed structures in the Universe. The left panel shows 220000 galaxies observed in the 2-degree Field Galaxy Redshift Survey in the southern sky. The right wedges show the simulated mock galaxy surveys.

profile is inferred from dark matter dominated galaxies [45]. These are low surface brightness galaxies, i.e. dark matter dominated gas-rich disk galaxies, or dwarf galaxies. In both cases evidence for a cored dark matter profile was found by many different authors (see Ref. [44] and references therein). Thus, before numerical simulations became technically feasible with increasing computation power, flat dark matter cores in galaxies were widely accepted and commonly described by an isothermal profile. This profile is derived from hydrostatic equilibrium of an ideal gas in a gravitational potential, regularized at the origin. It is parameterized by [46]

$$\rho_{\text{ISO}}(r) = \frac{\rho_s}{1 + (\frac{r}{r_s})^2}, \quad (1.6)$$

where for the scale radius a value of  $r_s = 5 \text{ kpc}$  [47] is adopted for the halo of the Milky Way in this thesis. Here and in all following profiles, the parameter  $\rho_s$  is chosen such that the adopted local dark matter density of  $\rho(r_\odot) = 0.4 \text{ GeV/cm}^3$  is obtained (see below).  $r_\odot$  denotes the

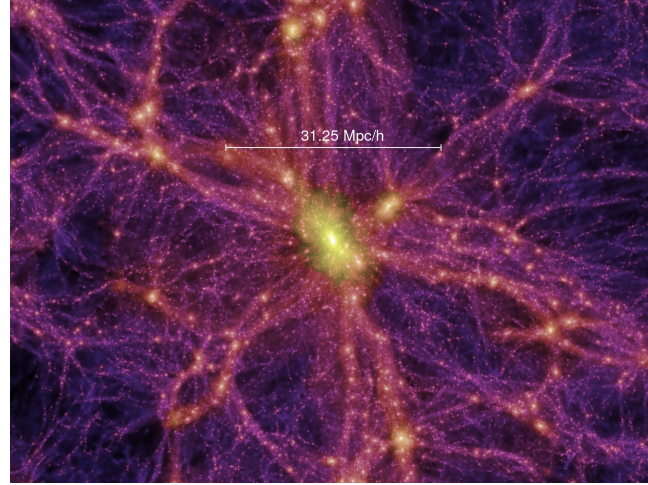


Figure 1.4: Self-similar (sub)structure found in the Millennium Simulation of the dark matter distribution. The figure is taken from Ref. [43].

distance of the Sun from the Galactic center and is taken to be  $r_\odot = 8.5 \text{ kpc}$  [48] throughout this thesis.

On the other hand, the halos found in numerical N-body simulations of structure formation are well fitted by cuspy profiles. A commonly used parameterization of such profiles is the Navarro-Frenk-White (NFW) profile [49], which was found to be universal over a mass range of 20 orders of magnitude [39] in early simulations:

$$\rho_{\text{NFW}}(r) = \frac{\rho_s}{\left(\frac{r}{r_s}\right)^\gamma \left(1 + \frac{r}{r_s}\right)^{3-\gamma}}, \quad (1.7)$$

where  $\gamma = 1$  and  $r_s = 20 \text{ kpc}$  are used throughout. As it became technically possible to increase the resolution and resolve the innermost parts of the dark halos, the simulation revealed that in dark matter halos the density can be significantly larger in the center than in the best-fit NFW profile. In order to describe these halos, an additional parameter is needed. To this aim, a generalized NFW profile can be employed, where  $\gamma$  is the additional parameter that determines the slope of the inner part of the profile. As recent gamma-ray observations of the Galactic center [50] can be well explained by a contracted NFW profile ( $\gamma = 1.1 \sim 1.3$ ), the generalized NFW profile with  $\gamma = 1.2$  is also considered in this thesis.

Alternatively, the Einasto profile [51] can be used to describe the centrally denser halos

$$\rho_{\text{Ein}}(r) = \rho_s \exp \left\{ -\frac{2}{\alpha} \left[ \left(\frac{r}{r_s}\right)^\alpha - 1 \right] \right\}. \quad (1.8)$$

Here  $\alpha = 0.17$  and  $r_s = 20 \text{ kpc}$  [52] are taken.

A possible solution to the cusp-to-core problem is that cusps cannot form in the process of galaxy formation. This could arise for instance through feedback processes and is currently studied in simulations. As found in Ref. [53], supernova feedback can remove the dark matter

cusps and lead to flat cores in the dark matter distribution of Milky Way-like galaxies. In order to employ a more realistic parameterization with respect to the idealized isothermal scenario we use an  $(\alpha, \beta, \gamma)$ -profile that is parameterized with

$$\rho_{\alpha,\beta,\gamma}(r) = \frac{\rho_s}{\left(\frac{r}{r_s}\right)^\gamma \left(1 + \left(\frac{r}{r_s}\right)^\alpha\right)^{(\beta-\gamma)/\alpha}}. \quad (1.9)$$

We make use of the parameters that were found for the Milky Way-like halo B of Ref. [53], where  $(\alpha, \beta, \gamma) \simeq (2.9, 2.5, 0)$  and  $r_s \simeq 4.4$  kpc. All dark matter profiles discussed above are shown in Fig. 1.5.

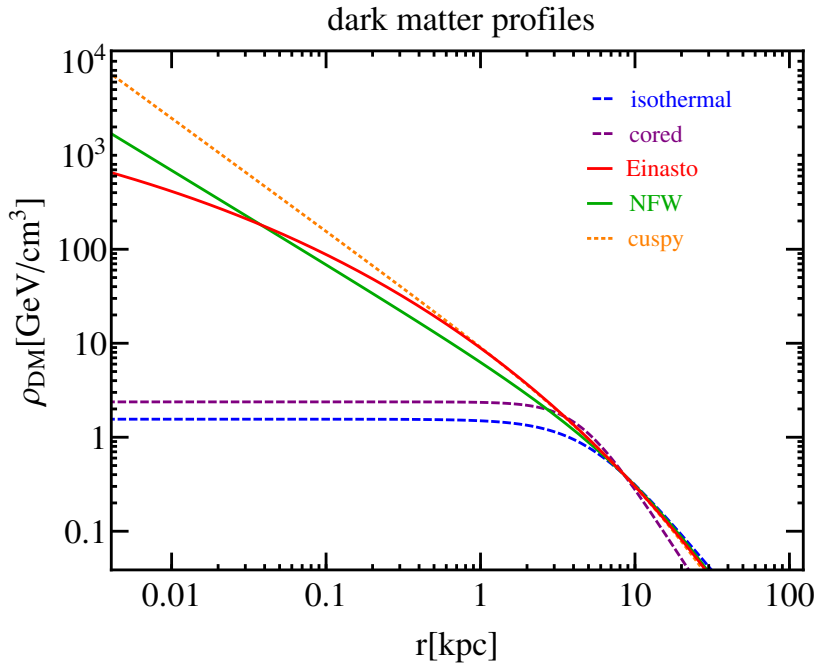


Figure 1.5: Dark matter profiles used in this thesis as a function of the distance  $r$  to the Galactic center. From top to bottom (at  $r = 0.01$  kpc), the lines indicate the generalized NFW profile with index 1.2, the NFW profile, the Einasto profile, the cored profiles obtained from simulations and the isothermal profile. All lines intersect at  $r = 8.5$  kpc, where all profiles are normalized to the local dark matter density  $\rho_\odot = 0.4$  GeV/cm<sup>3</sup>.

An important quantity that enters in the dark matter profiles through their normalizations is the local dark matter density,  $\rho(r_\odot) = \rho_0$ . Slightly different results are obtained by various authors (see Ref. [11] and references therein). Generally speaking, there are two main methods to derive the local density, either global measurements using the rotation curve of the Milky Way and assuming a spherical dark matter halo, or local measurements using stars near the Sun as kinematic tracers. The measured values of the local dark matter density lie in a range of  $\rho_0 = 0.2 \sim 1$  GeV/cm<sup>3</sup>, with typical  $1\sigma$ -errors of more than 30% of the central value. In the literature,  $\rho_0 = 0.3$  GeV/cm<sup>3</sup> is commonly used [46]. However, as recent works found a slightly

higher central value, we adopt  $\rho \simeq 0.4 \text{ GeV/cm}^3$  in this study. Recent simulations found that the inclusion of baryons can modify the shape of the dark matter halo towards more oblate geometries and lead to an enhancement of the local density [54].

### 1.3 The dark matter particle

Although we have a plethora of gravitational evidence for dark matter (see Sec. 1.1), very little is known about its particle physics properties. There is a wide parameter space in terms of viable dark matter properties such as the dark matter mass or its interactions. Many regions in that parameter space contain well motivated dark matter candidates. The possible masses range from  $10^{-22} \text{ eV}$  [55] to the grand unification scale [56] and the interaction strength spans more than 60 orders of magnitude [57]. The spin of the dark matter particle is also still unknown. However, some dark matter properties are well-founded today and are listed below.

- Dark matter must be **neutral**. Massive charged particles (CHAMPS) have been proposed as dark matter candidates. The combination of various constraints on different mass scales excludes such particles as dark matter [58]. These constraints are for instance derived from searches of heavy water in the oceans of the Earth, where CHAMPS could form heavy hydrogen-like atoms with electrons. Other constraints arise because CHAMPS could modify the galactic and stellar evolution or they could be detected in cosmic ray experiments or underground detectors.

However, it is still viable that dark matter is millicharged, i.e. it carries fractional charge  $\pm \epsilon e$ . These dark matter candidates lie in regions in the mass-charge parameter space that are not excluded by various experiments [59, 60].

- Dark matter must be **cold**. As already discussed in Sec. 1.1.3, dark matter has to be cold enough to allow for structure formation. If the dark matter velocity is too high when the structure starts to form, overdensities are washed out and the observable structure would be much smoother today [58].
- Dark matter must amount to the correct **relic density** today and throughout the evolution of the Universe (see Sec. 1.1.3). Thus, its lifetime must be much larger than the age of the Universe in order to be in agreement with cosmological observations.
- Dark matter must be consistent with the bounds on its **self-interactions**. Robust results on the dark matter self-interaction can be drawn from the Bullet Cluster (see Sec. 1.1.2),  $\sigma/m < 1 \text{ cm}^2/\text{g}$  [27]. Self-interacting dark matter with rather high self-interactions is well studied in the literature as it can solve problems in structure formation, for instance the cusp-to-core problem. Simulations with self-interacting dark matter [61] exhibit flat cores in Milky Way-like galaxies, which is in agreement with observations. From the non-observation of dark acoustic oscillations, it can be inferred that at most 5% of the dark matter can interact very strongly with dark radiation [62].

- Dark matter **cannot** be made of **Standard Model particles**. BBN tells us that dark matter is not baryonic (see Sec. 1.1.3). Thus, quarks are excluded as building blocks of dark matter candidates. It cannot be charged (see above) and therefore charged leptons are ruled out. As explained earlier, dark matter has to be stable on cosmological time scales, which excludes weak gauge bosons and the Higgs boson. Furthermore, it must be massive, so photons cannot be dark matter. Gluonic states would interact strongly with SM particles and are therefore excluded (see below). Neutrinos cannot be the dark matter. Given the cosmological bound on the neutrino mass of 0.6 eV and the neutrino abundance, it can only contribute to at most a tenth of the dark matter abundance. Furthermore, neutrinos would be hot dark matter, in disagreement with structure formation [63].
- Dark matter must be **color-less**. This conclusion can be drawn from the combination of various constraints, namely from the Earth’s heat flow, the disruption of spiral galaxies through strongly interacting dark matter, from underground and balloon experiments as well as from neutrino production in the Sun [64]. These constraints do not only apply to dark matter particles with QCD interactions with baryons, but also to other interactions of this strength. Thus, dark matter must be truly weakly interacting with baryonic matter.

In this thesis we focus on a very well motivated class of dark matter candidates, so-called WIMPs (Weakly Interacting Massive Particles), which have all these required properties. The reason for their popularity is two-fold: Dark matter particles with masses of the order of the weak scale and with a weak interaction strength naturally acquire the correct relic abundance via thermal freeze-out. This is the so-called “WIMP miracle” and is further explained in Sec. 1.3.2.1. The second reason to believe in WIMP dark matter is the hierarchy problem. Unlike the Standard Model fermions or gauge bosons, the Higgs mass suffers from large quantum corrections. They are quadratic in the cutoff-scale  $\Lambda$ , i.e. the scale up to which the theory is valid. If there is no new physics up to the Planck scale  $\Lambda \sim 10^{18}$  GeV, the parameters of the theory must be fine tuned in order to obtain the measured Higgs mass [65]. In theories that were invented to solve the hierarchy problem, new physics at the weak scale is introduced. Then a dark matter candidate of WIMP type naturally emerges, as for instance in supersymmetry or in theories with extra dimensions (see Sec. 2.2.1).

Furthermore, the mass range where to expect the WIMP dark matter particle is bounded from above and below. These bounds will be briefly discussed below. Although the WIMP miracle is very appealing, a variety of other production mechanisms are put forward in the literature. The results derived in this thesis on spectral features do not require thermal freeze-out and are thus valid irrespective of the dark matter production mechanism.

There is no reason to believe that dark matter is absolutely stable as long as its lifetime is much larger than the age of the Universe. Decaying dark matter leads to similar signatures as annihilating dark matter and can therefore be searched for employing the same strategies. The main features of decaying dark matter will be discussed in the following section. Subsequently, the WIMP mechanism is explained and alternative production mechanisms are briefly presented.

### 1.3.1 Unstable dark matter

That dark matter today exhibits the correct relic abundance is a crucial requirement for any particle physics model. However, the dark matter particle does not have to be absolutely stable, although its lifetime must be much larger than the age of the Universe in order to be abundant today. The origin of the long lifetime can be understood in analogy to the proton stability [66]. A proton could in principle decay into a positron and a neutral pion  $p \rightarrow e^+ \pi^0$ . From the non-observation of this process, a lifetime of  $\tau > 8.2 \cdot 10^{33} \text{ yr}$  is inferred. This long lifetime has its origin in baryon number conservation, an accidental symmetry in the renormalizable part of the Standard Model Lagrangian that could be broken by higher dimensional operators. The same principle could be responsible for a very long dark matter lifetime. If the dark matter decay arises through higher dimensional operators, the rate is suppressed by the cutoff scale  $M$  to some power. For dimension six operators it follows from dimensional analysis [67]:

$$\Gamma \propto \frac{1}{M^4} m_{\text{DM}}^5. \quad (1.10)$$

This yields

$$\tau = 10^{27} \text{ s} \left( \frac{1 \text{ TeV}}{m_{\text{DM}}} \right)^5 \left( \frac{M}{10^{16} \text{ GeV}} \right)^4. \quad (1.11)$$

This lifetime range is very interesting from the observational point of view today, as many experiments are now sensitive enough to detect signals from such a dark matter decay. Special attention was put on decaying dark matter in the light of the PAMELA anomaly (see Sec. 1.4). Decaying dark matter models were put forward in order to explain this positron excess (see e.g. Ref. [66]). A dark matter candidate that has about the right lifetime to explain the rise of the positron fraction is the gravitino. Emerging from supersymmetry, it is a natural dark matter candidate that could well fit the measurements. However, gravitino dark matter as the unique source of positrons in the excess is by now ruled out by gamma-ray observations and the high-precision positron measurements of AMS-02 [68].

### 1.3.2 Dark matter production

In general, dark matter production scenarios can be divided in two classes: thermal production and non-thermal production [69]. The candidates, however, cannot be easily split in these two categories because there are dark matter candidates that can be produced thermally or non-thermally, as the gravitino for instance. In this section, the focus lies on scenarios relevant for dark matter candidates that can produce anti-matter and gamma-ray signatures.

#### 1.3.2.1 Thermal relics

The WIMP miracle is maybe the best reason to expect dark matter at the weak scale. It arises in the computation of the dark matter relic abundance when dark matter is thermally produced through the freeze-out mechanism. Qualitatively, the production of thermal relics can

be understood as follows [70]: When the temperature of the thermal plasma is much larger than the dark matter mass  $T \gg m_{\text{DM}}$ , dark matter is in kinetic and chemical equilibrium with the Standard Model particles,  $\text{SM SM} \leftrightarrow \text{DM DM}$ . As the Universe cools down, the dark matter number density becomes exponentially suppressed since only Standard Model particles in the tail of the Boltzmann distribution have enough kinetic energy to produce a pair of dark matter particles, whereas the annihilation of dark matter continues. The equilibrium number density for a non-relativistic particle is given by [70]

$$n_{\text{eq,DM}} = g \left( \frac{mT}{2\pi} \right)^{3/2} e^{-m/T}, \quad (1.12)$$

where  $m$  is the dark matter mass and  $g$  the number of internal degrees of freedom of the dark matter particle. For a non-expanding universe, this exponential suppression continues until the dark matter density vanishes. In an expanding Universe, however, the number density gets diluted additionally through the expansion. When the interaction rate is smaller than the Hubble expansion rate, the annihilation of dark matter particles is not efficient any more. Then the number density becomes constant per comoving volume, i.e. it freezes out (chemical decoupling). For any thermal relic, the evolution of the number density can be calculated quantitatively from solving the Boltzmann equation [70]:

$$\frac{dn}{dt} + 3Hn = -\langle \sigma v \rangle (n^2 - n_{\text{eq}}^2), \quad (1.13)$$

with the number density of dark matter particles  $n$ , the Hubble constant  $H$ , the cross section  $\sigma$ . The brackets indicate the thermal average. After combining this equation with the corresponding equation for the entropy density  $s$  and a change of variables, introducing the comoving number density  $Y = n/s$  and  $x = m/T$ , the resulting equation can be solved numerically [71]. A qualitative visualization of the solution to this equation is plotted in Fig. 1.6. The smaller the thermally averaged cross section, the larger is the relic density. Since dark matter is non-relativistic at freeze-out, the thermal cross section is typically expanded in powers of  $v$ ,  $\langle \sigma v \rangle \approx a + 6b/x$  [6], the first term being the s-wave and the second term the p-wave contribution. The solution for late times corresponds to the relic density and can be cast as [73]

$$\Omega h^2 \simeq 0.1 \left( \frac{x_{\text{f.o.}}}{20} \right) \left( \frac{60}{g_{\text{eff}}} \right)^{1/2} \frac{3 \cdot 10^{-26} \text{ cm}^3/\text{s}}{a + 3b/x_{\text{f.o.}}}, \quad (1.14)$$

where  $x_{\text{f.o.}} = m/T_{\text{f.o.}}$  is the particle mass divided by the freeze-out temperature  $T_{\text{f.o.}}$  and  $g_{\text{eff}}$  is the effective number of degrees of freedom in the thermal bath.  $g_{\text{eff}}$  amounts to about 60 at  $T = 1 \text{ GeV}$  and 90 at  $T = 100 \text{ GeV}$ .  $x_{\text{f.o.}}$  values of the order of 20 can be estimated from the following consideration [67]. Chemical decoupling occurs when the annihilation rate equals the Hubble expansion rate. Then the dark matter density is so diluted that annihilations cannot take place anymore. This means

$$\Gamma = \sigma n = H. \quad (1.15)$$

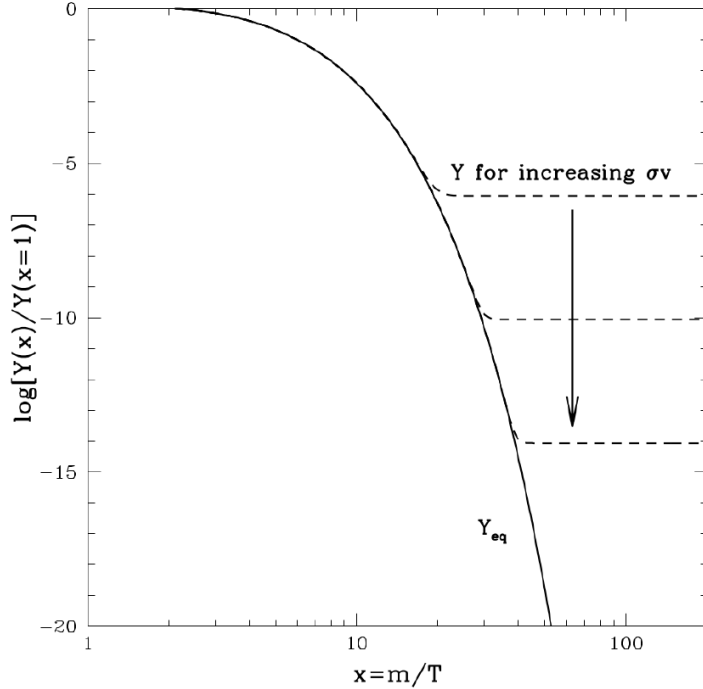


Figure 1.6: The qualitative behavior of the comoving number density  $Y$  as a function of  $x$ . The figure is taken from Ref. [72].

Plugging in Eq. (1.12) for the number density and  $H \sim T^2/M_P$  yields for  $x = m/T$ :

$$\sqrt{x}e^{-x} = \frac{1}{m M_P \sigma} \sim 10^{-14} \quad (1.16)$$

for a 100 GeV WIMP and a weak interaction cross section  $\sigma \propto G_F^2 m^2$ , where  $G_F$  denotes the Fermi constant. Thus,  $x_{\text{f.o.}} \approx 30$ . This value does not depend strongly on the WIMP mass and cross section. Typically,  $x_{\text{f.o.}} \sim 20 - 30$  for WIMP masses in the GeV to TeV range with featuring weak cross sections is obtained. Plugging that value in Eq. (1.14) now shows that just about the right relic abundance is acquired for dark matter masses at the weak scale and a typical weak cross section of  $3 \cdot 10^{-26} \text{ cm}^3/\text{s}$ . This value of the WIMP cross section is commonly referred to in the literature. For s-wave annihilations, this cross section can be compared to the bounds for the cross section today found in indirect searches (see below), as  $\langle \sigma v \rangle_{\text{f.o.}} \approx \langle \sigma v \rangle_{\text{today}}$ . In other cases, for instance for annihilations with large p-wave contributions, when a resonance in the cross section is met or when threshold effects become relevant, the values for the cross section at freeze-out and today are numerically different. Care must also be taken if there are other particles ( $\text{DM}'$ ) with masses similar to the WIMP mass that share a quantum number with it. Then co-annihilations, for instance  $\text{DM DM}' \rightarrow \text{SM SM}'$  are possible and must be taken into account. In these cases, the Boltzmann equation must be modified accordingly [6].

The freeze-out mechanism is of course not restricted to  $\mathcal{O}(100 \text{ GeV})$  dark matter particles. A thermal WIMP, however, cannot arise at any arbitrary mass. Its mass range is bounded both

from above and below. The upper bound is the so-called unitarity bound and follows from partial wave unitarity [74]. A Dirac (Majorana) fermion that was in thermal equilibrium in the early Universe, cannot be heavier than 84 TeV (118 TeV). In this calculation the most recent determination of the relic density [35] is used. These estimates also hold for complex (real) scalars. The lower bound on the thermal WIMP mass, however, is still discussed in the literature (see Ref. [75] and references therein). An early result on the lower bound of the WIMP mass can be found for instance in Refs. [76, 77]. It is called Lee-Weinberg bound and arises for weakly interacting fermions, often quoted with  $m_{\text{DM}} > 2 \text{ GeV}$ . Fermionic WIMPs below this mass would be overproduced at freeze-out. However, there are models proposed where this limit can be evaded. A model-independent lower bound of about 0.1 keV arises for fermionic dark matter from the phase space distribution in dwarf galaxies [78]. The requirement that dark matter cannot be hot at the time of structure formation leads to a lower bound of  $\mathcal{O}(\text{keV})$  for the dark matter mass [75].

Of course the WIMP miracle is not a proof that dark matter is a WIMP and the miracle could merely be a coincidence. But from the theoretical point of view, the WIMP relic density is produced in a very natural way, whereas in many other scenarios fine tuning is required. Thus, it is a strong motivation to investigate stable weakly interacting massive dark matter particles theoretically and to conduct dedicated experimental searches. This motivation is further strengthened by the fact that a WIMP dark matter candidate also emerges from theories that solve the hierarchy problem (see Sec. 1.3). In fact, the lightest supersymmetric neutralino was probably the most popular and most widely discussed dark matter candidate through the past decades.

### 1.3.2.2 Beyond freeze-out

The thermal freeze-out mechanism is described in Sec. 1.3.2.1. Thermal production, however, does not only refer to the freeze-out mechanism, but also to other thermal production processes, such as the so-called freeze-in mechanism. In this scenario, the correct relic density can be obtained as well. The corresponding dark matter candidate is even less than weakly interacting, and is dubbed superWIMP. It can be produced in scatterings of other particles in the thermal plasma. In the freeze-in framework, the dark matter abundance increases until the scatterings in which the superWIMPs are produced cannot take place any more. An example for such a dark matter candidate, which can acquire the correct relic abundance through thermal freeze-in, is the gravitino [79]. Even if a particle's abundance is thermally overproduced, it can still be a good dark matter candidate. A mechanism that dilutes the dark matter density must be invoked in order to make these candidates viable again. An example of such a mechanism is late time inflation [80].

Non-thermal production can again be divided into various scenarios. In the following two examples are briefly explained (for extensive discussions see Refs. [69, 81]).

A possible scenario is that dark matter consists of decay products from heavier particles.

The heavy particles can be thermally produced. In this case, the dark matter inherits the relic abundance from its progenitor. This is for instance the second option for gravitino production. The gravitino abundance could emerge from the decay of thermally produced WIMPs. On the other hand, the heavy particle can as well be produced non-thermally itself, as it is the case for the inflaton. This kind of production mechanism could also lead to a non-thermal production of WIMPs.

Another possible scenario is asymmetric dark matter. The observation that the baryon and dark matter abundance are of the same order,  $\Omega_{\text{DM}}/\Omega_B \approx 5$ , could suggest that the production of dark matter and baryons are related. The production mechanism of asymmetric dark matter is thus similar to the baryogenesis process, which gives rise to the baryon asymmetry. This asymmetry between matter and antimatter is the reason why all the antimatter is annihilated away, while only matter remains. Therefore we observe that the Universe consists mostly of matter.

## 1.4 Dark matter searches

A lot of experimental effort is undertaken in order to search for the dark matter particle and uncover its properties. Interestingly, WIMP dark matter is now in reach of many experiments that have not been (exclusively) designed for its search, such as cosmic-ray experiments, or ground based and balloon borne telescopes. The exquisite results from these experiments can also be used to search for decaying dark matter candidates with similar masses.

Generally, there are three main approaches to search for dark matter and eventually identify its particle physics properties. These are direct detection, production at colliders and indirect detection. The latter strategy is employed in this thesis to constrain annihilating and decaying dark matter.

### 1.4.1 Direct searches

The idea of direct dark matter searches is to measure the nuclear recoils induced by a dark matter particle passing through the detector. Most of the direct detection experiments are low background experiments, i.e. all backgrounds have to be suppressed or must be precisely known in order to identify recoils induced by WIMPs. Thus these experiments are conducted in underground laboratories, in order to suppress the cosmic-ray background, and are surrounded by various layers of shielding for the different kinds of backgrounds, namely muons, neutrons and gamma rays for instance [82]. The experiments can be divided into three categories: cryogenic crystal detectors [83], liquid noble gas detectors [84] and superheated liquid experiments [82]. In order to identify a WIMP-nucleus interaction and to discriminate it from the remaining background events, either scintillation light, ionization, phonons or a combination of these signals is used. In superheated liquids, a nuclear recoil leaves a signature as in a bubble chamber.

Depending on the target nucleus, the experiment is sensitive to the spin-independent, or in case

of unpaired nucleons in the nucleus, also to the spin-dependent WIMP-nucleon scattering. Due to the resonant enhancement, the spin-independent WIMP-nucleon cross section is proportional to the square of the mass number  $\sigma \propto A^2$ , and is in general better constrained than the spin-dependent cross section. The latter is only proportional to the spin of the nucleus  $J(J+1)$  and thus leads to weaker limits [85]. Further important quantities that enter the calculation of the event rate in the detector are the nuclear form factor, the WIMP velocity distribution and the local dark matter density. The main theoretical uncertainties here are the velocity distribution and local dark matter density. Thus, effort is undertaken in order to determine halo independent direct detection limits [86, 87].

In addition to the aforementioned experiments, there is an alternative approach in order to directly detect WIMP-nucleus interactions. These experiments search for an annually modulated dark matter signal on top of a constant background. Such a modulation of the dark matter signal is expected due to the relative velocity of the Earth in the dark halo, leading to an annual modulation in the WIMP signal with a maximum on June 2<sup>nd</sup> [85, 88]. This modulation can show up in addition to a constant background. Indeed, such a modulation is found by the DAMA/LIBRA Collaboration and it is measured now with a statistical significance of  $8.9\sigma$  [88]. However, it is difficult to reconcile this signal with the null results obtained by most other experiments [89].

### 1.4.2 Collider searches

A second possibility to search for dark matter is to produce it in a particle collider and search for specific experimental signatures associated with the dark matter production. Typically, such a signature is a single jet or photon, for instance, plus missing energy, because the dark matter particles evade detection [90]. These so-called mono-X searches are conducted at the Large Hadron Collider (LHC), a prime experiment to produce dark matter due to its high center of mass energy. Many LHC dark matter limits are based on effective theories of dark matter, where a heavy mediator particle can be integrated out, and operator by operator is constrained [91]. However, as the LHC is probing physics at very high energies, it is questioned in the literature whether the effective field theory is still valid at the energies involved [92]. As an alternative, one can instead constrain simplified models, i.e. benchmark scenarios for more complicated theories, such as supersymmetry for instance [93]. Commonly, LHC results for dark matter are compared to the results from direct detection experiments. Typically the results on spin-dependent interactions supersede the ones from direct detection experiments [90]. However, a discussion is ongoing about the best way to compare results from direct detection experiments to collider searches. Note that it is not possible to determine whether a new particle is long-lived enough to be a good dark matter candidate with the LHC.

### 1.4.3 Indirect searches

The third strategy to uncover the nature of dark matter is the indirect search. Concretely, one searches for signatures of dark matter annihilations or decays in gamma-rays, charged cosmic-rays or neutrinos. In the following a brief overview of possible messengers and target regions is given. In the rest of this thesis we focus on positrons and Galactic gamma rays.

Generally speaking, the region of interest is chosen in order to maximize the signal for a given background and particle species. In principle, the region of interest could be galactic or extragalactic. Depending on the instruments, the backgrounds can be different and optimal targets may vary accordingly.

In the case of cosmic rays, one often chooses anti-particles to search for dark matter [94], because they naturally have a lower background and a possible dark matter signal can be detected more easily. Cosmic rays are confined to our Galaxy up to rigidities of about  $10^{17} \text{ ZeV}$  [95] and are of galactic origin in this energy range. The different species, however, probe a very different volume of the Galaxy. Charged particles do not propagate freely in the Milky Way, but they undergo scatterings on the random component of the Galactic magnetic fields. This means that they diffuse through the Galaxy and (almost) any directional information about their origin is lost. The volume probed by different particles depends on the diffusion properties and the relevant energy loss processes of the cosmic rays. Positrons originating from a 100 GeV dark matter particle, and that are detected at Earth stem from a sphere of only a few kpc around the Sun, whereas anti-protons from such a dark matter particle can probe the Galactic center [63]. In addition to positrons and anti-protons, anti-nuclei such as anti-deuterons [94] or anti-helium [96, 97] are considered in dark matter searches.

Gamma-rays propagate on straight lines from their origin to the location of detection. Thus, instruments search for signals in regions where a large dark matter signal is expected [98]. In the case of annihilations a rather small region around the Galactic center is commonly chosen, for decays usually larger regions are taken. Other possible targets are (larger regions of) the Galactic halo, dwarf galaxies, galaxy clusters or even unidentified point sources that could be dark matter subhalos. A further possibility is to search for a dark matter signal from all the halos in the Universe in the extragalactic background [98].

In terms of target regions, the situation for neutrinos is similar to the one of gamma-rays [94]. However, there is an extra class of targets for neutrino telescopes compared to gamma rays, namely heavy celestial bodies like stars or the Earth, where dark matter is captured and can accumulate. The neutrinos from dark matter annihilation can escape the heavy body and reach the detector [99, 100]. Commonly the neutrinos from the Sun are investigated in this kind of studies. However, if capture and annihilation are in equilibrium, the quantity that is constrained is not the annihilation cross section as in practically all other indirect searches, but the scattering cross section with nuclei, which has to be compared to direct detection constraints [101].

So far, no unambiguous dark matter signal has been found. Thus, only constraints on the dark matter lifetime and annihilation cross section can be derived. In particular, limits can be set on

the various annihilation channels using the different messengers. As a result, many dark matter models are severely constrained when they are confronted with all observations. However, we currently live in an exciting era of indirect dark matter searches. In fact, many possible indirect dark matter signatures have been identified in the fluxes of different messengers at very different energy scales. Two of these possible signals can be explained by WIMP dark matter:

- **The Galactic center excess**

Lately, a bump-like signal that peaks at about 2 GeV was found in gamma-rays data from the Galactic center [102]. The origin of this excess is still debated in the literature, be it astrophysical, such as millisecond pulsars [103], a recent burst-like event [104], or the signal of dark matter annihilations. Nonetheless, it is intriguing that the spectrum and morphology is very well described by a vanilla dark matter candidate annihilating e.g. into  $b\bar{b}$ , with a cross section of a few times  $10^{-26} \text{ cm}^3/\text{s}$  and a slightly contracted NFW profile [105].

- **The positron excess**

The measurement of the anomalous positron fraction by the PAMELA experiment [106] revealed that in addition to conventional secondary positron production an extra source of high-energy positrons is needed in order to explain the observations. Positrons are known to be produced in spallation processes of primary cosmic rays with interstellar matter in the Galaxy. However, the resulting positron fraction, i.e. the ratio of the positron flux and the total  $e^- + e^+$  flux, is expected to decrease with energy. Instead of this behavior, a rising positron fraction was measured above 10 GeV. Indeed, the positron flux from dark matter annihilations or decays provides a good fit to the excess. However, other positron measurements with increasing precision by the AMS-02 instrument and limits from other messengers severely constrain the corresponding dark matter models [107]. In addition to the dark matter interpretation, astrophysical sources have been considered as the explanation of the positron anomaly. In fact, positrons produced by one or several pulsars, positron production inside the sources of primary cosmic rays, or positrons originating from a nearby gamma-ray burst can reproduce the measurements (see Sec. 2.1).

In addition to these possible WIMP signatures, other potential signals also aroused a lot of interest recently. A X-ray line at  $\sim 3.5 \text{ keV}$  has been found in an analysis of the Chandra and XMM-Newton data of galaxy clusters [108]. This line could be explained by the decay of a sterile neutrino into an active neutrino and a photon. However, the correct treatment of the background from atomic transition lines in this search is still discussed in the literature [109, 110]. Furthermore, the IceCube neutrino telescope has observed events at PeV energies [111]. Also in this case, a dark matter explanation has been invoked (see e.g. Refs. [112, 113]). On the other hand, neutrinos of these energies are for instance expected from sources that can accelerate cosmic rays to ultra-high energies [114].

## 1.5 Relevance of spectral features

Spectral studies have played an important role in discoveries in chemistry, physics and astronomy, since they were first employed by Isaac Newton in the 17th century. One of the most prominent examples of historically important spectral observations are probably the Fraunhofer lines, dark lines in the optical spectrum of the Sun. They are named after Joseph von Fraunhofer, a German optician, who thoroughly studied these features and measured their wavelengths in 1814. Later, these lines were identified as absorption lines of chemical elements in the atmospheres of the Sun and the Earth [115]. Thus, the Faunhofer lines are used to deduce the chemical composition of the Sun and its temperature. Until today the analysis of spectra plays a key role in astrophysics. Again, Fraunhofer lines are used to identify the temperature and chemical composition of stars and to classify them accordingly [116]. Furthermore, the composition of the interstellar medium in galaxies, including the Milky Way, is determined from absorption and emission spectra [117].

Analogously, the observation of spectral features from dark matter annihilations and decays can be used to uncover the nature of the dark matter particle. The energy at which the spectral feature occurs is related to the dark matter particles mass, for instance, and the type and strength of the feature are related to the particle physics properties of dark matter. In indirect dark matter searches not only features in the electromagnetic spectrum, namely in gamma-rays for the masses of interest in this thesis, but also features in the spectra of other kinds of messenger particles are searched for. These can be all particle species used in indirect searches, see Sec. 1.4.3. In this thesis, electron and positron spectra are investigated in addition to gamma-ray spectral features.

Apart from the particle physics information that spectral features can provide, there is another big advantage of using of sharp features in dark matter searches. The astrophysical background that has to be taken into account, is expected to be smooth at GeV to TeV energies. It can be well described by a simple power law, at least locally in a limited energy range. Thus, spectral features are very distinct from the background and can be searched for efficiently. This is a great benefit with respect to searches for continuous, broad spectra that are commonly analyzed in dark matter searches employing different experimental and statistical techniques. In order to cover a broad variety of possible final states in dark matter annihilations and decays it is crucial to pursue both approaches.

## **Part II**

# **Dark matter searches with positrons**



# **Chapter 2**

## **Phenomenology of cosmic-ray electrons and positrons**

This chapter is dedicated to the phenomenology of electrons and positrons. First, electrons and positrons of astrophysical origin, which constitute the background for dark matter searches with positrons, are discussed. Afterwards, the positron signals produced in dark matter annihilations and decays and the corresponding spectra are introduced. Even though our results are completely model-independent, we briefly present examples of models that can produce the spectral features investigated in this thesis. Irrespective of their origin, cosmic rays diffuse from their sources through the Milky Way until they are eventually detected at Earth. Therefore, the propagation of charged particles is described and specified for the case of electrons and positrons. Subsequently, the positron experiments whose data is employed in this work in order to derive limits on the dark matter parameters are presented.

### **2.1 Astrophysical electron and positron background**

In the search for excesses or dark matter signals in the positron flux, the precise knowledge of the cosmic-ray backgrounds is crucial. Cosmic rays, as energetic charged particles from outer space are commonly referred to, have been studied for more than 100 years now. Today, their composition and spectrum are precisely measured [29]. Roughly speaking, the largest contribution consists of protons with about 79% in mass followed by  $\alpha$  particles with about 15%. Electrons as well as heavier nuclei and antimatter contribute each less than 1%. Up to energies of  $10^{15.5}$  eV the all-particle cosmic-ray spectrum is well described by a featureless power law with index 2.7. The steepening to an index of 3.1 [118] is often denoted “knee”. Above  $10^{17}$  eV, the so-called “second knee”, the spectrum gets softer again but hardens at the “ankle” at  $10^{18.5}$  eV until it is cut off above  $\sim 5 \cdot 10^{19}$  eV. Explanations for the breaks in the power law are put forward in the literature. Below the knee, the dominant contribution are primary cosmic rays, accelerated in supernova remnants via Fermi acceleration in the shock wave of expanding gas created by the supernova explosion [119]. The knee can be explained for instance by the acceleration mechanism itself leading to a break in the source spectra or by less efficient confinement of the cosmic rays in the Galaxy at these energies [118]. The ankle is thought to indicate the transition to a harder

extragalactic cosmic-ray component. The cutoff is most likely explained by the GZK effect, i.e. the efficient energy loss of protons in scatterings with CMB-photons, where at the cutoff energy the  $\Delta^+$ -resonance is met [29].

Cosmic-ray electrons and positrons constitute only a small fraction of the total cosmic-ray fluxes. The total  $e^- + e^+$  spectrum has been observed up to energies of 1 TeV by the AMS-02 experiment [120] and at higher energies by the H.E.S.S. telescope [121].

As the other primary cosmic-ray species, cosmic-ray electrons originate mainly from supernova remnants and are accelerated in shock waves. The resulting electron injection spectrum is constrained by radio observations of the synchrotron radiation emitted by these electrons. In Ref. [122] a spectral index of 2 is found, which is in good agreement with the expectation from Fermi shock acceleration. The determination of the normalization of the source spectrum, however, is a difficult task. It depends on the supernova explosion rate in our Galaxy, the total energy output in the explosion and the energy fraction that is released in the form of electrons. The product of these quantities determines the source normalization and exhibits uncertainties of several orders of magnitude [122]. The spatial distribution of the electron sources is given by the distribution of supernova remnants. In many models, a smooth distribution of supernova remnants in the Galaxy is assumed [122]. Gamma-ray observations indicate that the cutoff energy of the electron source spectrum is greater than a few TeV [122].

A subdominant contribution to the cosmic-ray fluxes is of secondary origin, created in spallation processes of hadronic cosmic rays and the interstellar medium. In fact, these processes give rise to cosmic-ray anti-matter and are the origin of cosmic-ray positrons. Generally speaking, the secondary cosmic-ray fluxes are more than one order of magnitude smaller than the primary fluxes. Thus, the anti-matter fluxes are always weaker than the corresponding matter fluxes. This is the reason why a dark matter signal is typically searched for in the anti-matter fluxes and not in the matter fluxes, which are dominantly of primary origin.

Among lighter nuclei, neutrons, protons and pions are produced in spallation processes. Secondary electrons and positrons originate from the decays of the charged pions. Regarding the abundances, the largest contribution to positron production originates from collisions of protons and  $\alpha$  particles with hydrogen and helium in the Galaxy [123]. In order to predict the secondary cosmic-ray positron flux, various quantities must be determined: the spallation cross sections, the primary cosmic-ray fluxes and the composition and distribution of the interstellar matter. Indeed, our imperfect knowledge of these quantities constitutes the main uncertainty in the computation of the secondary positron flux [123].

For a long time, the interstellar positron flux was believed to constitute mainly of secondary particles. However, through the measurement of the anomalous positron fraction by the PAMELA experiment [106] it became apparent that the positron flux cannot be explained by conventional secondary production above  $\sim 10$  GeV. This anomaly has been confirmed not only by the Fermi-LAT [124] telescope but also up to 500 GeV [125, 126] by the AMS-02 experiment with high precision. Fig. 2.1 shows the positron fraction together with the calculated secondary production

## 2.1 Astrophysical electron and positron background

---

depicted by the black line. The discrepancy at low energies can be lifted by taking into account

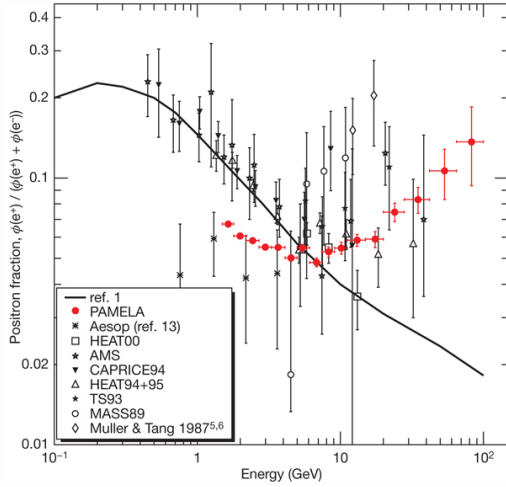


Figure 2.1: Measurements of the positron fraction of the PAMELA experiment and other instruments taken from Ref. [106] together with the calculated positron flux from Ref. [127] (black line), which is Ref. 1 of that article.

solar modulation (see Sec. 2.3.4), whereas at high energies a positron excess is found. Concretely, the positron fraction rises at energies above about 10 GeV, while a decreasing fraction is expected from pure secondary production in the interstellar medium. It has been thought that this rise in the positron fraction could be due to a deficit in electrons instead of an excess in positrons, but this possibility has been ruled out by the precise measurements of the electron plus positron flux by Fermi-LAT [128], providing complementary information to the positron fraction. Also in the  $e^- + e^+$  flux measurements an excess with respect to conventional cosmic-ray physics is observed, which is consistent with the additional source inferred from the PAMELA positron fraction. However, a tension was found between the AMS-02 positron fraction and the Fermi-LAT  $e^- + e^+$  flux with respect to conventional cosmic-ray propagation models, which can however be resolved with a broken power law primary injection spectrum [129].

The cosmic-ray lepton excesses have drawn a lot of attention to primary electron and positron sources, which have subsequently been extensively investigated in the literature. In fact, a variety of astrophysical sources can explain the positron anomaly: Positrons from one or several pulsars, positron production inside the sources of primary cosmic rays, and positrons from a nearby gamma-ray burst are able to reproduce the measurements. These possible solutions to the cosmic-ray lepton puzzle are summarized in the following. In addition, dark matter annihilations or decays have been invoked to explain the excess and are also briefly discussed below for completeness.

- **Pulsars**

Pulsars are rapidly spinning magnetized neutron stars that are predicted to emit positrons with a spectrum that is harder compared to secondary production. In the pulsar's magne-

tosphere electrons and positrons can be accelerated and initiate an electromagnetic cascade through the emission of curvature radiation. The radiated photons in turn are energetic enough for the pair production of electrons and positrons, which are then accelerated themselves in the strong magnetic fields of the pulsar [130]. Both the positron contribution from nearby pulsars as well as the contribution from all known pulsars in the Galaxy that are listed in pulsar catalogs can explain the cosmic-ray electron and positron anomalies [131, 132]. However, the pulsar parameters, the spin down energy, the conversion factor of the total energy output into electron positron pairs, the distance from the Solar system, the age and the spectrum are not well known. It is thus not surprising that within the uncertainties of these parameters the positron anomalies can be accommodated in various ways [133]. A feature that could potentially identify the positron flux from many pulsars is the structure at high energies in the positron spectrum that results from the superposition of the individual pulsar spectra [132]. Despite the diffusion of electrons and positrons, a nearby pulsar that can produce the excess positron flux is expected to generate a positron anisotropy. The detection of such an anisotropy would thus point towards nearby pulsars as the explanation of the positron excess [131].

- **Production inside cosmic-ray sources**

Electrons and positrons can be produced by spallation processes not only in the interstellar medium but also inside the same sources that accelerate primary cosmic rays [134]. Thus secondary positrons are accelerated in the shock front of the supernova remnant together with the primary particles. The spectrum of the accelerated secondary positrons is expected to be significantly harder than the spectra of the primaries [135]. Analogously, the same behavior is predicted for other secondary cosmic-ray species. Not only the contribution of the ensemble of all supernova remnants is investigated, but also the contribution of a single nearby remnant provides a good fit to the cosmic-ray lepton fluxes [136]. However, there is a discussion ongoing in the literature to what extent the B/C ratio measured by AMS-02 is compatible with this scenario since the resulting spectra depend on the details of the propagation as well as on the local environment inside the cosmic-ray sources [137, 138].

- **Nearby Gamma-ray burst**

Gamma-ray bursts are the most luminous objects in the Universe. The short (1-100 sec) flashes of collimated gamma-rays are thought to be associated with the collapse of a massive star that evolves in a black hole or a neutron star. In the burst, electron-positron pairs can be created via the process  $\gamma\gamma \rightarrow e^+e^-$ . A single burst event  $\sim 6 \cdot 10^5$  yr ago at a distance of  $\sim 1$  kpc to the Earth can explain the positron excess [139].

- **Dark matter**

As another possible interpretation of the positron excess dark matter annihilations and decays have been invoked. Dark matter annihilations into various final states provided a good fit to the PAMELA lepton data. The corresponding dark matter models, however,

are severely constrained by the absence of the associated signals in antiprotons or and gamma-rays [140]. Dark matter annihilations into intermediate particles that later decay into  $\mu^+\mu^-$  or  $\pi^+\pi^-$  [107], for instance, remain a viable option in view of the precise AMS-02 data. For the explanation of the positron excess with dark matter annihilations, however, the cross section must be enhanced with respect to the expectation from a thermal relic. This could be achieved either by the Sommerfeld effect [141], i.e. resonant enhancement through the exchange of force carriers [142] (see also Sec. 5.3.2), or by boosts due to dense substructure in the dark matter halo of the Milky Way [143, 144].

## 2.2 Positrons from dark matter

The idea to constrain dark matter using a positron line was put forward already in 1989 [145, 146]. In dark matter annihilations typically both electrons and positrons are produced. As the astrophysical background for positrons is lower by a factor of  $\sim 10 - 20$  compared to electrons, the positron signal from dark matter annihilations or decays is used to derive limits. Spectral features that can be searched for with positron data are not only produced in the direct annihilation or decay into electron and positron pairs, but also in annihilations into other channels such as  $\mu^+\mu^-$ . Even though these features are smeared out due to the propagation of charged particles in the Galaxy, the peak in the positron spectrum is still pronounced enough to lead to severe constraints on positron “lines”. Furthermore, channels that exhibit a soft positron spectrum are worth considering since the limits from positrons are complementary to constraints from other messengers.

A broad variety of models that yield positron spectral features have been discussed in the literature. Some examples of such models will be briefly described in the following. As the final states considered in this thesis are common to a plethora of dark matter models, but the branching ratios are strongly model-dependent, the bounds on the dark matter cross section are presented in a model-independent way, assuming always 100% branching fraction into the respective final states.

### 2.2.1 Dark matter models with sharp positron features

In this section, we discuss classes of models in which positron spectral features can emerge. Annihilation or decay into charged leptons is a very generic feature present in a variety of dark matter models. The scenarios listed in the following serve merely as an illustration of the broad applicability and relevance of the results derived in the remainder of this part of the thesis and is by no means exhaustive. Concretely, some specific analyses are mentioned that make use of the positron limits derived in this thesis.

- **Kaluza Klein dark matter**

In theories with universal extra dimensions (UED) all Standard Model fields can propagate

in the extra dimensions [147]. In such theories a tower of Kaluza Klein (KK) particles is predicted. At tree level the masses read [148]

$$m_{X^{(n)}}^2 = \frac{n^2}{R^2} + m_{X^{(0)}}^2, \quad (2.1)$$

where  $X^{(0)}$ , the zero mode, is the Standard Model field and  $X^{(n)}$  the  $n$ -th Kaluza Klein excitation. As the inverse of the size of the extra dimension  $R^{-1} \sim \text{TeV}$  is much larger than the mass of any Standard Model particle, the KK spectrum of a given level  $n$  is highly degenerate. This degeneracy, however, is lifted by loop corrections and thus all KK excitations will eventually decay into the lightest KK particle, which is stable due to conservation of KK parity [148]. The first excitation of the hypercharge gauge boson  $B^{(1)}$ , for instance, is a viable dark matter candidate with a large annihilation cross section into electron positron pairs [149]. The branching ratio amounts to about 20% [148]. The KK photons annihilate through diagrams with the first excitation of the electron in the t- or u-channel. Annihilations into muons and taus occur with about the same branching fractions. For  $R \gtrsim 800 \text{ GeV}$ , the KK photon  $B^{(1)}$  is indeed the lightest KK particle in 4+1 dimensions. Depending on the details of the model, the relic density is achieved for KK photons with  $m_B^{(0)} = 600 \sim 1050 \text{ GeV}$  [149]. UED scenarios can be constrained with various strategies in present and future direct and indirect detection experiments as well as collider searches (see e.g. Refs. [148, 150–155]).

- **Supersymmetric dark matter**

In supersymmetry (SUSY) [156] every Standard Model particle has a supersymmetric partner, where the partners of the fermions are bosons and vice versa. In exact SUSY the supersymmetric particles have the same masses as their Standard Model partners. Thus supersymmetry must be broken in order to obtain supersymmetric particles with large enough masses in agreement with observations. Furthermore, one additional Higgs doublet must be introduced in order to achieve correct mass generation of the Standard Model particles and gauge anomaly cancellation. The dark matter candidate that naturally emerges in such a scenario is the lightest neutralino. It is the mixture of the fermionic partners of the neutral bosons in the Standard Model, the neutral electroweak gauginos, the wino and the bino, and the two neutral higgsinos and is stable due the conservation of a  $Z_2$  symmetry under which all supersymmetric particles are charged. This symmetry is called  $R$ -parity and was introduced in order to forbid rapid proton decay. The lightest neutralino can annihilate via tree level diagrams into monochromatic electrons, muons or taus. The annihilation can occur through sfermions in the t-channel, or  $Z$  or Higgs bosons in the s-channel. However, in the absence of left-right sfermion mixing, the s-wave annihilation cross section into light fermions  $f$  is helicity suppressed and thus proportional to  $m_f^2/m_{\text{DM}}^2$ . In scenarios where the left- and right-handed selectron masses are not equal, a substantial branching fraction into electron-positron pairs is possible [146]. In models with  $R$  parity violation, the gravitino can be the lightest supersymmetric particle and a viable dark matter

candidate. One possible decay channel of the gravitino,  $\Psi_{3/2} \rightarrow W^\pm l^\mp$  often exhibits a large branching fraction and contains charged leptons in the final state [157]. The process  $\Psi_{3/2} \rightarrow W^- l^+$  generates a positron line [158]. Our positron limits are shown in the  $m\text{-}\tau$  parameter space of gravitino dark matter in Ref. [159]. Supersymmetric models are widely studied in the literature and constrained from various experiments (see Refs. [159, 160] and references therein).

- **Leptophilic dark matter**

The explanation of the lepton anomalies in cosmic rays (see Sec. 2.1), if interpreted as a dark matter signal, often invoke dark matter candidates that dominantly couple to leptons in order to avoid other constraints from e.g. antiprotons [66, 161]. Such scenarios can be constrained with the exquisite positron data employed in this thesis. In this case, constraints from other observables can also severely impact the viable parameter space and can be more important than the indirect detection constraints [162]. In general, as the positron measurement delivers strong constraints for leptonic final states, all models that invoke large couplings to leptons have to face these bounds (see e.g. Ref. [163]).

- **Models motivated from the Galactic Center excess**

Recently, the discovery of a bump-like feature in the gamma-ray spectrum at about 2 GeV has attracted much attention in the literature [102] (see Sec. 1.4.3). The origin of this excess is still debated. Besides astrophysical processes, dark matter annihilations have been put forward as a possible explanation. It has been demonstrated that various final states, for instance  $b\bar{b}$  [105] or democratic annihilations into leptons [164] yield a good fit to the excess. A contracted NFW dark matter density profile reproduces well the observed morphology [105]. However, the democratic scenario as well as dominant annihilation into tau leptons [165] has been shown to be in tension with the limits from positron measurements [166]. When only partly annihilating into bottom quarks, the branching fractions into leptons that are still allowed by positron constraints are investigated [165].

- **Asymmetric dark matter**

It is interesting that the dark matter density and the baryon density  $\Omega_{\text{DM}}/\Omega_B \approx 5$  are of the same order, even though their production mechanisms are not a priori related. A possible explanation is asymmetric dark matter, where a dark matter asymmetry is connected to the baryon asymmetry (see Ref. [167] and references therein). Also in this scenario, dark matter is in general not absolutely stable but could decay through the asymmetric interactions. Our positron limits are used, together with other bounds, to constrain an asymmetric dark matter scenario with continuous flavor symmetries [168].

### 2.2.2 Spectra at production

In order to calculate limits on the dark matter properties from positron measurements, their spectrum per annihilation has to be calculated. In this thesis we consider annihilations and

decays into the following unpolarized final states:  $e^+e^-$ ,  $\mu^+\mu^-$ ,  $\tau^+\tau^-$ ,  $b\bar{b}$  and  $W^+W^-$ . For the computation of the dark matter constraints with positron data, the positron spectra resulting from decay and hadronization of these final states are needed. We make use of the spectra provided in Ref. [46] for dark matter masses from 5 GeV to 100 TeV, a sufficient range for our analysis. In that calculation the spectra are obtained with the event generator PYTHIA [169], where parton shower algorithms and QCD (quark, gluon) final state radiation are considered in the Monte Carlo simulation. The subsequent hadronization depends on non-perturbative parameters that are fitted together with other quantities to experimental data, LEP data in this case, i.e. at the typical energy scale of 100 GeV. Also QED (photon) final state radiation as well as photon branching into quarks and lepton pairs is included. However, photon radiation from  $W^+W^-$  final states was added by hand to the PYTHIA code. This is also done for electroweak correction that are not implemented in the PYTHIA version 8.135 employed for the computation of the spectra. As has been shown in Ref. [170], the inclusion of  $W$  and  $Z$  emission yields more final state hadrons and thus significantly changes the  $\gamma$  and  $e^\pm$  fluxes at low energies  $E \ll m_{\text{DM}}$ . The resulting  $\bar{p}$  contribution is absent if electroweak corrections are neglected. Furthermore, the decay of hadrons, such as pions and kaons, is taken into account.

The positron (and other particle) spectra are obtained by simulating a large number of events in the Monte Carlo generator. In Ref. [46] the results obtained with PYTHIA are compared to an alternative generator, HERWIG [171]. While the resulting spectra of the quark modes and the positron spectra from  $W^+W^-$  agree reasonably well, they find a significant disagreement in the leptonic modes below  $E/m_{\text{DM}} < 10^{-2}$ . However, this discrepancy is not further considered, as in the following work the spectra of the leptonic modes above this energy range contribute in the calculation of the limits.

For the purpose of computation, the same spectra at production can be used for dark matter annihilations and decays, since the decay of dark matter particle with mass  $2m_{\text{DM}}$  can be treated as the s-wave non relativistic dark matter annihilation of two dark matter particles with mass  $m_{\text{DM}}$  [172].

In Fig. 2.2 the positron spectra from the final states under consideration are presented for three dark matter masses,  $m_{\text{DM}} = 10 \text{ GeV}$ ,  $m_{\text{DM}} = 100 \text{ GeV}$  and  $m_{\text{DM}} = 1000 \text{ GeV}$ .

## 2.3 Propagation of electrons and positrons in the Milky Way

Irrespective of their origin, electrons and positrons and all charged cosmic rays undergo diffusion in the magnetic fields of the Milky Way. As a result, directional information about their sources is lost and the charged cosmic ray fluxes are isotropic. This section reviews the propagation of cosmic rays in the Milky Way from their sources to detection in the solar system. As the Galactic environment determines the propagation of cosmic rays, the main features of the Milky Way relevant in this context are summarized. Subsequently, the diffusion loss equation for charged particles is introduced and specified for electrons and positrons. Two methods to solve

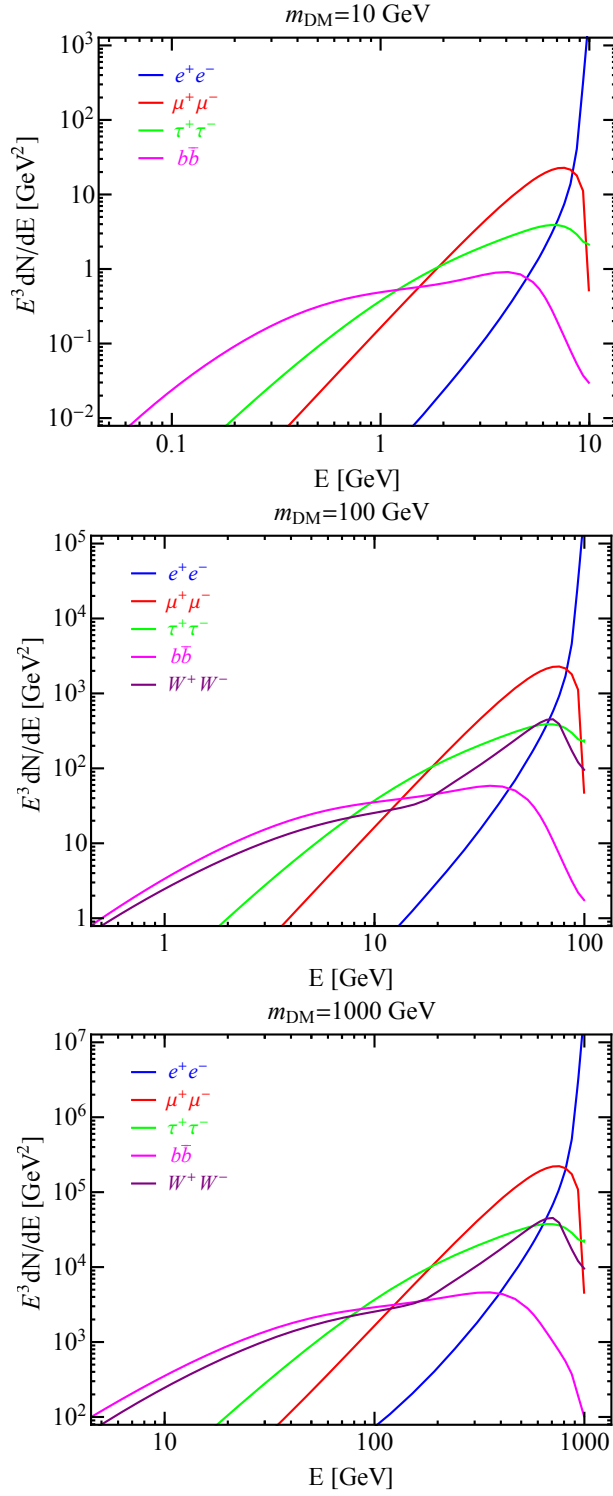


Figure 2.2: Positron spectra at production for annihilations or decays into  $e^+e^-$ ,  $\mu^+\mu^-$ ,  $\tau^+\tau^-$ ,  $b\bar{b}$  and  $W^+W^-$ . The spectra are shown for three dark matter masses in the energy range of interest,  $m_{\text{DM}} = 10 \text{ GeV}$ ,  $m_{\text{DM}} = 100 \text{ GeV}$  and  $m_{\text{DM}} = 1000 \text{ GeV}$ .

this equation, the semi-analytical and the numerical method are described in the following. Furthermore, we briefly describe how to determine the parameters of the propagation equation experimentally. Lastly, solar modulation, the effect of the solar magnetic field on the cosmic ray fluxes, is discussed.

### 2.3.1 The Milky Way

Our Galaxy is a barred spiral galaxy where the solar system is located in an inter-arm region at a distance of about 8.5 kpc [48] from the Galactic center. The Galaxy rotates around its center, which contains a supermassive black hole. The properties of the black hole [173], Sagittarius A\*, and the surrounding environment (see Ref. [174] and references therein) have been extensively studied. The stellar component is typically modeled with four contributions (see e.g. Refs. [175, 176]): the thin disk with a height of about  $\sim 200$  pc and the thick disk with a height of about  $\sim 1$  kpc extending to radii of about 25 – 30 kpc, the halo extending to more than 30 kpc and the bulge, a triaxial rotating bar [177]. The Milky Way is embedded in the dark matter halo that extends well beyond the visible disk. In dark matter simulations virial radii of hundreds of kpc are found for Milky Way like halos (see e.g. Ref. [53]). The distribution of gas in the Milky Way can be mapped with multi-wavelength observations. They reveal that the gas is mostly confined to the stellar disc. Galactic magnetic fields as well as the interstellar radiation fields also play an important role in the transport of charged cosmic rays. In this section the most important components of the Milky Way relevant for cosmic-ray propagation are briefly described, following Ref. [177].

- **The interstellar medium**

The interstellar medium (ISM) generally comprises two components: interstellar gas and cosmic rays, which are discussed in Sec. 2.1. The interstellar matter is relevant in the context of cosmic rays, as it constitutes the spallation targets in secondary production. By number, it consists of 90.8% of hydrogen, 9.1% of helium and 0.12% of heavier elements. One distinguishes different forms of interstellar matter, molecular gas, neutral atomic gas, ionized gas and dust, i.e. tiny solid particles, which can be identified experimentally through their distinct emission pattern. Neutral hydrogen for instance can be observed through the Lyman emission lines in the ultraviolet or the 21-cm line from the hyperfine structure of the hydrogen atom, whereas hot ionized gas emits x-rays. Thus the distribution of interstellar matter can be mapped. Roughly speaking, it is found to be distributed inhomogeneously in the form of clouds and widespread material in-between, with gas temperatures ranging from  $\sim 10$  K to  $\sim 10^6$  K. The density of the interstellar matter varies over several orders of magnitude ranging from  $\sim 10^{-26}$  g/cm<sup>3</sup> in the hot gas to  $\sim 10^{-18}$  g/cm<sup>3</sup> in the densest molecular clouds.

- **The Galactic magnetic field**

The Galactic magnetic field consists essentially of two components: a large scale steady

component as well as a random component that is connected to the turbulent interstellar medium [178]. The latter is crucial for cosmic-ray transport as it causes the diffusion of charged particles in the Galaxy. The strength of both components has been determined to be of the order of  $\mu\text{G}$  in the Galactic plane through the observation of the Zeemann splitting of radio lines that is proportional to the magnetic field strength.

- **The interstellar radiation field**

The interstellar radiation field (ISRF) [179] plays an important role in cosmic-ray transport, as charged particles lose energy through inverse Compton scattering. For high-energy electrons and positrons, energy losses contribute significantly to the propagation. The interstellar radiation field consists of three components: the cosmic microwave background, star light and light that is absorbed and re-emitted by dust. The cosmic microwave background is very well described by a black body spectrum of 2.7255 K [29]. The other two components are spatially dependent. For the determination of the star light component, the spatial distribution of stars is modeled. Their spectra are inferred from observations. For the calculation of the third component, the spatial distribution of gas in the Milky Way is taken into account. The resulting spectra at different locations in the Galaxy are shown in Fig. 2.3 together with an earlier determination of the interstellar radiation field [180].

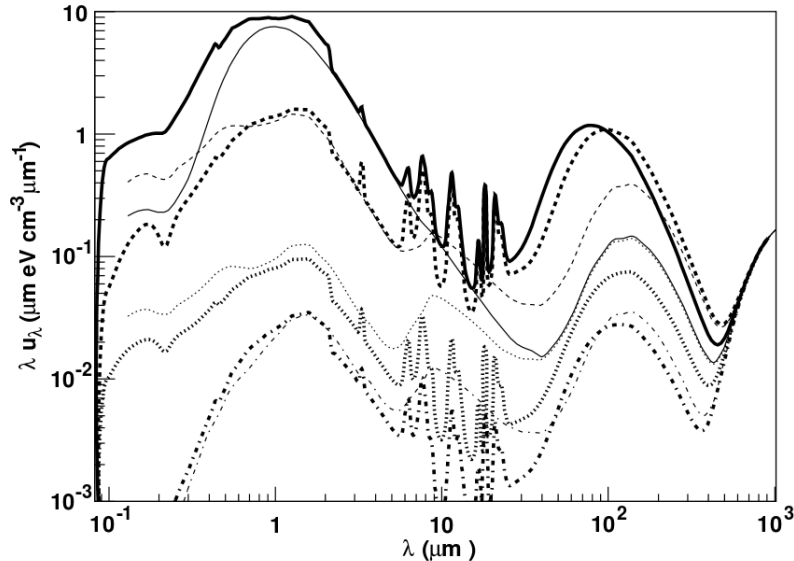


Figure 2.3: Interstellar radiation field as determined in Ref. [181] (thick lines) compared to Ref. [180] (thin lines). The interstellar radiation field is plotted at different locations in the Galaxy. From top to bottom the lines depict the interstellar radiation field at  $(R, z) = (0 \text{ kpc}, 0 \text{ kpc})$ ,  $(R, z) = (4 \text{ kpc}, 0 \text{ kpc})$ ,  $(R, z) = (12 \text{ kpc}, 0 \text{ kpc})$  and  $(R, z) = (16 \text{ kpc}, 0 \text{ kpc})$ .

### 2.3.2 The propagation equation

In this section the propagation of cosmic rays in the Milky Way is presented and the relevant effects giving rise to the different terms in the propagation equation are briefly discussed, before it is particularized to electrons and positrons. There are various strategies for solving the transport equation depending on the simplifying assumptions that can be made. As the dark matter fluxes after propagation used in this work are obtained in a semi-analytical way, this solution technique is explained in the next section. Afterwards, the full numerical approach to the transport equation is summarized.

In general terms the propagation equation reads [182]:

$$\begin{aligned} \frac{\partial \Psi(\vec{r}, p, t)}{\partial t} &= Q(\vec{r}, p, t) + \vec{\nabla} \cdot (D_{xx} \vec{\nabla} \Psi - \vec{V} \Psi) \\ &+ \frac{\partial}{\partial p} p^2 D_{pp} \frac{\partial}{\partial p} \frac{1}{p^2} \Psi - \frac{\partial}{\partial p} \left[ \dot{p} \Psi - \frac{p}{3} (\vec{\nabla} \cdot \vec{V}) \Psi \right] - \frac{1}{\tau_f} \Psi - \frac{1}{\tau_r} \Psi. \end{aligned} \quad (2.2)$$

Here  $\Psi(\vec{r}, p, t)$  denotes the cosmic-ray density per unit momentum  $p$ . In general, this quantity is also time and position dependent. The sources of cosmic rays are taken into account in the source term  $Q(\vec{r}, p, t)$ . Furthermore,  $D_{xx}$  denotes the spatial diffusion coefficient,  $\vec{V}$  the convection velocity,  $\tau_f$  the fragmentation and  $\tau_r$  the radioactive decay time scale. Diffusion in momentum space is described by the coefficient  $D_{pp}$ ,  $\dot{p}$  is the time derivative of the momentum, i.e. the rate of momentum loss or gain. In the following all terms are shortly commented, following Ref. [182]:

- **Time dependence**

Typically the first term in the propagation equation is set equal to zero as the stationary case is considered. As for cosmic rays the typical confinement time amounts to 15 Myr [29], a time scale on which the propagation conditions are not expected to change, this is a well justified assumption. However, if the effect of phenomena with a smaller time scale is investigated, the time dependence has to be taken into account (see e.g. Ref. [183]).

- **Source term**

In this term, the different cosmic-ray sources are taken into account. In the case of primary cosmic rays, its spatial dependence follows the distribution of supernova remnants. In the case of secondary cosmic rays, the sources depend on the primary cosmic-ray fluxes as well as the density and distribution of the interstellar medium. For cosmic rays originating from dark matter annihilations and decays, the source term scales with  $\rho_{DM}^2$  or  $\rho_{DM}$ , respectively. The source term for the latter case is specified in the next section.

- **Diffusion**

Diffusion of cosmic rays is caused by the scattering off random magnetohydrodynamical turbulences. Effectively, charged particles perform a random walk in a magnetic field with an irregular component, which results from the propagation of magnetohydrodynamical waves in the interstellar medium. Thus, directional information about the sources of the charged cosmic rays is washed out and an isotropic distribution is observed. Typically,

the diffusion coefficient amounts to  $D_{xx} \sim (3 - 5) \cdot 10^{28} \text{ cm}^2/\text{s}$  at  $1 \text{ GeV}/n$ . It depends on the magnetic rigidity  $D \propto R^\delta$ , where  $\delta$  lies in the range of  $0.3 \sim 0.6$ , depending on the spectrum of the interstellar turbulences. Practically, these parameters are inferred from the cosmic-ray spectra. However, some degeneracies in the propagation parameters remain (see Sec. 2.3.3). Often cosmic-ray diffusion is assumed to be isotropic and spatially independent, but the respective dependencies can also be taken into account [184, 185].

- **Reacceleration**

Reacceleration is closely related to diffusion. It describes the energy gain in the scattering processes that also cause spatial diffusion. Thus the coefficient  $D_{pp}$  depends on the diffusion coefficient  $D_{xx}$ , but also on the speed of the magnetohydrodynamical disturbances  $V_a$ , denoted Alfvén velocity,  $D_{pp} = p^2 V_a^2 / (9D_{xx})$ . For electrons and positrons this effect can be neglected with respect to the large energy losses.

- **Convection**

The velocity of convective winds, outflows of material in star forming regions, appears in two terms in the propagation equation. The first one describes the spatial transport of cosmic rays in Galactic winds. The other term arises due to adiabatic energy losses that depend on the derivative of the convection velocity.

- **Energy losses**

The main processes contributing to energy losses of charged particles in the Milky Way are inverse Compton scattering on photons of the interstellar radiation field, synchrotron emission in the magnetic fields of the Galaxy as well as bremsstrahlung, ionization and Coulomb losses. However, the relevance of the different energy loss mechanisms differs significantly between electrons and nuclei [186]. In the next section, the energy losses relevant for electrons and positrons are further discussed. In the GeV energy regime these are inverse Compton scattering and synchrotron radiation.

- **Fragmentation and decay**

These two terms take into account the destruction of nuclei due to spallation reactions in the interstellar medium as well as the radioactive decay in the case of unstable nuclei. In the case of antimatter, the corresponding term takes into account annihilations.

For electrons and positrons, the general propagation equation Eq. (2.2) can be simplified because only the diffusion term and the energy loss term are relevant [123]. In the stationary case it can be cast as [46]

$$Q(E, \vec{x}) + \nabla(K(E, \vec{x}) \nabla f(E, \vec{x})) + \frac{\partial}{\partial E}(b(E, \vec{x}) f(E, \vec{x})) = 0, \quad (2.3)$$

where  $f(E, \vec{x}) = dN_{e^\pm}/dE$  is the number density of electrons and positrons per unit energy. In the energy loss coefficient  $b(E, \vec{x}) = -dE/dt$  contributions from synchrotron losses and inverse Compton scattering, the dominant energy loss mechanisms for high-energy electrons, have to be

taken into account. The source term for electrons and positrons originating from dark matter annihilations reads [46]

$$Q_{\text{ann}}(E, \vec{x}) = \frac{1}{k} \left( \frac{\rho(\vec{x})}{m_{\text{DM}}} \right)^2 \sum_f \langle \sigma v \rangle_f \frac{dN_{e^\pm}^f}{dE}, \quad (2.4)$$

where  $k = 2$  for annihilations of identical particles  $k = 4$  for non self-conjugate particles. For decays the source term is given by [46]

$$Q_{\text{dec}}(E, \vec{x}) = \left( \frac{\rho(\vec{x})}{m_{\text{DM}}} \right) \sum_f \Gamma_f \frac{dN_{e^\pm}^f}{dE}. \quad (2.5)$$

Here  $\rho$  denotes the dark matter density distribution,  $m_{\text{DM}}$  the dark matter mass,  $\langle \sigma v \rangle$  the velocity-weighted annihilation cross section and  $\Gamma$  the decay rate. The spectra at production  $dN_{e^\pm}/dE$  of the different final states  $f$  are summed. Two approaches to solve this equation are described in the following.

### 2.3.2.1 Semi-analytical solution

This section describes the semi-analytical method to solve the diffusion-loss equation Eq. (2.3), following Ref. [46]. In that work the full spatial dependence of the energy losses is taken into account.

In order to solve the propagation equation, boundary conditions have to be imposed. This is done in the framework of the diffusion model. In this model, the Galaxy is described by a cylinder with height  $2L$ . The Galactic plane is sandwiched by the two half cylinders of height  $L$ . Inside the cylinder electrons and positrons diffuse, whereas outside the diffusion zone the particles can propagate freely and escape. Thus the number density is set to zero at the boundaries of the diffusion zone. In addition, for the semi-analytical solution, the diffusion coefficient is treated as isotropic and spatially independent,  $K(E, \vec{x}) = K_0(E/\text{GeV})^\delta$ . Interactions with the interstellar medium only take place within a second concentric cylinder with half height  $h = 0.1 \text{ kpc}$ . As these interactions are not relevant for our purpose, the propagation of the electron and positron fluxes from dark matter, they are not included in Eq. (2.3), but they must be considered for the calculation of the secondary production (see Sec. 3.1.1).

Although this model seems very simplistic, it describes cosmic-ray transport rather well. Even though a large fraction of the dark matter in the Milky Way is located outside the diffusion zone in the halo of the Milky Way, the resulting fluxes at Earth change at most by  $\sim 20\%$  when the diffusion zone is extended and spatial dependent diffusion is considered [184].

The energy loss term  $b(E, \vec{x}) = b_{\text{IC}}(E, \vec{x}) + b_{\text{syn}}(E, \vec{x})$  is calculated considering inverse Compton scattering and synchrotron radiation. Both can be given by analytic expressions. In inverse Compton scattering, a photon from the interstellar radiation field with energy  $\epsilon$  is upscattered to an energy  $\epsilon_1$  by a high-energy electron of energy  $E$ . For inverse Compton losses the energy loss

coefficient reads [187]

$$b_{\text{IC}}(E, \vec{x}) = 3\sigma_T \int_0^\infty d\epsilon \epsilon \int_{\frac{1}{4\gamma^2}}^1 dq n(E, \vec{x}) \frac{(4\gamma^2 - \Gamma_\epsilon)q - 1}{(1 + \Gamma_\epsilon q)^3} \times \left[ 2q \ln q + q + 1 - 2q^2 + \frac{1}{2} \frac{(\Gamma_\epsilon q)^2}{1 + \Gamma_\epsilon q} (1 - q) \right], \quad (2.6)$$

where  $q = \tilde{\epsilon}/(\Gamma_\epsilon(1 - \tilde{\epsilon}))$  with  $\Gamma_\epsilon = 4\epsilon\gamma/m$ ,  $\tilde{\epsilon}_1 = \epsilon_1/(\gamma m)$  and  $\gamma = E/m_e$ .  $\sigma_T$  denotes the Thomson cross section. In the case of energy loss through synchrotron radiation, the energy loss coefficient can be calculated by

$$b_{\text{syn}}(E, \vec{x}) = \frac{4}{6} \sigma_T \gamma^2 \beta^2 B^2(\vec{x}). \quad (2.7)$$

Here  $B$  denotes the magnetic field and  $\beta$  the velocity of the electron. In these calculations expressions for the photon density of the interstellar radiation field and the Galactic magnetic field are needed. The profile of the magnetic field can be parameterized as [46]

$$B(r, z) = B_0 \exp[-(r - r_\odot)/r_B - |z|/z_B]. \quad (2.8)$$

For the solution of the propagation equation  $r_\odot = 8.33$  kpc,  $B_0 = 4.78 \mu\text{G}$ ,  $r_B = 10$  kpc and  $z_B = 2$  kpc are adopted. The interstellar radiation field is modeled for the whole Galaxy (see Sec. 2.3.1). Maps of the ISRF are used in numerical codes such as GALPROP [188] that can also be employed here. When the spatial dependence is neglected, typical values of the magnetic and radiation fields at the position of the Solar system can be adopted. This is justified for very high-energy electrons and positrons, which lose energy very quickly and thus have a rather small diffusion length, where the environmental properties of the Galaxy do not vary dramatically. In the spatial dependent calculation of the energy losses it is found that except for the Galactic center, inverse Compton losses dominate everywhere. Even though high-energy positrons from the Galactic center cannot be detected at Earth, the spatial dependent analysis is important for the calculation of secondary radiation, for instance the inverse Compton gamma-rays.

In the semi-analytical approach, the diffusion loss equation is solved using the method of Green's functions. The Green's function  $I(E, E_s, \vec{x})$  is the solution of diffusion-loss equation that is obtained when the source term is replaced by a delta function  $\delta(E - E_s)$ . The full solution is then given by folding the Green's function with the source term (see Ref. [46] for details). In the case of spatially constant energy losses, the Green's function can be expressed analytically in terms of Bessel functions. In the spatial dependent case this is not possible in general and the respective equation is solved numerically.

The solution of the diffusion loss equation is given in terms of the differential  $e^\pm$  flux  $d\Phi/dE = v_{e^\pm} f/(4\pi)$  at each position  $\vec{x}$  in the Galaxy. For annihilations it reads

$$\frac{d\Phi_{\text{ann}}}{dE}(E, \vec{x}) = \frac{v_{e^\pm}}{4\pi b(E, \vec{x})} \frac{1}{2} \left( \frac{\rho(\vec{x})}{m_{\text{DM}}} \right)^2 \sum_f \langle \sigma v \rangle_f \int_E^{m_{\text{DM}}} dE_s \frac{dN_{e^\pm}^f}{dE}(E_s) I(E, E_s, \vec{x}) \quad (2.9)$$

	$K_0 [\text{kpc}^2/\text{Myr}]$	$\delta$	$L [\text{kpc}]$
MIN	0.00595	0.55	1
MED	0.0112	0.70	4
MAX	0.0765	0.46	15

Table 2.1: Propagation parameters for the MIN, MED and MAX propagation setups taken from Ref. [46].

and for decays it is given by

$$\frac{d\Phi_{\text{dec}}}{dE}(E, \vec{x}) = \frac{v_{e^\pm}}{4\pi b(E, \vec{x})} \frac{1}{2} \left( \frac{\rho(\vec{x})}{m_{\text{DM}}} \right) \sum_f \Gamma_f \int_E^{m_{\text{DM}}/2} dE_s \frac{dN_{e^\pm}^f}{dE}(E_s) I(E, E_s, \vec{x}). \quad (2.10)$$

The fluxes of electrons and positrons after propagation are given in Ref. [46] for three different sets of propagation parameters. These scenarios are thought to bracket the propagation uncertainties. They are deduced from cosmic ray fits to various data sets and yield minimal and maximal electron/positron fluxes (see also Sec. 2.3.3). The three scenarios are thus labeled MIN, MED and MAX. The corresponding propagation parameters are summarized in Table 2.1.

Fig. 2.4 shows the positron fluxes from dark matter annihilations and decays at Earth using MED propagation parameters for the final states considered in this thesis assuming dark matter masses of 10 GeV, 100 GeV and 1000 GeV with  $\langle \sigma v \rangle = 3 \cdot 10^{-26} \text{ cm}^3/\text{s}$  for annihilations and 200 GeV with  $\tau = 10^{28} \text{ s}$  for decays.

### 2.3.2.2 Numerical solution

In order to study the propagation of all nuclei in the Galaxy with full time and spatial dependence, numerical codes have been developed. The GALPROP [188, 189], DRAGON [190] and PICARD [191] cosmic ray propagation codes solve the transport equation numerically. To this end, the transport equation it is discretized on a grid of the spatial and momentum coordinates. The general propagation equation Eq. (2.2) is given for one specific nucleus  $i$ . The fragmentation and decay terms give rise to source terms for the spallation or decay products. Thus the propagation equation is first solved for the heaviest nucleus calculating the source terms for the lighter isotopes. When computations for all isotopes of a given charge  $Z$  are accomplished, the algorithm continues with the isotopes of charge  $Z - 1$ . The procedure is iterated down to protons. Typically these codes contain maps with the density distributions of the different components of interstellar gas and dust and the interstellar radiation field. In addition, radioactive decays and the spallation cross sections are implemented. The fluxes of secondary cosmic rays such as antiprotons and positrons are also calculated. The conventionally used two dimensional model has been extended to three spatial dimensions which allows modeling for instance the spiral arms of the Galaxy [185, 188, 192]. These codes are not only important in the context of cosmic rays but also for gamma-ray astronomy. The diffuse gamma-ray background that originates from

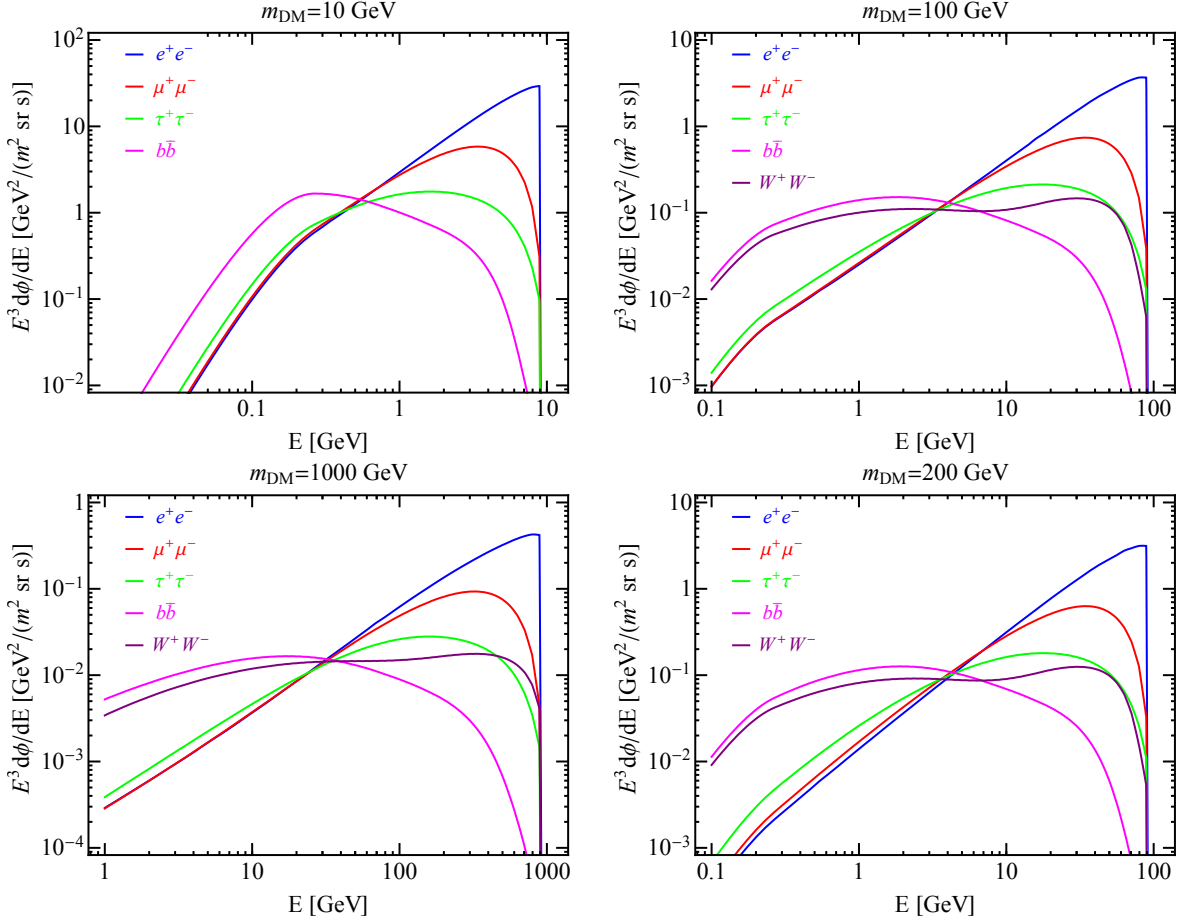


Figure 2.4: Positron spectra at Earth after propagation for annihilations and decays into  $e^+e^-$ ,  $\mu^+\mu^-$ ,  $\tau^+\tau^-$ ,  $b\bar{b}$  and  $W^+W^-$  (lines from top to bottom at  $0.3 m_{\text{DM}}$ ). The spectra are shown for three dark matter masses in the energy range of interest for annihilations,  $m_{\text{DM}} = 10 \text{ GeV}$ ,  $m_{\text{DM}} = 100 \text{ GeV}$  and  $m_{\text{DM}} = 1000 \text{ GeV}$  with  $\langle \sigma v \rangle = 3 \cdot 10^{-26} \text{ cm}^3/\text{s}$  as well as for  $m_{\text{DM}} = 200 \text{ GeV}$  with  $\tau = 10^{28} \text{ s}$  for decays. The fluxes stem from an Einasto dark matter density profile using MED propagation parameters.

neutral pion decay in the spallation reactions of cosmic rays and the interstellar gas, inverse Compton scattering with the interstellar radiation field and bremsstrahlung of cosmic rays in the interstellar medium at each position in the Galaxy is typically calculated based on cosmic-ray propagation codes.

### 2.3.3 Determination of the propagation parameters

The propagation equation contains parameters that have to be determined experimentally. In the diffusion model these are the height of the diffusion zone  $L$ , the diffusion coefficient  $K_0$ , the spectral index  $\delta$  in the diffusion term, the convection velocity  $V_c$  as well as the Alfvén velocity  $V_a$  [193]. Whereas the ratio of primary-to-primary cosmic-ray species is insensitive to

the variation of the diffusion parameters because they originate from the same sources and share the same propagation history, this is not the case for secondary-to-primary ratios like B/C, and stable-to-unstable ratios like Be<sup>10</sup>/Be<sup>9</sup>. While the former depends on  $K_0/L$  the latter is sensitive to  $L^2/K_0$ . In this way the degeneracy in the propagation parameters from the fit to only one data set can be broken. In practice, however, this determination is very challenging, as the measurements of the stable-to-unstable ratios exhibit large error bars to date. The best measured ratio Be<sup>10</sup>/Be<sup>9</sup> contains only data up to 3 GeV/n [194]. The AMS-02 experiment is currently taking data and is expected to significantly improve previous measurements. Their recently released measurement of the boron-to-carbon ratio already allows reducing the propagation uncertainties and to determine with high accuracy  $K_0/L$  [195, 196], where a harder spectral index  $\delta$  is found compared to previous analyses [193]. Using the most recent B/C data it is possible to explain the  $\bar{p}/p$  ratio measured by AMS-02 with pure secondary production within the remaining propagation and production uncertainties [196].

With the exquisite AMS-02 data cosmic-ray physics enters a precision era, where systematic uncertainties become important and simplifying assumptions could affect the results. Lifting the usual assumption that boron is purely secondary, it has been shown that the inclusion of a primary boron component significantly alters the best-fit value of  $\delta$  [197]. Furthermore, the nuclear uncertainties in the production cross sections of secondary cosmic rays start to dominate over the propagation uncertainty [196, 197].

Propagation parameters that are commonly used in the context of indirect dark matter searches with positrons are given in Table 2.1. They are obtained in the analysis performed in Ref. [198], where 1600 propagation models compatible with the B/C ratio were scanned. The MIN (MAX) propagation parameters were found to minimize (maximize) the positron flux from dark matter annihilations for various final states. However, positron data from the PAMELA experiment disfavors small diffusion heights and excludes the MIN propagation scenario [199].

### 2.3.4 Solar modulation

Low energy charged particles with  $E \lesssim 5$  GeV that enter the Solar system are affected by the magnetic fields of the Sun and the solar wind, the outflow of particles from the Sun. This effect can be taken into account with the simple force field approximation [200, 201]. For electrons and positrons, the solar modulated flux at the top of the atmosphere (TOA) is given by [202, 203]

$$\Phi^{\text{TOA}}(E) = \frac{E^2}{(E + e\phi_F)^2} \Phi^{\text{IS}}(E + e\phi_F), \quad (2.11)$$

where  $\Phi_{\text{IS}}$  denotes the interstellar flux.  $\phi_F$  is the so-called solar modulation parameter that varies between  $\sim 0.5$  GV and  $\sim 1.3$  GV as the solar magnetic fields evolve. The Sun's magnetic field exhibits an 11-year solar cycle according to the variations in the solar activity and magnetic field polarity reverses every 11 years. It has been shown that this simple modeling of solar modulation describes the measured proton fluxes extremely well [203]. However, there are indications that the solar modulation parameter is charge sign dependent. The positron fraction

can only be brought into agreement with earlier measurements at low energies, if charge sign dependent modulation is considered [203, 204]. This can be done by extending the force field approximation and introducing different solar modulation parameters for particles with different charge signs [203].

As for the propagation of cosmic rays in the Galaxy there exist numerical codes for cosmic-ray propagation in the heliosphere. In the HELIOPROP code diffusion inside the heliosphere, the geometry of the solar magnetic field, drifts due to magnetic irregularities and adiabatic energy losses in the solar wind are implemented [204].

## 2.4 Positron experiments

In this section the experiments relevant for this thesis are described. Data taken by the balloon borne instrument HEAT and the space based experiments PAMELA and AMS-02 are used in the following to constrain the dark matter annihilation cross section and lifetime for various channels that produce positrons.

Positron measurements have to be conducted at high altitudes, as cosmic rays in the GeV to TeV energy range cannot reach the Earth due to interactions in the atmosphere. Thus balloon flights are undertaken with cosmic-ray detectors on board, to measure the cosmic-ray fluxes. An experiment that collected data up to GeV energies is the High-Energy Antimatter Telescope (HEAT). In order to improve the quality of the measurements by increasing the statistics and to extend the energy range of the measured particles, a dedicated antimatter satellite experiment was designed, the Payload for Antimatter Matter Exploration and Light nuclei Astrophysics (PAMELA). Its results aroused a lot of interest of the high energy physics community in cosmic-ray positrons, because the rising positron fraction measured by PAMELA was not expected from standard cosmic-ray physics (see Sec. 2.1). The most precise measurement to date of electrons, positrons, their combined flux and the positron fraction is delivered by the Alpha Magnetic Spectrometer (AMS-02), on board of the international space station (ISS). The exquisite data confirms the positron anomaly and allows deriving stringent limits for dark matter candidates that produce electrons and positrons.

All positron experiments considered below are magnetic spectrometers [205]. They measure the rigidity and charge sign of the incident particles by determining their trajectories in a magnetic field. In addition, all of them contain an electromagnetic calorimeter to measure the energies of the particles. Besides, the instruments are equipped with additional detectors that allow for particle identification that is necessary for isotopic studies. Several subdetectors often deliver redundant information in order to reduce systematic uncertainties. In the case of AMS-02, for instance, the particle's charge is measured by the tracker, the time-of-flight system and the ring imaging Cherenkov detector. Combining all the subdetectors, proton rejection can be typically improved. This is crucial for positron measurements, because electrons only comprise a fraction of  $\sim 10^{-2}$  of the total cosmic-ray flux and positrons are even less abundant. Protons on the

other hand are the most abundant particles in cosmic rays and must be rejected efficiently in order to detect the rare positrons.

### **2.4.1 HEAT**

The High-Energy Antimatter Telescope experiment measured electrons and positrons in two balloon flights in 1994 and 1995 [206]. The first flight started from Fort Sumner, New Mexico, and collected data during 29 hours. The second one was conducted at Lynn Lake, Manitoba, where data was taken during 26 hours.

The detector size is of the order of 2 m with a geometrical acceptance of  $495 \pm 1 \text{ cm}^2\text{sr}$  [206]. It consists of several subdetectors, such that all particle properties of interest can be determined. Details on the HEAT detector are taken from Ref. [207]. The core of the instrument is a superconducting magnet spectrometer, a drift tube hodoscope mounted in the bore of the magnet. Time-of-flight scintillators measure the magnitude of the particle's charge and the time the particle takes to transverse the detector. This information is used to determine the particle's velocity. Furthermore, transition radiation detectors allow discriminating between electrons and protons in the energy range of interest, i.e. between 5 GeV and 50 GeV. Lastly, an electromagnetic calorimeter measures the particle's energy and is also used for further proton discrimination by analyzing the pattern of energy deposition in the detector. Combining all the subdetectors, the HEAT experiment achieves a proton rejection of  $10^{-5}$  and an energy resolution of about 17% at 1 GeV that improves down to 9% at 10 GeV.

The results on the electron and positron flux as well as the combined flux are presented in several publications. In this thesis the combined data from both flights in 1994 and 1995 [206] is used.

### **2.4.2 PAMELA**

The Payload for Antimatter Matter Exploration and Light nuclei Astrophysics was launched on June 15<sup>th</sup>, 2006 and is still operating today. It is a satellite borne experiment that orbits the Earth in a height of  $350 \sim 600 \text{ km}$  [208]. The PAMELA space mission was initiated in order to study in great detail the antimatter component in cosmic rays as well as the cosmic rays themselves. The instrument is capable of measuring not only electrons and positrons, but also antiprotons, protons, and heavier cosmic-ray nuclei.

The satellite is about 7.4 m high, with a solar array span of 14 m [209]. The size of the PAMELA instrument amounts to about 1.3 m with a geometrical factor of  $21.5 \text{ cm}^2\text{sr}$  [209]. As in the case of HEAT, the detector consists of several subdetectors that allow identifying the incident particles and measure their energy and velocity [208, 209].

The magnetic spectrometer that consists of microstrip silicon detectors in the magnetic field of the permanent magnet measures the tracks of the particles to determine their rigidity and charge sign. The calorimeter measures the energy of the particle. From the shower topology, leptonic and hadronic particles can be distinguished at a level of  $10^5$ . Further improvement

of lepton/hadron discrimination is achieved by the shower tail scintillator that measures the energy, which is not deposited in the calorimeter. Furthermore the time-of-flight system is used to reject albedo particles and to determine the velocity of low energy particles. Spurious tracks are rejected by an anticoincidence system around the magnet. In addition, the PAMELA experiment contains a neutron detector in order to further improve lepton/hadron separation by measuring the neutrons from the cascades in the calorimeter. Using the background counting for the lepton/hadron separation, it is possible to measure solar neutrons and their temporal variation.

The PAMELA instrument achieves an energy resolution better than 10% for high-energy electrons and an overall separation power between electromagnetic and hadronic components of  $2 \cdot 10^5$  [209]. In this thesis, positron data taken from July 2006 until December 2009 are used. In this period, 24500 positrons were collected with energies above 1.5 GeV, ranging up to maximum positron energies of 300 GeV [210].

### 2.4.3 AMS-02

The Alpha Magnetic Spectrometer was mounted on the International Space Station (ISS) on May 11<sup>th</sup>, 2011 [211]. It is still operational today and will take data for the lifetime of the ISS. The instrument is more than 3 m high [125] with a geometrical acceptance of  $950 \text{ cm}^2 \text{sr}$  [212]. Originally, the spectrometer was planned to contain a superconducting magnet, which was changed for a permanent one as the operation time of the ISS got extended [213]. This change allows operating the experiment for more than 10 years, compared to only 3 years with the superconducting magnet. AMS-02 is designed to measure cosmic rays with high precision, the matter as well as the antimatter component. Again, the experiment consists of several subdetectors [211, 214]. The magnet and a silicon tracker constitute the spectrometer, which measures the particle's charge and rigidity. Furthermore, it allows determining the arrival direction of the incoming particle. Similar to the PAMELA experiment, AMS-02 contains a time-of-flight system in order to trigger the other detectors, a transition radiation detector to discriminate leptons and hadrons, an electromagnetic calorimeter to measure the total energy and an anticoincidence counter to reject particles entering the instrument through the magnet. In addition, AMS-02 comprises a ring imaging Cherenkov detector that measures the particle's velocity with very high precision by analyzing the pattern of Cherenkov light produced by the incident particle. This precision measurement enables AMS-02 to determine the particle's mass accurately and thus to distinguish light isotopes in cosmic rays. Lastly, a Star Tracker determines the orientation of AMS-02 in space more precisely than the ISS in order to infer the arrival direction of the incoming particles.

For the positron measurement, AMS-02 reaches a proton rejection of about  $10^6$  [125]. The energy resolution is about 7.5% at 2 GeV, going down to 1.7% at 100 GeV [125]. In their publications, the AMS Collaboration analyzed tens of billions of events in order to determine with high precision among other cosmic-ray fluxes the positron fraction up to 350 GeV [125] as

well as the electron flux up to 700 GeV and positron flux up to 500 GeV [212, 215]. The first positron fraction measurement by AMS-02 is based on  $6.8 \cdot 10^6$  electron and positron events [125].

# Chapter 3

## Limits from positrons

In this chapter, we derive constraints on the dark matter annihilation cross section and lifetime from positron measurements. The recently presented exquisite measurements by AMS-02 of the positron and electron fluxes as well as the positron fraction allows computing stringent limits [1]. In this work we use for the first time the positron flux, in contrast to the positron fraction employed in other studies, e.g. in Refs. [172, 216, 217]. We do not only consider the latest results of AMS-02, but we also include previous positron measurements from PAMELA and HEAT in our analysis.

This section is structured as follows: First, we describe our approach to compute the dark matter constraints. Then, the limits on dark matter annihilations and decays obtained from the positron flux and from the positron fraction are presented and compared to other limits from indirect dark matter searches. Some of the material presented in this chapter has been published in Ref. [1].

### 3.1 Methodology

In order to derive limits on the dark matter parameters we employ a physically motivated background model for the positron flux. To this background model we add the positron contribution from dark matter, which we fit to the positron data in order to compute the  $2\sigma$  upper limits. The same procedure is repeated for the positron fraction. To this end a parameterization of the electron flux is needed. As the latter is difficult to model, we simply fix the electron flux at the top of the atmosphere using measured data. In fact, one of the main advantages of our approach from the theoretical point of view is that no knowledge of the electron flux is needed when the positron flux is used to derive limits. A further optimization of the limits can be achieved by sampling over various energy windows as explained in the next section. In this work we use the data from different experiments, AMS-02 [125, 212], PAMELA [106, 210] and HEAT [206], and finally compare the limits that can be derived from their measurements. The data sets of the positron flux, the electron flux and the positron fraction from these experiments that are used in our analysis are presented in Fig. 3.1.

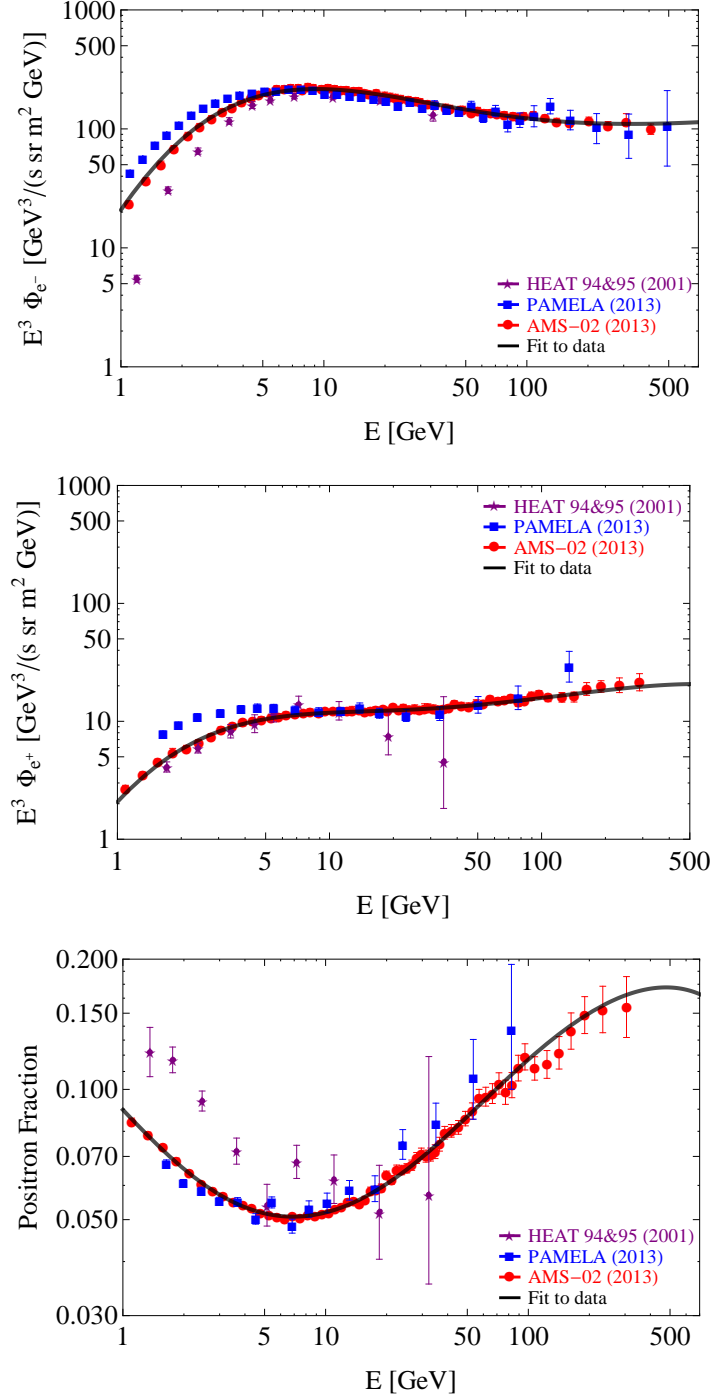


Figure 3.1: The figures show the measurements of HEAT, PAMELA and AMS-02 of the electron flux (upper panel), the positron flux (middle panel) and the positron fraction (lower panel). The black line depicts the best fit of our background model to the AMS-02 data. These plots have been published in Ref. [1].

### 3.1.1 Background model

Our background model for the positron flux consists of three pieces: i) the spallation background of secondary positrons that are produced in collisions of primary cosmic rays with particles in the interstellar medium; ii) an additional source that is known to contribute to the positron flux from the PAMELA positron fraction measurement and iii) solar modulation. The concrete parameterization used in the computation of constraints from the positron flux and fraction are described in the following.

#### 3.1.1.1 Positron flux

The positron flux is modeled by the sum of a power law that models the secondary positron background

$$\Phi_{e^+}^{\text{sec,IS}}(E) = C_{e^+} E^{-\gamma_{e^+}}, \quad (3.1)$$

and an additional source parameterized by a power law with an exponential cutoff

$$\Phi_{e^+}^{\text{source,IS}}(E) = C_s E^{-\gamma_s} \exp(-E/E_s), \quad (3.2)$$

featuring a harder index than the secondary contribution. Thus the total interstellar positron background reads

$$\Phi_{e^+}^{\text{IS}}(E) = \Phi_{e^+}^{\text{sec,IS}}(E) + \Phi_{e^+}^{\text{source,IS}}(E). \quad (3.3)$$

The flux at the top of the atmosphere is given by the solar modulated interstellar flux using the force field approximation (see Sec. 2.3.4)

$$\Phi_{e^+}^{\text{TOA}}(E) = \frac{E^2}{(E + \phi_{e^+})^2} \Phi_{e^+}^{\text{IS}}(E + \phi_{e^+}), \quad (3.4)$$

where the solar modulation parameter  $\phi_{e^+}$  varies between  $\sim 500 \text{ MV} - 1.3 \text{ GV}$  over the eleven-year solar cycle. Each of the terms in the positron background model is physically motivated:

- **Secondary positrons**

Different calculations of the secondary positron flux [123, 127] suggest that it follows a power law above a few GeV. These calculations have been put forward in order to accurately quantify the anomaly in the positron flux observed by PAMELA. In Ref. [123] the secondary positron flux is calculated from the diffusion loss equation, where the source term is computed from the collisions of cosmic-ray protons and  $\alpha$  particles with hydrogen and helium in the interstellar medium. While the full spatial dependence of the cosmic-ray fluxes is taken into account, the local values for the gas density are adopted. This is justified as the positrons measured at Earth are produced in a relatively small volume around the Solar system in which the gas densities are not expected to change significantly. The spallation cross sections that appear in the source term are one of the main uncertainties

in this calculation. Several parameterizations of these cross sections exist in the literature that differ from each other and have been calibrated to different nuclear data sets. Another important uncertainty in the secondary positron flux stems from cosmic-ray propagation.

The interstellar and solar modulated positron fluxes as calculated in Ref. [123] are shown in Fig. 3.2, together with an earlier result [127] and data from different experiments. From the calculation it is evident that within the nuclear and propagation uncertainties the interstellar positron flux can be parameterized as a power law with an index  $\gamma_{e^+}$  in the range  $3.3 - 3.7$  above 2 GeV. We thus allow  $\gamma_{e^+}$  to vary within this range in the derivation of the constraints. As this power law parameterization is adopted in our work, we restrict the data used for the derivation of the positron limits in our analysis to data points with energies  $E > 2$  GeV.

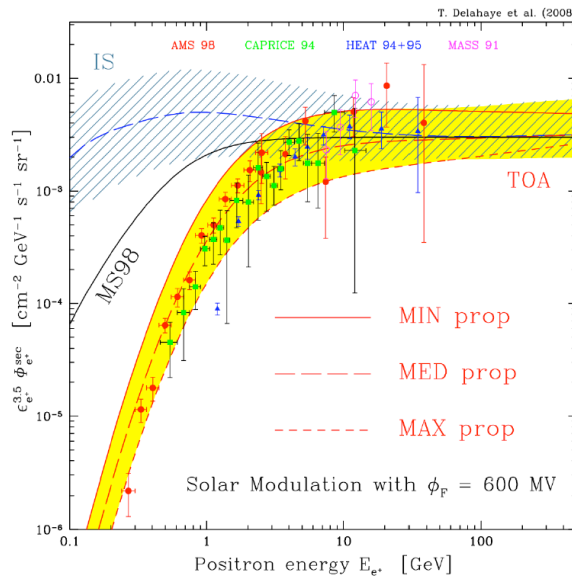


Figure 3.2: Calculated interstellar (blue line) and solar modulated (red line) secondary positron flux from Ref. [123] for MED propagation parameters. The bands correspond to the cosmic-ray propagation uncertainty as given by the MIN and MED propagation parameters, while the black line depicts the calculated interstellar positron flux from Ref. [127].

- **Additional source of electrons and positrons**

Today it is known from different measurements [106, 124–126] that the positron flux cannot be explained exclusively by secondary production. Various possible explanations have been put forward in the literature as discussed in Sec. 2.1. Irrespective of its nature, the excess can be parameterized by a power law with an exponential cutoff. The spectrum must be harder than the secondary contribution in order to fit the positron data. In our analysis we remain agnostic about the source of the excess positron flux, but we acknowledge its

### 3.1 Methodology

---

existence by including a generic power law contribution in our fit. Thus our results are valid regardless of the interpretation of the positron anomaly. Even if dark matter is indeed the reason for the lepton anomalies, our limits on other final states still apply and can be used to constrain the corresponding branching fractions.

- **Solar modulation**

As described in Sec. 2.3.4, the magnetic fields of the Sun affect the low energy part of the spectra of charged particles. This is taken into account with one additional solar modulation parameter  $\phi_{e^+}$  in the force field approximation.

Altogether, our background model contains 6 positron parameters. When minimizing the  $\chi^2$  in the fit of this positron background model to the AMS-02 positron flux data, we assume  $C_{e^+}, C_s \geq 0$ ,  $3.7 > \gamma_{e^+} > 3.3$ ,  $\gamma_{e^+} > \gamma_s$ ,  $E_s > 0$  and  $1.3 \text{ GeV} > \phi_{e^+} > 0.5 \text{ GeV}$ . We obtain the best fit with  $\chi^2/d.o.f = 10.05/52$  in the energy range  $E = 2 - 350 \text{ GeV}$  when  $C_{e^+} = 72 \text{ s}^{-1} \text{ sr}^{-1} \text{ m}^{-2} \text{ GeV}^{-1}$ ,  $\gamma_{e^+} = 3.70$ ,  $C_s = 1.6 \text{ s}^{-1} \text{ sr}^{-1} \text{ m}^{-2} \text{ GeV}^{-1}$ ,  $\gamma_s = 2.51$ ,  $E_s = 1.0 \text{ TeV}$  and  $\phi_{e^+} = 0.93 \text{ GV}$ . Our best-fit positron background is shown in the middle panel of Fig. 3.1 together with the positron data used in our analysis.

#### 3.1.1.2 Positron fraction

The positron fraction  $\Phi_f(E)$  is given by the positron flux divided by the electron plus positron flux. With the electron and positron fluxes  $\Phi_{e^-}^{\text{TOA}}(E)$  and  $\Phi_{e^+}^{\text{TOA}}(E)$  at the top of the atmosphere this reads

$$\Phi_f^{\text{TOA}}(E) = \frac{\Phi_{e^+}^{\text{TOA}}(E)}{\Phi_{e^-}^{\text{TOA}}(E) + \Phi_{e^+}^{\text{TOA}}(E)}. \quad (3.5)$$

For the evaluation of this expression the electron flux is needed. In our analysis we make use of the electron measurement by AMS-02 itself and find that this is well described by the solar modulated sum of two power laws

$$\Phi_{e^-}^{\text{TOA}}(E) = \frac{E^2}{(E + \phi_{e^-})^2} \left[ C_1 (E + \phi_{e^-})^{-\gamma_1} + C_2 (E + \phi_{e^-})^{-\gamma_2} \right], \quad (3.6)$$

where  $C_1 = 2.6 \times 10^3 \text{ s}^{-1} \text{ sr}^{-1} \text{ m}^{-2} \text{ GeV}^{-1}$ ,  $\gamma_1 = 3.83$ ,  $C_2 = 35 \text{ s}^{-1} \text{ sr}^{-1} \text{ m}^{-2} \text{ GeV}^{-1}$ ,  $\gamma_2 = 2.83$  and  $\phi_{e^-} = 1.3 \text{ GV}$ . The best-fit curve to AMS-02 electron flux yields a  $\chi^2/d.o.f = 10.95/53$  and is depicted in the top panel of Fig. 3.1. Note that we do not require the same force field parameter for electrons and positrons in order to allow for charge sign dependent solar modulation (see Sec. 2.3.4). In the computation of the constraints, the electron parameters are fixed to their best-fit values.

For the positron flux in Eq. (3.5), we use exactly the same 6 parameter background model as for the positron flux described above. This model reproduces very well the AMS-02 positron fraction data in the range  $E = 2 \text{ GeV} - 350 \text{ GeV}$  when  $C_{e^+} = 61 \text{ s}^{-1} \text{ sr}^{-1} \text{ m}^{-2} \text{ GeV}^{-1}$ ,  $\gamma_{e^+} = 3.70$ ,  $C_s = 2.4 \text{ s}^{-1} \text{ sr}^{-1} \text{ m}^{-2} \text{ GeV}^{-1}$ ,  $\gamma_s = 2.60$ ,  $E_s = 1.4 \text{ TeV}$  and  $\phi_{e^+} = 0.83$ , giving a  $\chi^2/d.o.f =$

27.78/52. Therefore, there is only little room left for an exotic component in the positron fraction. The best-fit positron fraction is depicted in the bottom panel of Fig. 3.1.

### 3.1.2 Statistical treatment

In order to calculate the constraints we introduce a dark matter component that is added to the positron flux. Here we make use of the positron fluxes from dark matter annihilations and decays after propagation given in Ref. [46] (see also Sec. 2.3.2.1) and take into account solar modulation effects as in the background fluxes with the force field approximation. The  $2\sigma$  limits are computed by performing a  $\chi^2$  fit to the data (see Appendix A). For fixed dark matter mass  $m_{\text{DM}}$ , annihilation channel and annihilation cross section  $\langle\sigma v\rangle$  or lifetime  $\tau$ , we recalculate the minimal  $\chi^2$  with respect to the positron parameters. This applies to the positron flux as well as to the positron fraction where the electron parameters are fixed to their best-fit values and are not refitted. The  $2\sigma$  upper (lower) limit is thus given by the cross section (lifetime) for which the global minimum of the  $\chi^2$  exceeds the minimal  $\chi^2$  of the pure background model by more than 4. In this case it is justified to start with the best fit of the pure background model in this procedure since  $\chi_{\text{bf}}^2 \approx \chi_{\text{bkg}}^2$ , i.e. the data is well compatible with the background-only hypothesis.

As described in the previous section, we restrict our analysis to data points above 2 GeV. This is the largest energy range where our background model is applicable. However, the selection of this energy range is somewhat arbitrary. We find that other energy windows can yield more stringent limits than the one obtained from the largest energy window. As the total positron flux must be compatible with all data that is available, the limits can be improved by sampling over all possible energy windows. Concretely, in the case of the AMS-02 with  $E > 2$  GeV, we compute the constraints on the dark matter parameters as described above for 53 energy windows and select the strongest limit among the 53 limits obtained. This is illustrated in Fig. 3.3 for annihilations and decays into  $\mu^+\mu^-$ .

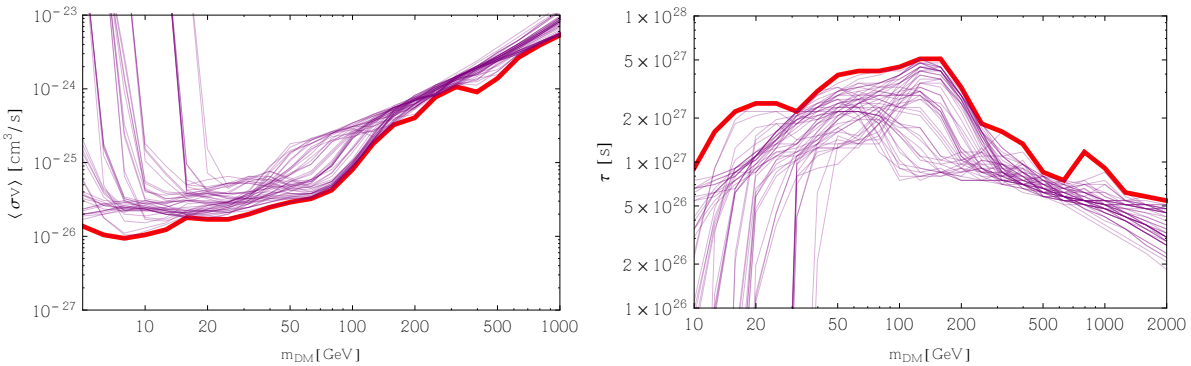


Figure 3.3:  $2\sigma$  limits from 53 energy windows (thin purple lines) are shown together with the best limit (thick red line) for annihilations (left panel) and decays (right panel) into  $\mu^+\mu^-$ . These plots have been published in Ref. [1].

Following this procedure we calculate constraints on dark matter annihilations and decays into the final states  $e^+e^-$ ,  $\mu^+\mu^-$ ,  $\tau^+\tau^-$ ,  $b\bar{b}$  and  $W^+W^-$ . In the section below we present for each final states two constraints. The limit obtained from all the data above 2 GeV is depicted by a solid line, whereas the dashed line denotes limits where we only select energy windows with  $E \geq 10$  GeV for all data points. The latter limits are only mildly affected by solar modulation effects and therefore more robust, as the solar magnetic fields mainly alter the low energy cosmic-ray spectra. Note that this is not possible in the case of HEAT due to the limited energy range of the data.

## 3.2 Constraints on dark matter parameters

In this section, we present the constraints derived from the positron measurements, the positron flux as well as the fraction and compare them with complementary limits. Furthermore, we investigate the dependence of our result on the cosmic-ray propagation parameters and the choice of the dark matter halo profile.

### 3.2.1 Limits for different final states

The constraints for annihilations and decays with 100% branching ratio into  $e^+e^-$ ,  $\mu^+\mu^-$ ,  $\tau^+\tau^-$ ,  $b\bar{b}$  and  $W^+W^-$  deduced from the AMS-02 positron flux are shown in Fig. 3.4. If not otherwise stated, all limits are depicted for the Einasto profile as parameterized in Eq. (1.8), normalized to  $\rho_\odot = 0.4$  GeV/cm<sup>3</sup>, and MED propagation parameters specified in Sec. 2.3.2.1. For annihilations

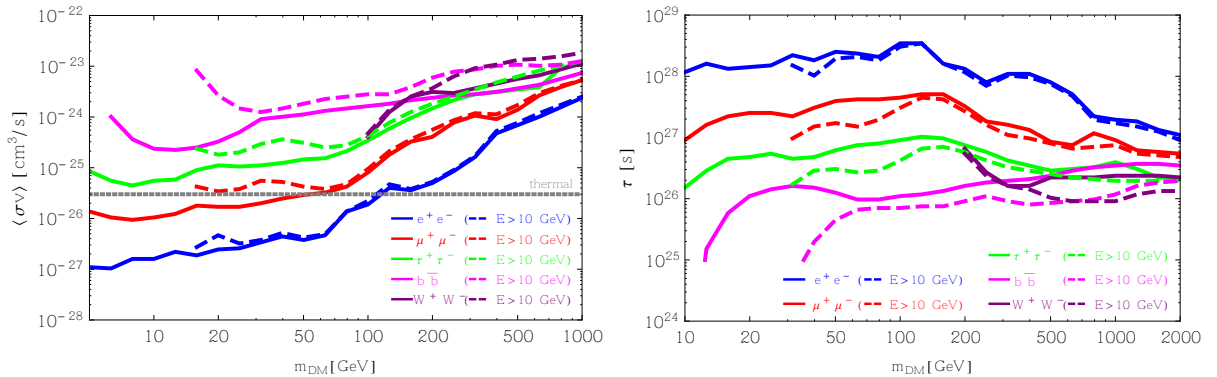


Figure 3.4: The plot shows the  $2\sigma$  upper limits on the annihilation cross section (left panel) and the dark matter lifetime (right panel) derived from the AMS-02 positron flux measurement. For each limit, concretely for  $e^+e^-$ ,  $\mu^+\mu^-$ ,  $\tau^+\tau^-$ ,  $b\bar{b}$  and  $W^+W^-$  final states, a branching fraction of 100% is assumed, using an Einasto dark matter profile and MED propagation parameters. The solid (dashed) lines denote the limit, when the data above 2 GeV (10 GeV) is taken into account. These plots have been published in Ref. [1].

the gray line indicates the thermal cross section  $\langle\sigma v\rangle = 3 \cdot 10^{-26}$  cm<sup>2</sup>/s for reference. The limits

for the  $e^+e^-$  final state are very strong, since in this case the most pronounced spectral feature is produced, probing the thermal cross section for dark matter masses below 100 GeV. In the case of annihilations into  $\mu^+\mu^-$  the limits lie below the thermal cross section for  $m_{\text{DM}} \lesssim 60$  GeV.

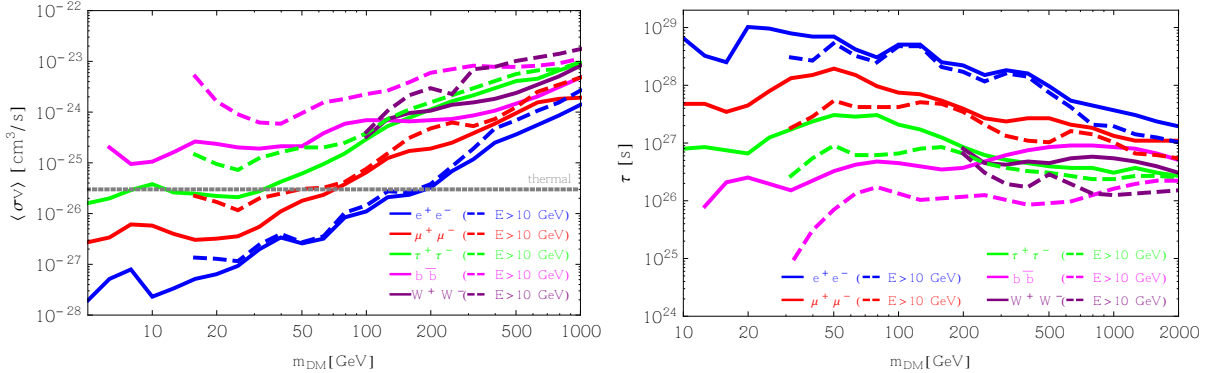


Figure 3.5: Same as Fig. 3.4, but using the AMS-02 positron fraction measurement. These plots have been published in Ref. [1].

In Fig. 3.5 we present the constraints on the same channels - again from annihilations and decays - that are obtained from the positron fraction. We find that the limits from the fraction are stronger than the corresponding limits from the positron flux by a factor of  $\sim 4 - 5$  depending on the mass. However, the modeling of the positron fraction requires knowledge about the electron flux, which makes the limits from the positron flux cleaner from a theoretical perspective.

### 3.2.2 Dependence on the diffusion parameters and halo profile

Now we test the robustness of our results and release the assumptions made on the propagation parameters and the dark matter profile. We take into account the propagation uncertainty by considering the MIN and MAX propagation parameters, which yield minimal and maximal positron fluxes from dark matter as discussed in Sec. 2.3.2.1. The limits remain unchanged in the case of MAX parameters as shown in Fig. 3.6, while they are very mildly altered when MIN parameters are used. After all, such a small height of the diffusion halo is already excluded [199].

Next, we compute the constraints for the isothermal and NFW dark matter profiles, parameterized in Eqs. (1.6) and (1.7). It turns out that the resulting limits are not affected by the choice of the halo profile (see Fig. 3.7) despite their significant discrepancies in the Galactic center. This behavior of the constraints is expected from the local origin of high-energy positrons. On the one hand, they only probe a relatively small volume of the Galaxy, concretely, the diffusion length positrons with an initial energy of 1 TeV amounts to  $\sim 1$  kpc [133]. On the other hand, the dark matter profile of the Milky Way is rather well known at large radii leading to at most mild variations at distances of a few kpc around the Solar system (see Fig. 1.5).

### 3.2 Constraints on dark matter parameters

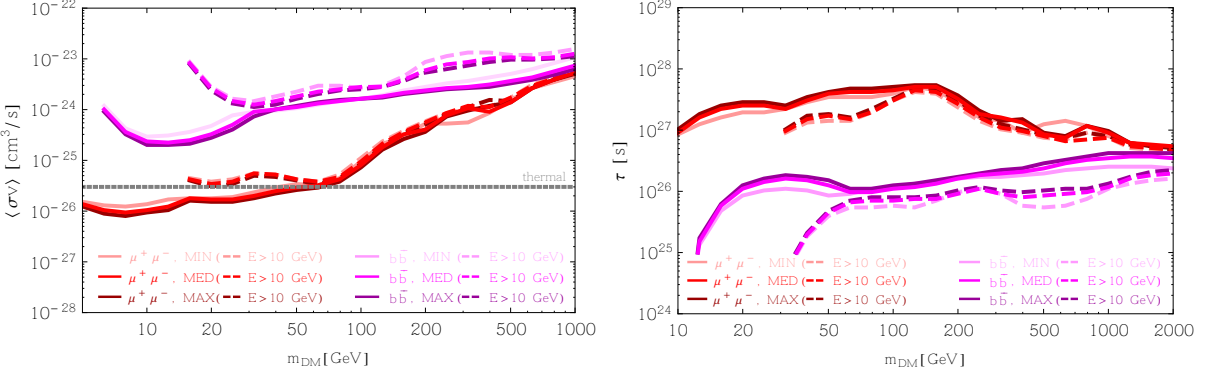


Figure 3.6: Same as Fig. 3.4 depicting the impact of the propagation parameters on the limits for  $\mu^+\mu^-$  and  $b\bar{b}$  final states. These plots have been published in Ref. [1].

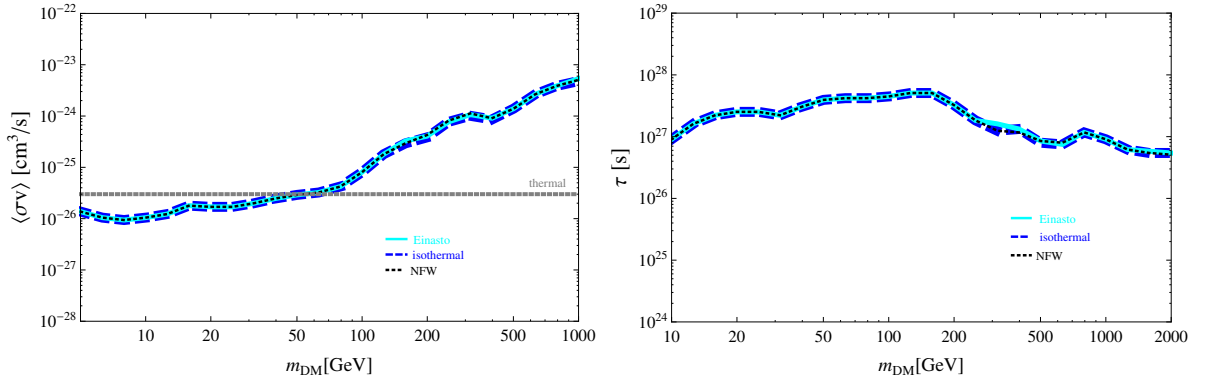


Figure 3.7: Impact of the choice of the dark matter profile on the results for annihilations (left) and decays (right) into  $\mu^+\mu^-$  derived from the positron flux data with  $E > 2$  GeV.

#### 3.2.3 Comparison with limits from other experiments and messengers

In this section, we compare the positron constraints with limits obtained from PAMELA and HEAT data in Figs. 3.8 and 3.9 for annihilations and decays into  $\mu^+\mu^-$  and  $b\bar{b}$ . As expected, due to larger errors, these limits are weaker by up to about 2 orders of magnitude with respect to the positron fraction constraints on the dark matter cross section and lifetime.

Before comparing the positron limits to constraints from other messenger particles, let us comment on the simultaneous analysis [217] of the AMS-02 positron data that appeared during the completion of our work. In Ref. [217] only the positron fraction is used to derive constraints on  $e^+e^+$ ,  $e^+e^-\gamma$ ,  $\mu^+\mu^-$  and  $\tau^+\tau^-$  final states, resulting in limits that are stronger than the positron fraction limits presented in this thesis. The reason for that is twofold. Firstly, the modeling of the energy losses lead to stronger limits by a factor of about 2. Secondly, another factor of 2 results from the different choice of the electron flux that is needed in the positron fraction. The electron plus positron flux measured by Fermi-LAT that is used in Ref. [217] is

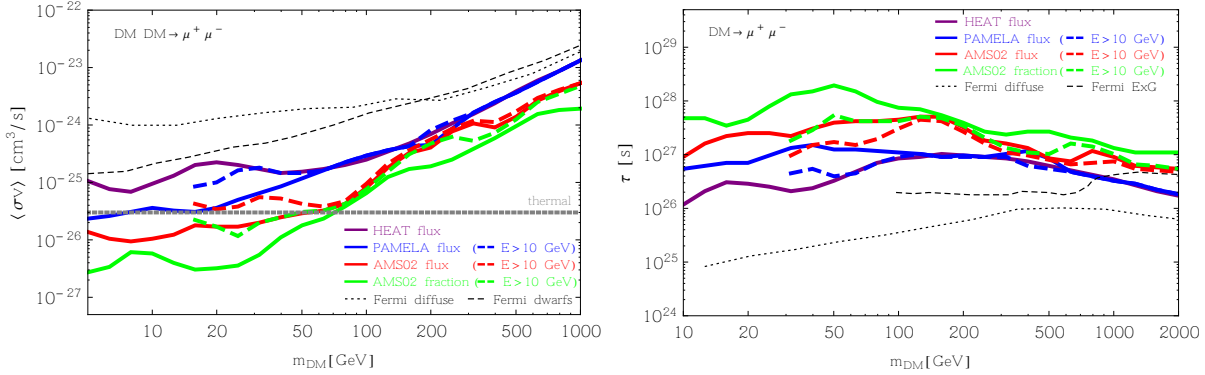


Figure 3.8: Comparison of the limits derived from positron flux data of AMS-02, PAMELA and HEAT, positron fraction data of AMS-02 together with gamma-ray limits provided from Fermi-LAT observations for dark matter annihilations (left plot) and decays (right plot) into  $\mu^+\mu^-$ . These plots have been published in Ref. [1].

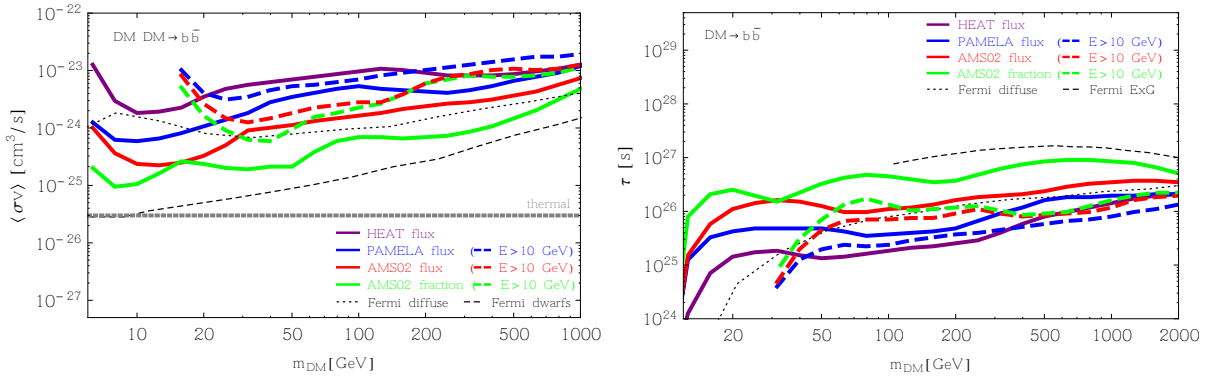


Figure 3.9: Same as in Fig. 3.8, but for the  $b\bar{b}$  final state. These plots have been published in Ref. [1].

smaller compared to AMS-02, resulting again in stronger limits. In agreement with the discussion in the previous section they find that the limits are insensitive to the choice of the different cosmic-ray propagation scenarios, but instead can vary by a factor of a few depending on the value of the local dark matter density and the value of the interstellar radiation field, which determines the rate of energy loss for high-energy positrons.

The same final states that are investigated in this work also produce other messenger particles, such as gamma rays, antiprotons and neutrinos. A comparison of the respective limits shows their complementary since, depending on the final state, different messengers deliver the best constraints. For electron and muon final states, positrons deliver the most stringent limits.

In Figs. 3.8 and 3.9, we overplot gamma-ray constraints from an analysis of 25 dwarf galaxies performed by the Fermi Collaboration [218] and from diffuse gamma-rays [219] in the case of annihilations. The limits on decaying dark matter are also compared to gamma-ray constraints

from diffuse gamma-rays shown in the same analysis [219], but also to constraints on the lifetime from the residual isotropic gamma-ray flux [220]. In the case of annihilations into  $\mu^+\mu^-$  we find that the limits derived from the positron data of all experiments under consideration surpass the gamma-ray limits in the whole energy range. Concretely, the positron flux limits are, at 10 GeV, two orders of magnitude stronger than the limit from diffuse gamma-ray measurement reported by the Fermi Collaboration, while superseding the limits from dwarf galaxies by about one order of magnitude. It is remarkable that even the HEAT measurements, conducted 20 years ago, are already more constraining in this channel than recent Fermi-LAT data. For annihilations and decays into  $b\bar{b}$ , on the other hand, the positron limits are weaker than the gamma-ray constraints from the Milky Way satellite galaxies, while in this channel the limit from diffuse gamma-rays is comparable to the limit from the positron flux and slightly worse than the limit from the fraction, as shown in Figs. 3.8 and 3.9. This is expected since annihilations and decays into  $b\bar{b}$  produce softer positrons and harder gamma-rays compared to  $\mu^+\mu^-$ , the limits are expected to be weaker.

Similar to the positron limits, the presented gamma-ray constraints are very robust as they do not depend strongly on the dark matter profile. As the limits from the diffuse gamma-rays are derived from a ROI that covers the whole sky (without the Galactic plane but including the Galactic center), the limits vary only by up to a factor of about 2 between the different profiles for annihilations, while for decays the limits are very similar for all profiles. Also the dwarf limits only depend mildly on the profile, weakening by about 15% when a cored Burkert instead of a cuspy NFW profile is considered. For the limits from the isotropic gamma ray background on decaying dark matter, the different halo profiles give almost indistinguishable results.

Since the publication of these results, the aforementioned gamma-ray limits have been updated [221–223]. Despite the improvement of the constraints with more recent data, our conclusions remain unchanged.

Very recently, the AMS-02 Collaboration released their measurement of the antiproton flux, which was subsequently employed for the improvement of previous antiproton limits. This can be achieved due to the very precise measurement and reduced propagation uncertainties. Updated results have been reported in Ref. [224]. Generally speaking, antiprotons are very constraining in hadronic channels that comprise a large antiproton yield. However, in contrast to the positron limits, they still suffer from large astrophysical uncertainties, since they probe a larger volume of the Galaxy. Despite these uncertainties, antiprotons limits are stronger in the  $b\bar{b}$  or  $W^+W^-$ -channel, for instance, whereas they are not competitive for leptonic final states. Also, note that in the derivation of the antiproton constraints the astrophysical background is often fixed to the calculated flux and not refitted as for the positron limits. In some works [225, 226], the theoretical uncertainty on the background is taken into account in the total error of the measured flux by summing experimental and theoretical uncertainties. Generally speaking, the resulting limits depend on the concrete treatment of the background, for instance which background parameters are fixed and which are refitted, and the theoretical uncertainties in the

fit [165, 225, 226], making the antiproton limits less robust compared to the positron constraints.

Dark matter limits from the IceCube or ANTARES neutrino telescopes as presented in Refs. [227–229] are in the mass range of our interest, depending on the channel, about 1 – 3 orders of magnitudes weaker than our positron limits for an NFW profile. Again, the limits from the Galactic center suffer from halo profile uncertainties. Concretely, the constraints degrade by up to one order of magnitude if a Burkert profile is assumed, as shown in Ref. [228]. In Ref. [227], where the whole northern hemisphere is considered, the dependence of the result on the profile is negligible.

Concluding this comparison, it is evident that exploiting the complementarity of the different messengers is important to derive the most stringent limits on all possible final states, which allows probing the plethora of different dark matter models put forward in the literature.

## **Part III**

# **Dark matter searches with gamma rays**



# Chapter 4

## Phenomenology of high-energy gamma rays

In this chapter, the high-energy gamma-ray emission from astrophysical sources, which constitute the background for dark matter searches, and the potential gamma-ray signals from dark matter are presented. Subsequently, the space borne and ground based gamma-ray experiments relevant for this thesis are introduced.

### 4.1 The gamma-ray sky

As gamma rays propagate essentially freely and thus provide directional as well as spectral information about their sources, they are a prime tool for dark matter searches. Sharp spectral features in the GeV to TeV energy range are a smoking gun for dark matter since they cannot be mimicked by astrophysical backgrounds. Focusing on the energy range of interest for this work, the smooth gamma-ray background is discussed in Sec. 4.1.1. Given the featureless background, sharp spectral signatures can be efficiently searched for in the gamma-ray sky. In this thesis, the ability of current and future gamma-ray telescopes to investigate sharp features, namely gamma-ray lines, gamma-ray boxes and virtual internal bremsstrahlung is studied. These gamma-ray signatures and the continuum gamma-ray signal from dark matter annihilations and decays are introduced in Sec. 4.1.2 and possible target regions for the dark matter search are presented. In addition, the effect the optical depth in the Milky Way, which is relevant in the TeV energy range, is investigated in Sec. 4.1.3.

#### 4.1.1 Astrophysical gamma-ray background

The gamma-ray sky has been extensively studied in full-sky surveys for more than 20 years with the gamma-ray telescopes EGRET (see e.g. Ref. [230]) and its successor Fermi [231] in the energy range from 20 MeV to 500 GeV. At higher energies Cherenkov telescopes are sensitive. However, these instruments cannot scan the whole sky but concentrate on particular astrophysical objects or interesting regions like the Galactic center. The observations have revealed rich structures in the gamma-ray emission. One can distinguish several components: gamma-ray point sources and the cosmic-ray induced Galactic diffuse emission. Recently, large gamma-ray emitting structures contributing to the Galactic diffuse emission, the so called Fermi bubbles, have been found in the Fermi data. After subtracting all aforementioned known contributions from the measured data,

an isotropic residual flux remains, which is believed to be extragalactic. The sky map measured by Fermi with two years of full-sky observation is shown in Fig. 4.1. In order to search for a dark

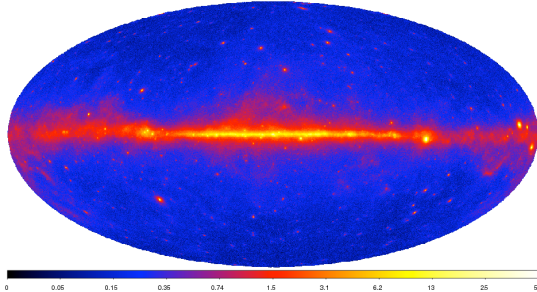


Figure 4.1: This figure shows the two year all-sky Fermi-LAT map of the gamma-ray energy flux between 100 MeV and 10 GeV taken from Ref. [232]. The color coding legend at the bottom refers to the flux in units of  $10^{-7} \text{ erg cm}^{-2} \text{ s}^{-1} \text{ sr}^{-1}$ .

matter signal in gamma rays, all the gamma-ray flux components must be taken into account in the background model. A model of the gamma-ray emission is for instance put forward by the Fermi Collaboration, where the different contributions are accounted for in spatial templates that are fitted to the measured data. The various contributions to the gamma-ray flux are briefly discussed in the following.

- **Point sources**

Above the diffuse and isotropic background, the Fermi-Telescope has detected thousands of sources: 1873 in the second [232] and 3033 in the third source catalog [233]. One can already identify some of the point sources in Fig. 4.1 by eye as bright spots within the dark background. The discovered sources can be divided into two categories: Galactic and extragalactic sources. The former are identified as pulsars, supernova remnants, globular clusters or binary systems [233, 234]. The latter comprise active galactic nuclei as well as gamma-ray bursts and exhibit, in contrast to the Galactic sources, an extreme variability [234]. However, not all gamma-ray sources can be identified or correlated to counterparts at other wavelengths. In the third Fermi source catalog, for instance, about one third of the discovered sources remains unassociated [233].

- **Galactic diffuse emission**

The origin of the Galactic diffuse emission is closely connected to cosmic-ray propagation. The same processes that lead to destruction terms and energy losses in the propagation equation Eq. (2.2) give rise to the gamma rays that constitute the diffuse background. Three components can be distinguished. Firstly, neutral pions and other neutral mesons are produced in the spallation reactions of cosmic rays and the interstellar medium. The neutral pions in turn decay into pairs of gamma rays. Secondly, bremsstrahlung is emitted in the interactions of cosmic-ray electrons with the interstellar gas. Thirdly, gamma rays

from the interstellar radiation field are upscattered to high energies by inverse Compton scattering (ICS) with cosmic ray electrons. Due to their different origins, each of the diffuse components exhibits a distinct morphology. While the emission from pions and bremsstrahlung tracks the interstellar gas distribution, the ICS contribution traces the interstellar radiation field and thus extends to higher latitudes compared to the other two components.

In order to compute the gamma-ray fluxes from the contributions to the diffuse emission, the cosmic ray fluxes in the Galaxy, the interstellar radiation field as well as the distribution and composition of the interstellar medium must be modeled (see Sec. 2.3). The Galactic plane shines bright in gamma rays as can be seen in Fig. 4.1 because most of the interstellar gas is located there. Using numerical propagation codes such as GALPROP (see Sec. 2.3.2.2) and a diffuse emission model encompassing the aforementioned components, it is possible to reproduce well the measured gamma-ray flux in the whole sky [235]. The gamma-ray fluxes of the three diffuse emission components are shown in Fig. 4.2. They are calculated from a self-consistent cosmic ray propagation model that can reproduce the measured gamma-ray flux with high accuracy.

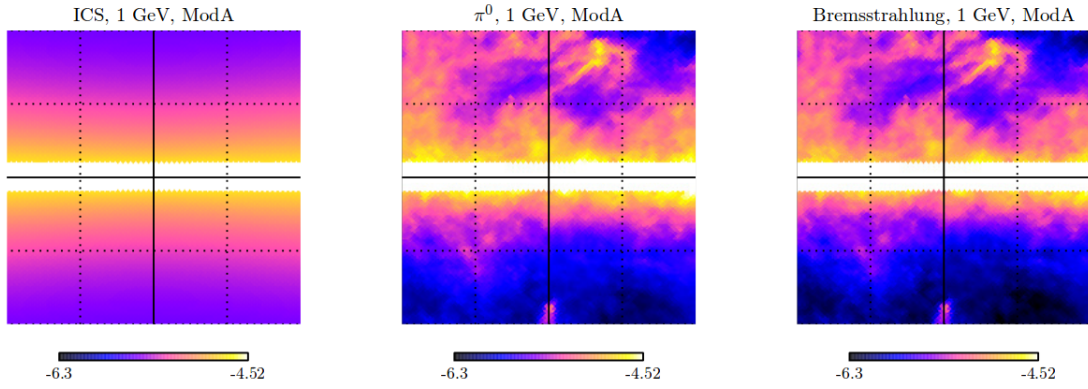


Figure 4.2: Different components of the diffuse gamma-ray emission shown in Ref. [236] for  $40^\circ \times 40^\circ$  region around the Galactic center, where  $|b| < 2^\circ$  is masked out. The color coding refers to units of  $\log_{10}(\text{GeV}^{-1} \text{cm}^{-2} \text{s}^{-1} \text{sr}^{-1})$ .

The systematic uncertainties in the modeling of the Galactic diffuse gamma rays, connected to our imperfect knowledge of the environmental properties in the Milky Way, has recently raised interest in the literature in the context of the GeV excess in the Galactic center [236, 237].

- **Fermi bubbles**

Only recently another feature in the gamma-ray sky was discovered in the Fermi-LAT data: two giant bubbles, extending  $50^\circ$  in latitude above and below the Galactic plane, spanning  $40^\circ$  in longitude [238]. The spectrum was found to be harder than the diffuse emission

spectrum in the Galactic plane, and the intensity is spatially constant. Furthermore, they are spatially correlated with the WMAP microwave haze and the features found in the ROSAT X-ray maps [238]. By now, the bubbles have also been extensively studied by the Fermi Collaboration itself [239] and accounted for in the latest interstellar gamma-ray emission model [240]. The residual gamma-ray flux after subtracting all known contributions to the gamma-ray emission reveals the bubbles and is shown in Fig. 4.3. This map is used to create a spatial template in order to include the Fermi bubbles in the emission model. The origin of the bubbles is however not yet fully understood. Possible explanations

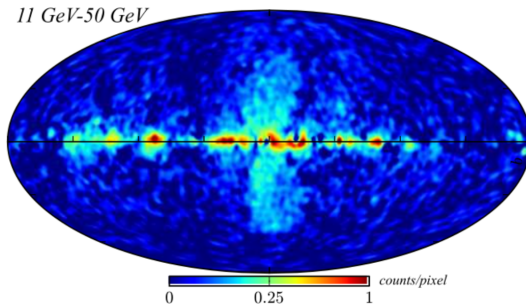


Figure 4.3: Fermi-LAT count map after subtracting all known contributions to the gamma-ray flux. The figure is taken from Ref. [240].

include recent activity of the supermassive black hole at the center of our Galaxy, nuclear star formation [241], an active galactic nucleus, inverse Compton scattering or hadronic interactions inside the bubbles [239].

- **Isotropic emission**

Fitting the contributions of the gamma-ray emission described above to the data leaves an isotropic residual flux. This flux is thought to be truly extragalactic and comprises the sum of all sources from the edge of the Milky Way to the edge of the observable Universe. In fact, this residual flux constitutes an upper limit to the extragalactic flux because unresolved Galactic sources also contribute.

#### 4.1.2 Gamma rays from dark matter

This section discusses the expected gamma-ray flux from dark matter annihilations and decays. First, the calculation of the gamma-ray flux is reviewed, followed by the discussion of possible sharp and continuous dark matter signals. Afterwards, possible target regions for dark matter searches are presented. Lastly, the optical depth of the Milky Way is calculated, which is relevant for very high-energy gamma rays.

### 4.1.2.1 Gamma-ray flux from dark matter annihilations and decays

The gamma-ray flux from dark matter depends on the dark matter profile. In fact, the dependence is different for annihilations and decays. In the former case the dependence is quadratic whereas in the latter case the dependence is linear. This results in different optimal target regions for indirect searches with gamma rays.

In the case of annihilations the gamma-ray flux from dark matter is given by

$$\frac{d\Phi_\gamma}{dE_\gamma} = \frac{1}{k} \frac{1}{4\pi m_{\text{DM}}^2} J_{\text{ann}} \sum_f \langle \sigma v \rangle_f \frac{dN_\gamma^f}{dE_\gamma}, \quad J_{\text{ann}} = \int_{\Delta\Omega} d\Omega \int_{\text{l.o.s.}} ds \rho(r)^2, \quad (4.1)$$

with  $k = 2$  for self conjugate particles and  $k = 4$  otherwise, whereas for decays it reads

$$\frac{d\Phi_\gamma}{dE_\gamma} = \frac{1}{4\pi} \frac{1}{m_{\text{DM}}} J_{\text{dec}} \sum_f \Gamma_f \frac{dN_\gamma^f}{dE_\gamma}, \quad J_{\text{dec}} = \int_{\Delta\Omega} d\Omega \int_{\text{l.o.s.}} ds \rho(r). \quad (4.2)$$

Here  $m_{\text{DM}}$  denotes the dark matter mass,  $\langle \sigma v \rangle_f$  and  $\Gamma_f$  the velocity-weighted annihilation cross section and the decay rate for a particular final state  $f$ , respectively. The astrophysical  $J$ -factor encodes the information on the dark matter distribution in a particular direction in the sky. It is calculated by the integral over the region of interest  $\Delta\Omega$  and over the line of sight (l.o.s.). The coordinate  $r$ , i.e. the distance from the Galactic center, can be parameterized as  $r(s, \theta) = (r_\odot^2 + s^2 - 2r_\odot s \cos \theta)^{1/2}$ , where  $\theta$  is the angle between the line of sight and the connecting line between the Earth and the Galactic center [46].

The spectral shape of the differential number density of photons per annihilation or decay depends on the annihilation/decay channel. Sharp features as well as a gamma-ray continuum can be produced as discussed in the following sections.

The absorption of high-energy gamma rays through electron-positron pair production with photons from the interstellar radiation field leads to a modification of the  $J$ -factor. Since the absorption depends on the gamma-ray energy, the  $J$ -factor also gets energy-dependent. It turns out that it is reduced by up to tens of percent at multi-TeV energies. The energy-dependent  $J$ -factor is computed in Sec. 4.1.3.

### 4.1.2.2 Sharp features

Different annihilation or decay processes can lead to sharp gamma-ray features. The possible signatures are monochromatic lines, gamma-ray boxes and internal bremsstrahlung. They are discussed one by one below. All these processes have in common that the resulting gamma-ray spectrum is very distinct from the smooth astrophysical background. Such a feature cannot be mimicked by astrophysical processes at these energies and their detection would be a smoking gun for dark matter.

The processes that lead to the aforementioned gamma-ray features are depicted in Fig. 4.4 and their spectrum is shown in Fig. 4.5 for the case of annihilations. Furthermore, in all cases, the features in the photon spectrum are directly related to (half) the mass of the dark matter

particle for annihilations (decays). The following discussion as well as Figs. 4.4 and 4.5 refer to annihilations, however it is completely general and also applies to decays with  $m_{\text{DM}} \rightarrow m_{\text{DM}}/2$ .

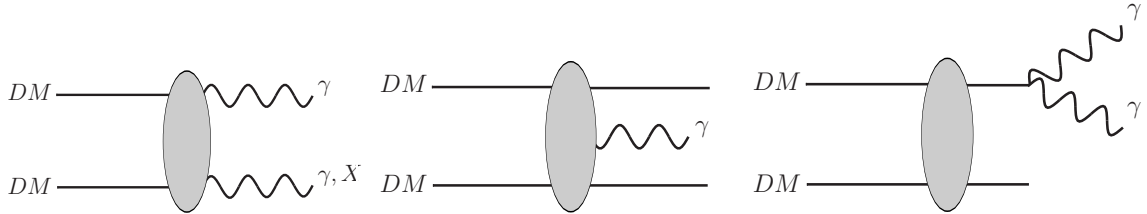


Figure 4.4: Three examples of annihilation processes that give rise to sharp spectral features: annihilation into monochromatic photons (left), virtual internal bremsstrahlung (middle) and gamma-ray boxes (right).

- **Monochromatic lines**

The most intensively studied spectral feature are gamma-ray lines [242–244] coming from dark matter annihilations into monochromatic photons shown in Fig. 4.4. If there are two gamma rays in the final state, their energy just corresponds to the dark matter mass  $E_\gamma = m_{\text{DM}}$  in the center of mass frame. For annihilations into a photon and another particle  $X$  of mass  $m_X$  energy-momentum conservation leads to a gamma-ray energy of

$$E_\gamma = m_{\text{DM}} \left( 1 - \frac{m_X^2}{4m_{\text{DM}}} \right), \quad (4.3)$$

where  $X$  could be any neutral boson, such as the  $Z$  or Higgs boson for instance. In both cases the spectral feature corresponds to a line in the gamma-ray flux. When  $m_{\text{DM}} \gg m$ , the gamma-ray line in the latter case it is also located at the dark matter mass. In practice, the width of the gamma-ray line is determined by the energy resolution of the gamma-ray telescope. The resulting spectrum is plotted in Fig. 4.5. As dark matter does not couple to photons directly, these processes are typically loop-suppressed with  $\mathcal{O}(\alpha^2)$ , leading to a relatively small gamma-ray flux.

- **Gamma-ray boxes**

Gamma-ray boxes arise in cascade processes, when the dark matter particles annihilate into intermediate scalars that in turn decay in flight into photons. The scalars have a fixed energy in the center of mass frame of the annihilation, but the energy of the photon depends the direction in which it is emitted with respect to the direction of motion of the intermediate scalar. As the decay of the intermediate scalar is isotropic, all directions are equally probable and thus all kinematically allowed energies are populated, resulting in a flat spectrum. The width of the box thus depends on the mass difference between the dark matter particle and the intermediate scalar. An example of this process is shown in Fig. 4.4 and the resulting spectrum in Fig. 4.5. In the case of boxes, there is in general

no suppression like in the case of gamma-ray lines, however for a concrete model the corresponding branching fractions have to be taken into account. Gamma-ray boxes are discussed in more detail in Sec. 5.2.1.

- **Virtual internal bremsstrahlung**

In the annihilation of dark matter particles, tree level diagrams with photons can occur. Dark matter cannot directly couple to photons, but instead to charged particles that subsequently emit the photon, resulting in a three-body final state [245–250]. When the photon is emitted from virtual charged states, the process is dubbed virtual internal bremsstrahlung and is depicted in Fig. 4.4. Another contribution typically arises in the same process from final state radiation, where charged particles can also emit gammas. Despite its tree level nature, this process is phase space suppressed with respect to the two-body annihilation. Another suppression of  $\mathcal{O}(\alpha)$  arises due to the additional electromagnetic coupling to the photon.

While the final state radiation spectrum is roughly featureless with a sharp cutoff at the kinematic endpoint, virtual internal bremsstrahlung can produce sharp line-like features. This contribution can be significant when the virtual charged particle that emits the photon appears in the t-channel and its mass is degenerate with the dark matter mass [245, 246, 250]. This is the case for minimal dark matter and further investigated in Sec. 5.3. An example of a sharp virtual internal bremsstrahlung spectrum is shown in Fig. 4.5.

#### 4.1.2.3 Continuum gamma rays

A continuum of gamma rays occurs in the decay and hadronization of  $q\bar{q}$ ,  $W^+W^-$  and  $ZZ$  final states and, to a lesser extent, also from leptonic final states. The resulting gamma-ray spectrum can be obtained from Monte Carlo event generators [46], for instance PYTHIA, in analogy to the positron spectrum (see Sec. 2.2.2). In the case of annihilations into  $W^+W^-$  and  $ZZ$  the gamma-ray spectrum can be parameterized as [251]

$$\frac{dN}{dx} = \frac{0.73}{x^{1.5}} e^{-7.8x} \quad \text{for } x \leq 1, \quad \frac{dN}{dx} = 0 \quad \text{otherwise,} \quad (4.4)$$

where  $x = E_\gamma/m_{DM}$ . This parameterization is adopted in Sec. 5.3, where the continuum emission is investigated in the minimal dark matter framework. Other parameterizations of the gamma-ray spectrum  $dN/dx$  that fit well the gamma-ray flux obtained with PYTHIA are provided in a more recent study [252] for annihilations into quarks, muons, taus as well as  $W$  and  $Z$  bosons. A fit function with 8 parameters is found to describe well the gamma-ray spectra for  $W^+W^-$  and  $ZZ$  final states, where the fit parameters depend on the dark matter mass. The parameterizations are valid down to  $x = 2 \cdot 10^{-4}$  and  $x = 2 \cdot 10^{-5}$  for annihilations into  $W$  and  $Z$  bosons, respectively. In the mass range of our interest, above 1 TeV, however, the photon spectrum does not change. Even though somewhat different fit parameters are found for the annihilations into  $W$  and  $Z$ ,

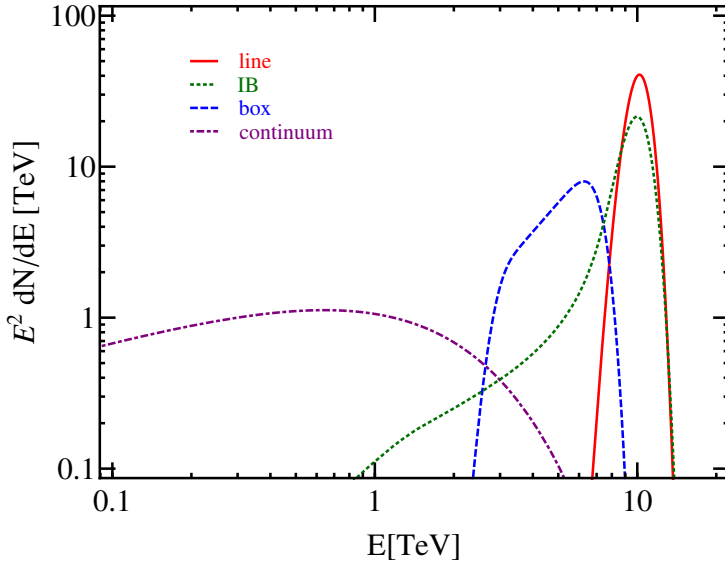


Figure 4.5: This figure shows example spectra of a gamma-ray line, a gamma-ray box and internal bremsstrahlung (all normalized to one photon per annihilation) together with the continuum emission from  $W^+W^-/ZZ$  according to Eq. (4.4) from the annihilation of dark matter particles with mass  $m_{\text{DM}} = 10 \text{ TeV}$ . In the figure, an energy resolution of 10% is adopted.

both function agree with the simpler parameterization given by Eq. (4.4) within  $\sim 30\%$  above  $x = 5 \cdot 10^{-3}$ , which is sufficient for our purposes.

Featureless gamma rays not only arise as prompt radiation as described above, but also as secondary emission, resulting from inverse Compton scattering of electrons and positrons from dark matter annihilations with photons from the interstellar radiation field. As charged particles diffuse in the Galaxy, inverse Compton radiation is expected from all directions in the sky, including regions where the background is reduced. In addition, synchrotron radiation is produced in the Galactic magnetic fields, contributing, however, to the microwave radiation.

#### 4.1.2.4 Targets for dark matter searches

Since gamma rays deliver directional information about their sources, gamma-ray telescopes have to observe target regions or objects where dark matter is expected to produce potentially observable gamma-ray fluxes. There are several such targets that are commonly studied in the literature (see Ref. [253] and references therein). The Galactic halo including the Galactic center, dwarf galaxies, galaxy clusters and the extragalactic signal are briefly discussed below. Other targets investigated in the literature are dark matter subhalos in the Milky Way [254] or external galaxies [255].

Generally speaking, there is always a trade-off between the intensity of the expected gamma-

#### 4.1 The gamma-ray sky

---

ray signal from dark matter and the importance of astrophysical backgrounds. Note that these considerations are in general different for dark matter annihilations and decays since the dark matter signal depends linearly on the dark matter density in the case of decays, while featuring a quadratic dependence in the case of annihilations. In gamma-ray observations, the morphological information on the expected dark matter distribution can also be taken into account and potentially improve the sensitivity to a dark matter signal (see e.g. Refs. [256, 257]). The expected dark matter annihilation signal calculated from the dark matter simulation Via Lactea II is shown in Fig. 4.6. It contains contributions to the gamma-ray flux from the smooth dark matter distribution of the Milky Way, Galactic subhalos as well as extragalactic halos and subhalos [52]. In order to obtain a qualitative picture of the relative intensities of the signal and the background, this has to be compared to the gamma-ray sky map shown in Fig. 4.1.

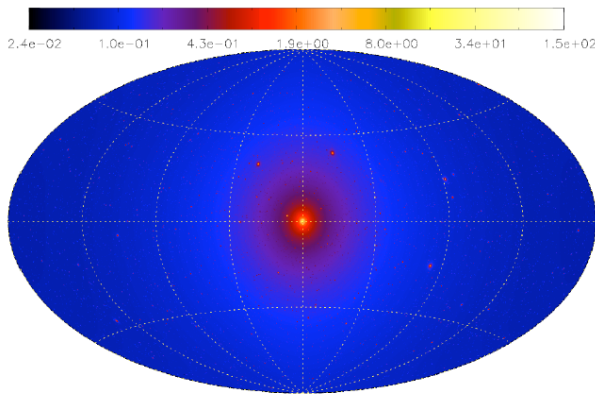


Figure 4.6: Full-sky map in Galactic coordinates of the photon counts from dark matter annihilations above 3 GeV as expected from the Via Lactea II simulation. The figure is taken from Ref. [52].

- **Galactic halo**

An obvious target to search for a gamma-ray flux from dark matter is the halo of the Milky Way [253]. As evident from Fig. 4.6, the largest flux from annihilations is expected from the Galactic center, especially when the dark matter profiles exhibits a central cusp. However, from this region as well as from the Galactic plane large diffuse backgrounds are observed that are not yet fully understood, as discussed above. An additional background consists of the gamma-ray sources in the Galactic center and plane. Therefore, the very center of the Galaxy is excluded in some analyses in order to reduce systematic uncertainties from the gamma-ray background as well as the halo profiles (see e.g. Ref. [258]). In other works, larger regions in the sky are considered, where the Galactic plane, with the exception of the Galactic center, is excluded (see e.g. Ref. [259]).

Regions that exhibit relatively small astrophysical backgrounds are for instance regions at higher latitudes. In these regions, on the other hand, the gamma-ray signal from dark

matter annihilations is also expected to be weak due to the smaller dark matter density compared to the center of the Galaxy. In order to enhance the sensitivity of dark matter searches, optimized search regions have been put forward in the literature [260–262] that differ depending on the morphology of the background and the dark matter profile. The regions presented by the Fermi Collaboration are described in Sec. 5.1.2.2.

In the remainder of the thesis, target regions in the Galactic center and the Galactic halo are considered in the search for gamma-ray spectral features from dark matter.

- **Dwarf Galaxies**

Dwarf galaxies are gravitationally bound satellite galaxies orbiting the Milky Way. They constitute a promising target for dark matter searches since they are among the most dark matter dominated objects in the Universe, which was revealed by the study of stellar dynamics. As they lack recent star formation and contain little interstellar gas as target material for cosmic rays to produce gamma rays, their observation does not suffer from large gamma-ray backgrounds. The dark matter profile - a large uncertainty in many targets - can be constrained in the case of dwarf spheroidals from dynamical arguments [263].

- **Galaxy Clusters**

As the mass of galaxy clusters is dominated by dark matter, they have also been considered as targets in indirect dark matter searches. However, gamma rays are not only expected to arise from dark matter annihilations or decays in these objects. Gamma-ray point sources such as active galactic nuclei and radio galaxies contribute to the gamma-ray background. Furthermore, gamma rays are produced in the intercluster medium in collisions with cosmic rays. As galaxy clusters extend up to a few degrees in the sky, the gamma-ray flux from dark matter is also expected to be spatially extended [263].

- **Extragalactic signal**

The extragalactic dark matter gamma-ray signal originates from the summed emission of all extragalactic dark matter halos and is expected to be isotropic. This signal can be searched for in the isotropic gamma-ray background presented in the previous section. However, there is also a residual flux from the Galactic halo, the minimal flux expected with respect to all directions in the sky, with also comprises an isotropic contribution [220].

Common to all these targets is the imperfect knowledge of the dark matter profile, the shape of the smooth component as well as the amount of substructure within the smooth component. It has been shown that the higher density of dark matter subhalos can lead to an enhanced annihilation signal. The so-called boost factor is expected to be of order unity for the Galactic center, while it can be as large as  $\mathcal{O}(1000)$  for galaxy clusters compared to the expectation from a smooth density distribution (see Ref. [264] and references therein).

### 4.1.3 Optical depth in the Milky Way

In this section we consider the absorption of gamma rays in the Milky Way. Due to the process  $\gamma + \gamma \rightarrow e^+ + e^-$  with photons from the interstellar radiation field the gamma-ray flux gets attenuated. The importance of this effect was pointed out in Refs. [265, 266] not only for extragalactic, but also for Galactic high-energy gamma-rays right after the discovery of the CMB [267]. In the calculation of the dark matter limits from gamma rays this effect is manifest in a modification of the  $J$ -factor that as a result gets energy-dependent and is reduced by up to tens of percent for multi-TeV gamma-ray energies. The energy-dependent  $J$ -factor that encodes the attenuation is calculated in the following and used in Sec. 5.2 in the calculation of the CTA prospects.

First, the attenuation of the gamma ray flux must be calculated. For a photon with initial energy  $E_\gamma$  the attenuation is given by  $e^{-\tau(E)}$  [268, 269] with

$$\tau(E_\gamma) = \frac{1}{2} \int_{\text{l.o.s.}} ds \int_{-1}^1 d(\cos \theta) (1 - \cos \theta) \int_{E_{\min}}^{\infty} dE'_\gamma n(E'_\gamma, R(s, b, \ell)) \sigma_{\gamma\gamma}(E_\gamma, E'_\gamma, \theta), \quad (4.5)$$

where  $n(E'_\gamma, r)$  is the number density of photons with energy  $E'_\gamma$  of the ISRF,  $\theta$  the angle between the two colliding photons and the  $\sigma_{\gamma\gamma}$  the electron-positron pair production cross section with its threshold energy  $E_{\min}$ . The spatial integral has to be performed along the line of sight  $s$  between the observer and the gamma-ray source,  $\ell$  and  $b$  denote the longitude and latitude in Galactic coordinates. In our calculation, we assume a cylindrically symmetric interstellar radiation field and neglect its  $z$ -dependence. This is justified since we are only interested in the attenuation in a relatively small region around the Galactic center, where the radiation field does not change significantly. Thus, the interstellar radiation field only depends on the radial coordinate  $R$  that has to be parameterized with the line of sight  $s$ . It is given by [46]

$$R = \sqrt{r(s, \ell, b) - s^2 \sin^2 b} \quad \text{with} \quad r = \sqrt{r_\odot^2 + s^2 - 2r_\odot \cos \ell \cos b}. \quad (4.6)$$

The pair production cross section for gamma-rays with initial energies  $E_\gamma$  and  $E'_\gamma$  is given by

$$\sigma_{\gamma\gamma}(E_\gamma, E'_\gamma, \theta) = \frac{3\sigma_T}{16} (1 - \beta^2) \left[ 2\beta(\beta^2 - 2) + (3 - \beta^4) \ln \left( \frac{1 + \beta}{1 - \beta} \right) \right], \quad (4.7)$$

where  $\sigma_T$  denotes the Thomson cross section and  $\beta(E_\gamma, E'_\gamma)$  is given by

$$\beta(E_\gamma, E'_\gamma) = \sqrt{1 - \frac{2m_e^2}{E_\gamma E'_\gamma (1 - \cos \theta)}}. \quad (4.8)$$

The energy threshold  $E_{\min}$  for pair production, which is reached when the center of mass energy equals four times the electron rest mass squared, reads

$$E_{\min} = \frac{2m_e^2}{E'_\gamma (1 - \cos \theta)}. \quad (4.9)$$

For the ISRF (see Sec. 2.3.1) we use the model presented in Ref. [181], where the photon spectra are given at various locations in the Galaxy: at  $(r, z) = (0 \text{ kpc}, 0 \text{ kpc})$ , at  $(4 \text{ kpc}, 0 \text{ kpc})$ , at

(12 kpc, 0 kpc) and at (16 kpc, 0 kpc). We adopt these spectra and interpolate logarithmically in the radius from the Galactic center between these curves. The ISRF spectra at these locations are plotted in Fig. 2.3.

As the energy of the photons in the ISRF is very low  $E \lesssim \mathcal{O}(\text{eV})$ , the attenuation becomes only relevant at very high gamma-ray energies, i.e. at about a few TeV in the case of starlight and infrared radiation from dust, resulting in the first dip in the attenuation factor. As a result, at 100 TeV the gamma-ray flux from the Galactic center gets reduced by about 25%. At a few hundred TeV gamma-ray energies, the CMB becomes relevant leading to a further decrease in the attenuation factor. In fact, our calculation is in good agreement with the results presented in Ref. [181], where the full spatial model of the ISRF field is used.

Now, the calculation of the  $J$ -factor has to be modified in order to take into account the attenuation of the gamma rays on their way from their location of production to detection. The new  $J$ -factor can be calculated for annihilations by

$$J_{\text{ann}}^\tau(E_\gamma) = \iint_{\Delta\Omega} db d\ell \int_{\text{l.o.s.}} ds e^{-\tau(E_\gamma, s, b, \ell)} \rho(r(s, b, \ell))^2, \quad (4.10)$$

and for decays by

$$J_{\text{dec}}^\tau(E_\gamma) = \iint_{\Delta\Omega} db d\ell \int_{\text{l.o.s.}} ds e^{-\tau(E_\gamma, s, b, \ell)} \rho(r(s, b, \ell)), \quad (4.11)$$

where  $s$  is the distance between the location of the Earth and the location of the dark matter annihilation. The  $J$ -factor is now energy dependent. The ratio of the energy dependent  $J$ -factor and the conventional one without considering the optical depth for dark matter annihilations is plotted in Fig. 4.7.

In this figure we consider the same region of interest of  $2^\circ \times 2^\circ$  around the center of the Galaxy as in Sec. 5.2, where the attenuation of the gamma-ray flux from this region is taken into account in the dark matter annihilation limits. The ratio of the  $J$ -factors exhibits two dips, the first originating from the ISRF without the CMB, the second starting when the CMB becomes relevant at a few hundred TeV. At 100 TeV, which corresponds to the highest energies considered in the remainder of the thesis, the  $J$ -factor is reduced by about 25%.

## 4.2 Gamma-ray experiments

This section is dedicated to current and future gamma-ray experiments that are considered in the remainder of the thesis. Either the measured data in the case of H.E.S.S. or, in the case of CTA and HERD, simulated data are employed in this part in order to derive limits for the dark matter properties by searching for sharp features in the galactic gamma-ray flux. In addition, the Fermi-LAT experiment is also briefly introduced.

High-energy gamma rays can be measured employing two different methods. In the energy regime up to  $\sim 1$  TeV they are measured with satellites experiments. At energies up to  $\sim 100$  TeV very high-energy gamma rays are detected by observing the extensive air showers initiated in the

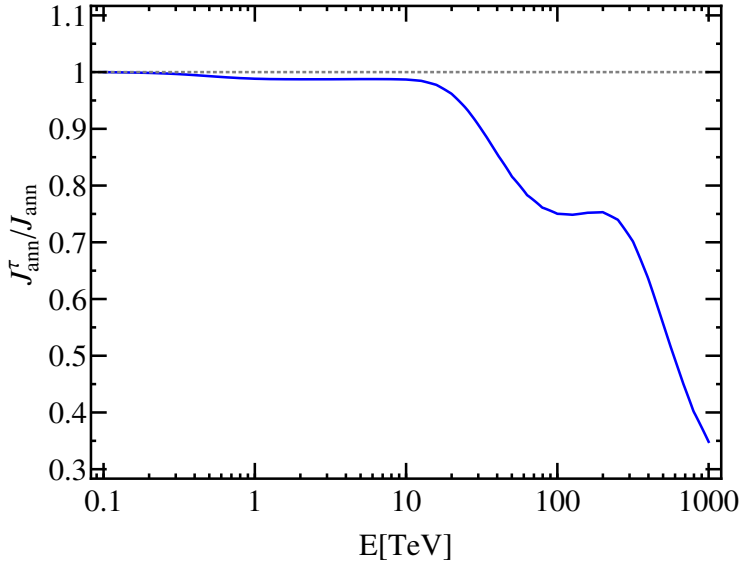


Figure 4.7: Ratio of the conventional and the energy dependent  $J$ -factor that encodes the optical depth of the Milky Way for dark matter annihilations in a  $2^\circ \times 2^\circ$  target region around the center of the Galaxy.

atmosphere with ground based experiments. The reason for the use of different experimental techniques in these two energy regimes is the following Ref. [174]: The gamma-ray flux above 1 TeV is very low, well below  $1 \text{ m}^{-2} \text{ yr}^{-1}$  from the Galactic center, which is a strong gamma-ray emitter. These fluxes are too low to be measured with space based experiments that feature small effective areas of  $\sim 1 \text{ m}^2$ . Ground based Cherenkov telescopes on the other hand exhibit large effective areas of  $\sim 10^4 - 10^6 \text{ m}^2$ . With typical observation times up to hundreds of hours, enough statistics can be collected even at very high energies. The energy threshold for the gamma-ray detection of these telescopes lies at  $\sim 30 - 300 \text{ GeV}$ , because the Cherenkov light in showers from gamma rays with smaller energies cannot be detected in these telescopes. As the energy dependence of the high-energy gamma rays typically follows a power law  $d\Phi/dE \propto E^{-\Gamma}$  with  $\Gamma \sim 2 - 3$ , the fluxes at lower energies are however large enough to be detected with enough statistics by space based instruments despite their small effective areas.

Space based gamma-ray experiments are typically pair conversion detectors [205]. In foils of high- $Z$  material the incident gamma ray converts into an electron-positron pair, which in turn enters in the calorimeter where its energy is measured. An anticoincidence system vetos incoming charged particles.

Ground based gamma-ray telescopes on the other hand, use the Earth atmosphere as a calorimeter. A high-energy gamma-ray initiates a shower in the atmosphere. An electron-positron pair is created in the vicinity of a nucleus. The charged particles emit bremsstrahlung photons, which in turn undergo pair production. In the electromagnetic shower that is created

by the alternation of these processes, the charged particles have a velocity that is greater than the speed of light in the atmosphere and thus Cherenkov radiation is emitted. The Cherenkov light in turn is detected by optical telescopes in order to reconstruct the gamma-ray energy and arrival direction. As Cherenkov light from a shower covers a surface with a diameter of several hundred meters, multiple telescopes are needed in order to record sufficient information on the event. Typically, Cherenkov telescopes are located at high altitudes, because the maximum number of particles in the shower is reached at altitudes of about 10 km for gamma rays of GeV to TeV energies. In order to avoid dilution of the emitted Cherenkov light in the atmosphere, the instruments are located a few thousand meters above sea level. The standard observation conditions correspond to moonless nights, i.e. with both Sun and Moon below the horizon, leaving typically about 1650h/year of possible dark observation time [270].

Depending on the detection technique, the characteristics of the instruments can be very different. Satellites can survey the whole sky, whereas Cherenkov telescopes can point in the region of interest, but only within a limited region in the sky due to their location on the Earth. Typically, space based instrument have a wider field of view in comparison with ground based telescopes. Furthermore, the importance of the backgrounds that have to be taken into account in dark matter searches depends on the type and details of the experiment. For Cherenkov telescopes, for instance, electrons are an irreducible background, because the electromagnetic showers caused by electrons and gamma rays cannot be distinguished. The situation is different in the case of satellite experiments because charged particles can be identified with veto-systems around the detector. The satellite experiments relevant for this work are the Fermi Large Area Telescope (Fermi-LAT) and the High Energy cosmic-Radiation Detection (HERD) instrument, which is foreseen to be installed onboard the Chinese space station. Due to their larger effective area, Cherenkov telescopes can measure gamma rays up to very high energies. Thus data measured by the High Energy Spectroscopic System (H.E.S.S.) and simulated Cherenkov Telescope Array (CTA) data are used in this work to explore a dark matter mass range, which cannot be probed with any other detection method.

#### 4.2.1 Fermi-LAT

The Fermi Large Area Telescope is the main instrument onboard the Fermi Gamma Ray Space Telescope [231]. The satellite was launched on June 11<sup>th</sup>, 2008 and the Fermi-LAT is taking data since then. It orbits the Earth in an altitude of about 565 km allowing the LAT to cover the full sky uniformly within two orbits. Fermi-LAT is a pair conversion telescope that consists of a precision conversion-tracker, a calorimeter and an anticoincidence system. In order to reconstruct the direction of the incident gamma-ray, the path of the created electron-positron pair is recorded in the tracker. Besides the energy measurement, the calorimeter contributes to the background rejection by imaging the shower development. The anticoincidence system mounted around the detector rejects charged particles better than  $10^{-5}$ . Its large effective area of  $9500\text{ cm}^2$  and large field of view of  $2.4\text{ sr}$  make the LAT a prime instrument for gamma-ray astronomy. Its energy

resolution is better than 18% in the whole energy range of 20 MeV to 300 GeV.

### 4.2.2 HERD

The High Energy cosmic-Radiation Detector [271] is foreseen to be one of the scientific payloads of the future Chinese Space Station, which is planned to be launched around 2020. The scientific aim of the HERD instrument is to measure high-energy electrons and gamma rays from 100 MeV to 10 TeV and the spectra of primary cosmic rays from 10 GeV to PeV energies.

The HERD detector itself has a large effective area compared to its volume of about  $70^3 \text{ cm}^3$ . This originates in the detector layout. The calorimeter is surrounded by silicon trackers and pair conversion foils from 5 sides. This is unique to the HERD instrument. In previous pair conversion telescopes only the top layer contains an electron-positron converter. Thus HERD can achieve a very good performance. It has an effective area of  $3000 \text{ cm}^2$  at 5 GeV that degrades to  $1500 \text{ cm}^2$  at 1 TeV. Naively one would expect a larger effective area in view of the detector layout. These numbers refer in fact only to one side of the instrument, since the improvement that is gained from covering 5 sides of the instruments with detectors is taken into account in the exposure. The calorimeter measures not only the particle energy but also serves to discriminate electrons from protons. The particle's charge and direction is obtained from the tracker. Due to its high granularity calorimeter, HERD can measure gamma rays with an energy resolution better than 2% above 10 GeV. However, the energy resolution is limited to be larger than 1% because of the readout uncertainty. The projected energy resolution and effective area for gamma rays are shown in Fig. 4.8. HERD also performs very well in rejecting backgrounds. It can

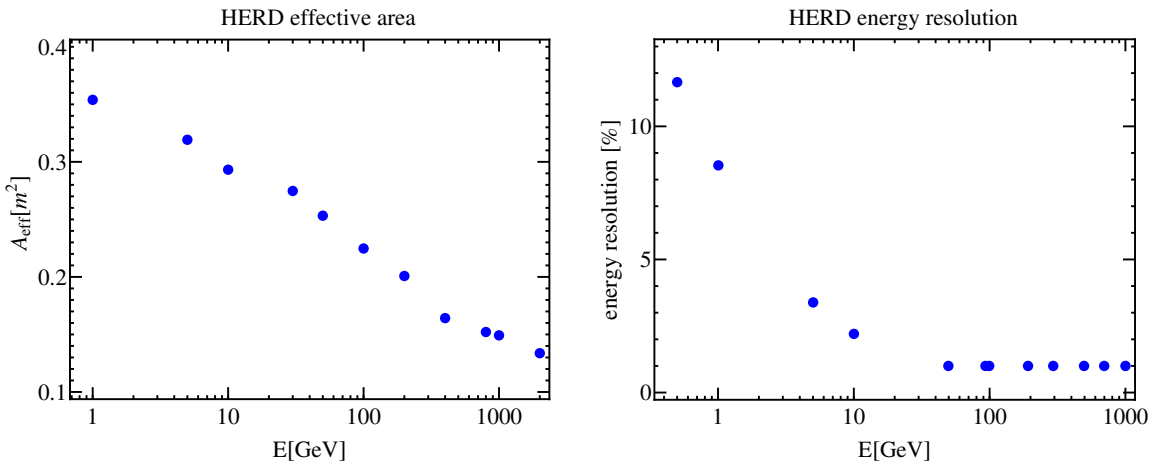


Figure 4.8: The left panel shows the effective area of the HERD facility, the right panel the energy resolution for gamma rays.

discriminate gamma rays and electrons with a rejection power of  $10^{-3}$ , electrons and protons with  $10^{-5}$  and gamma rays and protons better than  $10^{-8}$ . For the simulation of the data, the gamma-ray detection efficiency has to be taken into account. In the case of HERD, it amounts

to 0.57.

### 4.2.3 H.E.S.S.

The High Energy Stereoscopic System [272] experiment is located in Namibia, at an altitude of 1800 m above sea level. H.E.S.S. consists of four telescopes, a square array of 120 m side length. The full array is taking data since December 2003. Each telescope has a diameter of 13 m and is composed of 382 round mirrors. At the focal distance of the dish, cameras consisting of 960 photomultiplier tubes record the Cherenkov light reflected by the mirrors. The field of view of the instrument has a diameter of  $5^\circ$  and an effective area larger than  $10^5 \text{ m}^2$  above a few hundred GeV. For the H.E.S.S. datasets used in this thesis [258, 273], gamma rays were measured between 300 GeV and 30 TeV and an energy resolution of 17% at 500 GeV and 11% at 11 TeV [258] is achieved. A point source sensitivity of 10 miliCrab is obtained with 25 hours of observation. In 2012, the H.E.S.S. array was upgraded with an additional telescope of 28 m diameter [274].

### 4.2.4 CTA

The Cherenkov Telescope Array is still in its design phase [270]. It is planned to consist of an array in the southern hemisphere and a smaller northern array. As the region of interest considered in this thesis is the Galactic center, the focus lies on the southern array in the following. The site of the experiment is still being negotiated, possible options are locations in Namibia and Chile for the southern array [275].

The CTA experiment will consist of an array of various telescopes of three different sizes: small ones with a diameter of 7.4 m, medium sized ones with  $d = 12.3 \text{ m}$  and large telescopes with  $d = 24 \text{ m}$  [270]. However, the exact configuration of the array, the number of the telescopes as well as the spacing of the telescopes is not yet fixed. The performance of the instrument depends on the size of the array, number of large and small telescopes and the altitude of the location and is investigated in detail for various candidate arrays in Ref. [270]. In this work we make use of the candidate array  $\mathbf{I}$  [270], consisting of 3 large 18 medium size and 56 small telescopes. The field of view differs for the three telescope types, amounting to  $4.9^\circ$  for the large,  $8^\circ$  and  $9^\circ$  for the medium size and small telescopes, respectively. The aim of this balanced array configuration is to obtain a good sensitivity over a large energy range. The candidate array  $\mathbf{I}$  will measure gamma rays in the energy range of 20 GeV to above 100 TeV with a resolution better than 20% above 100 GeV and an effective area that exceeds  $10^6 \text{ m}^2$  above a few TeV. The dependence of energy resolution and effective area on the estimated gamma-ray energy is shown in Fig. 4.9. As these quantities are given at the analysis level, no further efficiency factors for the gamma-ray or electron detection have to be taken into account ( $\epsilon_\gamma = \epsilon_e = 1$ ). In addition to the balanced array  $\mathbf{I}$ , we consider the larger array configuration presented on the CTA website [276]. This array consists of 4 large, 24 medium size and 72 small telescopes and achieves a better performance compared to the candidate array  $\mathbf{I}$ . Its effective area is better by up to a factor of  $\sim 8$  at low energies ( $\sim 1.5$  at high energies) and its energy resolution by a factor of about 1.5

## 4.2 Gamma-ray experiments

---

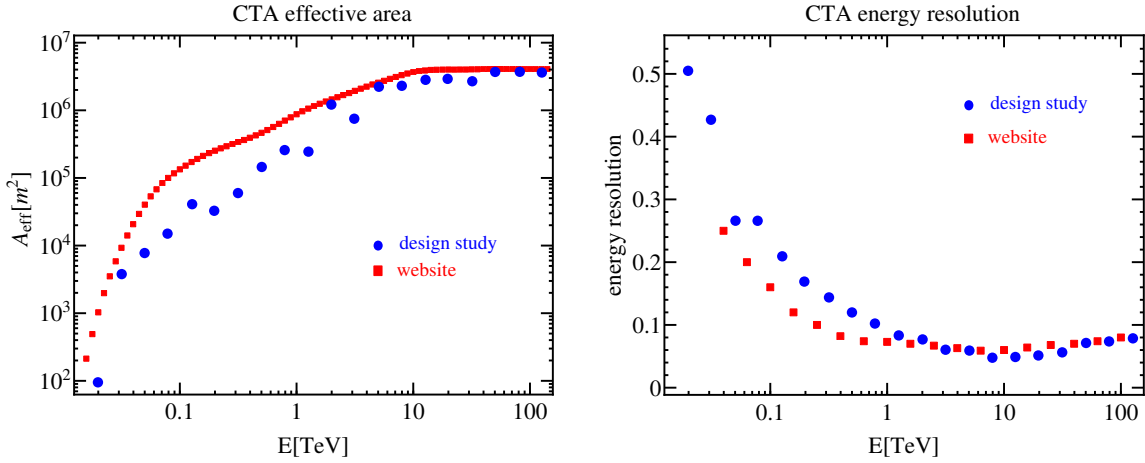


Figure 4.9: The left panel shows the effective area of the CTA array  $\mathcal{I}$  (blue dots) as presented in Ref. [270], the right panel its energy resolution (blue dots). The performance of the array presented on the CTA website [276] is overplotted (red squares).

below 1 TeV. Gamma rays and protons are distinguished by the shower shape as the distribution of Cherenkov light emitted in electromagnetic and hadronic showers differs. Typical proton acceptances lie in the range of  $\epsilon_p = 0.01 - 0.2$  for a 70% gamma-ray acceptance [277] for array  $\mathcal{I}$  and can improve by a factor of 10 for the candidate array presented on the CTA website. The CTA experiment is designed to supersede the sensitivity of existing Cherenkov telescopes by one order of magnitude [278]. For 50 hours of observation time a point source sensitivity of a few miliCrab at 1 TeV is expected [270].



# Chapter 5

## Limits from gamma rays

As shown in the previous chapter, HERD and CTA will surpass existing experiments with their instrument properties. HERD features an excellent energy resolution, which is crucial in the search for sharp spectral features. CTA on the other hand can detect gamma rays up to over 100 TeV with a very good energy resolution, which allows constraining very heavy dark matter candidates that cannot be probed in other search strategies. The LHC will only be able to detect WIMP signals for dark matter masses up to about 1.5 TeV in the 14 TeV run with  $300 \text{ fb}^{-1}$  of collected data [279, 280]. Future colliders with higher center-of-mass energies, for example the high-energy upgrade of the LHC with 33 TeV center-of-mass energy [281] or a post-LHC 100 TeV proton-proton collider [282], will be able to probe higher dark matter masses, but these machines, if they are realized, will not become operational in the next decades. Direct detection experiments are most sensitive for dark matter masses at tens of GeV and the constraints degrade quickly at TeV energies [283, 284]. Only in specific scenarios direct detection can probe very heavy WIMPs (see e.g. Ref. [163]).

In this chapter we derive gamma-ray constraints on annihilating and decaying dark matter that produce sharp spectral features, focusing on the HERD and CTA instruments. First, our approach for the calculation of prospects for these future experiments, as well as the methodology for the computation of constraints from H.E.S.S. observations is described. Afterwards, we apply these methods in order to constrain the three gamma-ray spectral features under consideration: gamma-ray boxes, internal bremsstrahlung and gamma-ray lines.

We already presented some of the material used in this chapter in Refs. [3–5].

### 5.1 Methodology

In this section, the methods employed for the calculation and forecast of dark matter constraints are presented. First, we focus on the H.E.S.S. experiment and review how to derive constraints for continuum gamma rays as well as spectral features. After that, we discuss the future experiments CTA and HERD and present our approach to compute projected limits on dark matter spectral features. While in the case of H.E.S.S. a phenomenological parameterization is used to describe the data in the whole energy range, for CTA and HERD the sliding energy window technique is used. This method relies on the assumption that the gamma-ray background is well fitted by a

simple power law in a certain limited energy range. As we show in the following, this depends on the curvature of the background and limits the size of the allowed sliding energy windows.

### 5.1.1 Current experiment: H.E.S.S.

In order to calculate limits from the H.E.S.S. measurements, we make use of the data presented in Refs. [258, 273]. Both datasets are derived from 112 h of Galactic center observations and were taken during the years 2004-2008. Concretely, the gamma-ray fluxes are given in the energy range of 300 GeV – 30 TeV for the central Galactic halo region (CGH), a circular target region of  $1^\circ$  radius, excluding the Galactic plane by requiring  $|b| > 0.3^\circ$  (see Fig. 5.1).

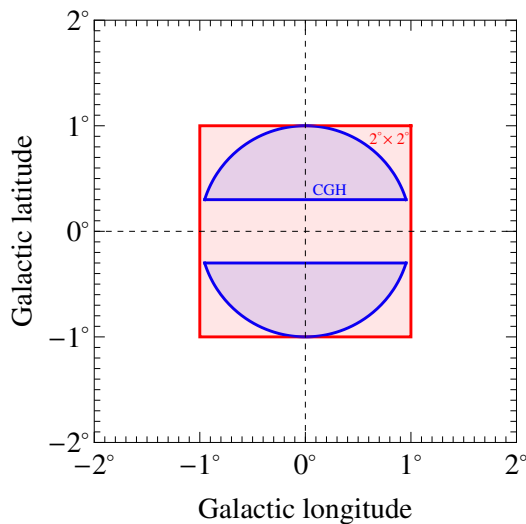


Figure 5.1: The central Galactic halo region is shown in blue. The surrounding red square denotes the  $2^\circ \times 2^\circ$  region of interest used in the forecast for CTA.

In the remainder of this section we describe the computation of the dark matter constraints, both for continuum gamma rays and spectral features, closely following Refs. [258, 273].

#### 5.1.1.1 Spectral features

In Ref. [258] the H.E.S.S. Collaboration presented their search for line-like dark matter signals. Concretely they present limits for gamma-ray lines and some benchmark scenarios containing internal bremsstrahlung. In this thesis the H.E.S.S. data is used to constrain a concrete particle physics scenario, namely the minimal dark matter model (see Sec. 5.3). For this we closely follow the approach of the collaboration to obtain limits on this model.

The constraints on the dark matter parameters can be computed with a  $\chi^2$  fit to the gamma-ray flux from the Galactic center shown in Fig. 5.2. We adopt the 7-parameter background model

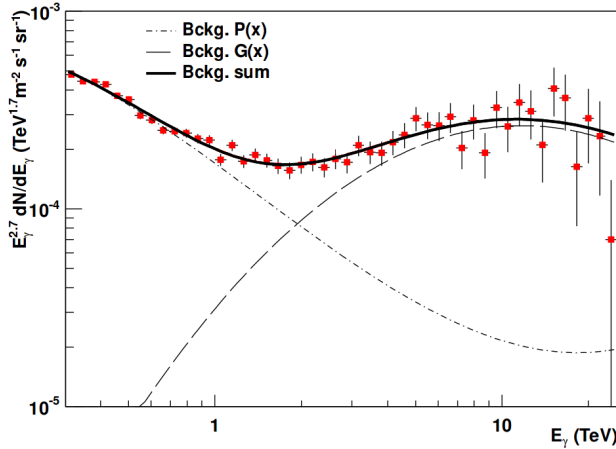


Figure 5.2: This figure shows the gamma-ray flux measured by the H.E.S.S. instrument in the central Galactic halo region, together with the best-fit background model. The two contributions to the background model are depicted separately. The figure is adopted from Ref. [258].

put forward by the collaboration that gives a very good fit to the data

$$\frac{d\Phi_\gamma}{dE_\gamma} = a_0 \left( \frac{E_\gamma}{1 \text{ TeV}} \right)^{-2.7} [P(x) + \beta G(x)] \quad (5.1)$$

with

$$P(x) = \exp(a_1 x + a_2 x^2 + a_3 x^3) \quad \text{and} \quad G(x) = \frac{1}{\sqrt{2\pi}\sigma_x} \exp\left(-\frac{(x - \mu_x)^2}{2\sigma_x^2}\right), \quad (5.2)$$

where  $x = \log_{10}(E_\gamma/\text{TeV})$  and  $a_0, a_1, a_2, a_3, \beta, \mu_x$  and  $\sigma_x$  are the 7 background parameters. In the fit, the  $\chi^2$  is minimized with respect to these parameters. In order to calculate the limit, we add to this background the sharp dark matter signal, folded with a Gaussian of width  $\sigma_E$  given by the resolution of the instrument. Starting from the best fit  $\chi^2$  of the background plus the dark matter signal, we increase the signal normalization until the  $\chi^2$  has increased by more than 2.71, which gives the one-sided 95% CL upper limit (see Appendix A). We adopt the resolution quoted in Ref. [258], i.e. 17% at 500 GeV and 11% at 10 TeV. In analogy to the analysis conducted by the collaboration we compute the limits for dark matter masses between 500 GeV and 20 TeV. The best fit background parameterization is shown together with the data in Fig. 5.2.

For the computation of the constraints we employ a cuspy as well as a cored profile. Concretely, we use the Einasto profile (Eq. (1.8)) and the isothermal profile (Eq. (1.6)). The corresponding  $J$ -factors for dark matter annihilations in the GCH region read  $4.43 \cdot 10^{21} \text{ GeV}^2 \text{ sr/cm}^5$  [273] for the Einasto and  $3.23 \cdot 10^{19} \text{ GeV}^2 \text{ sr/cm}^5$  for the isothermal profile assuming a local dark matter density of  $\rho_\odot = 0.39 \text{ GeV/cm}^3$ .

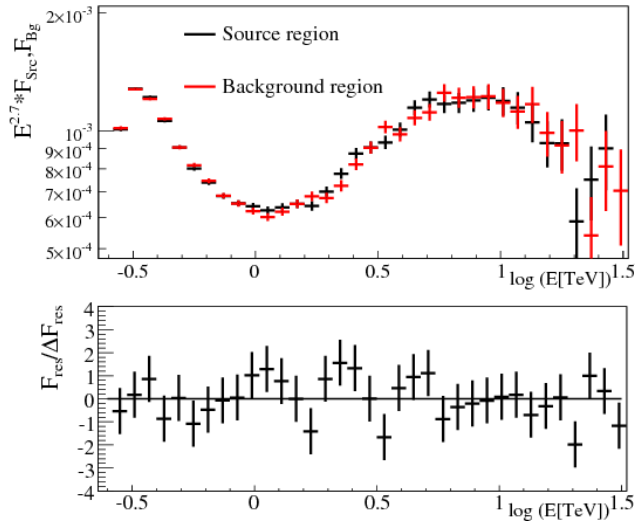


Figure 5.3: Top panel: differential gamma-ray flux measured by the H.E.S.S. experiment in the source and background regions in units of  $\text{TeV}^{1.7} \text{ m}^{-2} \text{ s}^{-1} \text{ sr}^{-1}$ . Bottom panel: Flux residua  $F_{\text{res}} / \Delta F_{\text{res}}$  where  $\Delta F_{\text{res}}$  denotes the statistical error on  $F_{\text{res}}$  that is given by  $F_{\text{res}} = F_{\text{src}} - F_{\text{bkg}}$ . The figure is taken from Ref. [273].

### 5.1.1.2 Continuum

The limits on the gamma-ray continuum produced in dark matter annihilations and decays is derived using the “on-off-region” technique [273]. Here the background is not modeled but subtracted. The gamma-ray flux  $F_{\text{src}}$  is measured in the search (“on”) region, which is again the central Galactic halo region. The background  $F_{\text{bkg}}$  on the other hand is measured in several background (“off”) regions that are located close to the search region [273]. The residual flux  $F_{\text{res}} = F_{\text{src}} - F_{\text{bkg}}$  is found to be compatible with zero. In order to derive the dark matter limits, we perform a  $\chi^2$  fit of the gamma-ray continuum spectrum to the residual flux. When the minimal  $\chi^2$  for a certain signal normalization has increased with respect to the best fit value by 2.71, the 95% CL upper limit is found (see Appendix A). The  $J$ -factor for the dark matter signal, however, is reduced with respect to the CGH, because parts of the signal are also subtracted from the search region together with the true background. For our limits, we employ the Einasto profile (Eq. (1.8)), in analogy to the H.E.S.S. Collaboration. The average  $J$ -factor for the source and background regions are given by  $\bar{J}_{\text{src}} = 7.42 \cdot 10^{24} \text{ GeV}^2/\text{cm}^5$  and  $\bar{J}_{\text{bkg}} = 3.62 \cdot 10^{24} \text{ GeV}^2/\text{cm}^5$  [273] where  $\rho_{\odot} = 0.39 \text{ GeV}/\text{cm}^3$  is assumed. This corresponds to a reduction of the potential dark matter signal, which is searched for in the residual flux, by 49% with respect to the flux expected in the signal region. Note that this search strategy is not applicable for cored profiles, since the dark matter signal would get completely subtracted. The fluxes measured in the source and background region as well as the residual flux are shown in Fig. 5.3.

### 5.1.2 Future experiments: CTA and HERD

This section is dedicated to the forecast of constraints on the dark matter parameters with the future experiments CTA and HERD. In this section we focus solely on gamma-ray spectral features. First, general aspects applicable to both experiments are discussed. Then the method is specified for the two instruments. In particular, the different backgrounds for Cherenkov telescopes and space based instruments as well as their implications on the details of the method are described. In order to compute the expected limits or the sensitivity for upcoming instruments, mock data must be generated. After that, using the mock data, the forecast is made with a profile likelihood analysis [157, 260, 261, 285, 286] using the sliding energy window technique [157, 260, 261, 286–288]. These two steps are presented in the following.

#### Mock data

The mock data, the simulated number of counts detected in the instruments, is calculated from the expected number of counts in the respective region of interest. For its calculation a detailed model of the gamma-ray background, but also of misidentified cosmic rays that constitute an experimental background is necessary. The expected number of counts  $n_{\text{exp}}^i$  in an energy bin  $i$  is given by

$$n_{\text{exp}}^i = \Delta t \int_{\Delta E_i} dE \int dE' R(E, E') A_{\text{eff}}(E') \frac{d\Phi_{\text{tot}}}{dE_\gamma}(E'), \quad (5.3)$$

where  $\Delta t$  denotes the observation time and  $\Delta E_i$  the width of the  $i$ -th energy bin.  $A_{\text{eff}}$  and  $R(E, E')$  are the effective area and the energy resolution, assumed as a Gaussian with standard deviation  $\sigma_E$ . These instrument properties are given for the experiments under consideration in Sec. 4.2. Finally,  $\frac{d\Phi_{\text{tot}}}{dE_\gamma}$  is the total gamma-ray and cosmic-ray background of the instrument. This is specified for CTA and HERD in the following sections.

The mock number of counts, i.e. the simulated “observed” number of counts  $n_{\text{obs}}^i$  are given by random numbers, drawn from a Poisson distribution with mean  $n_{\text{exp}}^i$ . In fact, a large number of such mock data sets is generated. If not otherwise stated, our results are obtained from 300 realizations of the data. The quoted constraints then refer to the logarithmic average of all the limits obtained from the mock data sets.

#### Sliding energy windows

Now, after having generated the mock data, a likelihood analysis is performed (see Appendix A). In the likelihood function the expected number of counts, derived from the model expectation, is required. The expected model flux is just given by the sum of the expected background and signal flux

$$\frac{d\Phi_{\text{model}}}{dE_\gamma} = \frac{d\Phi_{\text{bkg}}}{dE_\gamma} + a \frac{d\Phi_{\text{sig}}}{dE_\gamma}. \quad (5.4)$$

From this, the expected number of counts are obtained by substituting the total background flux in Eq. (5.3) with the model expectation  $\frac{d\Phi_{\text{model}}}{dE_\gamma}$ , where the signal flux is given by Eq. (4.1)

or Eq. (4.2), respectively. The limit on the signal normalization  $a$  is derived in the likelihood analysis, concretely, the upper limit is found for the signal normalizations for which the quantity  $-2 \log(\mathcal{L}(a))$  has increased by more than 2.71 with respect to the overall best fit. Here  $\mathcal{L}$  denotes the likelihood function (see Appendix A). Similarly, the sensitivity for a  $5\sigma$  detection (see Appendix A) is calculated. To this end, mock data that does not only include the background, but also a dark matter signal has to be generated. Concretely, for various signal normalizations, a large number of mock data must be produced. To this end the total background flux in Eq. (5.3) has to be replaced by  $\frac{d\Phi_{\text{tot}}}{dE_\gamma} + A \frac{d\Phi_{\text{sig}}}{dE_\gamma}$ . The signal normalization  $A$  for which, averaged over all the realizations,  $-2 \log(\mathcal{L}(A))$  with dark matter signal exceeds the background only fit by more than 23.7 gives the  $5\sigma$  detection sensitivity.

In our work the background is modeled by a simple power law and thus contains just two background model parameters, the normalization  $n$  and the index  $\gamma$  of the power law. However, the total astrophysical background typically does not follow a simple power law in the whole energy range. Our background model can be applied nevertheless, but only in a smaller energy window, i.e. a subset of the whole data, where indeed the mock data is well described by a power law. The gamma-ray flux from a sharp spectral feature, on the other hand, is only sizable within some small energy range, given by the resolution of the instrument. As a consequence the data inside the energy window suffices to constrain dark matter candidates that produce sharp spectral features.

The size of the sliding energy window with mean energy  $\bar{E}$  is parameterized by  $[\bar{E}/\sqrt{\epsilon}, \bar{E}\sqrt{\epsilon}]$ . The parameter  $\epsilon$  and thus the window size is determined from the requirement that the mock data can be well described by a power law within the window and thus depends on the curvature of the background. Ideally, the window should be a few times larger than the energy resolution. This criterion can, however, not always be met depending on the curvature of the background. A large background curvature leads to a small allowed window size, and for a relatively large energy resolution at these energies, the feature cannot be captured inside the window. This situation occurs in Sec. 5.2.

In our analysis, we adopt the following procedure for the selection of valid energy windows: First, we generate 300 mock data sets, assuming background only given by  $\frac{d\Phi_{\text{tot}}}{dE_\gamma}$ . To each data set we fit a pure power law with the two background model parameters, using energy windows of constant width in the range of  $\epsilon = 1.2 - 10$ , which are centered across the full energy range under consideration. For each window and central energy, we thus obtain 300  $\chi^2$  values for the best fit power laws. These 300  $\chi^2$  values should follow a  $\chi^2$  distribution with the appropriate degrees of freedom, namely the number of bins minus two fitted parameters. Thus we perform a test whether our distribution of the 300  $\chi^2$  values is plausibly drawn from a  $\chi^2$  distribution. When the resulting p-value of this distribution test is smaller than 0.01, the window and thus the corresponding value of  $\epsilon$  is rejected. All functions  $\epsilon(\bar{E})$  that lie within the surviving  $\epsilon - \bar{E}$  parameter space constitute valid energy window parameterizations.

### 5.1.2.1 CTA

An important difference between space based and ground based gamma-ray telescopes is their observation strategy. Since Cherenkov telescopes cannot survey the sky with reasonable statistics, we assume a fixed pointing direction for the purpose of this forecast, and thus focus on observations of the Galactic center. This is done for two reasons. First, the largest dark matter signal is expected from the Galactic center, and second, it is expected that a relatively long observation time is dedicated to this in itself interesting target from an astrophysical point of view. Our target thus must be contained in the field of view of the instrument, i.e.  $4.9^\circ$  for the large telescopes. Concretely, we consider two target regions, a  $2^\circ \times 2^\circ$  rectangular region around the center of the Galaxy (i.e.  $|\ell| < 1^\circ$  and  $|b| < 1^\circ$ ) and, for the purpose of comparison with the limits from the H.E.S.S. instrument, the CGH region (a circular target region of  $1^\circ$  radius, excluding the Galactic plane by requiring  $|b| > 0.3^\circ$ ) [258, 273]. Both target regions are depicted in Fig. 5.1. Note, however, that it is possible to optimize the target region with respect to the signal-to-noise ratio [261] or to implement a full morphological analysis [257]. We leave this optimization to further studies that should be undertaken when the final layout of the instrument and its properties are known.

As we are interested in constraining heavy dark matter candidates with CTA, we present the background model in our energy range of interest  $E_\gamma \simeq 40\text{ GeV} - 110\text{ TeV}$ . For the observation time, we adopt  $\Delta t = 100\text{ h}$  for the  $2^\circ \times 2^\circ$  region, whereas we assume for the CGH the observation time of the H.E.S.S. instrument  $\Delta t = 112\text{ h}$  for the sake of comparison.

Indirect dark matter searches with Cherenkov telescopes are typically affected by three types of backgrounds: misidentified cosmic rays, electrons and gamma rays from astrophysical sources. In the following, we present the parameterizations used for the different background contributions.

- **Cosmic-rays nuclei**

In principle, the air showers from hadronic cosmic rays can be distinguished from gamma-ray initiated showers by means of the shower shape and other observables. Typically the hadron acceptances lie in the range of 1% – 20% for a 70% gamma-ray acceptance [289]. However, due to the large fluxes of cosmic rays, they still constitute a sizable background for Cherenkov telescopes. In this work we include only the proton background, since protons are the most abundant cosmic-ray species, while neglecting heavier nuclei. A good fit to a large set of proton data taken before 2002 [290] is given by

$$\frac{d^2\Phi_p}{dE_p d\Omega} = 8.73 \times 10^{-6} \left( \frac{E_p}{\text{TeV}} \right)^{-2.71} \text{TeV}^{-1} \text{cm}^{-2} \text{s}^{-1} \text{sr}^{-1} \quad (5.5)$$

from around 10 GeV up to PeV energies. We checked that including the latest proton [291] data does not significantly affect the best fit power law. Therefore, we employ the above parameterization throughout.

When a hadronic air shower, initiated by a proton, is misclassified as an electromagnetic shower, the reconstructed energy is typically a factor of 2 – 3 smaller than the true

proton energy. The reason for this is the different Cherenkov light yield in hadronic and electromagnetic showers. Concretely, the Cherenkov yield of a photon shower with a primary energy of  $E_0 \gtrsim 100$  GeV is a factor  $\rho \simeq 2 - 3$  larger than that of a proton shower of the same energy, while both yields are proportional to the primary energy [292]. Therefore, a proton-initiated shower with energy  $E_p$  exhibits the same light yield as a shower triggered by a photon of a smaller primary energy  $E_\gamma \simeq E_p/\rho$ . In fact, it is expected that this factor is energy dependent, but, in the absence of detailed information on that subject, we adopt a constant correction factor  $\rho = 3$  throughout. The proton acceptances used in our analysis are inferred from the background counts simulated for CTA as explained below.

- **Electrons**

Air showers that are triggered by electrons and positron are indistinguishable from photon induced ones (even though the shower maximum occurs on average slightly later for photons [121]). Thus they also constitute an important background.

The  $e^- + e^+$  spectrum has been precisely measured, namely below several hundred GeV by the AMS-02 [120] experiment and at TeV energies by the H.E.S.S. [121] telescope. The AMS-02 data is well fit by a power law

$$\frac{d^2\Phi_e^{le}}{dE_e d\Omega} = 9.93 \times 10^{-9} \left( \frac{E_e}{\text{TeV}} \right)^{-3.17} \text{TeV}^{-1} \text{cm}^{-2} \text{s}^{-1} \text{sr}^{-1} \quad (5.6)$$

for energies above 30.2 GeV, and the H.E.S.S. data can be parameterized by

$$\frac{d^2\Phi_e^{he}}{dE_e d\Omega} = 1.17 \times 10^{-8} \left( \frac{E_e}{\text{TeV}} \right)^{-3.9} \text{TeV}^{-1} \text{cm}^{-2} \text{s}^{-1} \text{sr}^{-1}. \quad (5.7)$$

We ensure a smooth transition between the two regimes by a generalized mean of index  $-2$ . The total all-electron flux is then given by

$$\frac{d^2\Phi_e}{dE_e d\Omega} = \left[ \left( \frac{d^2\Phi_e^{le}}{dE_e d\Omega} \right)^{-2} + \left( \frac{d^2\Phi_e^{he}}{dE_e d\Omega} \right)^{-2} \right]^{-\frac{1}{2}}. \quad (5.8)$$

As the instrument properties of CTA (see Sec. 4.2.4) are given at the analysis level, no further electron acceptance ( $\epsilon_e = 1$ ) is included in the background model.

- **Gamma rays**

Eventually the sensitivity of Cherenkov telescopes to dark matter signals is restricted by astrophysical gamma-ray backgrounds. In our region of interest, one can distinguish two types of gamma-ray backgrounds, a very high-energy point source in the Galactic center [293] as well as the diffuse gamma-ray background [294].

The gamma-ray point source HESSJ1745-290 in the Galactic center region has been discovered simultaneously by the Whipple, Cangaroo-II and H.E.S.S. telescopes [174]. Within the resolution of the instruments, its location coincides with the position of Sagittarius

## 5.1 Methodology

---

A\*. Apart from the black hole, a supernova remnant as well as a pulsar wind nebula in the vicinity of the Galactic center or a cumulative effect from many sources, for instance from a large population of millisecond pulsars have been considered as the origin of this gamma-ray emission [174]. At lower energies the energy spectrum is measured by the Fermi-LAT which is, in the energy range  $5 - 100$  GeV, well described by [295]

$$\frac{d\Phi_{\gamma,gc}^{le}}{dE_\gamma} = 1.11 \times 10^{-12} \left( \frac{E_\gamma}{\text{TeV}} \right)^{-2.68} \text{TeV}^{-1} \text{cm}^{-2} \text{s}^{-1}. \quad (5.9)$$

The H.E.S.S. data in the energy range  $160$  GeV –  $30$  TeV can be parameterized by [293]

$$\frac{d\Phi_{\gamma,gc}^{he}}{dE_\gamma} = 2.34 \times 10^{-12} \left( \frac{E_\gamma}{\text{TeV}} \right)^{-2.25} \text{TeV}^{-1} \text{cm}^{-2} \text{s}^{-1}. \quad (5.10)$$

Again, we make use of the generalized mean, this time with an index of 5 in order to ensure a smooth transition between the two energy regimes

$$\frac{d\Phi_{\gamma,gc}}{dE_\gamma} = \left[ \left( \frac{d\Phi_{\gamma,gc}^{le}}{dE_\gamma} \right)^5 + \left( \frac{d\Phi_{\gamma,gc}^{he}}{dE_\gamma} \right)^5 \right]^{\frac{1}{5}}. \quad (5.11)$$

The diffuse gamma-ray emission from the Galactic center ridge has been detected by the H.E.S.S. instrument in the region given by  $-0.8^\circ < l < 0.8^\circ$  and  $|b| < 0.3^\circ$ . The emission is spatially correlated with the dense central molecular cloud, indicating that the origin of this emission are cosmic-ray interactions [294]. The Galactic ridge emission in the region  $|\ell| < 0.8^\circ$  and  $|b| < 0.3^\circ$  measured by H.E.S.S. [294] is well fitted by the power law

$$\frac{d^2\Phi_{\gamma,gr}}{dE_\gamma d\Omega} = 1.73 \times 10^{-8} \left( \frac{E_\gamma}{\text{TeV}} \right)^{-2.29} \text{TeV}^{-1} \text{cm}^{-2} \text{s}^{-1} \text{sr}^{-1}. \quad (5.12)$$

As for electrons, no additional gamma-ray efficiency is included in the calculation of the background counts, i.e.  $\epsilon_\gamma = 1$ .

The total background is then given by the sum all the contributions described above

$$\begin{aligned} \frac{d\Phi_{bkg}}{dE_\gamma}(E_\gamma) &= \Delta\Omega \left( \epsilon_p(E_\gamma) \rho \frac{d^2\Phi_p}{dE_p d\Omega} (\rho E_\gamma) + \epsilon_e \frac{d^2\Phi_e}{dE_e d\Omega}(E_\gamma) + \epsilon_\gamma \frac{d^2\Phi_{\gamma,gr}}{dE_\gamma d\Omega}(E_\gamma) \right) \\ &+ \epsilon_\gamma \frac{d\Phi_{\gamma,gc}}{dE_\gamma}(E_\gamma), \end{aligned} \quad (5.13)$$

where  $\Delta\Omega$  is the solid angle of the respective region of interest,  $\Delta\Omega_{2\times2} = 1.22 \times 10^{-3}$  sr for the  $2^\circ \times 2^\circ$  region  $\Delta\Omega_{HESS} = 0.60 \times 10^{-3}$  sr for the CGH region. Note that for the latter case the last term in Eq. (5.13) is not included. In order to be conservative, we upscale the diffuse gamma-ray flux measured in the Galactic ridge ( $|\ell| < 0.8^\circ$  and  $|b| < 0.3^\circ$ ) in our region of interest assuming the same flux per unit solid angle in the whole target region. The electron and gamma-ray background contributions have not been measured up to 110 TeV, which is the highest energy

under consideration in this work. Thus we simply extrapolate the parameterizations of our background components above the energy range where they are measured.

The proton acceptance is deduced from the cosmic-ray background rates presented in Ref. [270] (see Fig. 16 therein) and in Ref. [276] for the updated performance. With an energy dependent proton acceptance of  $\epsilon_p(E_\gamma) = 0.01 + 0.02(E_\gamma/20\text{ TeV})^{1.4}$  i.e. a proton acceptance of 1% below  $\sim 1\text{ TeV}$  that increases to about 20% at 100 TeV, the reported background rate can be reproduced within a factor 1.5 – 3. For the updated performance [276] the same procedure leads to  $\epsilon_p(E_\gamma) = 0.001 + 0.002(E_\gamma/20\text{ TeV})^{1.4}$ . This behavior of the proton background is roughly in agreement with Ref. [296], where a full CTA simulation is used to compute the cosmic-ray background rate. The background rates presented by the CTA Collaboration together with our calculations are shown in Fig. 5.4.

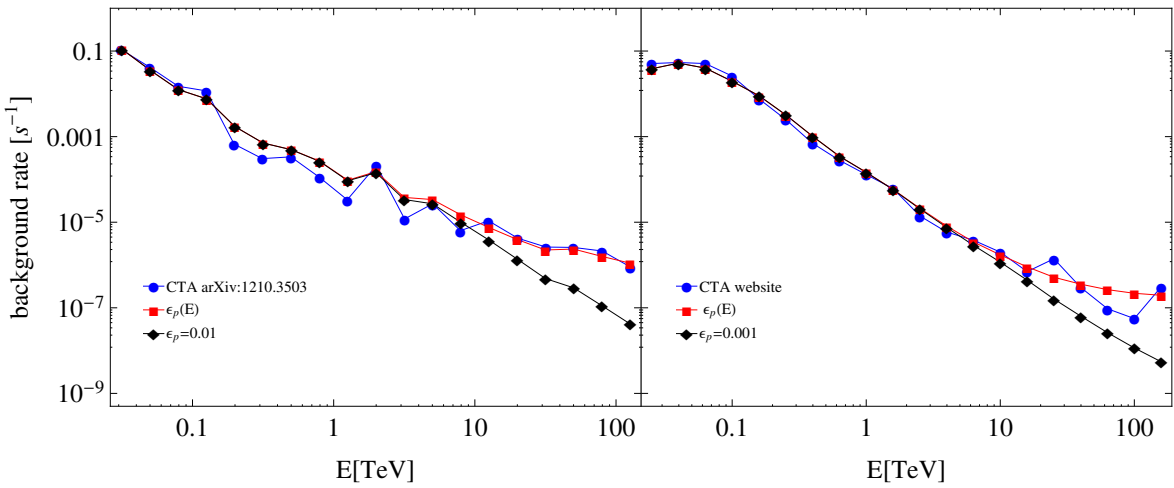


Figure 5.4: Cosmic-ray background rate given by the CTA Collaboration (blue) together with our calculation for a constant proton rejection (black) and the energy dependent proton rejection (red).

The different contributions to the total background in Eq. (5.13) are shown in Fig. 5.5. It is evident from the plot that cosmic-ray electrons and positrons constitute the dominant background below a few hundred GeV, while at TeV energies and above the gamma-ray emission from the Galactic ridge becomes relevant. Eventually, protons supersede all other contributions due to the worsening of the proton rejection at high energies. The gamma-ray flux from the Galactic center point source is always subdominant.

300 mock data sets are then generated using this background. Following the procedure described above the valid energy windows are determined. The largest valid window size corresponds to  $\epsilon_2 = 2$ , but we also consider small windows of  $\epsilon_{1.5} = 1.5$  and  $\epsilon_{1.2} = 1.2$  in order to quantify the dependence of the results on the energy window size. In Fig. 5.6 the excluded window sizes are marked with gray dots. Overplotted are the three valid windows under consideration.

## 5.1 Methodology

---

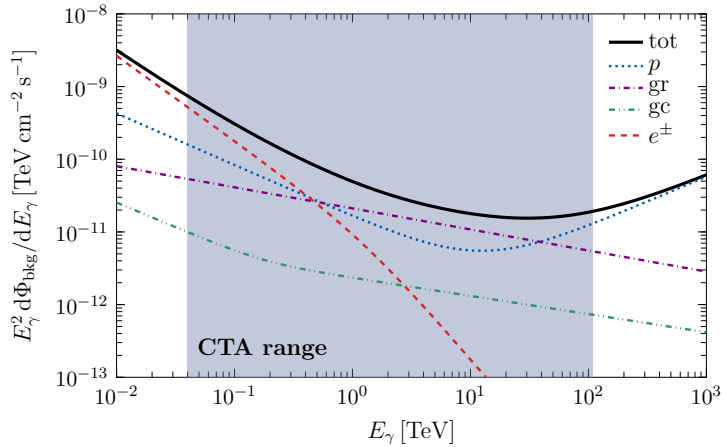


Figure 5.5: The background for CTA gamma-ray searches in the  $2^\circ \times 2^\circ$  target region around the Galactic center. The different contributions to the total background in Eq. (5.13), coming from protons, electrons and positrons, as well as gamma rays from the Galactic center source and the Galactic ridge are shown together with their sum, i.e. the total background for the CTA instrument. This plot has been presented in Ref. [3].

As evident from Eq. (4.1) and Fig. 1.5, the choice of the dark matter profile has a large impact in our regions of interest since  $1^\circ$  corresponds to  $\sim 150$  pc at the Galactic center. Thus we consider various profiles in our analysis, cuspy profiles as well as cored ones to bracket the uncertainty due to the dark matter distribution. Table 5.1 shows the  $J$ -factors for the adopted halo profiles in the  $2^\circ \times 2^\circ$  and the CGH region of interest.

ROI	GCH			$2^\circ \times 2^\circ$		
Profile	Einasto	isothermal	Einasto	NFW	cored	cuspy
$J$ -factor [ $10^{20} \text{ GeV}^2 \text{ sr cm}^{-5}$ ]	44.3	0.323	102	63.4	1.60	363

Table 5.1:  $J$ -factors for dark matter annihilations for the target regions adopted for the CTA prospects.

### 5.1.2.2 HERD

The space based HERD instrument can survey the whole sky with about uniform exposure. The observation strategy of this instrument therefore does not, in contrast to Cherenkov telescopes, restrict the target regions for dark matter searches. For the purpose of this forecast and also for the sake of comparison, we adopt the target regions put forward by the Fermi Collaboration [259, 262]. In fact, the regions of interest (ROI) differ for the various halo profiles, because the regions are optimized with respect to the signal-to-noise  $S/N_{\text{ROI}}$  ratio, which depends on the dark matter

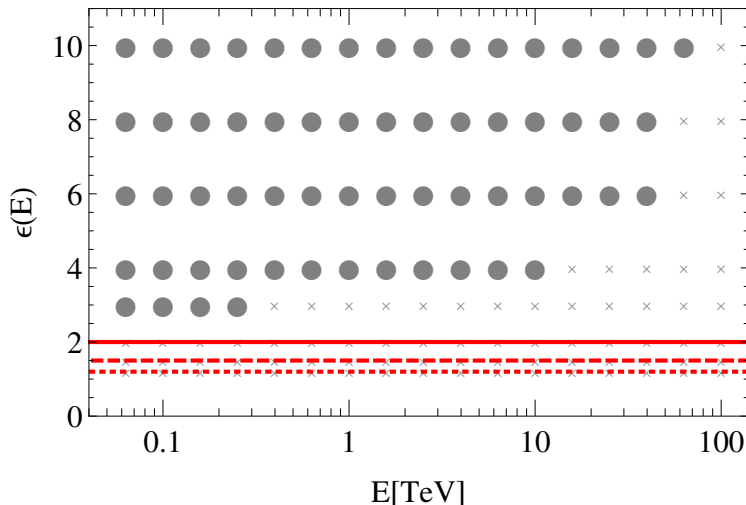


Figure 5.6: The red lines show the window sizes adopted in this work,  $\epsilon_2 = 2$  (solid),  $\epsilon_{1.5} = 1.5$  (dashed) and  $\epsilon_{1.2} = 1.2$  (dotted). The circles indicate the window sizes that are excluded for  $2^\circ \times 2^\circ$  target region by the criterion described in the text, whereas the gray crosses indicate all the window sizes for which the test described in the text has been performed.

density distribution. In the following, we briefly discuss the method for the optimization pursued by the Fermi Collaboration [259, 262].

The signal-to-noise ratio is given by

$$\frac{S}{N_{\text{ROI}}} = \frac{\int^{\text{ROI}} \int^{\text{FOV}} S(\hat{p}) \mathcal{E}(\hat{p}) d\Omega_{\hat{v}} d\Omega}{\sqrt{\int^{\text{ROI}} \int^{\text{FOV}} B(\hat{p}) \mathcal{E}(\hat{p}) d\Omega_{\hat{v}} d\Omega}}, \quad (5.14)$$

where  $\mathcal{E}$  is the exposure of the instrument,  $S$  and  $B$  are the gamma-ray intensities of the dark matter signal and the gamma-ray background in the direction  $\hat{p}$ ,  $d\Omega$  refers to the region of interest while  $d\Omega_{\hat{p}}$  refers to the field of view and  $\hat{v}$  stands for the gamma-ray direction in the LAT reference frame. The region for which this quantity is maximized is adopted as target region for a given dark matter profile. Concretely, the region is assumed as a circular region around the Galactic center with radius  $R$ , where the Galactic plane is masked out by requiring  $|b| > 5^\circ$  and  $|l| > \Delta l$ . In the optimization for the different profiles,  $\Delta l$  is found to be close to  $6^\circ$  in all cases. Therefore  $\Delta l = 6^\circ$  is adopted throughout. The radius of the region, however, depends on the dark matter profile in the case of annihilations. The signal-to-noise ratio is maximized for  $R = 16^\circ$  for the Einasto profile, for  $R = 41^\circ$  for the NFW profile and  $R = 90^\circ$  for the isothermal profile. This means that the larger the density in the Galactic center, the smaller is the optimal search region. In the case of decays, on the other hand, the same target region with  $R = 180^\circ$  is found to be close to optimal for all profiles. This region corresponds to the whole sky, with the Galactic plane masked out. Note that this procedure has originally been applied on a pixel by

## 5.1 Methodology

---

pixel basis, leading to hour-glass shaped optimal target regions [260].

The resulting regions of interest, R16, R41, R90 and R180 are shown in Fig. 5.7 and the corresponding  $J$ -factors for the Einasto, NFW and isothermal profiles presented in Sec. 1.2 are given in Table 5.2. However, once the HERD facility is operational, the optimization should

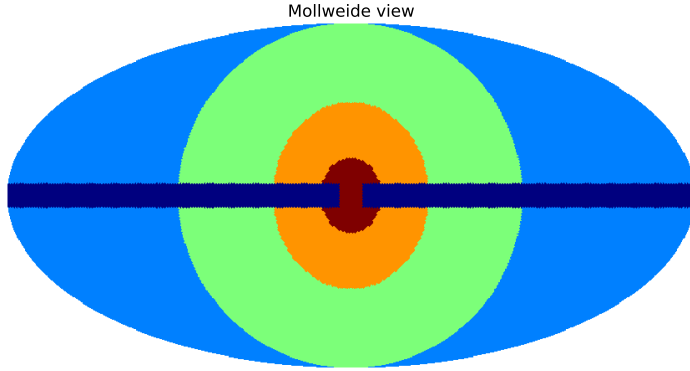


Figure 5.7: The different target regions considered in this work (from inside to outside), R16 (red), R41 (orange), R90 (green) and R180 (light blue). The part of the Galactic plane ( $|b| < 5^\circ$  and  $|\ell| > 6^\circ$ ) that is always masked out is colored in dark blue. This figure is also presented in Ref. [5].

Profile	annihilations			decays	
	ROI	$J$ -factor		ROI	$J$ -factor
			$[10^{22} \text{ GeV}^2 \text{ sr cm}^{-5}]$		$[10^{23} \text{ GeV} \text{ sr cm}^{-2}]$
Einasto	R16	9.39		R180	2.55
NFW	R41	9.17		R180	2.52
isothermal	R90	6.95		R180	2.56

Table 5.2:  $J$ -factors for the Einasto, NFW and isothermal profile for annihilations and decays in the optimized target regions.

be repeated considering that the backgrounds vary due to different instrument properties from experiment to experiment.

We proceed by discussing the background for the HERD instrument. In contrast to the previous section, the whole sky must be considered. For the isotropic cosmic-ray fluxes, the treatment is the same as described for CTA taking into account the different efficiencies. However the gamma-ray backgrounds vary for different regions in the sky. Again, we discuss the different contributions one by one, in the energy range of interest from 5 GeV to 2 TeV.

- **Cosmic-ray nuclei**

In analogy to the Cherenkov telescopes, misidentified cosmic rays contribute to total background of dark matter searches. For the cosmic-ray background, we adopt a parameterization for the proton spectrum that fits the AMS-02 measurements well [297], again neglecting heavier nuclei

$$\frac{d^2\Phi_p}{dE_p d\Omega} = 7.8 \cdot 10^{-2} \left( \frac{E_p}{\text{GeV}} \right)^{-0.9} \left[ 1.0 + \left( \frac{E_p}{4.9 \text{ GeV}} \right)^{1.87} \right]^{-1} \text{GeV}^{-1} \text{cm}^{-2} \text{s}^{-1} \text{sr}^{-1}. \quad (5.15)$$

However, due to the excellent proton rejection ( $\epsilon_p = 10^{-8}$ ) of the HERD instrument, the proton background turns out to be negligible in our analysis.

- **Electrons**

Electrons and positrons can also be misidentified as gamma rays in the HERD detector. For total cosmic-ray  $e^- + e^+$  flux we employ a parameterization that is obtained from the fit to AMS-02 [120] and H.E.S.S. [121] data. In the energy range of our interest, from 5 GeV to 2 TeV the spectrum is well described by

$$\begin{aligned} \frac{d^2\Phi_e}{dE_e d\Omega} &= 1.85 \cdot 10^{-3} \left( \frac{E_e}{\text{GeV}} \right)^{-0.71} \left[ 1.0 + \left( \frac{E_e}{3.5 \text{ GeV}} \right)^{2.63 - 0.05 \log_{10}(E_e/\text{GeV})} \right]^{-1} \\ &\times \left[ 1 + \left( \frac{E_e}{1300 \text{ GeV}} \right)^5 \right]^{-0.3} \text{GeV}^{-1} \text{cm}^{-2} \text{s}^{-1} \text{sr}^{-1}. \end{aligned} \quad (5.16)$$

Since the background is needed down to 5 GeV for the mock data generation for HERD, this parameterization differs from the one adopted for CTA. Note that the electron background does not follow a single power law over the whole energy range.

Despite the good electron efficiency of  $\epsilon_e = 10^{-3}$ , electrons constitute an important background in regions that exhibit a low astrophysical gamma-ray flux, for instance at high latitudes. Thus the electron background is mainly relevant for larger regions of interest. Since the electron background is softer in comparison to the gamma-ray background, it is only important at energies below 100 GeV, as it is the case for CTA shown above.

- **Gamma rays**

In the case of HERD, gamma rays are the dominant contribution to the background over the whole energy range. As discussed in Sec. 4.1.1, different contributions are taken into account, namely the three Galactic diffuse components, the isotropic gamma-ray background and point or extended gamma-ray sources. Because the bright sources can be effectively subtracted in the data analysis, and the residual weak sources are expected to contribute less than 10% to the diffuse gamma-rays [262], we do not take them into account in our analysis. For the modeling of the diffuse components we make use of the templates provided by the Fermi Collaboration, which are derived from data taken by the Fermi-LAT telescope. In order to take into account the Fermi bubbles and for the

purpose of quantifying their impact on our results we employ two different templates, one template with and one without the Fermi bubbles. For the Galactic diffuse gamma-ray background, a simple analytic parameterization cannot be given for all regions of interest. In fact, the Fermi Collaboration provides templates containing the fluxes of the three diffuse components for each pixel. These fluxes are obtained from the fit of spatial templates to the Fermi sky map. Actually, the fit is performed independently in each energy bin in the range 20 MeV – 300 GeV. In this way the spectrum for each component is determined without making any assumption on the spectral shape. Concretely, we make use of the p6v11 templates<sup>1</sup>, where the Fermi bubbles are not yet included as well as the p7v6 templates<sup>2</sup>, where a template for the Fermi bubbles is added in the fit. The total Galactic diffuse gamma-ray flux is given by the sum over all pixels  $i$  in the region of interest

$$\frac{d^2\Phi_{\gamma,\text{diff}}}{dE_\gamma d\Omega} = \frac{1}{N} \sum_{i \in \Delta\Omega} \left( \frac{d^2\Phi_{\gamma,\pi^0}^i}{dE_\gamma d\Omega} + \frac{d^2\Phi_{\gamma,\text{brems}}^i}{dE_\gamma d\Omega} + \frac{d^2\Phi_{\gamma,\text{IC}}^i}{dE_\gamma d\Omega} + \frac{d^2\Phi_{\gamma,\text{bubble}}^i}{dE_\gamma d\Omega} \right), \quad (5.17)$$

where the last term is only present in the case of p7v6 template and  $N$  denotes the total number of pixels. In the energy range above 300 GeV, we simply extrapolate the total diffuse gamma-ray background.

Lastly, we consider the isotropic gamma-ray background. Here we employ the fitting formula provided by the Fermi Collaboration [298]

$$\frac{d^2\Phi_{\gamma,\text{iso}}}{dE_\gamma d\Omega} = I_{0.1} \left( \frac{E}{0.1 \text{GeV}} \right)^{-\gamma} \exp \left( -\frac{E}{E_{\text{cut}}} \right). \quad (5.18)$$

The concrete values of the fit parameters depend on the foreground model assumptions [298]. For our analysis, we use  $I_{0.1} = 0.95 \times 10^{-4} \text{ GeV}^{-1} \text{cm}^{-2} \text{s}^{-1} \text{sr}^{-1}$ ,  $\gamma = 2.32$  and  $E_{\text{cut}} = 279 \text{ GeV}$ , which corresponds to model A in Ref. [298]. However, the isotropic background constitutes only a subdominant contribution to the total background for HERD as shown in Fig. 5.8. Therefore, choosing a different parameterization does not affect our dark matter search. In our analysis we take into account HERD’s gamma-ray efficiency of  $\epsilon_\gamma = 0.57$ .

The total background is then just given by the sum of all the contributions

$$\frac{d\Phi_{\text{bkg}}}{dE_\gamma}(E_\gamma) = \Delta\Omega \left( \epsilon_p \frac{d^2\Phi_p}{dE_p d\Omega} + \epsilon_e \frac{d^2\Phi_e}{dE_e d\Omega} + \epsilon_\gamma \frac{d^2\Phi_{\gamma,\text{diff}}}{dE_\gamma d\Omega} + \epsilon_\gamma \frac{d^2\Phi_{\gamma,\text{iso}}}{dE_\gamma d\Omega} \right). \quad (5.19)$$

In Fig. 5.8 the cosmic-ray contributions to the total background are plotted, together with the gamma-ray contributions at different latitudes as well as the isotropic gamma-ray background. The two panels correspond to the two templates adopted in this work, with and without the Fermi bubbles. This background is then used for the generation of 300 mock data sets. We consider 5 years of data collection with the instrument in full-sky survey mode, corresponding to

<sup>1</sup>[http://fermi.gsfc.nasa.gov/ssc/data/analysis/software/aux/gll\\_iem\\_v02\\_P6\\_V11\\_DIFFUSE.fit](http://fermi.gsfc.nasa.gov/ssc/data/analysis/software/aux/gll_iem_v02_P6_V11_DIFFUSE.fit)

<sup>2</sup>[http://fermi.gsfc.nasa.gov/ssc/data/analysis/software/aux/gll\\_iem\\_v05\\_rev1.fit](http://fermi.gsfc.nasa.gov/ssc/data/analysis/software/aux/gll_iem_v05_rev1.fit)

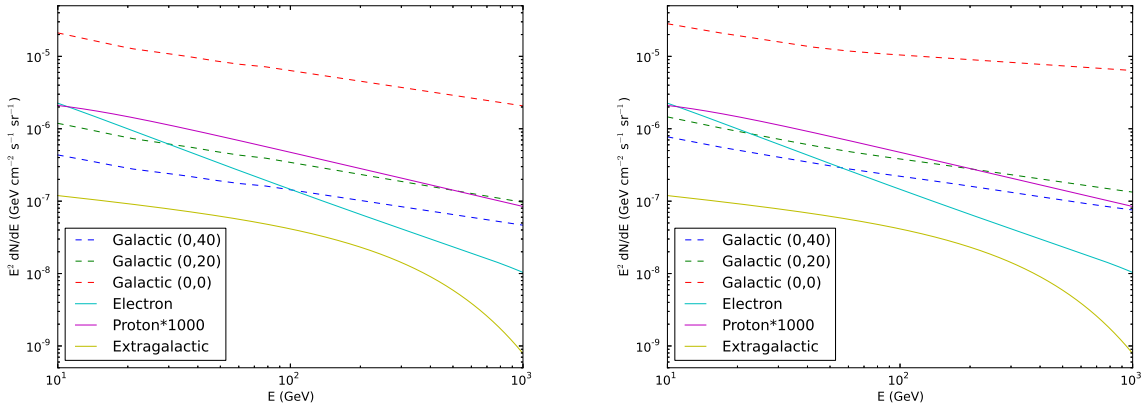


Figure 5.8: The left panel shows the contributions to the gamma-ray and cosmic-ray background for p6v11, the right panel for p7v6. The different lines denote (from top to bottom at 1 TeV) the Galactic diffuse gamma-ray flux at  $(\ell, b) = (0^\circ, 0^\circ)$ , at  $(\ell, b) = (0^\circ, 20^\circ)$ , the proton flux upscaled by a factor of 1000, the Galactic diffuse gamma-ray flux at  $(\ell, b) = (0^\circ, 40^\circ)$ , the electron flux and lastly the isotropic gamma-ray background (IGRB). These plots are also presented in Ref. [5].

an exposure time of  $1.07 \cdot 10^8$  s of our regions of interest. Again, we select our energy window following the procedure described in Sec. 5.1.2. The adopted energy window can be parameterized by

$$\epsilon(\bar{E}) = 3.97 \left( \frac{\bar{E}}{\text{TeV}} \right)^{0.23} . \quad (5.20)$$

This  $\epsilon(\bar{E})$  is allowed for all considered regions, and corresponds at low energies to the largest allowed window size for the large regions, where the electron background becomes important and which leads to a larger background curvature and thus to smaller allowed energy windows. The adopted window size is shown in Fig. 5.9 together with the excluded windows. At high energies energy windows with larger epsilons than the chosen window size are possible. We checked, however, that adopting larger windows at these energies leaves our limits unchanged, concretely for  $\epsilon'(\bar{E}) = 2\epsilon(\bar{E})$  the limits are not affected above 50 GeV for all profiles. This behavior is expected since the selected windows capture the line feature for all dark matter masses due to the excellent energy resolution of the HERD instrument.

Within these windows a profile likelihood analysis is then performed in order to determine the 95% CL upper limit on the dark matter parameters. Concretely, the limits are obtained for 300 mock data sets with 400 energy bins per decade in order to resolve the line feature.

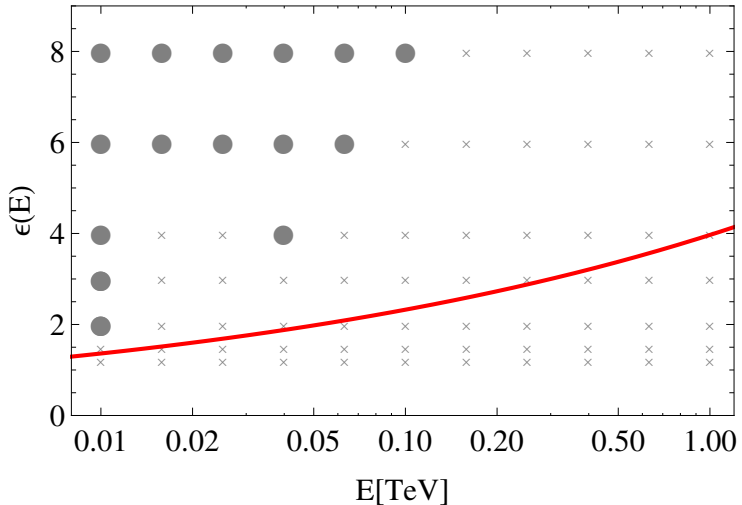


Figure 5.9: The red line shows the window size adopted in this work. The circles indicate the window sizes that are excluded for the R90 region by the criterion described in the text, whereas the gray crosses indicate all the window sizes for which the test described in the text has been performed.

## 5.2 Gamma-ray boxes

This section is dedicated to the search for gamma-ray box signatures with CTA that arise from heavy dark matter particles in the TeV energy range [3]. First, the rich phenomenology of gamma-ray boxes is discussed, followed by the presentation of the model-independent results. Afterwards, two models are introduced and the constraints for benchmark points in the parameter space of these models are shown. In this section we focus on dark matter annihilations only.

### 5.2.1 Model-independent considerations

Gamma-ray boxes have only recently been put forward as possible gamma-ray spectral features from dark matter annihilations or decays [299, 300]. Arising in cascade processes where dark matter annihilates into intermediate scalars  $\phi$ , the shape of the spectrum can be determined from kinematic considerations. A rich phenomenology emerges, since the resulting box can be very narrow and thus mimic a gamma-ray line at  $m_{\text{DM}}/2$  or, on the other hand, wide boxes can emerge that extend up to  $m_{\text{DM}}$  and which exhibit shoulders that could be searched for in the smooth astrophysical background.

In the lab frame, where the dark matter particles are non relativistic, the  $\phi$  particles have a monochromatic energy  $E_\phi = m_{\text{DM}}/2$ . In the rest frame of the scalars  $\phi$ , the gammas have in

turn an energy of  $E'_\gamma = m_\phi/2$ . In the lab frame, the gamma-ray energy reads [299]

$$E_\gamma = \frac{m_\phi^2}{2m_{\text{DM}}} \left( 1 - \cos \theta \sqrt{1 - \frac{m_\phi^2}{m_{\text{DM}}^2}} \right)^{-1}, \quad (5.21)$$

where  $\theta$  denotes the angle between the outgoing gamma-ray and the direction of motion of the parent scalar  $\phi$ .

The gamma-ray spectrum at production is simply given by step functions  $\Theta$  and is normalized to 4 photons per annihilation

$$\frac{dN_\gamma}{dE_\gamma} = \frac{4}{\Delta E} \Theta(E_\gamma - E_-) \Theta(E_+ - E_\gamma) \quad \text{with} \quad \Delta E = E_+ - E_- = \sqrt{m_{\text{DM}}^2 - m_\phi^2}. \quad (5.22)$$

Here  $E_+$  and  $E_-$  denote the kinematic endpoints of the spectrum

$$E_\pm = \frac{m_{\text{DM}}}{2} \left( 1 \pm \sqrt{1 - \frac{m_\phi^2}{m_{\text{DM}}^2}} \right). \quad (5.23)$$

It is evident from the above equations that the mass ratio  $m_\phi/m_{\text{DM}}$  of the intermediate scalar and the dark matter determines the width of the gamma-ray box, where degenerate masses give rise to narrow, line-like boxes, whereas for  $m_{\text{DM}} \gg m_\phi$  the kinematic endpoint lies at the dark matter mass,  $E_+ \rightarrow m_{\text{DM}}$ . In this work, we consider three different box sizes, a narrow box with  $m_\phi/m_{\text{DM}} = 0.999$ , an intermediate box with  $m_\phi/m_{\text{DM}} = 0.9$  and a wide box with  $m_\phi/m_{\text{DM}} = 0.1$ . The resulting spectra are shown in Fig. 5.10 together with the background for CTA in the  $2^\circ \times 2^\circ$  region presented in Sec. 5.1.2.1.

According to the procedure described in Sec. 5.1.2.1, the 95% CL upper limits and the  $5\sigma$  sensitivity are calculated in our baseline analysis for the largest allowed energy window  $\epsilon_2$  for the  $2^\circ \times 2^\circ$  region around the Galactic center assuming an Einasto profile (see Table 5.1) and 100 h of observation time. 300 mock data sets are generated for the CTA background described in Sec. 5.1.2.1 with  $N_b = 200$  bins per decade, assuming the instrument properties specified in the CTA design study Ref. [270] and in Sec. 4.2.4. In our calculation we take the upper edge of the gamma-ray box as the location of the center of the energy window  $\bar{E} = E_+$  (see Eq. (5.23)). The results for 100% branching ratio into gammas and 4 final state photons are shown in Fig. 5.11. Since the models considered in Sec. 5.2.2 feature Dirac dark matter candidates, all results are shown for non self conjugate dark matter particles.

The curves refer to the logarithmic mean of the results from 300 mock data sets, while the band denotes the corresponding standard deviation of the 95% CL upper limits on the annihilation cross section. Unless otherwise stated, the limits are presented for vanishing optical depth. Generally speaking, cross sections down to a few times  $10^{-27} \text{ cm}^3/\text{s}$  or smaller can be probed for dark matter masses ranging from 100 GeV to 10 – 20 TeV. The projected statistical variance, denoted by the violet band in Fig. 5.11, amounts to about a factor of 2 – 3. We find that the  $5\sigma$  detection sensitivity for all dark matter masses under consideration is about a factor of 3 – 5

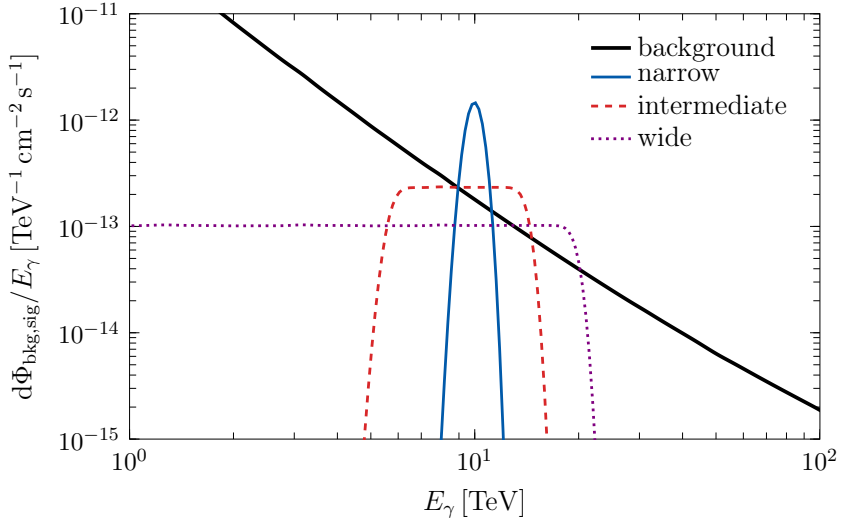


Figure 5.10: The spectra of the three box sizes under consideration  $m_\phi/m_\chi = 0.999, 0.9, 0.1$  originating from a dark matter scenario with  $\langle \sigma v \rangle_0^{4\gamma} = 10^{-24} \text{ cm}^3/\text{s}$  and  $m_\chi = 20 \text{ TeV}$  for the  $2^\circ \times 2^\circ$  region around the Galactic center. The total background flux from this region is overplotted. Both the background and the signal are convoluted with the CTA energy resolution from Ref. [270] as described in Sec. 4.2.4. This plot has been presented in Ref. [3].

worse than the corresponding average limit. Comparing the constraints for different box sizes it becomes clear that they are very similar at face value, in agreement with Refs. [299, 300]. Even though narrow boxes constitute the sharpest features, they are located below the dark matter mass, at  $m_{\text{DM}}/2$  in the case of line-like boxes, whereas wide boxes extend for the same dark matter mass to higher energies up to  $m_{\text{DM}}$ , where the background fluxes are smaller as can be seen in Fig. 5.10. These two effects, the relative softness and location of the feature, compensate each other, resulting in similar constraints.

In the following we relax our baseline assumptions and test the robustness of our results by including the optical depth and varying the energy window size, the dark matter profile, the observation time, the binning, shifting the energy window with respect to the signal as well as by including systematic uncertainties. Lastly we compare our results with the constraints from the Fermi-LAT and H.E.S.S. experiments.

- **Updated CTA performance**

The updated CTA instrument properties, presented on the CTA website [276], feature a better instrument performance, in particular a larger effective area and a better energy resolution (see Fig. 4.9). Furthermore, a proton rejection that is better by a factor of 10 compared to the instrument properties in Ref. [270] is found to reproduce the CTA background rate as shown in Sec. 5.1.2.1. The resulting projected constraints are shown by

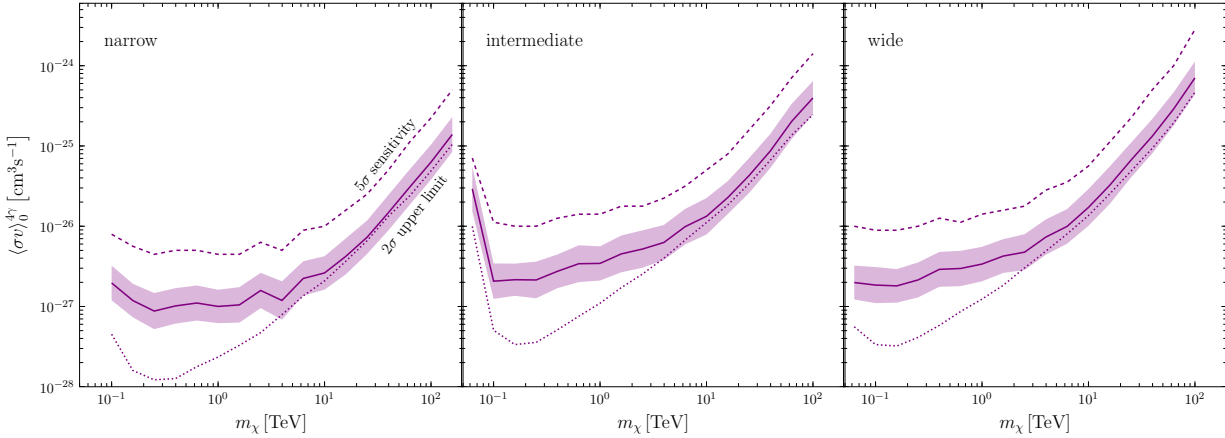


Figure 5.11: Projected 95% CL upper limits averaged over 300 mock data sets (solid line) and  $5\sigma$  detection sensitivity (dashed line) for gamma-ray boxes in a  $2^\circ \times 2^\circ$  region around the center of the Galaxy and the three box sizes under consideration, the narrow box (left), the intermediate box (middle) and the wide box (right). The band indicates the standard deviation of the corresponding upper limit. The results correspond to our baseline assumptions as described in the text. The dotted line depicts the 95% CL upper limit when the updated CTA performance [276] is assumed. These plots have been presented in Ref. [3].

the dotted line in Fig. 5.11. They are better by a factor of 8 (5.6) for narrow (wide) boxes at low energies, while improving the baseline limits by a factor of up to 1.6 above 4 TeV. An exhaustive analysis of the implications of the updated CTA performance in Ref. [276] is left for future studies.

- **Window size**

When changing the window size, the limits are affected significantly as shown in Fig. 5.12. The limits from  $\epsilon_{1.2}$  and  $\epsilon_2$  differ by more than one order of magnitude at lower energies. This difference arises because of the relatively large energy resolution, for which small window sizes cannot capture the gamma-ray feature. At higher energies, where the energy resolution significantly improves, the difference between the different sliding energy window sizes becomes less important. In order to make the best of the CTA measurements, it is crucial to choose the largest possible energy window that is suitable for the background in the target region under consideration.

- **Profile**

The effect of the choice of the dark matter profile is depicted in Fig. 5.13. In addition to our baseline Einasto profile, we consider the NFW profile as well as the cuspy and cored profiles specified in Sec. 1.2. Since the various profiles differ notably in the center of the Galaxy, the derived constraints are significantly affected by the choice of the dark matter

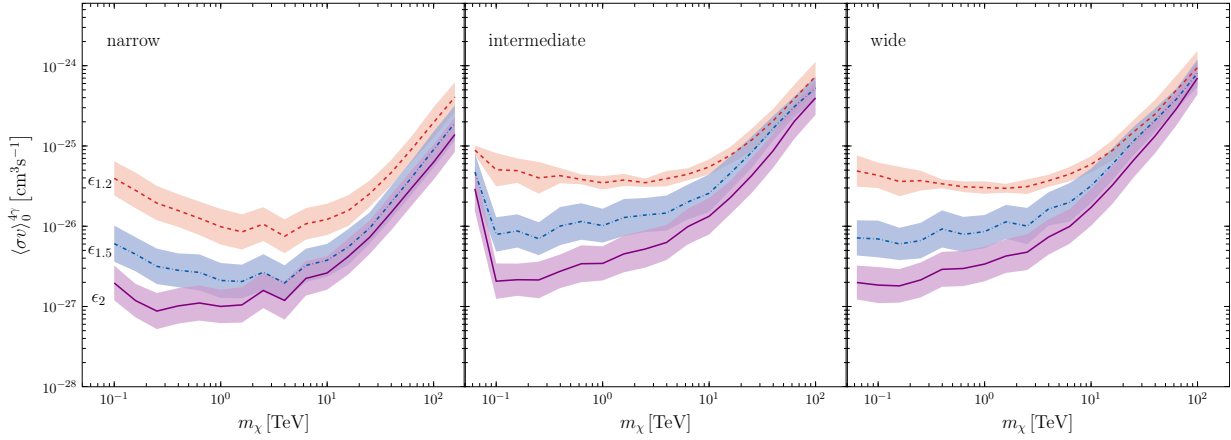


Figure 5.12: Expected 95% CL upper limits for narrow (left panel), intermediate (middle panel) and wide (right panel) boxes. The different lines correspond to the constraints with the three sliding window sizes, from top to bottom,  $\epsilon_{1.2}$ ,  $\epsilon_{1.5}$  and  $\epsilon_2$ , for our baseline assumptions specified in the text. These plots have been presented in Ref. [3].

density distribution. Thus the contracted profile with index  $\gamma = 1.2$  can improve the limits by a factor of 4, while they degrade by two orders of magnitude for the cored profile. The  $J$ -factors for all considered profiles are given in Table 5.1.

- **Optical depth**

The effect of the energy dependent  $J$ -factor that encodes the optical depth in the Milky Way, derived in Sec. 4.1.3 is shown in Fig. 5.13 assuming the Einasto profile. As expected from the effect on the  $J$ -factor, the limit worsens by about 20% when the optical depth is taken into account in the computation of the dark matter signal and the astrophysical background.

- **Observation time**

We further investigate the dependence of the constraints on the considered observation time. As our calculations are based on the background only assumption, they are expected to scale with  $1/\sqrt{\Delta t}$ . With an additional run assuming 50 h of observation time, we explicitly verified that this behavior roughly holds true for all three box sizes.

- **Binning**

In order to check the effect of the choice of the number of energy bins on our results, we repeated our calculation with  $N_b = 100$  and  $N_b = 50$  bins per decade. We found that our baseline upper limits do not change significantly for all box sizes under consideration.

- **Energy window position**

In our baseline analysis we fix the position of the sliding energy window at  $\bar{E} = E_+$ . While narrow boxes are located in the center of the window on a logarithmic scale, the feature

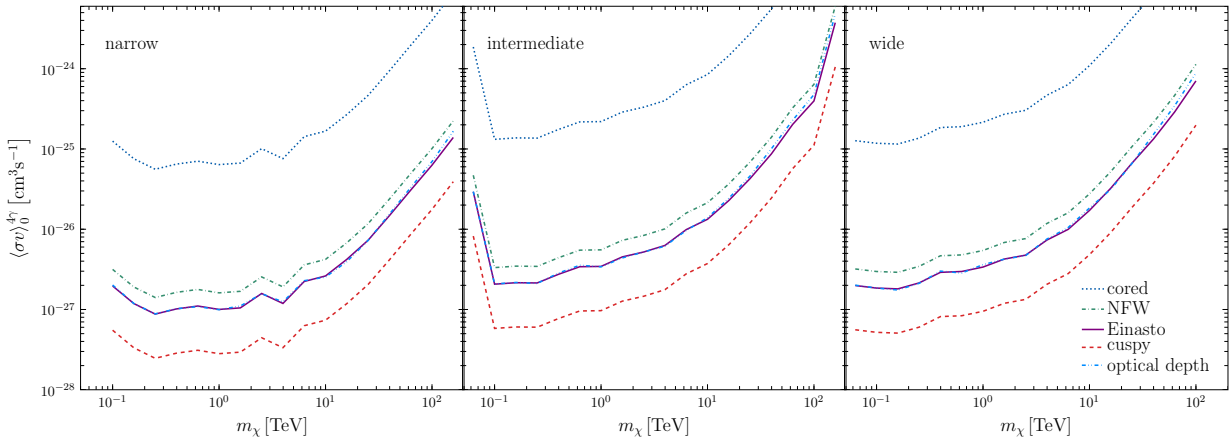


Figure 5.13: Projected CTA upper 95% CL upper limits for different dark matter halo profiles for narrow (left panel), intermediate (center) and wide (right) boxes. For the baseline Einasto profile the effect of including the optical depth is shown. All unspecified parameters or assumptions are fixed to our baseline assumptions. These plots have been presented in Ref. [3].

of wide boxes appears in the lower half of the window. Shifting the center of the window downward can improve the constraints for intermediate and wide boxes, because the feature is then better captured in the energy window. The effect of positioning the window center at  $\bar{E} = (1 + x)E_+$  is shown in Fig. 5.14 for various window positions  $x$  of the largest possible energy window  $\epsilon_2 = 2$ . We find the largest improvement of a factor of about 1.6 for downward shifts of 10% for wide and intermediate boxes, whereas to narrow boxes the best limit is already obtained for the default window location, i.e.  $x = 0$ .

- **Systematic uncertainties**

Following the method described in Ref. [257] we study the effect of systematic uncertainties on the dark matter constraints. To this end we extend the likelihood function with an extra term encoding the systematic uncertainties that enter multiplicatively in the expected number of counts. This is for instance the case for the effective area. In Ref. [257] systematic errors in the range 0.3% – 3% are considered. In our study, we employ the largest value within this range,  $\sigma_{\text{sys}} = 3\%$ . The resulting constraints for line-like boxes assuming  $N_b = 200$  and  $N_b = 50$  are shown in Fig. 5.15 together with the baseline constraints and the corresponding uncertainty band. At low energies, where the errors on the counts are dominated by systematics, the constraints change significantly when the systematic uncertainties are included. Concretely they worsen by a factor of 2.4 for  $N_b = 200$  and 4.3 for  $N_b = 50$ . At high energies, where the number of counts decreases, the data is statistics dominated and the constraints are not affected by the inclusion of a small systematic uncertainty of 3%. The difference between the two different binnings can also

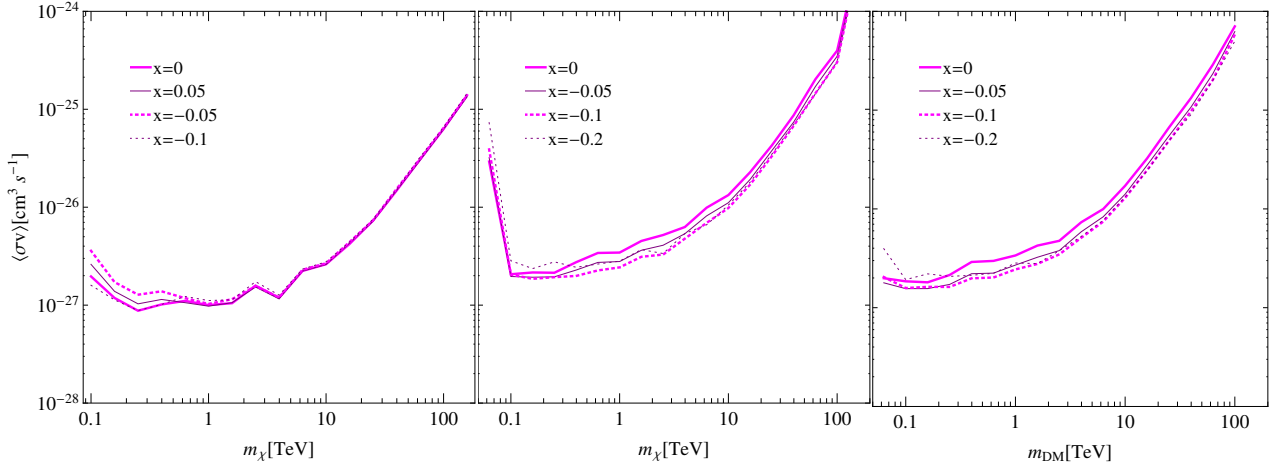


Figure 5.14: Projected CTA upper 95% CL upper limits for different window positions for narrow (left panel), intermediate (center) and wide (right) boxes. All unspecified parameters or assumptions are fixed to our baseline assumptions.

be understood considering the statistics. With a larger binning more counts per bin are measured which makes the systematic error relatively more relevant with respect to the statistical error.

However, these considerations can only serve as a first estimate of the systematic effects and as a consistency check of our analysis with respect to Ref. [257], where continuous gamma-ray spectra from dark matter are studied. According to the treatment of the systematics in the likelihood function, a bin by bin variation of the relevant quantity is allowed. Even though the uncertainty on the effective area and other quantities is expected to be energy dependent, such a rapid fluctuation might not be realistic. A detailed study of the systematics of CTA in searches for sharp features is left for future work.

- **Comparison with other experiments**

Lastly, we confront the forecasted CTA constraints with current limits on gamma-ray lines from the Fermi-LAT [262] and the H.E.S.S. [258] experiments in Fig. 5.16. To this end we perform a new run in order to calculate the CTA limits in the CGH region considered in the H.E.S.S. analysis (see Table 5.1 for the  $J$ -factor), where we also adopt the observation time of H.E.S.S., 112 h. For the comparison the line limits were appropriately rescaled to narrow boxes, i.e. to lines at half the dark matter mass with 4 photons in the final state. While the CTA and H.E.S.S. limits both correspond to the Einasto profile and the same target region, the Fermi-LAT limits are shown for an NFW contracted profile for a circular  $3^\circ$  region around the Galactic center with  $J_{\text{ann}} = 1.39 \times 10^{23} \text{ GeV}^2 \text{ sr/cm}^5$ . For convenience we also show the 95% CL upper limits on the gamma-ray flux in Fig. 5.16. We find that CTA can hardly supersede the bounds obtained from Fermi-LAT data with the performance of

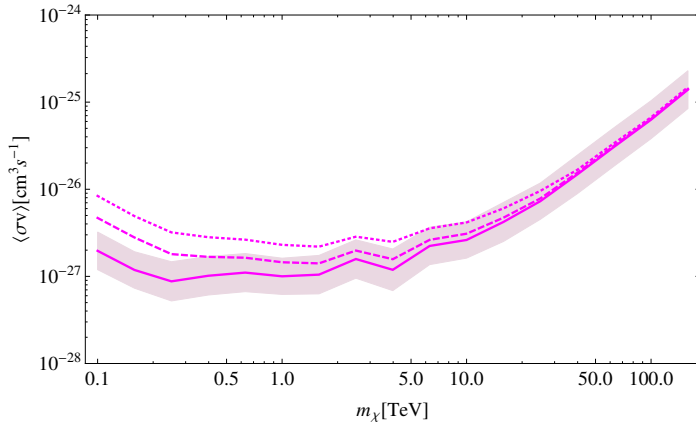


Figure 5.15: Projected 95% CL upper limits on narrow boxes, including 3% of systematic uncertainties for  $N_b = 200$  (dashed line) and  $N_b = 50$  (dotted line). The solid line and the shaded band denote the baseline limit and uncertainty, respectively.

Ref. [270]. At high energies, an improvement of the H.E.S.S. limits by up to one order of magnitude is possible. If the CTA instrument can indeed reach the performance presented in Ref. [276] it can improve the Fermi-LAT limits above  $\sim 250$  GeV by a factor of a few.

Summarizing, we obtain very stringent and robust constraints on gamma-ray boxes for TeV dark matter particles. Note that in this energy range no other dark matter search will be sensitive in the near future. Thus the measurements of the CTA instrument will be a unique opportunity to discover or rule out dark matter scenarios that produce gamma-ray boxes in the TeV range. In the following section we consider two concrete particle physics models featuring gamma-ray boxes and show that the constrained cross sections lie below the expectation from a thermal WIMP, even when the appropriate branching fractions are taken into account.

### 5.2.2 Constraining benchmark models

Many models that feature gamma-ray boxes typically contain a Dirac dark matter candidate and involve the breaking of global symmetries [300–305]. However, it was found that models with chiral fermion dark matter can as well produce gamma-ray boxes. Such a scenario is described in Ref. [306], where the intermediate scalar is a pseudo-Goldstone boson, which arises due to the spontaneous breaking of a global  $U(1)$  symmetry. Furthermore, in Next-to-Minimal Supersymmetric Standard Model (NMSSM) scenarios, where the MSSM is extended with one or more singlet superfields, gamma-ray boxes can be produced by the annihilation of neutralino or sneutrino dark matter as analyzed in Refs. [307, 308].

In the following we focus on Dirac dark matter and discuss two setups that we use as benchmark scenarios.

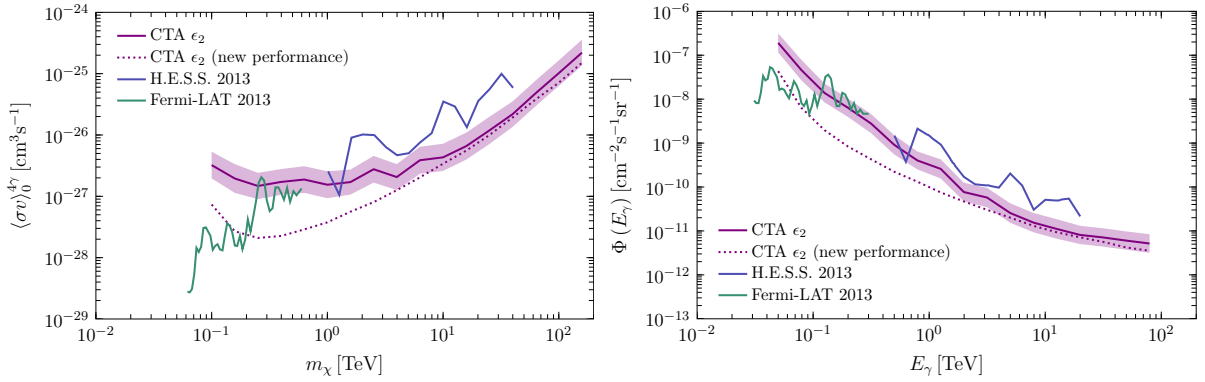


Figure 5.16: The comparison of the projected CTA limits with current constraints from Fermi-LAT (green lines) and H.E.S.S. (blue lines) are shown in the left panel, while the right panel depicts the corresponding flux upper limits. As in Fig. 5.11, the violet solid lines and bands denote the average upper limits obtained with the CTA performance of Ref. [270], while the dotted lines refer for the updated instrument properties [276]. All lines in this figure correspond to 95% CL upper limits. These plots have been presented in Ref. [3].

### 5.2.2.1 Model A

We proceed with the presentation of the model described in Refs. [300–302], where the Peccei-Quinn mechanism [309] is invoked. It is dubbed “Model A” in the remainder of this thesis. In this model, the Standard Model is extended by a Dirac fermion  $\chi$ , which is the dark matter candidate, as well as by a complex scalar field  $S$ . Both fields are charged under a global  $U(1)_{\text{PQ}}$  symmetry. This symmetry, however, is broken spontaneously and explicitly and the resulting pseudo-Goldstone boson  $a$  plays the role of the intermediate scalar  $\phi$  in the cascade process. The Lagrangian  $\mathcal{L}$  of this model reads

$$\mathcal{L} = \mathcal{L}_{\text{SM}} + \mathcal{L}_\chi + \mathcal{L}_S + \mathcal{L}_{\text{int}}, \quad (5.24)$$

where  $\mathcal{L}_{\text{SM}}$  is the Standard Model Lagrangian including the Higgs potential, while

$$\mathcal{L}_\chi = i\bar{\chi}\gamma^\mu\partial_\mu\chi, \quad (5.25)$$

$$\mathcal{L}_S = \partial_\mu S \partial^\mu S^* - m_S^2 |S|^2 - \lambda_S |S|^4 + \left(\frac{1}{2}m'_S S^2 + \text{c.c.}\right), \quad (5.26)$$

$$\mathcal{L}_{\text{int}} = -\lambda_\chi (S\bar{\chi}P_L\chi + S^*\bar{\chi}P_R\chi) - 2\lambda_{H,S}|H|^2|S|^2. \quad (5.27)$$

$\mathcal{L}_\chi$  and  $\mathcal{L}_S$  are the parts of the Lagrangian that contain only the fields  $\chi$  and  $S$ , respectively, while  $\mathcal{L}_{\text{int}}$  encodes their interaction terms. When the mass term  $m'_S$  vanishes, the Lagrangian is invariant under the  $U(1)_{\text{PQ}}$  symmetry transformation, i.e.  $\chi \rightarrow e^{i\gamma_5\alpha}\chi$  and  $S \rightarrow e^{2i\alpha}S$ , while all Standard Model fields are uncharged under this symmetry and thus do not transform. As the

field  $S$  acquires a vacuum expectation value, this symmetry is spontaneously broken, leaving instead a residual  $Z_2$  symmetry that ensures the stability of the dark matter particle. The  $S$  field can be decomposed into  $S = \langle S \rangle + \frac{1}{\sqrt{2}}(s + ia)$ . When the mass term  $m'_S$  does not vanish, the symmetry is also explicitly broken. Note that this does not affect the dark matter stability but gives a mass  $m_a = m'_S$  to the otherwise massless Goldstone boson  $a$ . Consequently, the pseudoscalar  $a$  can then decay into Standard Model particles. Through the mixing of the  $s$  field with the Standard Model Higgs  $h$  and the interactions of the dark matter with  $s$ , dark matter can reach thermal equilibrium with Standard Model particles. The correct relic abundance can then be realized via thermal freeze-out through the annihilations  $\chi\bar{\chi} \rightarrow aa, ss, sa$ , when kinematically allowed.

In order to generate gamma-ray boxes the scalar field  $S$  must couple to the Standard Model gauge fields which is not yet implemented in the above Lagrangian. In fact, such a coupling can arise, when new heavy fermions are introduced in the theory that couple to  $S$  via the anomaly loop

$$\mathcal{L}_{\text{int}} \supset \sum_{i=1,2} \frac{c_i \alpha_i}{8\pi v_s} a F_{\mu\nu}^i \tilde{F}^{i\mu\nu}. \quad (5.28)$$

This additional interaction term allows the decays  $a \rightarrow \gamma\gamma, \gamma Z, ZZ, W^+W^-$ . Here  $\tilde{F}_{\mu\nu} = \epsilon_{\mu\nu\rho\sigma} F^{\rho\sigma}/2$  denotes the dual field strength tensor and the parameters  $\alpha_i$  are given by  $\alpha_i = g_i^2/4\pi$  with the  $U(1)_Y$  and  $SU(2)_L$  coupling constants  $g_{1,2}$ . The  $c_{1,2}$  are constant parameters that depend on the details of the extended theory. Concretely, the introduction of vector-like doublet ( $q_y = \pm 1/2$ ) and vector-like singlet ( $q_y = \pm 1$ ) fermions to the models yields  $c_1/c_2 = 3$  and will be considered as our benchmark scenario in the remainder of this section. Furthermore  $m_a = m_s$  is assumed throughout. The full expressions for the anomaly coefficients, decay rates and annihilation cross section of this model can be found in Ref. [300].

The gamma-ray box now arises in the annihilation of a dark matter pair into a final state with at least one pseudoscalar  $a$  that in turn decays into to gammas, while the decay of  $s$  on the other hand produces a gamma-ray continuum through the mixing with the Higgs. The target cross section for indirect searches for gamma-ray boxes reads

$$\langle\sigma v\rangle_0^{4\gamma} = \langle\sigma v\rangle_0 \left( \text{BR}(\chi\bar{\chi} \rightarrow aa) + \frac{\text{BR}(\chi\bar{\chi} \rightarrow as)}{2} \right) \text{BR}(a \rightarrow \gamma\gamma), \quad (5.29)$$

where the relevant branching ratios and final state gamma-ray multiplicities as well as the present day annihilations cross section  $\langle\sigma v\rangle_0$  are taken into account. In our case, since  $m_a = m_s$  the branching ratios of the dark matter annihilations are constant for a fixed ratio  $m_a/m_\chi$ . They are shown for values of  $m_a/m_\chi$  under consideration in Table 5.3. This scenario is denoted A1 for narrow boxes with  $m_a/m_\chi = 0.999$ , A2 for intermediate boxes with  $m_a/m_\chi = 0.9$  and A3 for wide boxes with  $m_a/m_\chi = 0.1$ , respectively. The branching ratios of the  $a$  decays on the other hand depend on  $m_a$  and thus vary with the dark matter mass for our constraints since the ratio  $m_a/m_\chi$  is fixed. The dependence of these branching fractions on  $m_a$  is shown in Fig. 5.17. One

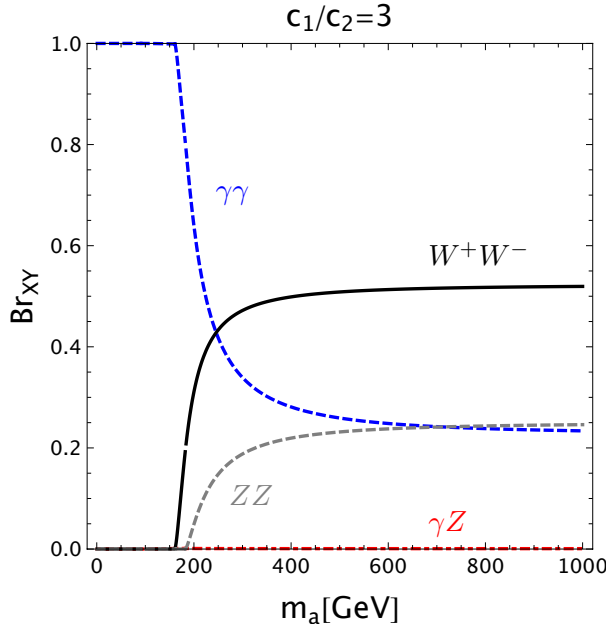


Figure 5.17: Mass dependence of the branching fractions for the decay of the pseudoscalar  $a$  into  $a \rightarrow \gamma\gamma$  (blue dashed line),  $\gamma Z$  (red dot-dashed line),  $ZZ$  (gray dashed line) and  $W^+W^-$  (black solid line) for  $c_1/c_2 = 3$ . The figure is taken from Ref. [300].

can see that the decay into  $\gamma\gamma$  amounts to 100% for  $m_a < 2m_W$  and decreases to about 20% when the  $W$  and  $Z$  channels open up.

The present day annihilation cross section is in general different from the thermal cross section, due to its dependence on the dark matter velocity. Since the dark matter velocity is much smaller compared to the velocity at freeze-out, the corresponding shift in the thermally averaged annihilation cross section has to be taken into account properly. The ratios  $\langle\sigma v\rangle_0/\langle\sigma v\rangle_{\text{th}}$  are shown in Table 5.3 for the three scenarios under consideration. The thermal average is calculated in the non-relativistic limit as in Ref. [300]. For the thermal cross section we adopt  $\langle\sigma v\rangle_{\text{th}} = 6 \times 10^{-26} \text{ cm}^3/\text{s}$ . The factor 2 with respect to the usual value of  $3 \times 10^{-26} \text{ cm}^3/\text{s}$  appears because the dark matter considered here is of Dirac nature and not Majorana.

### 5.2.2.2 Model B

Our second benchmark scenario is based on the model described in Refs. [303–305]. Similar to model A, the Standard Model is extended by a Dirac dark matter fermion and a complex scalar  $S$  that assumes a vacuum expectation value and can be decomposed in a real scalar  $s$  and a pseudoscalar  $a$ . The Peccei-Quinn symmetry of the Lagrangian in this model is also broken explicitly by a mass term of the  $S$  field. Again, the dark matter is stable due to a remnant symmetry under which it is charged. However, the interaction terms are different. This is a result of the original motivation of this model. In fact, model B has been designed in order to

explain the positron excess measured by PAMELA, Fermi-LAT and AMS-02 (see Sec. 3.1). Thus  $a$  has to decay dominantly into leptons, which means that the leptons must be charged under the Peccei-Quinn symmetry. To this end, an additional Higgs doublet is introduced.

As discussed in Ref. [303], the annihilations into  $aa$  and  $ss$  are s-wave suppressed, such that a dark matter pair can only annihilate via  $\chi\bar{\chi} \rightarrow as$ . The masses of the scalar  $s$  and the pseudoscalar  $a$ , in which the  $S$  field can be decomposed, are chosen in order to i) accommodate the positron excess and ii) satisfy the gamma-ray constraints from the direct decay of  $a$  into gammas or from the decay into neutral pions that in turn decay into photons. If  $m_s \ll m_a$  and  $m_a = 360 - 800$  MeV, these requirements can be met for  $\mathcal{O}(\text{TeV})$  dark matter particles, resulting in a branching ratio of  $BR(a \rightarrow \gamma\gamma) = 10^{-3}$ . This small branching fraction, however, is compensated by a boost factor of  $B_S \sim 10^3$  that arises because of Sommerfeld enhancement induced by the light scalar  $s$ . Due to the smallness of pseudoscalar mass this scenario gives rise to wide boxes only. Since the gamma-ray spectrum does not depend strongly on the concrete mass ratio for wide boxes, we consider  $m_a = m_s$  and  $m_a/m_\chi = 0.1$  for definiteness as benchmark values of this model in our phenomenological study. All parameters employed for this benchmark model B are summarized in Table 5.3. The target cross section then reads

$$\langle\sigma v\rangle_0^{4\gamma} = B_S \langle\sigma v\rangle_0 \frac{BR(\chi\bar{\chi} \rightarrow as)}{2} BR(a \rightarrow \gamma\gamma). \quad (5.30)$$

### 5.2.2.3 Benchmark limits

Finally, the projected CTA constraints for the models A and B discussed above are presented. In Table 5.3 we summarize all relevant quantities of the benchmark models under consideration. The limits on the benchmark models are shown for our baseline analysis as described in Sec. 5.2.1,

	$m_a/m_\chi$	$BR(\chi\bar{\chi} \rightarrow as)$	$BR(\chi\bar{\chi} \rightarrow aa)$	$BR(\chi\bar{\chi} \rightarrow ss)$	$\langle\sigma v\rangle_0/\langle\sigma v\rangle_{\text{th}}$
A1 (narrow)	0.999	0.99	$2 \times 10^{-3}$	$4 \times 10^{-3}$	0.13
A2 (intermediate)	0.9	0.64	0.12	0.24	0.76
A3 (wide)	0.1	0.25	0.25	0.50	0.96
B (wide)	0.1	1	0	0	1

Table 5.3: Mass ratios, branching fractions and ratios of the present day annihilation cross section to the corresponding value at freeze-out for the benchmark models. While model A [300–302] encompasses narrow (A1), intermediate (A2) and wide boxes (A3), scenario B [303–305] only gives rise to wide boxes. In all models we set  $m_s = m_a$ .

i.e. a  $2^\circ \times 2^\circ$  target region around the Galactic center, the Einasto profile, 100 h of observation time, vanishing optical depth and the sliding energy window size  $\epsilon_2$ . Fig. 5.18 shows the target cross sections for thermal dark matter candidates according to Eqs. (5.29) and (5.30) together with the model-independent gamma-ray box constraints. The shape of the target cross sections

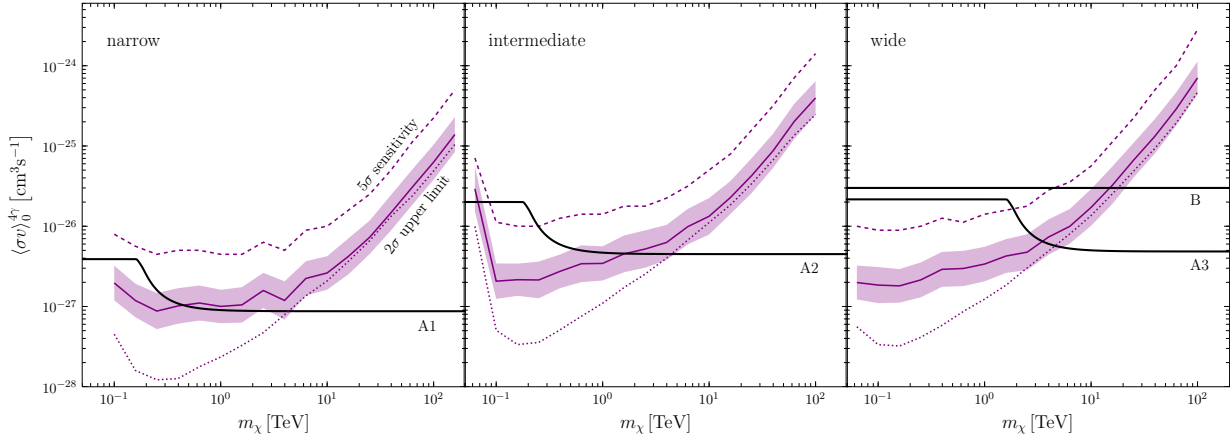


Figure 5.18: Same as Fig. 5.11 with the target cross sections for the different benchmark models for narrow (left), intermediate (middle) and wide (right) boxes overplotted.

for model A results from the dependence of the branching fraction into gammas on the value of the pseudoscalar mass as shown in Fig. 5.17.

As can be seen in the left panel of Fig. 5.18, the thermal cross section for narrow boxes can only be probed for relatively small masses below 1 TeV assuming the instrument properties of Ref. [270]. Since the updated instrument properties of Ref. [276] can significantly improve the limits at low masses, a thermal relic can be probed up to about 4 TeV. Nevertheless, a thermal WIMP that produces narrow boxes is never in the  $5\sigma$  sensitivity reach. Because the target cross section for intermediate boxes is larger than for narrow boxes, the prospects are better for this scenario as shown in the middle panel of Fig. 5.18. For both instrument performances under consideration, a thermal relic can be probed up to a few TeV. Within a small mass range around 200 GeV such a dark matter particle could even be detected with  $5\sigma$  significance with CTA. The most promising prospects are found for wide box scenarios. The corresponding constraints and target cross sections are plotted in the right panel of Fig. 5.18. While model A can be probed up to a few TeV, thermal relics can be excluded up to 10 TeV in model B. Also a  $5\sigma$  detection for dark matter masses up to over 1 TeV is possible with CTA in both wide box scenarios.

In Fig. 5.19 we present the results in form of the ratio of the 95% CL upper limit and the target cross section from a thermal WIMP. Note that these results are valid for the assumed smooth dark matter component. If, however, the annihilation cross section is enhanced by a factor of  $\sim 10$  due to the presence of dark matter substructure, all models under consideration can be probed up to tens of TeV.

Concluding this section, the above discussion shows that concrete particle physics models that produce gamma-ray boxes are indeed in the reach of the future Cherenkov Telescope Array. Especially for the wide box scenario CTA is probably the only instrument that can probe dark matter candidates in the multi TeV range where no other detection strategy will be sensitive in

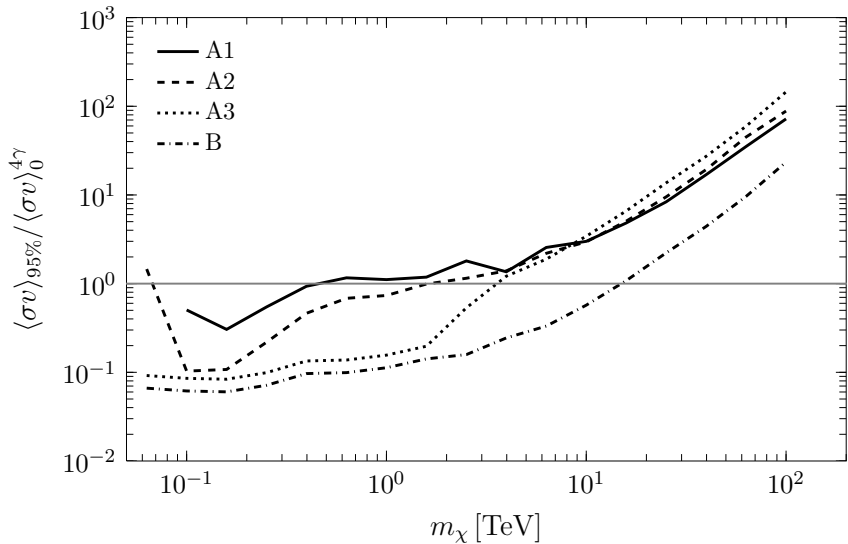


Figure 5.19: This figure shows the ratio of the average 95% CL expected CTA upper limit and the target cross section of thermally produced dark matter in the benchmark models A and B for our baseline analysis.

the near future.

### 5.3 Minimal dark matter

This section is dedicated to the gamma-ray constraints on the minimal dark matter models, in particular the fermionic 5-plet and the scalar 7-plet. It is organized as follows. First the main features of the models are reviewed. After that, the Sommerfeld effect, which is crucial in the calculation of the annihilation cross sections, is introduced. Then the Sommerfeld enhanced cross sections are presented, including internal bremsstrahlung. Lastly, the gamma-ray constraints arising from the continuum as well as from the gamma-ray line and the sharp internal bremsstrahlung feature are computed and compared to each other.

#### 5.3.1 Model

Many extensions of the Standard Model of particles physics have been put forward in the last decades in order to cure problems within the Standard Model, for instance the hierarchy problem. At the same time, these models often feature a weak scale dark matter candidate, which is by itself well motivated by the WIMP miracle (see Sec. 1.3.2.1). On the other hand, so far no sign of new physics has shown up at the LHC, pushing the scale of these models to higher and higher energies. This in turn means that some amount of fine tuning has to be introduced to the theories, making them less natural and lose some of their original motivation. In addition,

extra symmetries often have to be imposed by hand to ensure the stability of the dark matter candidate, which is the lightest particle that is charged under new symmetry.

In this situation, another more bottom-up approach to the dark matter identification is pursued, concentrating only on the dark matter sector leaving aside other issues of the Standard Model like the hierarchy problem. Examples of models that are appealing due to their simplicity are the extension of the Standard Model by a singlet scalar [310–312] or the inert doublet model [313–315].

In the former model an additional scalar that is a singlet under the Standard Model gauge group is introduced. A  $Z_2$  symmetry, under which only the new scalar is odd and all other particles are even, must be imposed in order to make the singlet scalar dark matter stable. It interacts with the Standard Model fields through a quartic coupling with the Higgs.

In the latter model the Standard Model is extended with a colorless  $SU(2)_L$  doublet with hypercharge 1/2. Again, a  $Z_2$  symmetry guarantees the stability of the dark matter candidate. Interactions terms with the electroweak gauge bosons as well as with the Higgs field are present in the inert doublet Lagrangian.

Both models have in common that extra symmetries have to be imposed by hand in order to ensure the stability of the dark matter candidate and that at least two additional parameters are required in order to produce the correct relic density in these models.

An alternative class of models that do not require new symmetries features so called minimal dark matter. These particularly predictive models were introduced in Ref. [316] and further studied e.g. in Refs. [317–319]. The main idea is to extend the Standard Model with extra  $SU(2)_L$  multiplets with minimal quantum numbers, in order to obtain a stable dark matter candidate that is still allowed by observations. The details of this model are explained in the remainder of this section, following Ref. [316].

The Lagrangian of the model is given by

$$\mathcal{L} = \mathcal{L}_{\text{SM}} + \frac{1}{2} \bar{\chi}(iD^\mu - M)\chi \quad (\text{fermion}) \quad (5.31)$$

or

$$\mathcal{L} = \mathcal{L}_{\text{SM}} + \frac{1}{2} (|D_\mu \chi|^2 - M^2 |\chi|^2) \quad (\text{scalar}), \quad (5.32)$$

where  $\mathcal{L}_{\text{SM}}$  denotes the Standard Model Lagrangian,  $\chi$  the dark matter multiplet and  $M$  its mass. The quantum numbers of  $\chi$  are chosen such that it is a good dark matter candidate. Hence it cannot have strong interactions and thus must be a  $SU(3)$  singlet, while being a  $SU(2)_L$   $n$ -plet. Since the electric charge of the  $n$ -plet is given by  $Q = T_3 + Y$ , where  $T_3$  is the third component of the weak isospin, the hypercharge  $Y$  has to be assigned to  $\chi$  such that it contains a neutral component. However, neutral scalar or Dirac dark matter candidates with  $Y \neq 0$  must be discarded, because they couple to the  $Z$  boson, which is excluded by direct detection experiments: The spin-independent elastic cross sections that arise due to vector-like interactions with the  $Z$  boson lie several orders of magnitude above the present bounds [316]. This excludes all multiplets

with even  $n$ . For Majorana dark matter, those candidates are still allowed observationally, however, insisting on minimality, we only consider candidates with zero hypercharge.

Next, the stability of the remaining dark matter candidates is considered. In fact, the automatic stability of the dark matter without imposing extra symmetries to suppress unwanted decay modes is one of the most attractive features of this framework. In the case of  $n = 3$ , the dark matter can decay through renormalizable operators, concretely, the scalar candidate into two Higgses and the fermionic candidate into a Higgs and a neutrino. For multiplets with  $n \geq 5$  however, no sizable couplings to Standard Model particles are possible at the renormalizable level in view of the respective quantum numbers.

In the remainder of the thesis we focus on the two smallest allowed multiplets, the 5-plet and the 7-plet. Concretely, we consider the fermionic 5-plet and the scalar 7-plet as benchmark scenarios. Computationally, the scalar and fermionic cross sections of a given multiplet differ only by a factor of 2.

The minimal dark matter triplet has been extensively studied in the literature (see e.g. Ref. [320–322]). In fact, it coincides with the supersymmetric wino dark matter candidate in the limit where the wino is much lighter than the other supersymmetric particles.

If the minimal dark matter model is assumed to be the only new physics up to the Planck scale, an upper bound on  $n$  can be derived by requiring perturbativity at  $E = M_{\text{Pl}}$ :  $n \leq 5$  for Majorana fermions and  $n \leq 8$  for real scalars.

Also, note that the fermionic 5-plet is even stable at the non-renormalizable level. For the scalar 5-plet and 7-plet on the other hand, decays can be induced through non-renormalizable operators [316, 323].

In components, the two multiplets under consideration read

$$\chi = \begin{pmatrix} \text{DM}^{2+} \\ \text{DM}^+ \\ \text{DM} \\ -\text{DM}^- \\ \text{DM}^{2-} \end{pmatrix} \text{ for the 5-plet, } \quad \chi = \begin{pmatrix} \text{DM}^{3+} \\ \text{DM}^{2+} \\ \text{DM}^+ \\ \text{DM} \\ -\text{DM}^- \\ \text{DM}^{2-} \\ -\text{DM}^{3-} \end{pmatrix} \text{ for the 7-plet,} \quad (5.33)$$

where the relative signs have been introduced in order to make the multiples isospin self conjugate.

Of course, the dark matter particles must be the lightest state of the multiplet. At tree level all components of  $\chi$  have the same mass  $M$  as can be seen in Eqs. (5.31) and (5.32). However, at one loop a mass difference is induced by the Standard Model gauge bosons. This mass splitting is computed in Ref. [316] and indeed, the neutral component is the lightest component of the multiplet when the loop effects are taken into account. Concretely, the mass splitting between the components of charge  $Q$  and  $Q'$  reads

$$M_Q - M_{Q'} \approx (Q^2 - Q'^2) \Delta, \quad \text{where} \quad \Delta \equiv \alpha_2 \sin^2 \left( \frac{\theta_W}{2} \right) M_W \approx 166 \text{ MeV}. \quad (5.34)$$

In the minimal dark matter framework the mass of the new multiplet  $M$  is the only new parameters that is added to the Standard Model. In fact, this parameter can be fixed by the requirement that dark matter is thermally produced with the correct relic abundance. It was noted in Ref. [317] that this calculation cannot be done perturbatively, since the exchange of multiple gauge bosons induces the so-called Sommerfeld enhancement. This effect must not only be taken into account in the calculation of the relic density, which is beyond the scope of this work, but also in the computation of the annihilation cross sections that are investigated here, and is further discussed in the next section.

A full non-perturbative calculation was performed in Refs. [317, 319], where  $M \approx 10 \text{ TeV}$  [317] ( $M \approx 9.4 \text{ TeV}$  [319]) and  $M \approx 25 \text{ TeV}$  [317] were found for the thermal masses of the 5-plet and 7-plet, respectively. Note that these values are shifted to higher masses by a factor of 2 – 3 with respect to the tree level calculation [316].

In the remainder of this work, however, we remain agnostic about the thermal history of the Universe, not requiring thermal dark matter production but allowing for alternative mechanisms (see Sec. 1.3.2.2). Such a non-thermal minimal dark matter scenario is for example discussed in Ref. [324], where the minimal dark matter model is extended by three right handed neutrinos. The lightest of those decays into dark matter after freeze-out, which can yield the correct relic density.

For  $M < M_{\text{th}}$  the minimal dark matter constraints can still be applied for thermal relics assuming a rich dark sector with more than one stable particle.

In this work, we consider electroweak dark matter in the mass range from 1 TeV to 30 TeV for the 5-plet and to 75 TeV for the 7-plet, corresponding to roughly three times their thermal mass values.

### 5.3.2 Sommerfeld enhancement

The Sommerfeld effect describes the enhancement of the annihilation rate of non-relativistic particles through the exchange of light mediators. In this situation the perturbative expansion of the matrix element breaks down and higher order diagrams contributing to the process have to be taken into account properly. Since the present day dark matter velocity is of the order of  $\sim 10^{-3}c$ , this effect can be sizable and is thus important in indirect detection phenomenology.

The breakdown of the perturbative expansion for dark matter annihilations was first realized in the context of supersymmetric dark matter. Concretely, a full one-loop calculation of the annihilation cross section of two higgsino dark matter particles into two photons was conducted in Refs. [243, 244]. In the limit where the different components of the  $SU(2)_L$  triplet are almost degenerate and much heavier than the  $W$  mass, the s-wave annihilation cross section reads [244]

$$\sigma v \simeq \frac{\alpha^4 \pi}{4m_W^2 \sin^4 \theta_W}, \quad (5.35)$$

where  $\theta_W$  denotes the Weinberg angle. In fact, this cross section remains constant irrespective of the dark matter mass. This, however, is in conflict with partial wave unitarity, as the upper

bound on the s-wave cross section is given by [74]

$$\sigma v \lesssim \frac{4\pi}{M^2 v}. \quad (5.36)$$

Since this cross section decreases quadratically with the dark matter mass  $M$ , clearly the one-loop higgsino annihilation exceeds the unitarity bound for large enough dark matter masses. This indicates that the perturbative treatment is insufficient and a full calculation is necessary.

The full non-perturbative analysis was thus carried out later [142] for higgsino- and wino-like dark matter candidates. Indeed, the correct asymptotic behavior of the cross section is recovered when all ladder diagrams, which are the most important higher order correction, are taken into account. The ladder diagrams that are considered in this calculation are illustrated in Fig. 5.20. They are enhanced by  $\alpha M/m_W$  for each weak gauge boson exchange [142]. As shown

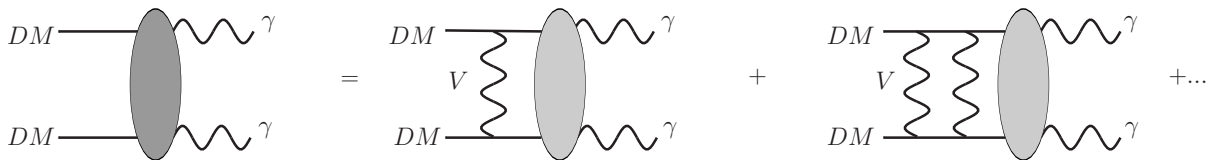


Figure 5.20: Ladder diagrams that contribute to the Sommerfeld enhancement for the annihilation of dark matter into two photons. The vector boson  $V$  that is exchanged stands for the electroweak gauge bosons  $W^\pm$ ,  $Z$  and  $\gamma$ . The dark gray ellipse denotes the full interactions, including the Sommerfeld enhancement. The light gray ellipse denotes only the short range interactions.

in Ref. [142] all these ladder diagrams can be properly taken into account in a non-relativistic effective theory framework. The non-perturbative calculation revealed that the annihilation cross section of non-relativistic heavy neutralinos can be enhanced by orders of magnitude for small mass splittings between the neutral and charged states.

When it was realized that Arnold Sommerfeld encountered a similar phenomenon in his studies of electron-nucleon scattering at low relative velocities [325], the non-perturbative enhancement of the dark matter annihilation cross section was dubbed the “Sommerfeld effect”.

Physically this effect can be understood as follows: The non-relativistic potential that is generated by the exchange of force carriers distorts the wave function of the two-body dark matter state. Whenever this is the case the annihilation cross section is modified significantly [142].

### 5.3.3 Cross sections

In the minimal dark matter framework all prerequisites for large Sommerfeld enhancements are given for heavy dark matter particles: i) non-relativistic two body initial states, ii) dark matter particles with  $M \gg m_W$ , iii) nearly mass degenerate states in the multiplet and iv) presence of ladder diagrams due to  $W$ ,  $Z$  and  $\gamma$  exchange. Consequently, the Sommerfeld effect has to be

taken into account in order to correctly derive indirect detection constraints for 5-plet and 7-plet dark matter candidates and we proceed by briefly summarizing how the Sommerfeld enhanced cross sections are calculated.

As shown in Ref. [142] the annihilation cross section involves enhancement factors that can be calculated by solving the Schrödinger equation for the matrix  $g(r)$

$$\frac{1}{M} g''(r) + \left( \frac{1}{4} M v^2 \mathbb{1} - V(r) \right) g(r) = 0, \quad (5.37)$$

where  $v$  denotes the relative velocity of the dark matter particles and  $V(r)$  is the effective potential generated by the gauge boson exchange. We assume  $v = 2 \cdot 10^{-3}c$  throughout. The matrix  $g(r)$  is connected to the two-body states involved in the dark matter annihilation process. There are three states for 5-plet dark matter,  $\text{DM DM}$ ,  $\text{DM}^+ \text{DM}^-$  and  $\text{DM}^{2+} \text{DM}^{2-}$ , which mix with each other due to the small mass splitting, and thus the corresponding matrix is of dimension 3. An additional state,  $\text{DM}^{3+} \text{DM}^{3-}$ , is present for 7-plet dark matter making the corresponding matrix 4-dimensional. The potential  $V(r)$  can be derived from the non-relativistic expansion of the effective action of the theory, where all relativistic particles are integrated out. The concrete expressions for the 5- and 7-plet are given in Ref. [4].

The boundary conditions for  $g(r)$  read

$$g(0) = \mathbb{1},$$

$$g(r) \rightarrow e^{(iMv/2)\sqrt{\mathbb{1}-4V(\infty)/(Mv^2)}} D = e^{irMv/2} \begin{pmatrix} 0 & \cdots & 0 \\ 0 & \cdots & 0 \\ \vdots & \ddots & \vdots \\ \cdots & d_{+-} & d_{00} \end{pmatrix} \text{ when } r \rightarrow \infty, \quad (5.38)$$

where  $D$  is a constant matrix. In practice, the second order Schrödinger equation is transformed to a first order differential equation, which remedies numerical instabilities that arise in the former equation for small mass splittings [4].

The solutions for  $g(r)$  contain oscillatory phases, which are factored out in order to obtain the enhancement factors  $d_{00}$  and  $d_{i+i-}$ . Then the annihilation cross section with final state  $f$  is given by

$$\sigma v (\text{DM DM} \rightarrow f) = \frac{1}{4M^2} \int \left( \prod_{a \in f} \frac{d^3 q_a}{2E_a (2\pi)^3} \right) (2\pi)^4 \delta^4(p_{\text{DM}} + p'_{\text{DM}} - \sum_{a \in f} q_a) \quad (5.39)$$

$$\cdot \left| d_{00} \mathcal{M}(\text{DM DM} \rightarrow f) + \sum_i \sqrt{2} d_{i+i-} \mathcal{M}(\text{DM}^{i+} \text{DM}^{i-} \rightarrow f) \right|^2,$$

where  $i = 1, 2$  for the 5-plet and  $i = 1, 2, 3$  for the 7-plet. The enhancement factors are in general complex. However, it turns out that they have one common phase, which is irrelevant in Eq. (5.39). The relative sign between them, can, however, lead to a destructive interference and thus to dips in the cross section.

The enhancement factors for the minimal dark matter multiplets under consideration are shown in Fig. 5.21 for the 5-plet and in Fig. 5.22 for the 7-plet.

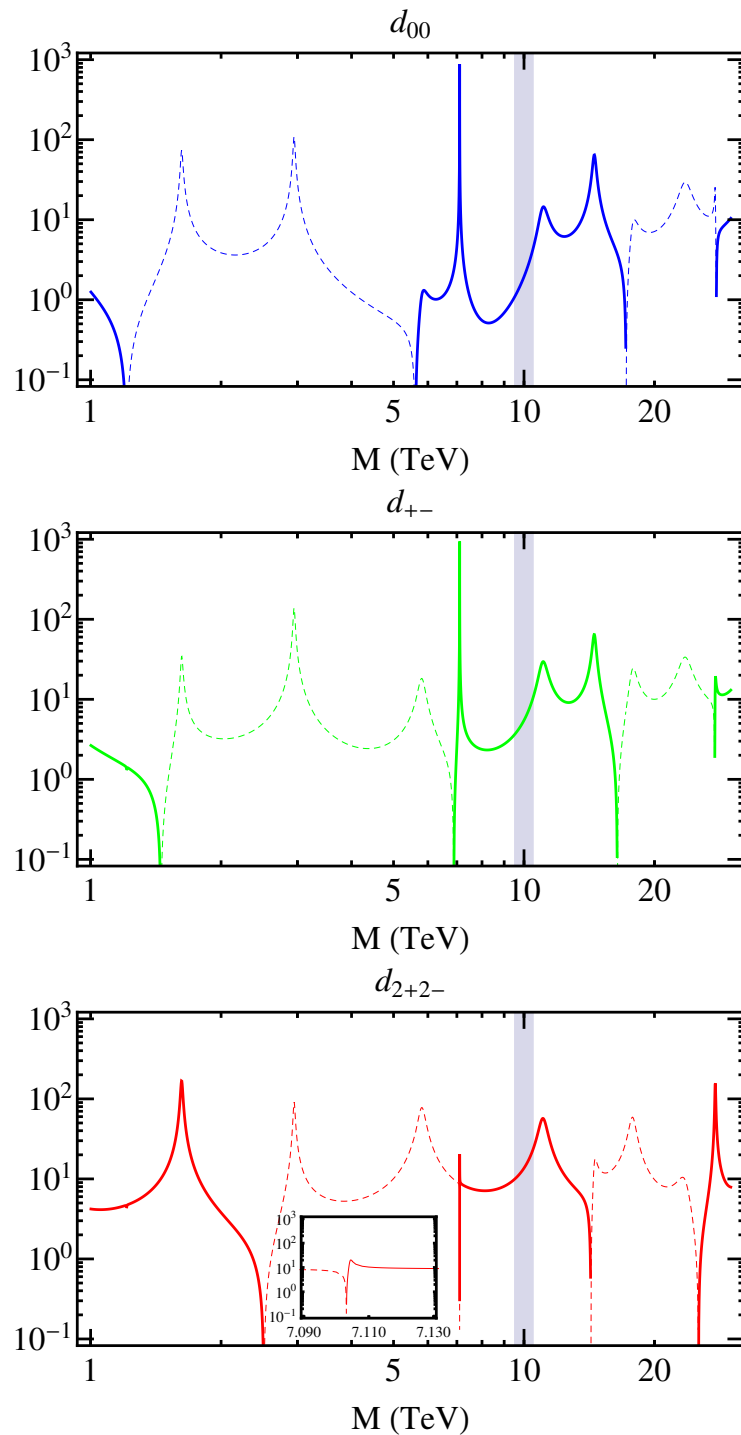


Figure 5.21: Sommerfeld enhancement factors for the 5-plet, where the solid (dashed) line denotes positive (negative) values. The mass for which the correct relic abundance is obtained via freeze-out [317] is indicated by the gray band.

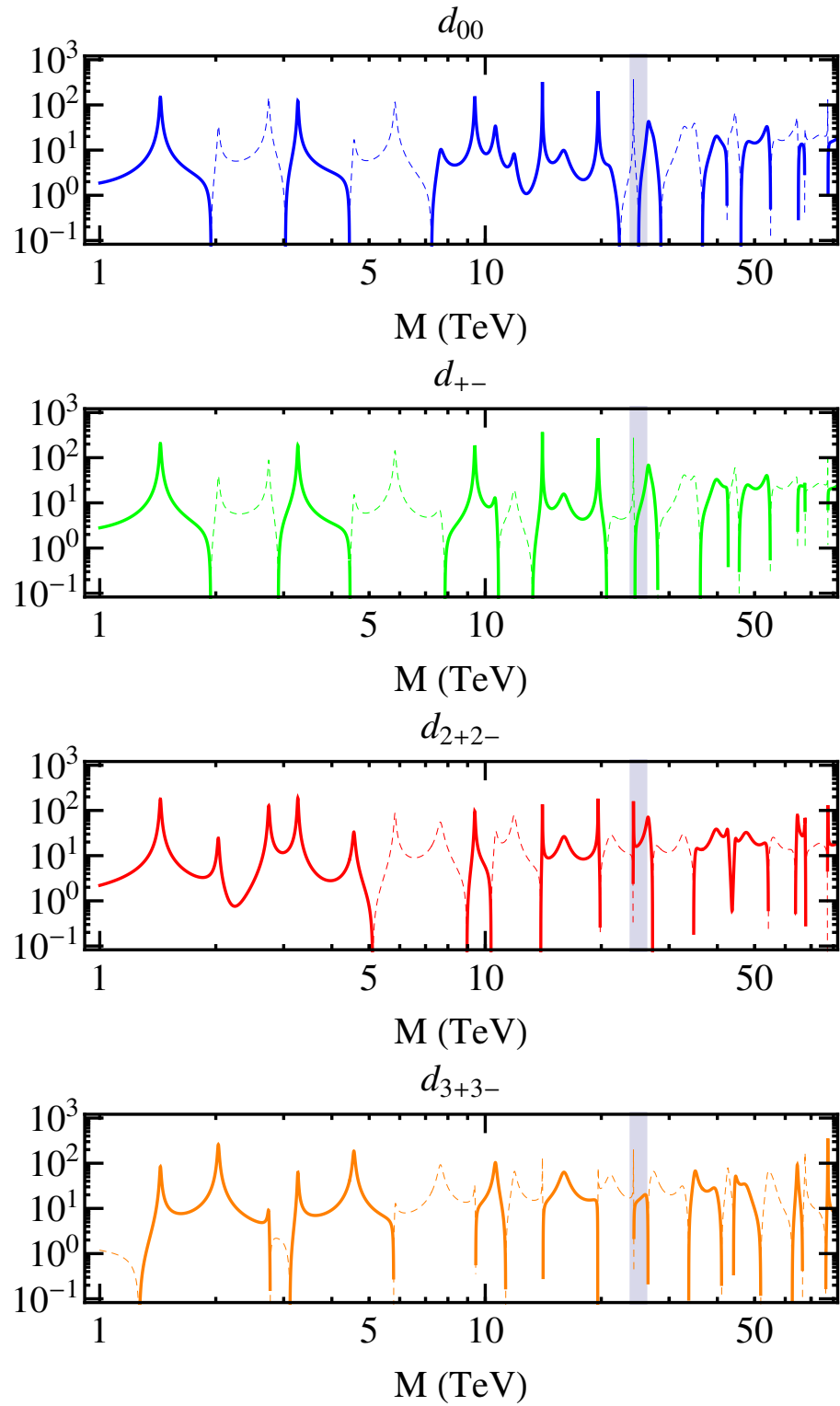


Figure 5.22: Same as Fig. 5.21, but for the 7-plet.

In this work we take into account the  $\gamma\gamma$ ,  $W^+W^-$ ,  $\gamma Z$ , and  $ZZ$  two body final states. For the 5-plet the two former ones are given by

$$(\sigma v_{\gamma\gamma}) = \frac{\xi\pi\alpha^2}{2M^2} |d_{+-} + 4d_{2+2-}|^2 \quad (5.40)$$

$$(\sigma v_{W^+W^-}) = \frac{\xi\pi\alpha_W^2}{4M^2} \left| 3\sqrt{2}d_{00} + 5d_{+-} + 2d_{2+2-} \right|^2, \quad (5.41)$$

while for the 7-plet they read

$$(\sigma v_{\gamma\gamma}) = \frac{\xi\pi\alpha^2}{2M^2} |d_{+-} + 4d_{2+2-} + 9d_{3+3-}|^2 \quad (5.42)$$

$$(\sigma v_{W^+W^-}) = \frac{\xi\pi\alpha_W^2}{4M^2} \left| 6\sqrt{2}d_{00} + 11d_{+-} + 8d_{2+2-} + 3d_{3+3-} \right|^2. \quad (5.43)$$

Here,  $\xi = 1$  for Majorana dark matter and  $\xi = 2$  for scalar dark matter. In Fig. 5.23 the annihilation cross sections into  $W^+W^-$  and  $\gamma\gamma$  final states are shown as a function of the dark matter mass  $M$ . The  $\gamma Z$  and  $ZZ$  cross sections can be obtained from the  $\gamma\gamma$  cross section via

$$(\sigma v)_{ZZ} = \frac{(\sigma v)_{\gamma\gamma}}{\tan^4 \theta_W}, \quad (\sigma v)_{\gamma Z} = \frac{2(\sigma v)_{\gamma\gamma}}{\tan^2 \theta_W}. \quad (5.44)$$

Indeed, dips are observed for instance for the 5-plet at  $\sim 2.4$  TeV in the  $\gamma\gamma$  cross section, which result from cancellations in the annihilation cross section. This behavior has been dubbed Ramsauer-Townsend effect and was also noted in Ref. [320] for the minimal dark matter multiplets under consideration here. We checked that the position of these dips does not change significantly with the dark matter velocity. Thus, when the full velocity distribution is taken into account, the overall picture would not change, even though the peaks are expected to be smeared out after the thermal averaging.

In addition to the four two body final states, we consider internal bremsstrahlung. The differential cross sections for the  $W^+W^-\gamma$  three body final state reads

$$\begin{aligned} \frac{d(\sigma v)_{WW\gamma}}{dE_\gamma} &= \frac{\xi}{128\pi^3 M^2} \int_{E_{W^+}^{\min}}^{E_{W^+}^{\max}} \left| \frac{1}{\sqrt{2}} d_{00} \mathcal{M}(\text{DM DM} \rightarrow W^+W^-\gamma) \right. \\ &\quad \left. + \sum_i d_{i+i-} \mathcal{M}(\text{DM}^{i+} \text{DM}^{i-} \rightarrow W^+W^-\gamma) \right|^2 dE_{W^+}. \end{aligned} \quad (5.45)$$

The differential cross section for all final states under consideration are shown in Fig. 5.24. Here the spectrum for the  $\gamma\gamma$  and  $\gamma Z$  final states is taken as a Gaussian whose width is given by the instrumental resolution. The continuous gamma-ray spectra from annihilations into  $W^+W^-$  and  $ZZ$  is given by Eq. (4.4).

### 5.3.4 Constraints

In the following, we present the gamma-ray constraints from spectral features but also from the gamma-ray continuum from the H.E.S.S. measurements. Prospects for the CTA limits are also derived.

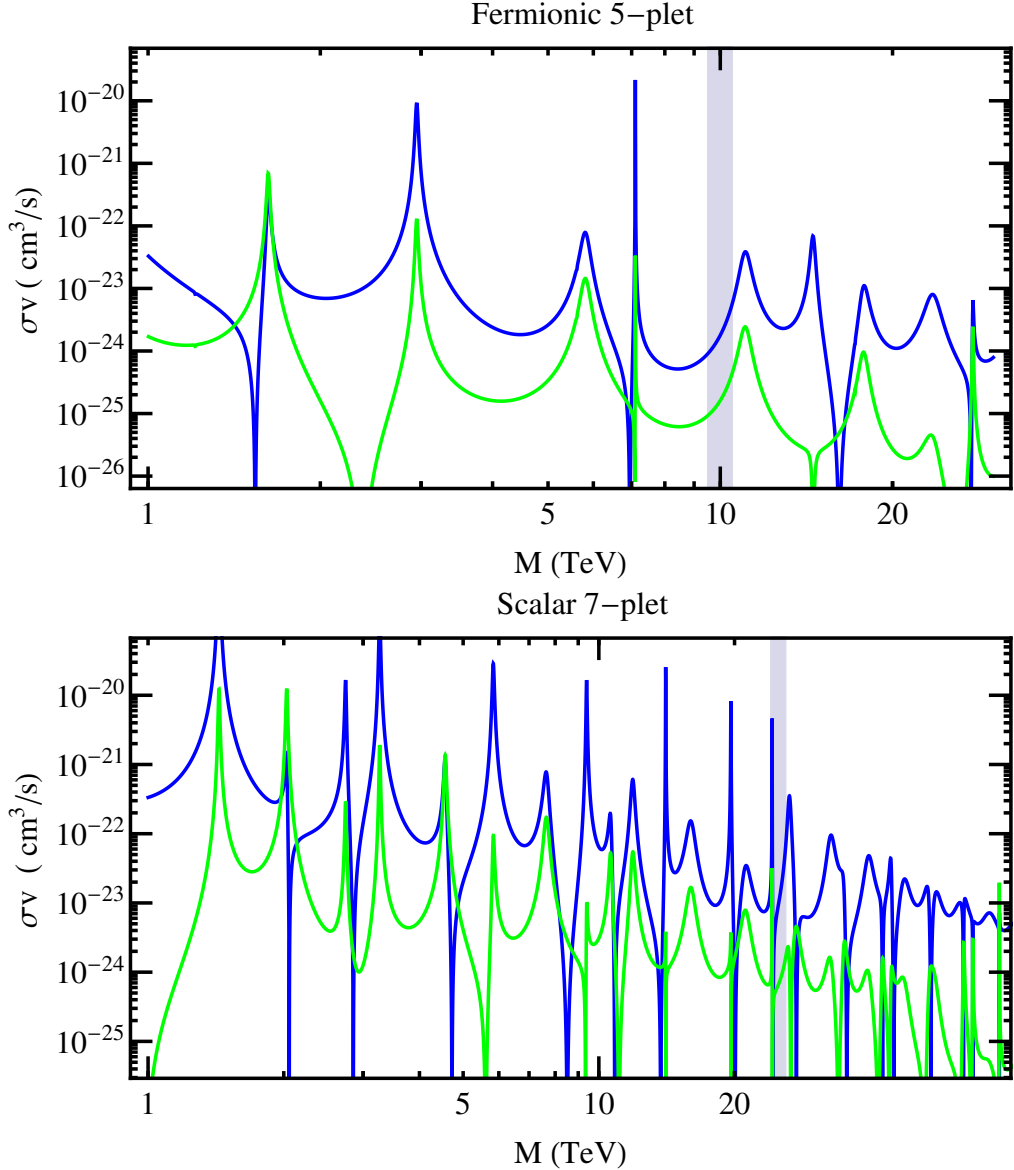


Figure 5.23: Dark matter annihilation cross sections into  $W^+W^-$  (blue line) and  $\gamma\gamma$  (green line) for the fermionic 5-plet (upper panel) and the scalar 7-plet (lower panel).

First, gamma-ray constraints from the H.E.S.S. data in the GCH region are computed for the Einasto and the isothermal profile. For the gamma-ray continuum from  $W^+W^-$  and  $ZZ$  we consider the residual flux obtained with the “on-off region” technique. As discussed in Sec. 5.1.1.2 this approach is only applicable for cuspy profiles and as a consequence only the results for the Einasto profile are shown in this case. Following the approach described in Sec. 5.1.1.2, we compute the 95% CL upper limit on the gamma-ray continuum flux. In addition, we compute the constraints for both profiles for the sharp gamma-ray spectral features that arise in the minimal

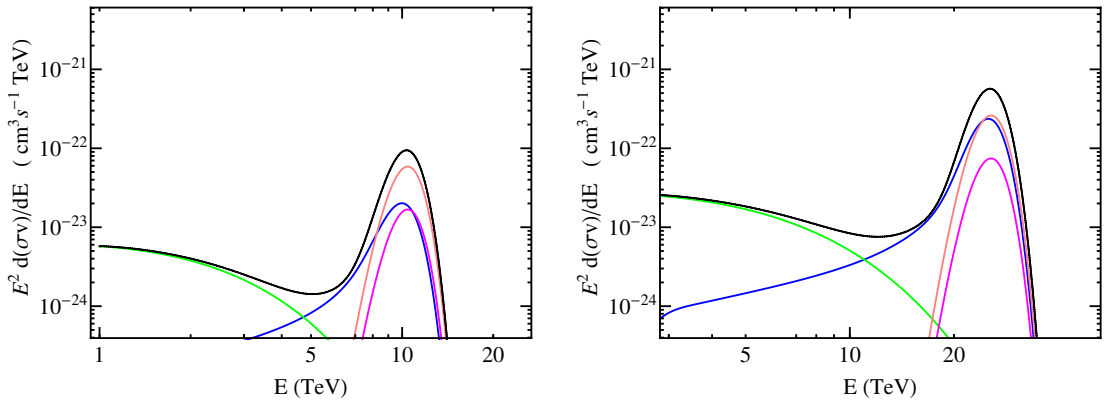


Figure 5.24: Differential annihilation cross sections into  $\gamma\gamma$  (magenta line),  $\gamma Z$  (pink line),  $W^+W^-\gamma$  (blue line) and continuum gamma-rays from  $ZZ$  and  $W^+W^-$  (green line). The total differential cross section is depicted by the black line. In the figure, a dark matter mass of 10 TeV is assumed for the 5-plet (left panel) and a mass of 25 TeV for the 7-plet (right panel). We consider an energy resolution of 10%, which is typical for current gamma-ray telescopes.

dark matter framework for  $\gamma\gamma$ ,  $\gamma Z$  and  $W^+W^-$  final states following the method described in Sec. 5.1.1.1. In particular, the constraints are calculated for the sum of the gamma-ray fluxes in all three channels, but also from gamma-ray monochromatic lines only, discarding the internal bremsstrahlung.

In Figs. 5.25 and 5.26 our results are shown for the fermionic 5-plet and the scalar 7-plet, respectively. The constraints are presented for the dark matter fraction, i.e. the square root of the signal normalization.

The importance of the inclusion of the internal bremsstrahlung is evident from these figures. For those dark matter masses, where the annihilation cross sections exhibit dips (see Fig. 5.23), the corresponding limits show peaks. This means that at these masses the gamma-ray line limits are very weak. This however changes, when internal bremsstrahlung is taken into account. Since its cross section does not exhibit dips at the same masses, the limits from the total spectral feature are very stringent, even at masses that are otherwise only weakly constrained.

In addition, we find that for dark matter masses above  $\sim 1.2$  TeV the constraints from sharp spectral features (including the internal bremsstrahlung) are more stringent than the continuum limits, concretely by a factor of  $1.5 \sim 8.5$  for the fermionic 5-plet and  $1.5 \sim 11$  for the scalar 7-plet.

With the H.E.S.S. measurements dark matter that consists exclusively of 5-plet or 7-plet neutral states can be excluded in the whole mass range for the Einasto profile, i.e. from  $M = 1$  TeV up to  $M = 20$  TeV. This includes in particular the thermal mass value for the 5-plet dark matter candidate. The thermal value of the neutral state of the 7-plet, however, lies beyond

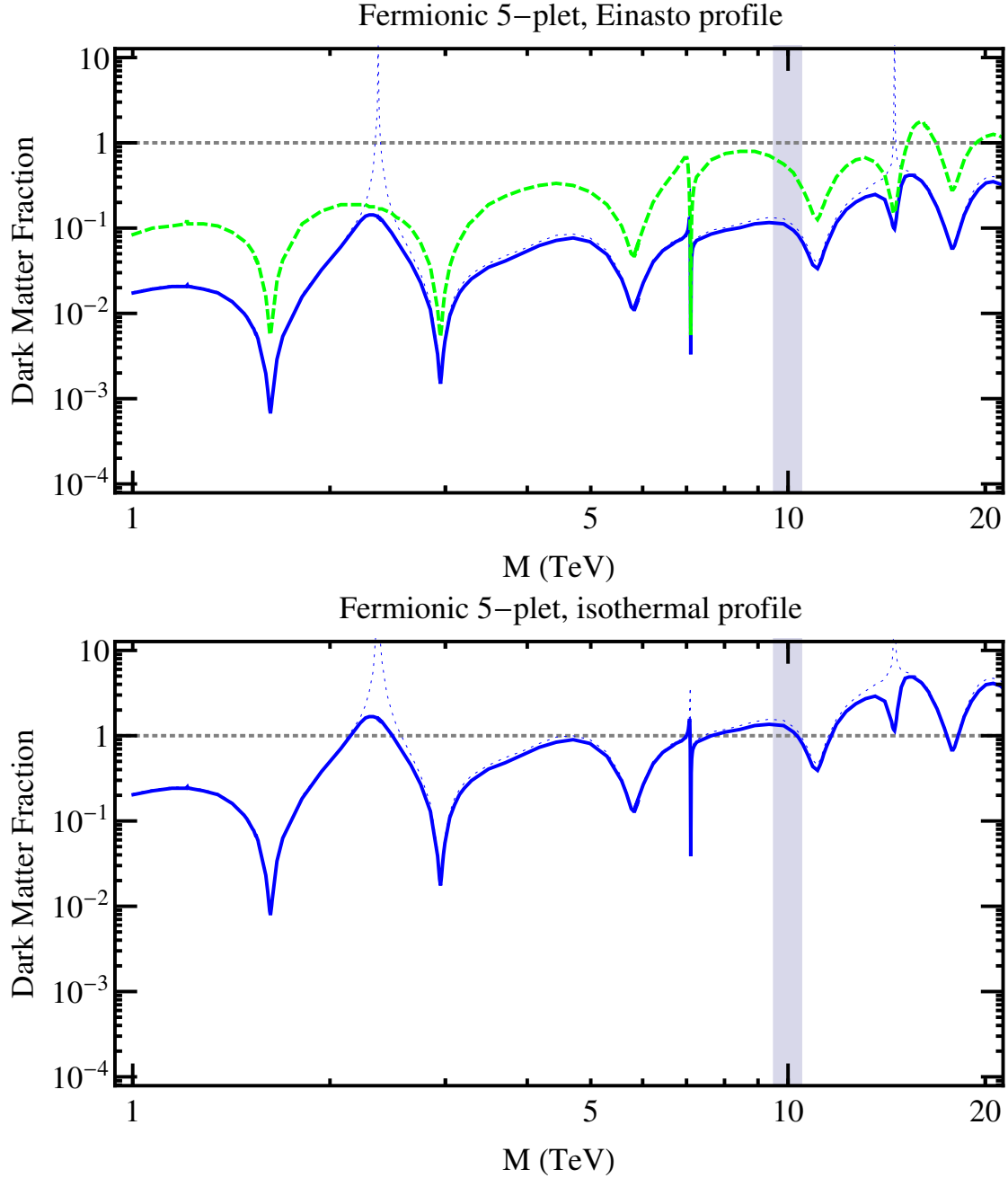


Figure 5.25: 95% CL limits on the dark matter fraction for the fermionic 5-plet from the non-observation by H.E.S.S. of sharp gamma ray spectral features, including (solid blue line) and neglecting (dotted blue line) the internal bremsstrahlung contribution, as well as from the non-observation of the continuum gamma-rays from annihilations into  $W^+W^+$  and  $ZZ$  (green line), assuming the Einasto profile (upper panel) and the isothermal profile (lower panel).

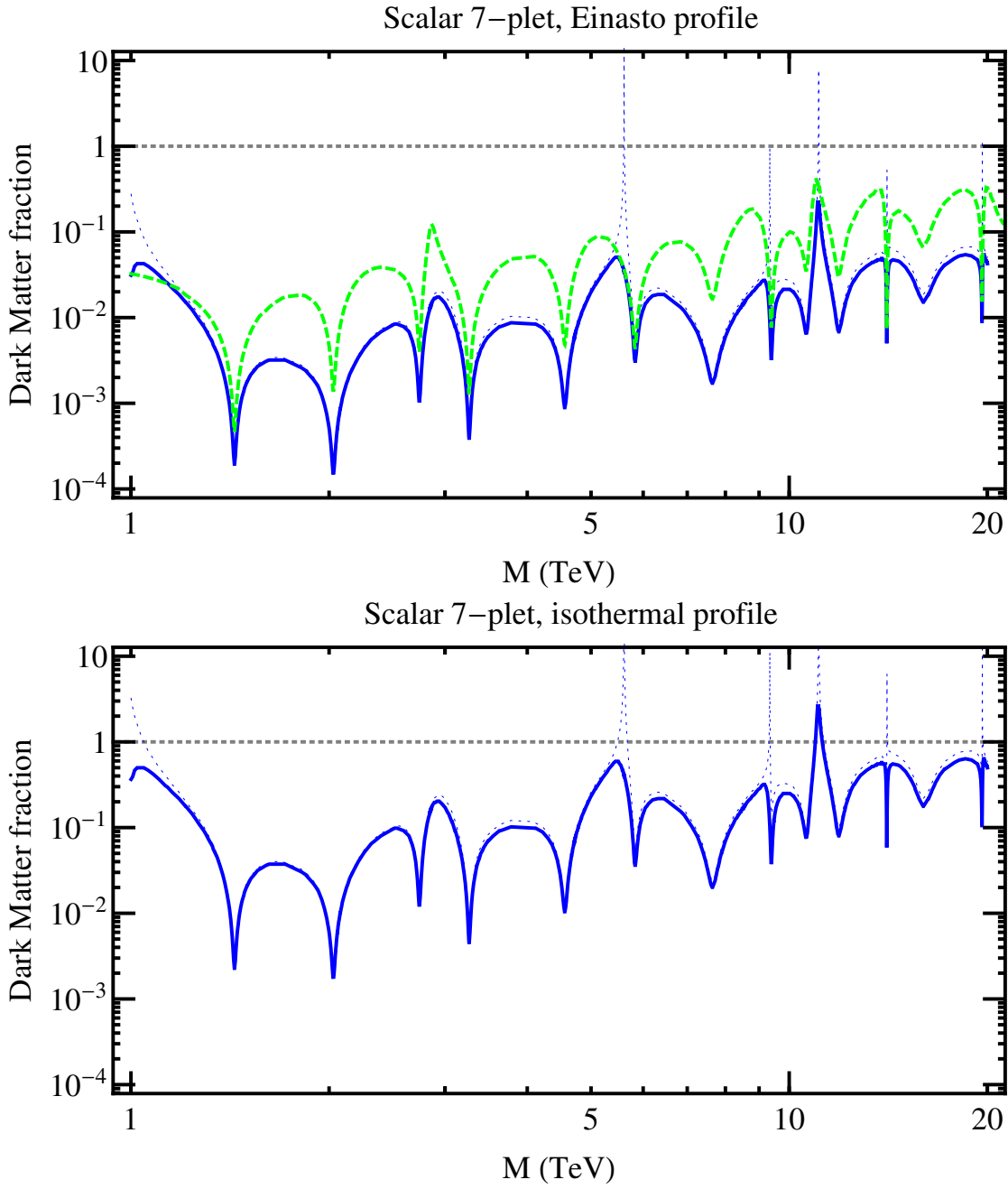


Figure 5.26: Same as Fig. 5.25, but for the scalar 7-plet.

the reach of the H.E.S.S. instrument. The obtained limits are very stringent, excluding a dark matter fraction of  $7 \times 10^{-4}$  ( $1.5 \times 10^{-4}$ ) for the 5-plet (7-plet) at  $M = 1.6$  TeV (2 TeV).

For the isothermal dark matter distribution, the 5-plet cannot be excluded in the whole mass range. In particular, thermally produced 5-plet dark matter remains a viable candidate in this case. The scenario with 100% 7-plet dark matter, on the other hand, is excluded for masses

between 1 and 20 TeV, except for a small mass region around 12 TeV.

We proceed with presenting the prospects for constraining spectral features with CTA. We only consider the sharp features in the following, since they are for almost all masses more constraining than the gamma-ray continuum. The constraints are computed for the GCH region of interest, assuming 112h of observations in order to compare them to the H.E.S.S. limits. Otherwise we employ the base line assumptions and follow the approach presented in Sec. 5.1.2.1. Concretely, we consider for the Einasto and the isothermal profile and the largest possible sliding energy window  $\epsilon_2$ . Throughout, the instrument properties presented in the CTA design study [270] are used. The constraints are presented as the geometric mean of the limits from 200 realizations of mock data, assuming 200 bins per decade  $N_b = 200$ . Again, we show the results for monochromatic lines only together with the limits from the total sharp feature including internal bremsstrahlung. In addition, we overplot the corresponding limits on the total feature from the H.E.S.S. measurements.

The constraints on the dark matter fraction for both dark matter profiles under consideration are presented in Figs. 5.27 and 5.28 for the 5-plet and the 7-plet, respectively. We find that CTA can improve the H.E.S.S. limits on the DM fraction by a factor of  $1.2 \sim 3$ . Using the CTA performance of [276], the limits from line-like gamma-ray features on the dark matter fraction improve up to a factor of 2.8 for low masses and up to a factor of 1.3 above 4 TeV (see Sec. 5.2.1).

In the case of the Einasto profile, dark matter entirely consisting of 5-plet and 7-plet neutral states can be excluded in the whole mass range under consideration in this work, i.e. up to 30 TeV and 75 TeV, respectively. Even for the isothermal profile CTA will be able to exclude 5-plet masses up to 13 TeV and 7-plet masses up to 40 TeV. This includes in particular the thermal masses of the 5-plet and 7-plet. Thus CTA will be able to rule out dark matter that exclusively consists of 5-plet or 7-plet neutral states and that is produced via freeze-out for both cuspy and cored profiles under consideration.

A simultaneous analysis has also studied the 5-plet dark matter candidate [319]. This analysis provides a compilation of the observational constraints on this dark matter model, where other target regions as well as other messengers are considered. Concretely, constraints from diffuse gamma-rays from the whole sky that is divided in various search regions, dwarf galaxies, antiprotons and the LHC are shown in addition to the limits from Galactic center observations. In fact, the limits from the Galactic center are found to be among the most stringent constraints on this model in the energy range of our interest, even without internal bremsstrahlung, which was not included in that analysis. Note that the mass range between 0.1 TeV and 1 TeV 5-plet dark matter is excluded from Fermi observations (7-plet dark matter was not considered in that study).

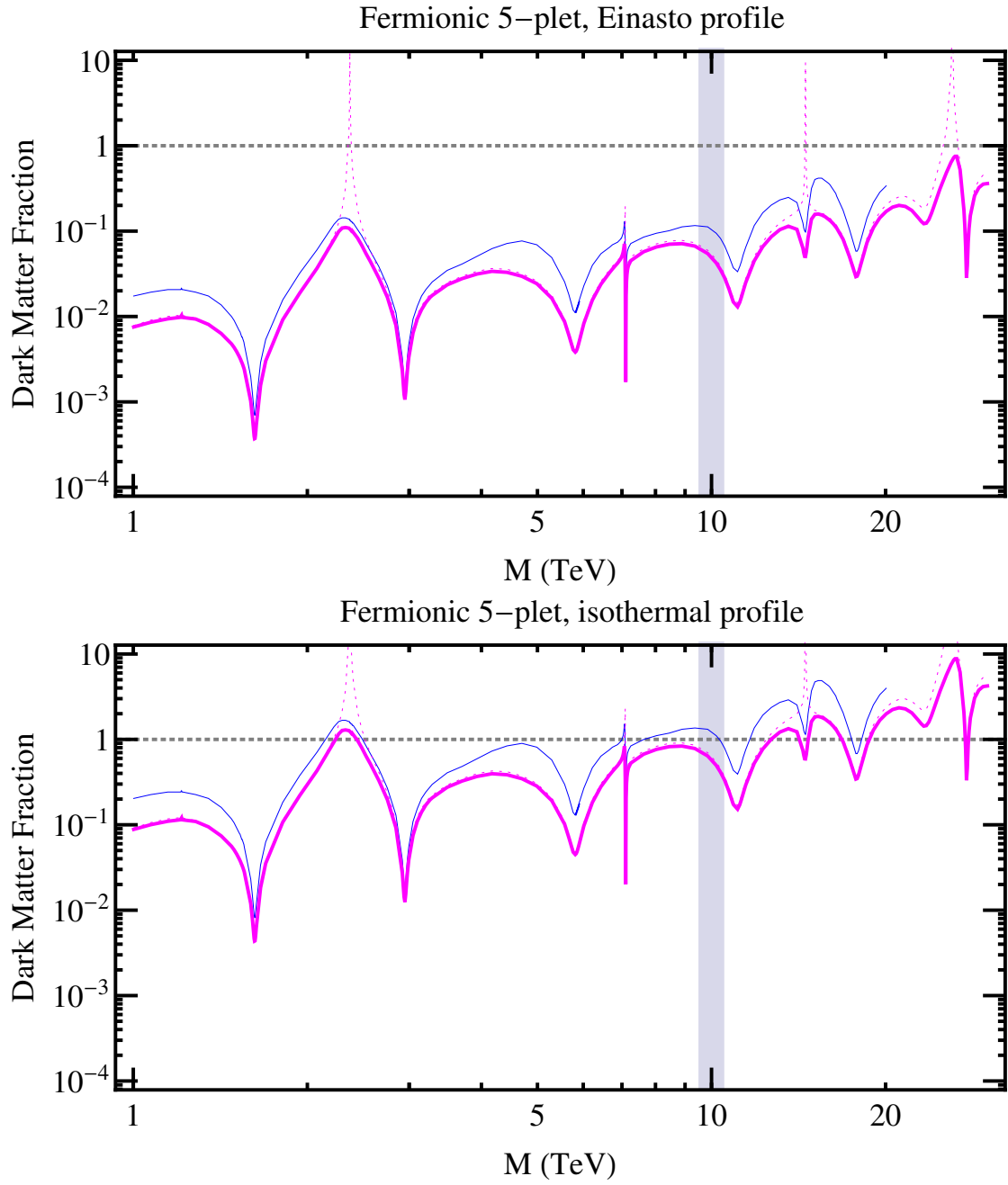


Figure 5.27: 95% CL projected limits on the dark matter fraction for the fermionic 5-plet from sharp spectral features, including (solid magenta line) and neglecting (dotted magenta line) the internal bremsstrahlung contribution. In the upper panel we assume the Einasto profile, in the lower panel the isothermal profile. The current H.E.S.S. limits (solid blue line) are overplotted for comparison.

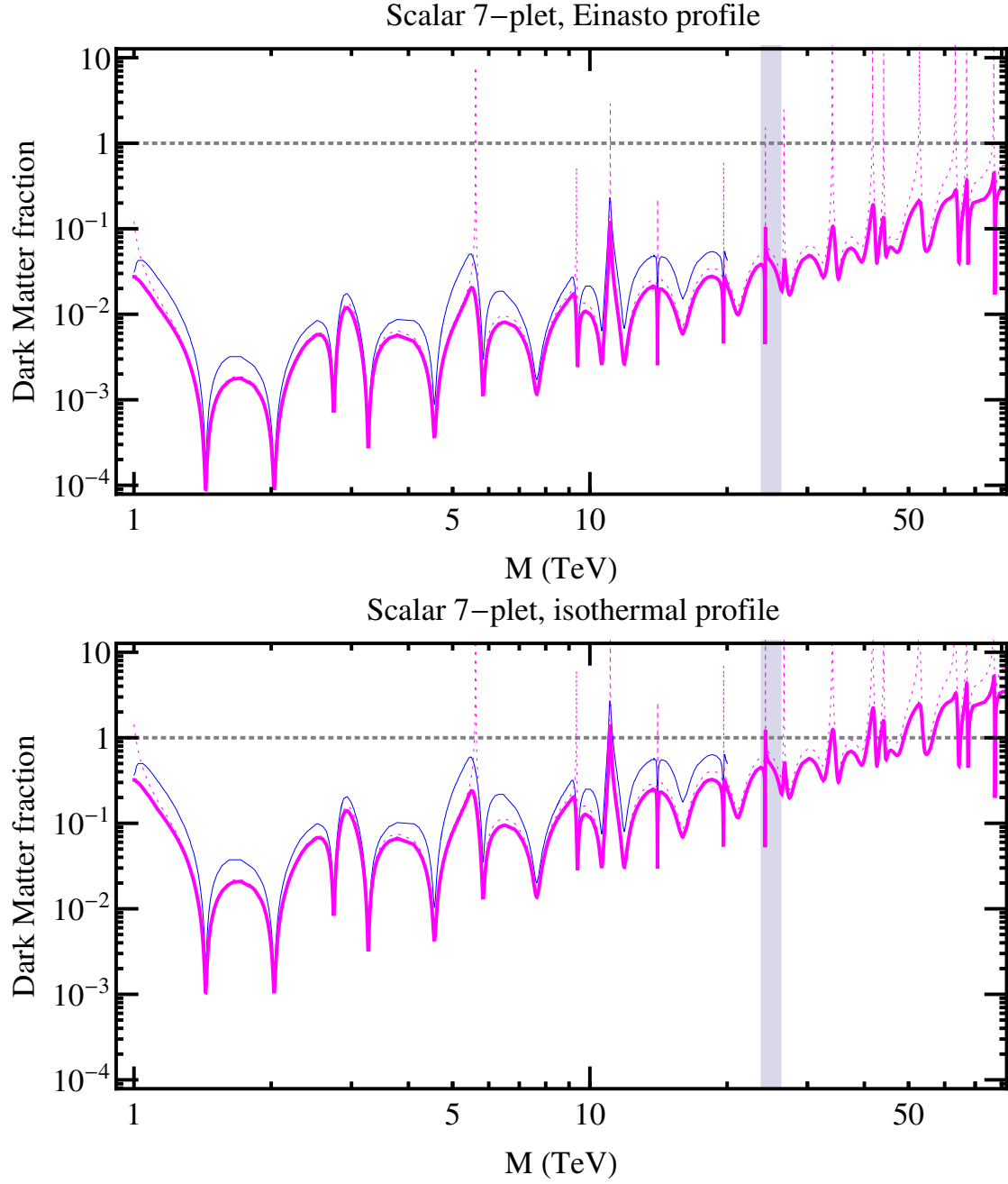


Figure 5.28: Same as Fig. 5.27, but for the scalar 7-plet.

## 5.4 Gamma-ray lines

In this section, the projected constraints from monochromatic gamma-ray lines from the HERD facility onboard China's future space station are presented. First, in Sec. 5.4.1 we show the model-independent limits on the dark matter annihilation cross section and lifetime. In Sec. 5.4.2, the results are applied to the p7MSSM for the  $\gamma\gamma$  and  $\gamma Z$  final states in order to point out their

relevance.

### 5.4.1 Model-independent results

In order to constrain monochromatic gamma-ray lines from dark matter annihilations, we scan dark matter masses from 10 GeV to 1 TeV. For each mass we calculate the profile likelihood in the four regions of interest, R16, R41, R90 and R180, described in Sec. 5.1.2.2 and find the 95% CL upper limit using 300 sets of mock data. In Fig. 5.29 we show the logarithmic mean of the 300 limits obtained for the different optimized ROIs for dark matter annihilations (left panel) and decays (right panel) and the two background templates, p7v6 (with Fermi bubbles) and p6v11 (without Fermi bubbles), assuming 5 years of full-sky survey.

Assuming branching fractions of 100%, we find very stringent limits both for annihilations into  $\gamma\gamma$  and decays with one photon in the final state. Our results are shown in Fig. 5.29. Concretely,

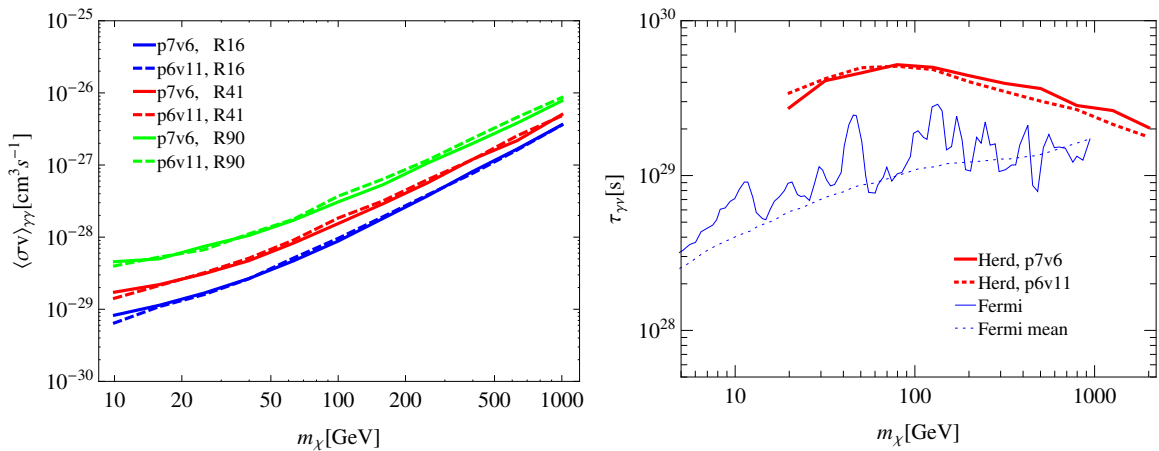


Figure 5.29: Projected 95% CL upper limit on the annihilation cross section into two gammas (left panel) and the lifetime for decays into  $\gamma\nu$  for the two background templates under consideration. We overplot the mean expected as well as the observed limit from 5.8 years of Fermi observations [259]. The dark matter profiles in the case of annihilations correspond to the different regions as described in the text. The limits in the right panel correspond all to the NFW profile.

the limits reach cross sections of  $\sim 6 \cdot 10^{-30} \text{ cm}^3/\text{s}$  to  $\sim 4 \cdot 10^{-29} \text{ cm}^3/\text{s}$  at 10 GeV in the case of annihilations and lifetimes of  $\sim 5 \cdot 10^{29} \text{ s}$  in the case of decays. We obtain very similar results for the two background templates in all three regions. At energies below 15 GeV, the limits drawn from the p7v6 background template, which includes the Fermi bubble, are slightly worse than the limits from the p6v11 template. The largest difference is found for the smallest region R16, in which the bubbles contribute to the flux in all pixels. Concretely, the limits worsen by about 30% at 10 GeV. For the largest region on the other hand, the relative contribution of the bubbles to the total background flux is smaller and thus the effect is weaker.

## 5.4 Gamma-ray lines

The limits obtained for R16 and R90 differ by a factor of  $\sim 5$  at 10 GeV and  $\sim 2$  at 1 TeV. Even though the  $J$ -factors for the three regions are rather similar, the limits differ due to the different background contributions in the various regions. Clearly, the background is larger in the R90 region, leading to worse limits. The difference is larger at low energies, where the electron contribution to the background becomes important (see Fig. 5.5). Since it is isotropic, it scales with the solid angle of the region of interest. At high energies, on the other hand, the anisotropic gamma-ray background dominates, which decreases for increasing latitudes (see Fig. 5.5). Consequently, the difference in the total background and thus in the limits for the different regions becomes smaller.

In the right panel of Fig. 5.30 we present our results in terms of flux upper limits for the different regions. Again, we observe that the behavior of the limits reflects the relative importance of the backgrounds. At low energies the difference in the limits for the four regions is larger compared to high energies, at which the diffuse background dominates.

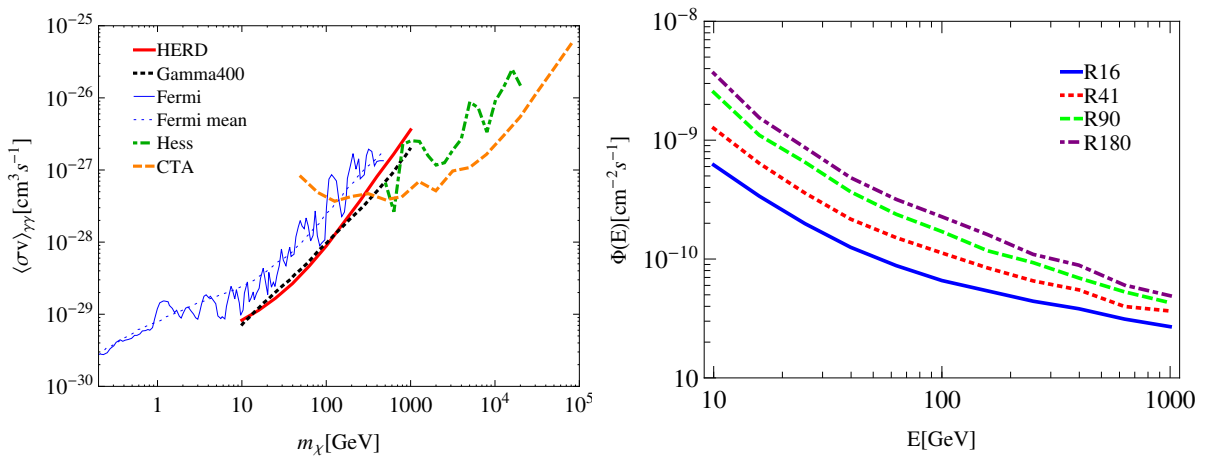


Figure 5.30: Left panel: Comparison of the HERD limits for the R16 region and p7v6 background template with limits the observed and expected limits from 5.8 years of Fermi-LAT observation for the same region, the future satellite Gamma-400, H.E.S.S. and CTA. All limits are shown for the Einasto profile. Right panel: Flux upper limits for the four regions of interest under consideration assuming the p7v6 background template.

Furthermore, we compare our results to limits from other existing and upcoming gamma-ray telescopes in the left panel of Fig. 5.30. All limits are derived for the Einasto profile. We overplot the HERD limits for the p7v6 background template for the R16 region with the observed and expected limits obtained by the Fermi Collaboration [259] for the same region. Furthermore we show the prospects for Gamma-400 for a region around the Galactic center with a radius of  $20^\circ$ , excluding the Galactic plane ( $|l| > 5^\circ$  and  $|b| < 5^\circ$ ) for 5 years of full-sky survey [326]. We also show the limits from 112 h of Galactic center observation with the H.E.S.S. telescopes [258] in the

CGH, a circular  $1^\circ$  region around the Galactic center, excluding  $|b| < 0.3^\circ$  (see Fig. 5.1), and the expected limits [3] for the future Cherenkov telescope CTA. These limits are derived for line-like gamma-ray boxes for the same region and observation time as the H.E.S.S. limits using the sliding energy window technique. In Fig 5.30 the limits are properly rescaled to gamma-ray line limits. Due to its excellent energy resolution, HERD can improve the observed Fermi limits [259] from 5.8 years of observation by up to a factor of  $\sim 7$  in the R16 region, a factor of  $\sim 6$  in the R41 region, and by a factor of  $\sim 5$  in the case of R90. The limits expected from 5 years of observation with HERD and Gamma-400 exclude roughly the same annihilation cross sections. However, the effective area of Gamma-400 and the efficiencies used to derive the constraints seem to be too optimistic [327]. In the energy range from 10 GeV to 300 GeV HERD is expected to give the most stringent limits, whereas at higher energies CTA is expected to be more constraining. For decaying dark matter our HERD constraints are compared to the expected and observed Fermi-LAT limits from 5.8 years of observations in right panel of Fig. 5.29. We find that HERD can improve existing Fermi-LAT limits by a factor of about  $2 - 7$ .

Note, however, that for the HERD limits only statistical errors are taken into account, while in the constraints from 5.8 years of Fermi-LAT observations systematic uncertainties are also included. The comparison with the limits from 3.7 years of Fermi-LAT observation shows the effect on the limits: Even though more data are collected in the 5.8 year data set, the limits that include systematic errors are worse than the limits from 3.7 years of observation. This is especially relevant at low energies, where the statistical errors are smaller and the systematic uncertainties are relatively more important. In the R180 region, this difference amounts to about one order of magnitude at a dark matter mass of 20 GeV [259].

### 5.4.2 Constraining the MSSM

A plethora of dark matter models can produce line-like gamma-ray features. Two such models have been introduced in Secs. 5.2 and 5.3. In this section, we focus on another scenario, the phenomenological Minimal Supersymmetric Standard Model with 7 parameters (p7MSSM) (see also Sec. 2.2.1) in order to illustrate the power of the HERD instrument. The dark matter candidate in this scenario is the lightest neutralino  $\chi_1^0$ , a linear combination of the superpartners of the neutral Standard Model bosons, the higgsinos  $\tilde{H}_u$  and  $\tilde{H}_d$ , the wino  $\tilde{W}$  and the bino  $\tilde{B}$

$$\chi_1^0 = Z_{\text{bino}} \tilde{B} + Z_{\text{wino}} \tilde{W} + Z_{H_u} \tilde{H}_u + Z_{H_d} \tilde{H}_d, \quad (5.46)$$

with the coefficients  $Z_{\text{bino}}$ ,  $Z_{\text{wino}}$ ,  $Z_{H_u}$  and  $Z_{H_d}$ . Via loop processes, this dark matter candidate can annihilate into  $\gamma\gamma$  and  $\gamma Z$ .

In its most general form, the MSSM possesses 124 parameters, 19 corresponding to the Standard Model parameters including  $\theta_{\text{QCD}}$ , and 105 new parameters [29]. For phenomenological studies, however, this large number can be reduced. In the CMSSM, for instance, only 5 new parameters are invoked [328]. In this study, we allow for 7 new parameters, where only the parameters relevant for the dark matter sector are considered, all others are set to some heavy scale in

order to avoid collider constraints. Concretely, the mass parameters of the pseudoscalar Higgs, the wino, the bino and the higgsino,  $m_A$ ,  $M_1$ ,  $M_2$  and  $\mu$ , as well as the ratio of the vacuum expectation values of the two Higgs fields  $\tan \beta$  are taken into account, while the masses of the gluinos ( $M_3$ ), squarks and sleptons are set to a large unified sfermion mass  $m_{\tilde{f}}$  in order to satisfy the stringent LHC constraints on the gluino and squark masses [329]. All trilinear couplings are set to a unique value  $A_0$ . In this scan, the  $\mu$ -term is assumed to be positive,  $\text{sgn}(\mu) = +1$ .

Here, we do not assume that the correct relic density is acquired with the freeze-out mechanism. However, we require that dark matter is not thermally overproduced in the early Universe (see below). When the relic abundance is not fully produced via thermal freeze-out, we assume an additional non-thermal dark matter production mechanism (see Sec. 1.3.2.2) that accounts for the right relic density.

Now, a scan over the 7 parameters is performed in order to identify valid points in the parameter space. The p7MSSM parameters may assume values within the following ranges:

$$\begin{aligned} 3 &< \tan \beta < 62, \\ 10 &< (M_1, M_2, \mu)/\text{GeV} < 4000, \\ 200 &< m_A/\text{GeV} < 8000, \\ \max[M_1, M_2, \mu, m_A, 800.0 \text{ GeV}] &< m_{\tilde{f}} < 8000 \text{ GeV}, \\ M_3 &= m_{\tilde{f}}, \\ -5 &< A_0/\text{TeV} < 5. \end{aligned} \tag{5.47}$$

In addition, experimental constraints listed below are taken into account in the scan:

- The relic density must be compatible with the dark matter energy density from the PLANCK measurement [330]. We require that dark matter is not thermally overproduced and thus  $\Omega_c h^2 \leq 0.1199 + 0.0054$ , which corresponds to the  $2\sigma$  error. An alternative production mechanism must then account for the correct relic density today.
- In order to be in agreement with constraints from LEP, the chargino masses are required to be greater than 103.5 GeV [331].
- The value of the Higgs mass is constrained with the most recent results from the combined analysis from ATLAS and CMS  $m_H = 125.09 \pm 0.21 \text{ (stat.)} \pm 0.11 \text{ (syst.)} \text{ GeV}$  [332]. In addition to the experimental error, a theoretical uncertainty of 2 GeV is taken into account.
- For dark matter masses close to the  $Z$  and Higgs mass, the contribution to their invisible decays may not exceed the experimental bounds  $\Gamma_Z(\text{invisible}) = 499.0 \pm 1.5 \text{ MeV}$  [29] and  $\text{BR}(H \rightarrow \text{inv}) = 0.17 \pm 0.17$  [333].
- The supersymmetric sector is further constrained by the measurements of  $b \rightarrow s\gamma$  with  $\text{BR}(b \rightarrow s\gamma) \times 10^4 = 3.43 \pm 0.22 \pm 0.21$  [334] and  $B_s \rightarrow \mu^+ \mu^-$  with  $\text{BR}(B_s \rightarrow \mu^+ \mu^-) \times 10^9 = 2.9 \pm 0.7$  [335]. In the case of  $B_s \rightarrow \mu^+ \mu^-$  a theoretical uncertainty of 10% is considered.

- Lastly, constraints from direct dark matter searches are included. The bound on the spin-independent neutron and proton cross section is adopted from the LUX [283]. The spin-dependent interactions with protons are constrained by PICO-2L [336], while the XENON100 experiment provides limits on the dark matter interactions with neutrons [337].

The methodology of the scan and the packages used for the computation of the different observables is presented in Ref. [338] and references therein. For the Higgs decay, which was not taken into account in that reference, the HDECAY package [339] is used. Finally, the annihilation cross sections into  $\gamma\gamma$  and  $\gamma Z$  are calculated for all the points in parameter space that are compatible at  $2\sigma$  with all constraints listed above. The results are shown in Fig. 5.31, where the points are classified according to their linear combinations of different neutralinos. Concretely, the fraction of a certain neutralino component is given by  $g_i$  where  $i$  refers to bino,

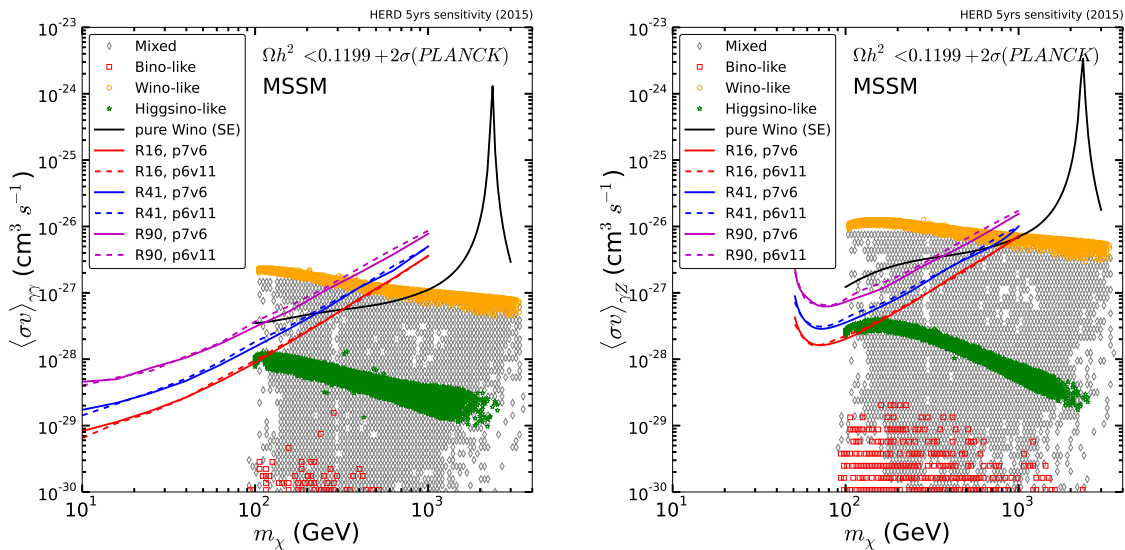


Figure 5.31: The points in parameter space that are compatible with observations at the  $2\sigma$  level. The red squares indicate bino-like, the orange cycles wino-like, the green stars higgsino-like and the gray diamonds mixed neutralinos. The Sommerfeld enhancement for pure wino ( $g_{\text{wino}} = 1$ ) dark matter is shown by the black line. The colored solid (dashed) lines depict from top to bottom the limits from 5 years of HERD observations on the  $\gamma\gamma$  (left panel) and  $\gamma Z$  annihilation cross section using the p7v6 (p6v11) background template.

wino, or higgsino. These parameters are related to the coefficients of Eq. (5.46) by  $g_{\text{bino}} = Z_{\text{bino}}^2$ ,  $g_{\text{wino}} = Z_{\text{wino}}^2$ , and  $g_{\text{higgsino}} = Z_{H_u}^2 + Z_{H_d}^2$ . A dark matter candidate is defined as bino-, wino- or higgsino-like when the corresponding fraction is  $g_i > 0.95$ . Neutralinos that correspond to other values of  $g_i$  are dubbed mixed neutralinos. In Fig. 5.31 the different neutralino classes are depicted with different colors.

Let us first describe the nature of the surviving points in the scatter plot for the annihilations into  $\gamma\gamma$  and  $\gamma Z$ . Since essentially the same Feynman diagrams contribute to the two annihilation processes, where in the  $\gamma Z$  case one photon is exchanged with a  $Z$ -boson [6], both plots look very similar. Due to the different couplings of the photon and the  $Z$  boson, the  $\gamma\gamma$  annihilation is a factor of a few smaller than the annihilations into  $\gamma Z$ . In addition, since the  $Z$  can be attached at the position of each of the two photons in the  $\gamma\gamma$  process, there are more diagrams contributing to the  $\gamma Z$  annihilation.

Furthermore, we observe a hierarchy in the annihilation cross section according to the neutralino classification: The annihilation cross section of the bino-like neutralino is lowest, while the wino-like cross section is largest. This can be understood as follows: The bino does not couple to the  $SU(2)_L$  gauge bosons and their superpartners and therefore there are fewer diagrams that contribute to the bino annihilations. In addition, the heavy sfermions suppress the bino cross sections. Furthermore, there are important diagrams that only exist for pure wino neutralinos (with W-bosons and charginos in the loop), but that do not exist for the pure higgsino. This makes the cross section of wino-like neutralinos larger than the cross section for higgsino-like dark matter.

In addition, we find that only neutralinos with masses  $m_\chi \gtrsim 100$  GeV survive all the constraints. This happens because, generally speaking, the neutralino annihilation cross section is very small in the parameter space under consideration, where the sfermions are heavy, leading to dark matter overproduction in the early Universe. However, there are scenarios in which the total annihilation cross section is enhanced and the relic abundance gets reduced. Typically, one can distinguish three cases: the focus point region, resonances and co-annihilations. Firstly, the focus point region is a particular region in parameter space featuring large annihilation cross sections into  $W^+W^-$ ,  $ZZ$  and  $Zh$  [340], which can reduce the relic density. Despite the enhancement of the annihilation cross section when these channels are kinematically allowed, the cross section is not yet large enough to reduce the relic density to the observed value. Secondly, co-annihilations are important when other supersymmetric particles exhibit similar masses as the lightest neutralino. Then, additional processes involving these particles in the initial state contribute to the annihilation and the relic density increases. Possible sparticles that can co-annihilate with the lightest neutralino are charginos, other neutralinos, gluinos or sfermions. However, the sfermion co-annihilation is neglected in this scan. On the one hand, since the sfermion masses  $m_{\tilde{f}}/\text{GeV} > \max[M_1, M_2, \mu, m_A, 800.0]$  and our energy range of interest is  $10 \text{ GeV} < E < 1 \text{ TeV}$ , they can only contribute in a rather small neutralino mass range. In addition, the points where the sfermion co-annihilations reduce the relic density below the observed value exhibit a very small annihilation cross section into monochromatic gamma-rays that lies well below the reach of HERD. Thirdly, resonances can occur, when the  $Z$ -boson, the Standard Model-like Higgs, the pseudoscalar or the heavy Higgs appear in an s-channel diagram, and the sum of the masses of the annihilating particles equals the mass of the s-channel mediator. This can not only reduce the relic density for direct neutralino annihilations, but also in the case

of co-annihilations. In the case of the  $Z$ -boson resonance, the annihilation into monochromatic gammas today is very small because it is p-wave suppressed. The Higgs resonance is only important in the early Universe, but does not enhance the  $\gamma\gamma$  or  $\gamma Z$  cross sections today [6]. The pseudoscalar and heavy Higgs resonances, however, are very important in this scan, and contribute basically for all surviving points in parameter space. The pseudoscalar Higgs resonance can also contribute to the large annihilation cross section of wino-like neutralinos today. The black line in Fig. 5.31 indicates the Sommerfeld enhanced pure wino cross section. For simplicity, Sommerfeld enhancement is not included in the scan and the pure wino cross section is just indicated for reference. The enhancement of the wino-like cross section due to the admixture of higgsinos and the pseudoscalar Higgs resonance is the reason why the wino-like neutralinos without Sommerfeld enhancement can exhibit a larger cross section than the Sommerfeld enhanced cross section of the pure wino.

Fig. 5.31 shows that 5 years of HERD observations can probe the remaining p7MSSM parameter space. Concretely, the wino-like region is constrained below a few hundred GeV. In addition, the HERD limits can cut out a fraction of the parameter space for mixed neutralinos and even start to probe the higgsino-like dark matter candidates. Bino-like dark matter candidates, however, lie beyond the reach of the HERD instrument. We find that for the points in parameter space in the reach of HERD dark matter is typically underproduced, while the correct relic density can be acquired for points featuring low cross section and/or very massive neutralinos. Since not only the annihilation into monochromatic gamma-rays but also the cross sections of other annihilation channels are enhanced, and the cross section into monochromatic photons is loop suppressed, also complementary indirect detection constraints, for instance the Fermi-LAT limits from dwarf galaxies [221], can be important. However, since the aim of this scan is to provide an illustration for the constraining power of the HERD instrument, this is not further investigated here.

# Conclusions

In this thesis dark matter searches for spectral features with positrons and gamma rays were studied. This method is very promising since sharp features can be very well discriminated against the smooth astrophysical background.

It was shown that the exquisite electron and positron measurements from the AMS-02 experiment allow constraining severely dark matter annihilations and decays. In this work, we used for the first time the positron flux in order to derive dark matter constraints. In our analysis, we used a well motivated physical background model for the positron flux. Concretely, we modeled the background above 2 GeV as the sum of two components: i) the secondary positrons, which can be described by a simple power law and ii) an additional source, parameterized as a power law with an exponential cut-off, which is generically expected from astrophysical positron sources. The flux at the top of the atmosphere was computed using the force field approximation. To this background we added the signal from dark matter annihilations or decays for the  $e^+e^-$ ,  $\mu^+\mu^-$ ,  $\tau^+\tau^-$ ,  $b\bar{b}$  and  $W^+W^-$  final states and perform a  $\chi^2$  fit to the data. Our constraints could be optimized by sampling over various energy windows: We computed the limits from 53 energy windows of different sizes and then chose the most stringent limit for each dark matter mass. The obtained limits are very strong and competitive to those from the positron fraction. In the channels that produce sharp features, the thermal mass could be probed. In particular, thermal dark matter is excluded below 100 GeV in  $e^-e^+$  and below 60 GeV in  $\mu^+\mu^-$  channel. We demonstrated that our limits are very robust because they do not depend significantly on the propagation model or the chosen halo profile. Comparing our results to limits from other positron experiments, PAMELA and HEAT, we showed that the best limits are obtained from the AMS-02 measurements. However, already the HEAT data taken about 20 years ago allowed setting strong constraints, in particular in the  $e^+e^-$  channel. We further confronted the limits to gamma-ray limits derived from Fermi-LAT data. We found that positron limits are competitive and in some channels stronger than the gamma-ray constraints.

Furthermore, we derived constraints on gamma-ray spectral features. To this end we calculated limits for existing as well as future experiments. On the one hand we computed limits from the current experiment H.E.S.S. using a  $\chi^2$  fit of the background model presented by the H.E.S.S. Collaboration, to which we added the dark matter signal. On the other hand, we considered the future experiments CTA and HERD, making use of realistic projections of the instrument performance. Here we first generated mock data for physical background consisting of the gamma-ray and misidentified cosmic rays. We identified the maximally allowed window for the sliding energy window method and apply this technique in order to derive constraints.

Concretely, we performed a maximum likelihood analysis, where we assumed, in addition to the dark matter signal, a simple power law background within the sliding energy window. The chosen target regions depend on the instrument: For the Cherenkov telescopes we focused on the Galactic center region, whereas for the space based HERD instrument we employed optimized search regions derived by the Fermi Collaboration, which differ for the various halo profiles.

Concretely, we considered three different kinds of gamma-ray spectral features: monochromatic gamma-ray lines, internal bremsstrahlung and gamma-ray boxes. For the latter, prospects for the expected limits and sensitivity were derived for CTA. We computed constraints for narrow, intermediate and wide boxes. Indeed, CTA will deliver stringent constraints, when a branching fraction of 100% is assumed. In order to test the robustness of our results we varied different assumptions with respect to our base line analysis. We found that the constraints depend rather strongly on the chosen sliding energy window size, the dark matter profile and the assumed instrument performance. Taking into account the optical depth of the Milky Way weakens the limits only by about 20% at highest energies. Compared to Fermi-LAT and H.E.S.S., we found that CTA will supersede the limits from those experiments, depending on the instrument properties, in the energy range from a few hundred GeV to TeV energies. We furthermore confronted our results with concrete particle physics models that feature gamma-ray boxes. In fact, CTA will be able to rule out or discover thermal WIMPs up to masses of tens of TeV, especially in scenarios with wide boxes. This is indeed a golden opportunity for CTA since no other instrument will be able to access this mass range in the near future.

The internal bremsstrahlung feature was investigated in minimal dark matter models, where the Standard Model is extended by an extra  $SU(2)_L$  doublet. This class of models is theoretically very attractive because only one new parameter has to be introduced. In particular, we considered the fermionic 5-plet and the scalar 7-plet, which are automatically stable at the renormalizable level, and for which the Sommerfeld effect, i.e. the multiple exchange of weak gauge bosons, leads to an enhancement of the annihilation cross sections. We investigated the constraints from the current H.E.S.S. experiment and the prospected limits from the future CTA instrument for a wide mass range from 1 TeV to about three times the thermal mass value of the multiplet under consideration, taking into account the internal bremsstrahlung feature in addition to the gamma-ray line produced in annihilations into  $\gamma\gamma$  and  $\gamma Z$ , but also continuum gamma rays originating from the  $W^+W^-$  and  $ZZ$  final states. Above 1.2 GeV and up to 20 TeV, which is the reach of the H.E.S.S. experiment, the H.E.S.S. limits from spectral features are more stringent than those from the continuum gamma rays. When the internal bremsstrahlung is included a dark matter fraction of 100% is excluded for otherwise unconstrained mass regions. Assuming the Einasto profile, the H.E.S.S. measurements can rule out dark matter consisting exclusively of 5-plet or 7-plet neutral states, which includes thermally produced 5-plet dark matter. For the isothermal profile, thermally produced 5-plet dark matter is still allowed, and the thermal 7-plet lies beyond the reach of the H.E.S.S. experiment. CTA, on the other hand, will be able to improve the H.E.S.S. limits on the dark matter fraction by a factor of 1.2 to 3 and to rule out 5-

and 7-plet dark matter up to 30 TeV and 75 TeV, respectively. Even for the isothermal profile, CTA will be able to probe dark matter consisting exclusively of thermal 5- and 7-plet neutral states.

Lastly, prospects for the sensitivity of the HERD instrument to gamma-ray lines were computed for dark matter annihilations and decays. Concretely, we employ optimized search regions for the Einasto, NFW and isothermal profile. We found that current bounds from Fermi-LAT for the same regions of interest can be improved by up to a factor of  $\sim 7$ , both for annihilations and decays. In addition, we confronted our results with current limits from H.E.S.S. and projected limits from the future instruments CTA and Gamma-400. In fact, HERD and Gamma-400 will deliver competitive limits, whereas below a few hundred GeV the HERD constraints supersede those from the Cherenkov telescopes. In addition, we investigated the power of HERD to constrain the parameter space of the MSSM with 7 parameters. We showed that the HERD constraints can probe a corner of the parameter space that cannot be excluded with other experiments.

All things considered, dark matter identification remains a highly interesting challenge. We showed that the search for sharp spectral features in the positron and gamma-ray fluxes will play an important role in this process. Even though a phenomenological approach to the background parameterization allows setting stringent limits on the dark matter properties, the understanding of the astrophysical contributions to the fluxes of the dark matter messengers is crucial. Further investigation and better insight into positron sources and the gamma-ray sky can help to discover a dark matter contribution in the astrophysical fluxes or to robustly rule out further regions in the dark matter parameter space. In addition, a better knowledge of the backgrounds will allow defining optimized search regions for future experiments and to further improve the search strategies. At the same time, systematic effects of the instruments on the one hand and the background on the other hand must be carefully studied and taken into account in the dark matter search in order to obtain robust results on the properties of the dark matter particle.

However, a signal in one channel does not allow us to pin down all dark matter properties and identify the correct underlying particle physics model. Eventually, signatures from various indirect detection channels, direct and collider searches must give a consistent picture in order to ultimately reveal the nature of dark matter.



# Appendix A

## Statistical Methods

In the following the statistical methods that are used in this thesis are presented. We review how the goodness-of-fit can be evaluated, upper limits on dark matter parameters can be derived and how the background hypothesis can be rejected in case of a signal. In large parts, this discussion follows [341].

### A.1 $\chi^2$ -distribution and goodness-of-fit

The need to quantify how well a fit function describes given data often arises in science. A method that is commonly used exploits the  $\chi^2$ -distribution. This distribution is given by

$$f(z; n) = \frac{1}{2^{n/2}\Gamma(n/2)} z^{n/2-1} e^{-z/2}, \quad (\text{A.1})$$

where  $n = 1, 2, 3, \dots$  is the number of degrees of freedom and the  $\Gamma(x)$  is the  $\Gamma$ -function that reads  $\Gamma(n) = (n - 1)!$  for integer  $n$ . In Fig. A.1 the  $\chi^2$ -distribution is shown for several values of  $n$ . The reason why this distribution is crucial for the determination of the goodness-of-fit is the following: The random variable  $z$

$$z = \sum_{i=1}^N \frac{(x_i - \mu_i)^2}{\sigma_i^2} \quad (\text{A.2})$$

for  $N$  Gaussian random variables  $x_i$  with means  $\mu_i$  and standard deviations  $\sigma_i$  is distributed according to the  $\chi^2$ -distribution with  $N$  degrees of freedom. In the case of  $N$  data points  $x_i$  with Gaussian errors  $\sigma_i$  this is used to compare the data to a prediction  $\mu_i$ . If this is a function of  $m$  model parameters  $\mu_i(\theta_1, \dots, \theta_m)$  and the random variable  $z$  is minimized with respect to the latter parameters, then  $z$  is distributed according to a  $\chi^2$ -distribution with  $N - m$  degrees of freedom. The random variable  $z$  is often denoted with  $\chi^2$  itself. The parameters that minimize  $z = \chi^2$  are called best-fit parameters. In the case of Poisson distributed data  $n_1, \dots, n_N$  with means  $\nu_1, \dots, \nu_N$  the  $\chi^2$ -distributed random variable reads

$$\chi^2 = \sum_{i=1}^N \frac{(n_i - \nu_i)^2}{\nu_i}. \quad (\text{A.3})$$

This is used when the counts detected in various energy bins by some instrument are given. However,  $n_i \gtrsim 5$  is required that the random variable defined in Eq. (A.3) follows reasonably

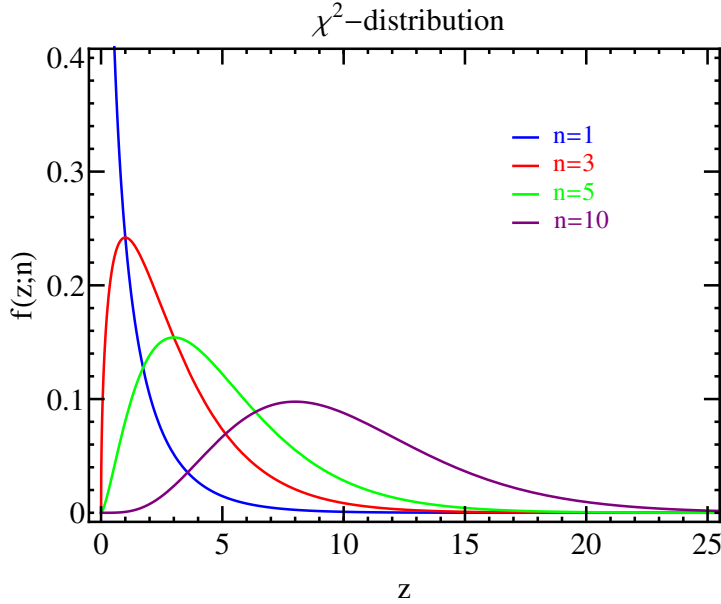


Figure A.1:  $\chi^2$ -distribution for  $n = 1$ ,  $n = 3$ ,  $n = 5$  and  $n = 10$  (from bottom to top at  $z = 10$ ).

well a  $\chi^2$ -distribution. To quantify the goodness of the fit, the p-value of the distribution is considered

$$p = \int_{\chi^2}^{\infty} f(z, n_d) dz, \quad (\text{A.4})$$

where  $\chi^2$  here denotes the observed  $\chi^2$  value and  $n_d$  the number of degrees of freedom. A small p-value indicates a disagreement of the data and the tested fit function. In the literature the  $\chi^2$  per degree of freedom  $\chi^2/n_d$  is often quoted to show the level of agreement between the data and a model.

## A.2 Parameter estimation

The aim of parameter estimation is to set limits or to compute a confidence intervals for certain parameters of interest, in the case of this thesis the dark matter lifetime or cross section. The confidence interval states by which fraction of times the true value would lie in the corresponding confidence region for a large number of repeated experiments. For a value given at 95% CL that means that the true value is contained in the confidence interval in 95% of the experiments. In order to calculate the confidence interval, a likelihood function has to be set up. In an experiment, where the number of counts  $n_i$  in a certain energy bin  $i$  is given that are compared to a model with  $\lambda_i$  expected counts in that bin, the likelihood function is the product of the Poisson distributions for all the bins and reads

$$\mathcal{L} = \prod_i \frac{(\lambda_i)^{n_i} \exp(-\lambda_i)}{n_i!}. \quad (\text{A.5})$$

In the case of data points  $x_i$  with Gaussian errors  $\sigma_i$  the likelihood function is given by

$$\mathcal{L} = \prod_i \frac{1}{\sqrt{2\pi\sigma_i^2}} \exp\left(\frac{-(x_i - \lambda_i)^2}{2\sigma_i^2}\right), \quad (\text{A.6})$$

where the  $\lambda_i$  are also calculated from the model that is tested. The model prediction can contain  $m$  nuisance parameters  $\{\theta_1, \dots, \theta_m\}$  that are minimized and other parameters for which the confidence interval is constructed. In general, the number of the latter parameters is not limited. However, in this thesis we are only interested in cases with one parameter. Thus we consider only one parameter  $\theta_0$  that is estimated in the following. Now we define the likelihood ratio  $\Lambda$  as

$$\Lambda = \frac{\mathcal{L}(\theta'_{\text{bf}}, \theta_0)}{\mathcal{L}(\theta_{\text{bf}}, \theta_{0,\text{bf}})}, \quad (\text{A.7})$$

where  $\theta_{\text{bf}}$  are the best fit parameters  $\{\theta_{1,\text{bf}}, \dots, \theta_{m,\text{bf}}\}$  that minimize  $-2 \log \mathcal{L}$ , while  $\theta_0$  is also fitted and attains the best fit value  $\theta_{0,\text{bf}}$ .  $\theta'_{\text{bf}}$  are the parameters that minimize  $-2 \log \mathcal{L}$ , while fixing (and not profiling over) the parameter of interest  $\theta_0$ . Wilks theorem [342] now states that in the large sample limit  $-2 \log \Lambda$  is  $\chi^2$ -distributed with  $n = 1$  degree of freedom in the case of one unknown parameter  $\theta_0$  that is estimated. Note that this holds as long as the total number of counts is large. Thus it can also be applied in the limit of very small energy bins, where the number of counts in each bin becomes small. For the  $\chi^2$ -distribution  $f(z; n = 1)$  the confidence interval  $[\theta^{**}, \theta^*]$  at given confidence level  $1 - \alpha$  is given as

$$\alpha = \int_{\chi^2}^{\infty} f(z; n = 1) dz. \quad (\text{A.8})$$

The corresponding  $\theta$ -values  $\theta^{**}$  and  $\theta^*$  are found by solving  $\chi^2 = -2 \log \Lambda(\theta_0)$  for  $\theta_0$ . In the case of  $\alpha = 5\%$  (i.e. at 95% CL) we get  $\chi^2 = 3.84$  ( $\chi^2 = 4$  for  $2\sigma$ ). Thus the condition  $\Lambda(\theta^*) = \chi^2$  for the upper limit reads

$$-2 \log \mathcal{L}(\theta'_{\text{bf}}, \theta_0) + 2 \log \mathcal{L}(\theta_{\text{bf}}, \theta_{0,\text{bf}}) = \Delta 2 \log \mathcal{L} = \chi^2. \quad (\text{A.9})$$

As in the case of dark matter annihilations or decays the normalization is always positive, often a one sided limit is calculated in the literature. In this case  $\Delta 2 \log \mathcal{L} = 2.7$  for 95% CL, because when  $\theta > 0$  is required then  $-2 \log \Lambda$  is distributed as the sum of two  $\chi^2$ -distributions [286, 343]:

$$-2 \log \Lambda(\theta > 0) = \frac{1}{2} \chi^2(z, n = 0) + \frac{1}{2} \chi^2(z, n = 1). \quad (\text{A.10})$$

The connection between the  $\chi^2$  and the likelihood ratio can be seen in the following consideration. Taking the logarithm of the Gaussian likelihood function Eq. (A.6) and multiplying by  $-2$  and dropping constant terms (that do not depend on  $\theta_0$ ) yields the  $\chi^2$  as defined in Eq. (A.1)

$$-2 \log \mathcal{L} = \sum_i \frac{(x_i - \lambda_i)^2}{2\sigma_i^2}. \quad (\text{A.11})$$

In the large sample limit the same relation holds for the Poisson likelihood given in Eq. (A.5). Thus Eq. (A.9) is equivalent to

$$\chi^2(\theta_{\text{bf}}, \theta_0) - \chi^2(\theta_{\text{bf}}, \theta_{0,\text{bf}}) = \Delta 2 \log \mathcal{L} \quad (\text{A.12})$$

and the  $\chi^2$  itself can be used in the same way as  $-2 \log \Lambda$  to derive confidence intervals.

### A.3 Hypothesis tests

This section describes how to reject a hypothesis  $H_0$  with a given significance level  $1 - \alpha$ . This means that the null hypothesis is rejected in  $100\% \cdot \alpha$  of repeated experiments, although it is true. In the case of dark matter searches, in particular in the case of a discovery, the hypothesis that we want to reject is the hypothesis of “background only”, i.e.  $\theta_0 = 0$  against the alternative hypothesis  $\theta_0 \neq 0$ . As above, the likelihood ratio is considered

$$\Lambda = \frac{\mathcal{L}(\theta'_{\text{bf}}, \theta_0 = 0)}{\mathcal{L}(\theta_{\text{bf}}, \theta_{0,\text{bf}})}. \quad (\text{A.13})$$

Again,  $-2 \log \Lambda$  follows a  $\chi^2$ -distribution and the significance level  $1 - \alpha$  at which the null hypothesis can be rejected is determined by Eq. (A.8). Thus for a rejection with  $5\sigma$  significance one gets  $\Delta 2 \log \mathcal{L} = 23$  requiring a positive signal normalization [286]. The construction of the upper limit presented in Sec. A.2 is thus equivalent to a hypothesis test with null hypothesis  $\theta = \theta_0$  where the  $100\% \cdot (1 - \alpha)$  CL limit is exactly the value of  $\theta_0$  for which the null hypothesis can be rejected at that confidence level [285].

## Acknowledgments

I would like to thank my supervisor Alejandro Ibarra for his continuous support, advice and fruitful collaboration during the past four years. I am also very thankful for the opportunity to experience several motivating summer schools and to present my work at many international conferences. In addition, I am grateful for having had the opportunity to collaborate with a number of excellent people, namely Gianfranco Bertone, Camilo Garcia-Cely, Sergio López Gehler, Xiaoyuan Huang, Miguel Pato, Joseph Silk, Yue-Lin Sming Tsai, Michel Tytgat, Qiang Yuan and Ming Xu. Furthermore, I am indebted to Camilo Garcia-Cely, Bhupal Dev, Maximilian Fallbacher, Xiaoyuan Huang, Miguel Pato, Yue-Lin Sming Tsai and Sebastian Wild for proofreading my manuscript. I have been lucky to conduct my work in the pleasant and inspiring atmosphere of the physics department at TUM and would also like to thank all my present and former colleagues of the T30 groups for creating an enriching environment, both at the professional and personal level. Special thanks go to my office mates throughout the years. Furthermore, I am thankful to Karin Ramm for helping me deal with a lot of bureaucracy. This work was partly funded by the DFG–Graduiertenkolleg “Particle Physics at the Energy Frontier of New Phenomena” and the TUM Graduate School, and I am thankful for their support. Last but not least I would like to thank my family for their everlasting support and encouragement.



# Bibliography

- [1] A. Ibarra, A. S. Lamperstorfer, and J. Silk, *Dark matter annihilations and decays after the AMS-02 positron measurements*, *Phys. Rev.* **D89** (2014), no. 6 063539, [[arXiv:1309.2570](#)].
- [2] A. S. Lamperstorfer, *Limits on dark matter parameters after the AMS-02 positron measurements*, in *26th Rencontres de Blois on Particle Physics and Cosmology Blois, Loire Valley, France, May 18-25, 2014*, 2014.
- [3] A. Ibarra, A. S. Lamperstorfer, S. L. Gehler, M. Pato, and G. Bertone, *On the sensitivity of CTA to gamma-ray boxes from multi-TeV dark matter*, *JCAP* **1509** (2015), no. 09 048, [[arXiv:1503.06797](#)].
- [4] C. Garcia-Cely, A. Ibarra, A. S. Lamperstorfer, and M. H. G. Tytgat, *Gamma-rays from Heavy Minimal Dark Matter*, [arXiv:1507.05536](#).
- [5] X. Huang, A. S. Lamperstorfer, Y.-L. S. Tsai, M. Xu, Q. Yuan, J. Chang, Y.-W. Dong, B.-L. Hu, J.-G. Lü, L. Wang, B.-B. Wu, and S.-N. Zhang, *Perspective of monochromatic gamma-ray line detection with the High Energy cosmic-Radiation Detection (HERD) facility onboard China's Space Station*, [arXiv:1509.02672](#).
- [6] G. Bertone, D. Hooper, and J. Silk, *Particle dark matter: Evidence, candidates and constraints*, *Phys. Rept.* **405** (2005) 279–390, [[hep-ph/0404175](#)].
- [7] V. C. Rubin and W. K. Ford, Jr., *Rotation of the Andromeda Nebula from a Spectroscopic Survey of Emission Regions*, *The Astrophysical Journal* **159** (Feb., 1970) 379.
- [8] V. C. Rubin, W. K. J. Ford, and N. . Thonnard, *Rotational properties of 21 SC galaxies with a large range of luminosities and radii, from NGC 4605 /R = 4kpc/ to UGC 2885 /R = 122 kpc/*, *The Astrophysical Journal* **238** (June, 1980) 471–487.
- [9] Y. Sofue and V. Rubin, *Rotation curves of spiral galaxies*, *Ann.Rev.Astron.Astrophys.* **39** (2001) 137–174, [[astro-ph/0010594](#)].
- [10] **SDSS Collaboration** Collaboration, X. Xue et al., *The Milky Way's Circular Velocity Curve to 60 kpc and an Estimate of the Dark Matter Halo Mass from Kinematics of 2400 SDSS Blue Horizontal Branch Stars*, *Astrophys.J.* **684** (2008) 1143–1158, [[arXiv:0801.1232](#)].

- [11] J. Read, *The Local Dark Matter Density*, *J.Phys.* **G41** (2014) 063101, [[arXiv:1404.1938](#)].
- [12] F. Iocco, M. Pato, and G. Bertone, *Evidence for dark matter in the inner Milky Way*, [arXiv:1502.03821](#).
- [13] F. Zwicky, *Die Rotverschiebung von extragalaktischen Nebeln*, *Helvetica Physica Acta* **6** (1933) 110–127.
- [14] F. Zwicky, *On the Masses of Nebulae and of Clusters of Nebulae*, *Astrophys.J.* **86** (Oct., 1937) 217.
- [15] S. Weinberg, *Cosmology*. Cosmology. OUP Oxford, 2008.
- [16] R. Sadat, *Clusters of galaxies and mass estimates*, *ASP Conf.Ser.* **126** (1997) 349, [[astro-ph/9702050](#)].
- [17] B. Ryden, *Introduction to cosmology*, .
- [18] G. M. Voit, *Tracing cosmic evolution with clusters of galaxies*, *Rev.Mod.Phys.* **77** (2005) 207–258, [[astro-ph/0410173](#)].
- [19] R. Sanders, *The Dark Matter Problem: A Historical Perspective*. Cambridge University Press, 2010.
- [20] L. Bergström and A. Goobar, *Cosmology and Particle Astrophysics*. Springer Praxis Books. Springer Berlin Heidelberg, 2006.
- [21] S. Warren, G. Lewis, P. C. Hewett, P. Moller, P. Shaver, et al., *A vlt color image of the optical Einstein ring 0047-2808*, *Astron.Astrophys.* **343** (1999) L35, [[astro-ph/9901271](#)].
- [22] J. A. Tyson, G. P. Kochanski, and I. P. Dell’Antonio, *Detailed mass map of CL0024+1654 from strong lensing*, *Astrophys.J.* **498** (1998) L107, [[astro-ph/9801193](#)].
- [23] A. Refregier, *Weak gravitational lensing by large scale structure*, *Ann.Rev.Astron.Astrophys.* **41** (2003) 645–668, [[astro-ph/0307212](#)].
- [24] **MACHO** Collaboration, C. Alcock et al., *The MACHO project LMC microlensing results from the first two years and the nature of the galactic dark halo*, *Astrophys.J.* **486** (1997) 697–726, [[astro-ph/9606165](#)].
- [25] M. Markevitch, A. Gonzalez, L. David, A. Vikhlinin, S. Murray, et al., *A Textbook example of a bow shock in the merging galaxy cluster 1E0657-56*, *Astrophys.J.* **567** (2002) L27, [[astro-ph/0110468](#)].
- [26] D. Clowe, M. Bradac, A. H. Gonzalez, M. Markevitch, S. W. Randall, et al., *A direct empirical proof of the existence of dark matter*, *Astrophys.J.* **648** (2006) L109–L113, [[astro-ph/0608407](#)].

- [27] M. Markevitch, A. Gonzalez, D. Clowe, A. Vikhlinin, L. David, et al., *Direct constraints on the dark matter self-interaction cross-section from the merging galaxy cluster 1E0657-56*, *Astrophys.J.* **606** (2004) 819–824, [[astro-ph/0309303](#)].
- [28] K. Jedamzik and M. Pospelov, *Big Bang Nucleosynthesis and Particle Dark Matter*, *New J.Phys.* **11** (2009) 105028, [[arXiv:0906.2087](#)].
- [29] **Particle Data Group** Collaboration, K. Olive et al., *Review of Particle Physics*, *Chin.Phys.* **C38** (2014) 090001.
- [30] B. D. Fields, *The primordial lithium problem*, *Ann. Rev. Nucl. Part. Sci.* **61** (2011) 47–68, [[arXiv:1203.3551](#)].
- [31] D. Fixsen, E. Cheng, J. Gales, J. C. Mather, R. Shafer, et al., *The Cosmic Microwave Background spectrum from the full COBE FIRAS data set*, *Astrophys.J.* **473** (1996) 576, [[astro-ph/9605054](#)].
- [32] **WMAP** Collaboration, C. Bennett et al., *Nine-Year Wilkinson Microwave Anisotropy Probe (WMAP) Observations: Final Maps and Results*, *Astrophys.J.Suppl.* **208** (2013) 20, [[arXiv:1212.5225](#)].
- [33] **Planck** Collaboration, R. Adam et al., *Planck 2015 results. IX. Diffuse component separation: CMB maps*, [arXiv:1502.05956](#).
- [34] W. Hu, *Lecture Notes on CMB Theory: From Nucleosynthesis to Recombination*, [arXiv:0802.3688](#).
- [35] **Planck** Collaboration, P. Ade et al., *Planck 2015 results. XIII. Cosmological parameters*, [arXiv:1502.01589](#).
- [36] M. Roos, *Dark Matter: The evidence from astronomy, astrophysics and cosmology*, [arXiv:1001.0316](#).
- [37] B. A. Bassett and R. Hlozek, *Baryon Acoustic Oscillations*, [arXiv:0910.5224](#).
- [38] **SDSS** Collaboration, D. J. Eisenstein et al., *Detection of the baryon acoustic peak in the large-scale correlation function of SDSS luminous red galaxies*, *Astrophys.J.* **633** (2005) 560–574, [[astro-ph/0501171](#)].
- [39] G. Bertone, ed., *Particle Dark Matter*. Cambridge University Press, 2010. Cambridge Books Online.
- [40] V. Springel, S. D. White, A. Jenkins, C. S. Frenk, N. Yoshida, et al., *Simulating the joint evolution of quasars, galaxies and their large-scale distribution*, *Nature* **435** (2005) 629–636, [[astro-ph/0504097](#)].

- [41] V. Springel, C. S. Frenk, and S. D. White, *The large-scale structure of the Universe*, *Nature* **440** (2006) 1137, [[astro-ph/0604561](#)].
- [42] V. Springel, S. D. M. White, A. R. Jenkins, C. S. Frenk, N. Yoshida, L. Gao, J. Navarro, R. Thacker, D. Croton, J. Helly, J. A. Peacock, S. Cole, P. Thomas, H. Couchman, A. A. Evrard, J. Colberg, and F. Pearce, *Simulations of the formation, evolution and clustering of galaxies and quasars.*, *Nature*. **435** (June, 2005) 629–636.
- [43] “Millennium simulation project.” <http://www.mpa-garching.mpg.de/galform/virgo/millennium/>. Accessed: 2015-07-01.
- [44] W. de Blok, *The Core-Cusp Problem*, *Adv.Astron.* **2010** (2010) 789293, [[arXiv:0910.3538](#)].
- [45] W. de Blok, S. S. McGaugh, A. Bosma, and V. C. Rubin, *Mass density profiles of LSB galaxies*, *Astrophys.J.* **552** (2001) L23–L26, [[astro-ph/0103102](#)].
- [46] M. Cirelli, G. Corcella, A. Hektor, G. Hutsi, M. Kadastik, et al., *PPPC 4 DM ID: A Poor Particle Physicist Cookbook for Dark Matter Indirect Detection*, *JCAP* **1103** (2011) 051, [[arXiv:1012.4515](#)].
- [47] J. N. Bahcall and R. M. Soneira, *The universe at faint magnitudes. I - Models for the galaxy and the predicted star counts*, *Astrophys. J. Suppl.* **44** (Sept., 1980) 73–110.
- [48] F. J. Kerr and D. Lynden-Bell, *Review of galactic constants*, *Mon.Not.Roy.Astron.Soc.* **221** (1986) 1023.
- [49] J. F. Navarro, C. S. Frenk, and S. D. White, *The Structure of cold dark matter halos*, *Astrophys.J.* **462** (1996) 563–575, [[astro-ph/9508025](#)].
- [50] A. Berlin, P. Gratia, D. Hooper, and S. D. McDermott, *Hidden Sector Dark Matter Models for the Galactic Center Gamma-Ray Excess*, *Phys.Rev.* **D90** (2014), no. 1 015032, [[arXiv:1405.5204](#)].
- [51] A. W. Graham, D. Merritt, B. Moore, J. Diemand, and B. Terzic, *Empirical models for Dark Matter Halos. I. Nonparametric Construction of Density Profiles and Comparison with Parametric Models*, *Astron.J.* **132** (2006) 2685–2700, [[astro-ph/0509417](#)].
- [52] L. Pieri, J. Lavalle, G. Bertone, and E. Branchini, *Implications of High-Resolution Simulations on Indirect Dark Matter Searches*, *Phys.Rev.* **D83** (2011) 023518, [[arXiv:0908.0195](#)].
- [53] P. Mollitor, E. Nezri, and R. Teyssier, *Baryonic and dark matter distribution in cosmological simulations of spiral galaxies*, *Mon.Not.Roy.Astron.Soc.* **447** (2015), no. 2 1353–1369, [[arXiv:1405.4318](#)].

- [54] M. Pato, O. Agertz, G. Bertone, B. Moore, and R. Teyssier, *Systematic uncertainties in the determination of the local dark matter density*, *Phys.Rev.* **D82** (2010) 023531, [[arXiv:1006.1322](#)].
- [55] W. Hu, R. Barkana, and A. Gruzinov, *Cold and fuzzy dark matter*, *Phys.Rev.Lett.* **85** (2000) 1158–1161, [[astro-ph/0003365](#)].
- [56] D. J. Chung, E. W. Kolb, and A. Riotto, *Superheavy dark matter*, *Phys.Rev.* **D59** (1999) 023501, [[hep-ph/9802238](#)].
- [57] H. Baer, *Collider Signal II: Missing ET Signatures and Dark Matter Connection*, in *Proceedings of Theoretical Advanced Study Institute in Elementary Particle Physics on The dawn of the LHC era (TASI 2008)*, pp. 211–258, 2010. [arXiv:0901.4732](#).
- [58] M. Taoso, G. Bertone, and A. Masiero, *Dark Matter Candidates: A Ten-Point Test*, *JCAP* **0803** (2008) 022, [[arXiv:0711.4996](#)].
- [59] S. Davidson, S. Hannestad, and G. Raffelt, *Updated bounds on millicharged particles*, *JHEP* **0005** (2000) 003, [[hep-ph/0001179](#)].
- [60] J. M. Cline, Z. Liu, and W. Xue, *Millicharged Atomic Dark Matter*, *Phys.Rev.* **D85** (2012) 101302, [[arXiv:1201.4858](#)].
- [61] D. N. Spergel and P. J. Steinhardt, *Observational evidence for selfinteracting cold dark matter*, *Phys.Rev.Lett.* **84** (2000) 3760–3763, [[astro-ph/9909386](#)].
- [62] F.-Y. Cyr-Racine, R. de Putter, A. Raccanelli, and K. Sigurdson, *Constraints on Large-Scale Dark Acoustic Oscillations from Cosmology*, *Phys. Rev.* **D89** (2014), no. 6 063517, [[arXiv:1310.3278](#)].
- [63] L. Bergstrom, *Dark Matter Candidates*, *New J.Phys.* **11** (2009) 105006, [[arXiv:0903.4849](#)].
- [64] I. F. Albuquerque and C. Perez de los Heros, *Closing the Window on Strongly Interacting Dark Matter with IceCube*, *Phys.Rev.* **D81** (2010) 063510, [[arXiv:1001.1381](#)].
- [65] P. Langacker, *Grand Unified Theories and Proton Decay*, *Phys. Rept.* **72** (1981) 185.
- [66] A. Ibarra, D. Tran, and C. Weniger, *Indirect Searches for Decaying Dark Matter*, *Int.J.Mod.Phys.* **A28** (2013) 1330040, [[arXiv:1307.6434](#)].
- [67] S. Profumo, *TASI 2012 Lectures on Astrophysical Probes of Dark Matter*, [arXiv:1301.0952](#).
- [68] E. Carquin, M. A. Diaz, G. A. Gomez-Vargas, B. Panes, and N. Viaux, *Confronting recent AMS-02 positron fraction and Fermi-LAT Extragalactic Gamma-Ray Background measurements with gravitino dark matter*, [arXiv:1501.05932](#).

- [69] H. Baer, K.-Y. Choi, J. E. Kim, and L. Roszkowski, *Dark matter production in the early Universe: beyond the thermal WIMP paradigm*, *Phys.Rept.* **555** (2014) 1–60, [[arXiv:1407.0017](#)].
- [70] D. Hooper, *TASI 2008 Lectures on Dark Matter*, [arXiv:0901.4090](#).
- [71] G. Gelmini and P. Gondolo, *DM Production Mechanisms*, [arXiv:1009.3690](#).
- [72] E. Kolb and M. Turner, *The Early Universe*. Frontiers in physics. Westview Press, 1994.
- [73] G. B. Gelmini, *TASI 2014 Lectures: The Hunt for Dark Matter*, [arXiv:1502.01320](#).
- [74] K. Griest and M. Kamionkowski, *Unitarity Limits on the Mass and Radius of Dark Matter Particles*, *Phys.Rev.Lett.* **64** (1990) 615.
- [75] C. Boehm, M. J. Dolan, and C. McCabe, *A Lower Bound on the Mass of Cold Thermal Dark Matter from Planck*, *JCAP* **1308** (2013) 041, [[arXiv:1303.6270](#)].
- [76] B. W. Lee and S. Weinberg, *Cosmological Lower Bound on Heavy Neutrino Masses*, *Phys.Rev.Lett.* **39** (1977) 165–168.
- [77] E. W. Kolb and K. A. Olive, *The Lee-Weinberg Bound Revisited*, *Phys.Rev.* **D33** (1986) 1202.
- [78] A. Boyarsky, O. Ruchayskiy, and D. Iakubovskyi, *A Lower bound on the mass of Dark Matter particles*, *JCAP* **0903** (2009) 005, [[arXiv:0808.3902](#)].
- [79] V. S. Rychkov and A. Strumia, *Thermal production of gravitinos*, *Phys.Rev.* **D75** (2007) 075011, [[hep-ph/0701104](#)].
- [80] H. Davoudiasl, D. Hooper, and S. D. McDermott, *Inflatable Dark Matter*, [arXiv:1507.08660](#).
- [81] G. L. Kane, P. Kumar, B. D. Nelson, and B. Zheng, *Dark Matter Production Mechanisms with a Non-Thermal Cosmological History - A Classification*, [arXiv:1502.05406](#).
- [82] T. Saab, *An Introduction to Dark Matter Direct Detection Searches & Techniques*, [arXiv:1203.2566](#).
- [83] G. Gerbier and J. Gascon, *Cryogenic detectors*, .
- [84] E. Aprile and L. Baudis, *Liquid noble gases*, .
- [85] D. G. Cerdeno and A. M. Green, *Direct detection of WIMPs*, [arXiv:1002.1912](#).
- [86] P. J. Fox, G. D. Kribs, and T. M. Tait, *Interpreting Dark Matter Direct Detection Independently of the Local Velocity and Density Distribution*, *Phys.Rev.* **D83** (2011) 034007, [[arXiv:1011.1910](#)].

- [87] P. Gondolo and G. B. Gelmini, *Halo independent comparison of direct dark matter detection data*, *JCAP* **1212** (2012) 015, [[arXiv:1202.6359](#)].
- [88] **DAMA, LIBRA** Collaboration, R. Bernabei et al., *New results from DAMA/LIBRA*, *Eur.Phys.J.* **C67** (2010) 39–49, [[arXiv:1002.1028](#)].
- [89] N. Fornengo, *Particle dark matter and the DAMA/NaI and DAMA/LIBRA annual modulation effect*, in *In "Bertone, G. (ed.): Particle dark matter"*, 383–390, 2010.
- [90] **ATLAS, CMS** Collaboration, A. Cortes Gonzalez, *Searches for mono-X at the LHC*, *PoS DIS2014* (2014) 116.
- [91] V. A. Mitsou, *Overview of searches for dark matter at the LHC*, [arXiv:1402.3673](#).
- [92] G. Busoni, A. De Simone, E. Morgante, and A. Riotto, *On the Validity of the Effective Field Theory for Dark Matter Searches at the LHC*, *Phys.Lett.* **B728** (2014) 412–421, [[arXiv:1307.2253](#)].
- [93] **LHC New Physics Working Group** Collaboration, D. Alves et al., *Simplified Models for LHC New Physics Searches*, *J.Phys.* **G39** (2012) 105005, [[arXiv:1105.2838](#)].
- [94] A. Ibarra, *Indirect dark matter detection*, *Acta Phys.Polon.* **B43** (2012) 2199–2224.
- [95] V. Ptuskin, *Propagation of galactic cosmic rays*, *Astropart.Phys.* **39-40** (2012) 44–51.
- [96] E. Carlson, A. Coogan, T. Linden, S. Profumo, A. , et al., *Antihelium from Dark Matter*, *Phys.Rev.* **D89** (2014), no. 7 076005, [[arXiv:1401.2461](#)].
- [97] M. Cirelli, N. Fornengo, M. Taoso, and A. Vittino, *Anti-helium from Dark Matter annihilations*, *JHEP* **1408** (2014) 009, [[arXiv:1401.4017](#)].
- [98] J. Conrad, *Statistical Issues in Astrophysical Searches for Particle Dark Matter*, *Astropart.Phys.* **62** (2014) 165–177, [[arXiv:1407.6617](#)].
- [99] W. H. Press and D. N. Spergel, *Capture by the sun of a galactic population of weakly interacting massive particles*, *Astrophys.J.* **296** (1985) 679–684.
- [100] M. Srednicki, K. A. Olive, and J. Silk, *High-Energy Neutrinos from the Sun and Cold Dark Matter*, *Nucl.Phys.* **B279** (1987) 804.
- [101] M. Dannerger and C. Rott, *Solar WIMPs unravelled: Experiments, astrophysical uncertainties, and interactive tools*, *Phys.Dark Univ.* (2014).
- [102] L. Goodenough and D. Hooper, *Possible Evidence For Dark Matter Annihilation In The Inner Milky Way From The Fermi Gamma Ray Space Telescope*, [arXiv:0910.2998](#).

- [103] K. N. Abazajian, *The Consistency of Fermi-LAT Observations of the Galactic Center with a Millisecond Pulsar Population in the Central Stellar Cluster*, *JCAP* **1103** (2011) 010, [[arXiv:1011.4275](#)].
- [104] E. Carlson and S. Profumo, *Cosmic Ray Protons in the Inner Galaxy and the Galactic Center Gamma-Ray Excess*, *Phys.Rev.* **D90** (2014), no. 2 023015, [[arXiv:1405.7685](#)].
- [105] T. Daylan, D. P. Finkbeiner, D. Hooper, T. Linden, S. K. N. Portillo, et al., *The Characterization of the Gamma-Ray Signal from the Central Milky Way: A Compelling Case for Annihilating Dark Matter*, [arXiv:1402.6703](#).
- [106] **PAMELA** Collaboration, O. Adriani et al., *An anomalous positron abundance in cosmic rays with energies 1.5-100 GeV*, *Nature* **458** (2009) 607–609, [[arXiv:0810.4995](#)].
- [107] I. Cholis and D. Hooper, *Dark Matter and Pulsar Origins of the Rising Cosmic Ray Positron Fraction in Light of New Data From AMS*, *Phys.Rev.* **D88** (2013) 023013, [[arXiv:1304.1840](#)].
- [108] E. Bulbul, M. Markevitch, A. Foster, R. K. Smith, M. Loewenstein, and S. W. Randall, *Detection of An Unidentified Emission Line in the Stacked X-ray spectrum of Galaxy Clusters*, *Astrophys. J.* **789** (2014) 13, [[arXiv:1402.2301](#)].
- [109] T. E. Jeltema and S. Profumo, *Discovery of a 3.5 keV line in the Galactic Centre and a critical look at the origin of the line across astronomical targets*, *Mon. Not. Roy. Astron. Soc.* **450** (2015), no. 2 2143–2152, [[arXiv:1408.1699](#)].
- [110] M. E. Anderson, E. Churazov, and J. N. Bregman, *Non-Detection of X-Ray Emission From Sterile Neutrinos in Stacked Galaxy Spectra*, [arXiv:1408.4115](#).
- [111] **IceCube** Collaboration, M. G. Aartsen et al., *Observation of High-Energy Astrophysical Neutrinos in Three Years of IceCube Data*, *Phys. Rev. Lett.* **113** (2014) 101101, [[arXiv:1405.5303](#)].
- [112] A. Esmaili and P. D. Serpico, *Are IceCube neutrinos unveiling PeV-scale decaying dark matter?*, *JCAP* **1311** (2013) 054, [[arXiv:1308.1105](#)].
- [113] A. Esmaili, S. K. Kang, and P. D. Serpico, *IceCube events and decaying dark matter: hints and constraints*, *JCAP* **1412** (2014), no. 12 054, [[arXiv:1410.5979](#)].
- [114] E. Waxman, *IceCube’s Neutrinos: The beginning of extra-Galactic neutrino astrophysics?*, in *Rencontres du Vietnam: Windows on the Universe Quy Nhon, Binh Dinh, Vietnam, August 11-17, 2013*. [arXiv:1312.0558](#).
- [115] G. Kirchhoff, *Ueber die fraunhofer’schen linien*, *Annalen der Physik* **185** (1860), no. 1 148–150.

- [116] A. Choudhuri, *Astrophysics for Physicists*. Cambridge University Press, 2010.
- [117] P. C. Frisch, *The interstellar medium of our galaxy*, [astro-ph/0112497](#).
- [118] J. Blumer, R. Engel, and J. R. Horandel, *Cosmic Rays from the Knee to the Highest Energies*, *Prog.Part.Nucl.Phys.* **63** (2009) 293–338, [[arXiv:0904.0725](#)].
- [119] M. Malkov and P. Diamond, *Modern theory of Fermi acceleration: a new challenge to plasma physics*, *Phys.Plasmas* **8** (2001) 2401, [[astro-ph/0102373](#)].
- [120] **AMS Collaboration** Collaboration, M. Aguilar et al., *Precision Measurement of the ( $e^- + e^+$ ) Flux in Primary Cosmic Rays from 0.5 GeV to 1 TeV with the Alpha Magnetic Spectrometer on the International Space Station*, *Phys.Rev.Lett.* **113** (2014), no. 22 221102.
- [121] **H.E.S.S. Collaboration** Collaboration, F. Aharonian et al., *The energy spectrum of cosmic-ray electrons at TeV energies*, *Phys.Rev.Lett.* **101** (2008) 261104, [[arXiv:0811.3894](#)].
- [122] T. Delahaye, J. Lavalle, R. Lineros, F. Donato, and N. Fornengo, *Galactic electrons and positrons at the Earth: new estimate of the primary and secondary fluxes*, *Astron. Astrophys.* **524** (2010) A51, [[arXiv:1002.1910](#)].
- [123] T. Delahaye, F. Donato, N. Fornengo, J. Lavalle, R. Lineros, et al., *Galactic secondary positron flux at the Earth*, *Astron.Astrophys.* **501** (2009) 821–833, [[arXiv:0809.5268](#)].
- [124] **Fermi-LAT Collaboration**, M. Ackermann et al., *Measurement of separate cosmic-ray electron and positron spectra with the Fermi Large Area Telescope*, *Phys. Rev. Lett.* **108** (2012) 011103, [[arXiv:1109.0521](#)].
- [125] **AMS** Collaboration, M. Aguilar et al., *First Result from the Alpha Magnetic Spectrometer on the International Space Station: Precision Measurement of the Positron Fraction in Primary Cosmic Rays of 0.5–350 GeV*, *Phys.Rev.Lett.* **110** (2013) 141102.
- [126] **AMS** Collaboration, L. Accardo et al., *High Statistics Measurement of the Positron Fraction in Primary Cosmic Rays of 0.5–500 GeV with the Alpha Magnetic Spectrometer on the International Space Station*, *Phys. Rev. Lett.* **113** (2014) 121101.
- [127] I. V. Moskalenko and A. W. Strong, *Production and propagation of cosmic ray positrons and electrons*, *Astrophys. J.* **493** (1998) 694–707, [[astro-ph/9710124](#)].
- [128] A. Morselli, *Indirect searches in the PAMELA and Fermi era*, *Nucl. Phys. Proc. Suppl.* **194** (2009) 105–110.
- [129] L. Feng, R.-Z. Yang, H.-N. He, T.-K. Dong, Y.-Z. Fan, et al., *AMS-02 positron excess: new bounds on dark matter models and hint for primary electron spectrum hardening*, *Phys.Lett.* **B728** (2014) 250–255, [[arXiv:1303.0530](#)].

- [130] P. A. Sturrock, *A Model of pulsars*, *Astrophys. J.* **164** (1971) 529.
- [131] D. Hooper, P. Blasi, and P. D. Serpico, *Pulsars as the Sources of High Energy Cosmic Ray Positrons*, *JCAP* **0901** (2009) 025, [[arXiv:0810.1527](#)].
- [132] P.-F. Yin, Z.-H. Yu, Q. Yuan, and X.-J. Bi, *Pulsar interpretation for the AMS-02 result*, *Phys. Rev.* **D88** (2013), no. 2 023001, [[arXiv:1304.4128](#)].
- [133] A. Panov, *Electrons and Positrons in Cosmic Rays*, *J.Phys.Conf.Ser.* **409** (2013) 012004, [[arXiv:1303.6118](#)].
- [134] P. Blasi, *The origin of the positron excess in cosmic rays*, *Phys. Rev. Lett.* **103** (2009) 051104, [[arXiv:0903.2794](#)].
- [135] P. D. Serpico, *Astrophysical models for the origin of the positron ‘excess’*, *Astropart. Phys.* **39-40** (2012) 2–11, [[arXiv:1108.4827](#)].
- [136] K. Kohri, K. Ioka, Y. Fujita, and R. Yamazaki, *Can we explain AMS-02 antiproton and positron excesses simultaneously by nearby supernovae without pulsars nor dark matter?*, [arXiv:1505.01236](#).
- [137] I. Cholis and D. Hooper, *Constraining the origin of the rising cosmic ray positron fraction with the boron-to-carbon ratio*, *Phys. Rev.* **D89** (2014), no. 4 043013, [[arXiv:1312.2952](#)].
- [138] P. Mertsch and S. Sarkar, *AMS-02 data confront acceleration of cosmic ray secondaries in nearby sources*, *Phys. Rev.* **D90** (2014) 061301, [[arXiv:1402.0855](#)].
- [139] K. Ioka, *A Gamma-Ray Burst/Pulsar for Cosmic-Ray Positrons with a Dark Matter-like Spectrum*, *Prog. Theor. Phys.* **123** (2010) 743–755, [[arXiv:0812.4851](#)].
- [140] V. C. Spanos, *The Price of a Dark Matter Annihilation Interpretation of AMS-02 Data*, [arXiv:1312.7841](#).
- [141] Z.-P. Liu, Y.-L. Wu, and Y.-F. Zhou, *Sommerfeld enhancements with vector, scalar and pseudoscalar force-carriers*, *Phys. Rev.* **D88** (2013) 096008, [[arXiv:1305.5438](#)].
- [142] J. Hisano, S. Matsumoto, M. Nagai, O. Saito, and M. Senami, *Non-perturbative effect on thermal relic abundance of dark matter*, *Phys. Lett.* **B646** (2007) 34–38, [[hep-ph/0610249](#)].
- [143] J. Diemand, M. Kuhlen, P. Madau, M. Zemp, B. Moore, D. Potter, and J. Stadel, *Clumps and streams in the local dark matter distribution*, *Nature* **454** (2008) 735–738, [[arXiv:0805.1244](#)].
- [144] V. Springel, J. Wang, M. Vogelsberger, A. Ludlow, A. Jenkins, A. Helmi, J. F. Navarro, C. S. Frenk, and S. D. M. White, *The Aquarius Project: the subhalos of galactic halos*, *Mon. Not. Roy. Astron. Soc.* **391** (2008) 1685–1711, [[arXiv:0809.0898](#)].

- [145] A. Tylka, *Cosmic Ray Positrons From Annihilation of Weakly Interacting Massive Particles in the Galaxy*, *Phys.Rev.Lett.* **63** (1989) 840–843.
- [146] M. S. Turner and F. Wilczek, *Positron Line Radiation from Halo WIMP Annihilations as a Dark Matter Signature*, *Phys.Rev.* **D42** (1990) 1001–1007.
- [147] T. Appelquist, H.-C. Cheng, and B. A. Dobrescu, *Bounds on universal extra dimensions*, *Phys.Rev.* **D64** (2001) 035002, [[hep-ph/0012100](#)].
- [148] D. Hooper and S. Profumo, *Dark matter and collider phenomenology of universal extra dimensions*, *Phys.Rept.* **453** (2007) 29–115, [[hep-ph/0701197](#)].
- [149] G. Servant and T. M. Tait, *Is the lightest Kaluza-Klein particle a viable dark matter candidate?*, *Nucl.Phys.* **B650** (2003) 391–419, [[hep-ph/0206071](#)].
- [150] G. Servant, *Status Report on Universal Extra Dimensions After LHC8*, [arXiv:1401.4176](#).
- [151] S. Arrenberg, L. Baudis, K. Kong, K. T. Matchev, and J. Yoo, *Kaluza-Klein Dark Matter: Direct Detection vis-a-vis LHC (2013 update)*, [arXiv:1307.6581](#).
- [152] T. Flacke, D. Hooper, and J. March-Russell, *Improved bounds on universal extra dimensions and consequences for LKP dark matter*, *Phys.Rev.* **D73** (2006) 095002, [[hep-ph/0509352](#)].
- [153] G. Landsberg, *Searches for Extra Spatial Dimensions with the CMS Detector at the LHC*, *Mod.Phys.Lett.* **A50** (2015) 1540017, [[arXiv:1506.00024](#)].
- [154] **HESS** Collaboration, . F. Aharonian, *Observations of the Sagittarius Dwarf galaxy by the H.E.S.S. experiment and search for a Dark Matter signal*, *Astropart.Phys.* **29** (2008) 55–62, [[arXiv:0711.2369](#)].
- [155] C. Arina, T. Bringmann, J. Silk, and M. Vollmann, *Enhanced Line Signals from Annihilating Kaluza-Klein Dark Matter*, *Phys.Rev.* **D90** (2014), no. 8 083506, [[arXiv:1409.0007](#)].
- [156] G. Jungman, M. Kamionkowski, and K. Griest, *Supersymmetric dark matter*, *Phys.Rept.* **267** (1996) 195–373, [[hep-ph/9506380](#)].
- [157] G. Vertongen and C. Weniger, *Hunting Dark Matter Gamma-Ray Lines with the Fermi LAT*, *JCAP* **1105** (2011) 027, [[arXiv:1101.2610](#)].
- [158] A. Ibarra and D. Tran, *Antimatter Signatures of Gravitino Dark Matter Decay*, *JCAP* **0807** (2008) 002, [[arXiv:0804.4596](#)].
- [159] R. Catena and L. Covi, *SUSY dark matter(s)*, *Eur.Phys.J.* **C74** (2014) 2703, [[arXiv:1310.4776](#)].

- [160] J. L. Feng, *Naturalness and the Status of Supersymmetry*, *Ann.Rev.Nucl.Part.Sci.* **63** (2013) 351–382, [[arXiv:1302.6587](#)].
- [161] P. J. Fox and E. Poppitz, *Leptophilic Dark Matter*, *Phys.Rev.* **D79** (2009) 083528, [[arXiv:0811.0399](#)].
- [162] P. Agrawal, Z. Chacko, and C. B. Verhaaren, *Leptophilic Dark Matter and the Anomalous Magnetic Moment of the Muon*, *JHEP* **1408** (2014) 147, [[arXiv:1402.7369](#)].
- [163] A. Ibarra and S. Wild, *Dirac dark matter with a charged mediator: a comprehensive one-loop analysis of the direct detection phenomenology*, *JCAP* **1505** (2015), no. 05 047, [[arXiv:1503.03382](#)].
- [164] T. Lacroix, C. Boehm, and J. Silk, *Fitting the Fermi-LAT GeV excess: On the importance of including the propagation of electrons from dark matter*, *Phys.Rev.* **D90** (2014), no. 4 043508, [[arXiv:1403.1987](#)].
- [165] T. Bringmann, M. Vollmann, and C. Weniger, *Updated cosmic-ray and radio constraints on light dark matter: Implications for the GeV gamma-ray excess at the Galactic center*, *Phys.Rev.* **D90** (2014), no. 12 123001, [[arXiv:1406.6027](#)].
- [166] K. Kong and J.-C. Park, *Bounds on dark matter interpretation of Fermi-LAT GeV excess*, *Nucl.Phys.* **B888** (2014) 154–168, [[arXiv:1404.3741](#)].
- [167] K. M. Zurek, *Asymmetric Dark Matter: Theories, Signatures, and Constraints*, *Phys.Rept.* **537** (2014) 91–121, [[arXiv:1308.0338](#)].
- [168] F. Bishara and J. Zupan, *Continuous Flavor Symmetries and the Stability of Asymmetric Dark Matter*, *JHEP* **1501** (2015) 089, [[arXiv:1408.3852](#)].
- [169] T. Sjostrand, S. Mrenna, and P. Z. Skands, *A Brief Introduction to PYTHIA 8.1*, *Comput.Phys.Commun.* **178** (2008) 852–867, [[arXiv:0710.3820](#)].
- [170] M. Kachelriess, P. Serpico, and M. A. Solberg, *On the role of electroweak bremsstrahlung for indirect dark matter signatures*, *Phys.Rev.* **D80** (2009) 123533, [[arXiv:0911.0001](#)].
- [171] G. Corcella, I. Knowles, G. Marchesini, S. Moretti, K. Odagiri, et al., *HERWIG 6: An Event generator for hadron emission reactions with interfering gluons (including supersymmetric processes)*, *JHEP* **0101** (2001) 010, [[hep-ph/0011363](#)].
- [172] M. Cirelli, M. Kadastik, M. Raidal, and A. Strumia, *Model-independent implications of the e<sup>+</sup>-, anti-proton cosmic ray spectra on properties of Dark Matter*, *Nucl.Phys.* **B813** (2009) 1–21, [[arXiv:0809.2409](#)].

- [173] A. Ghez, S. Salim, N. Weinberg, J. Lu, T. Do, et al., *Measuring Distance and Properties of the Milky Way’s Central Supermassive Black Hole with Stellar Orbits*, *Astrophys.J.* **689** (2008) 1044–1062, [[arXiv:0808.2870](#)].
- [174] C. van Eldik, *Gamma rays from the Galactic Centre region: a review*, *Astropart.Phys.* **71** (2015) 45–70, [[arXiv:1505.06055](#)].
- [175] W. Dehnen and J. Binney, *Mass models of the Milky Way*, *Mon.Not.Roy.Astron.Soc.* **294** (1998) 429, [[astro-ph/9612059](#)].
- [176] P. J. McMillan, *Mass models of the Milky Way*, *Mon.Not.Roy.Astron.Soc.* **414** (2011) 2446–2457, [[arXiv:1102.4340](#)].
- [177] K. M. Ferriere, *The interstellar environment of our galaxy*, *Rev.Mod.Phys.* **73** (2001) 1031–1066, [[astro-ph/0106359](#)].
- [178] M. Haverkorn, *Magnetic Fields in the Milky Way*, [arXiv:1406.0283](#).
- [179] T. A. Porter and A. Strong, *A New estimate of the Galactic interstellar radiation field between 0.1 microns and 1000 microns*, [astro-ph/0507119](#).
- [180] A. W. Strong, I. V. Moskalenko, and O. Reimer, *Diffuse continuum gamma-rays from the galaxy*, *Astrophys.J.* **537** (2000) 763–784, [[astro-ph/9811296](#)].
- [181] I. V. Moskalenko, T. A. Porter, and A. W. Strong, *Attenuation of vhe gamma rays by the milky way interstellar radiation field*, *Astrophys.J.* **640** (2006) L155–L158, [[astro-ph/0511149](#)].
- [182] A. W. Strong, I. V. Moskalenko, and V. S. Ptuskin, *Cosmic-ray propagation and interactions in the Galaxy*, *Ann.Rev.Nucl.Part.Sci.* **57** (2007) 285–327, [[astro-ph/0701517](#)].
- [183] I. Cholis, C. Evoli, F. Calore, T. Linden, C. Weniger, et al., *The Galactic Center GeV Excess from a Series of Leptonic Cosmic-Ray Outbursts*, [arXiv:1506.05119](#).
- [184] M. Perelstein and B. Shakya, *Remarks on calculation of positron flux from galactic dark matter*, *Phys.Rev.* **D82** (2010) 043505, [[arXiv:1002.4588](#)].
- [185] D. Gaggero, L. Maccione, G. Di Bernardo, C. Evoli, and D. Grasso, *Three dimensional modeling of CR propagation*, [arXiv:1306.6850](#).
- [186] A. Strong and I. Moskalenko, *Propagation of cosmic-ray nucleons in the galaxy*, *Astrophys.J.* **509** (1998) 212–228, [[astro-ph/9807150](#)].
- [187] G. R. BLUMENTHAL and R. J. GOULD, *Bremsstrahlung, synchrotron radiation, and compton scattering of high-energy electrons traversing dilute gases*, *Rev. Mod. Phys.* **42** (Apr, 1970) 237–270.

- [188] A. E. Vladimirov, S. W. Digel, G. Johannesson, P. F. Michelson, I. V. Moskalenko, et al., *GALPROP WebRun: an internet-based service for calculating galactic cosmic ray propagation and associated photon emissions*, *Comput.Phys.Commun.* **182** (2011) 1156–1161, [[arXiv:1008.3642](https://arxiv.org/abs/1008.3642)].
- [189] “Galprop:home.” <http://galprop.stanford.edu/>. Accessed: 2015-07-011.
- [190] C. Evoli, D. Gaggero, D. Grasso, and L. Maccione, *Cosmic-Ray Nuclei, Antiprotons and Gamma-rays in the Galaxy: a New Diffusion Model*, *JCAP* **0810** (2008) 018, [[arXiv:0807.4730](https://arxiv.org/abs/0807.4730)].
- [191] R. Kissmann, *PICARD: A novel code for the Galactic Cosmic Ray propagation problem*, *Astropart.Phys.* **55** (2014) 37–50, [[arXiv:1401.4035](https://arxiv.org/abs/1401.4035)].
- [192] M. Werner, R. Kissmann, A. Strong, and O. Reimer, *A new 3D transport and radiation code for galactic cosmic rays*, [arXiv:1308.2829](https://arxiv.org/abs/1308.2829).
- [193] D. Maurin, R. Taillet, F. Donato, P. Salati, A. Barrau, and G. Boudoul, *Galactic cosmic ray nuclei as a tool for astroparticle physics*, [astro-ph/0212111](https://arxiv.org/abs/0212111).
- [194] M. Pato, D. Hooper, and M. Simet, *Pinpointing Cosmic Ray Propagation With The AMS-02 Experiment*, *JCAP* **1006** (2010) 022, [[arXiv:1002.3341](https://arxiv.org/abs/1002.3341)].
- [195] H.-B. Jin, Y.-L. Wu, and Y.-F. Zhou, *Cosmic ray propagation and dark matter in light of the latest AMS-02 data*, [arXiv:1410.0171](https://arxiv.org/abs/1410.0171).
- [196] R. Kappl, A. Reinert, and M. W. Winkler, *AMS-02 Antiprotons Reloaded*, [arXiv:1506.04145](https://arxiv.org/abs/1506.04145).
- [197] Y. Genolini, A. Putze, P. Salati, and P. Serpico, *Theoretical uncertainties in extracting cosmic-ray diffusion parameters: the boron-to-carbon ratio*, [arXiv:1504.03134](https://arxiv.org/abs/1504.03134).
- [198] T. Delahaye, R. Lineros, F. Donato, N. Fornengo, and P. Salati, *Positrons from dark matter annihilation in the galactic halo: Theoretical uncertainties*, *Phys. Rev.* **D77** (2008) 063527, [[arXiv:0712.2312](https://arxiv.org/abs/0712.2312)].
- [199] J. Lavalle, D. Maurin, and A. Putze, *Direct constraints on diffusion models from cosmic-ray positron data: Excluding the minimal model for dark matter searches*, *Phys.Rev.* **D90** (2014) 081301, [[arXiv:1407.2540](https://arxiv.org/abs/1407.2540)].
- [200] L. J. Gleeson and W. I. Axford, *Cosmic Rays in the Interplanetary Medium*, *Astrophys.J.* **149** (1967) L115.
- [201] L. J. Gleeson and W. I. Axford, *Solar Modulation of Galactic Cosmic Rays*, *Astrophys.J.* **154** (1968) 1011.

- [202] J. S. Perko, *Solar modulation of galactic antiprotons*, *Astron. Astrophys.* **184** (1987) 119–121.
- [203] H. Gast, S. Schael, *Charge-dependent solar modulation in light of the recent PAMELA data*. Talk presented at the 31st International Cosmic Ray Conference, Lodz, 7-15 July 2009.
- [204] L. Maccione, *Low energy cosmic ray positron fraction explained by charge-sign dependent solar modulation*, *Phys.Rev.Lett.* **110** (2013), no. 8 081101, [[arXiv:1211.6905](https://arxiv.org/abs/1211.6905)].
- [205] L. Baldini, *Space-Based Cosmic-Ray and Gamma-Ray Detectors: a Review*, [arXiv:1407.7631](https://arxiv.org/abs/1407.7631).
- [206] M. DuVernois, S. Barwick, J. Beatty, A. Bhattacharyya, C. Bower, et al., *Cosmic ray electrons and positrons from 1-GeV to 100-GeV: Measurements with HEAT and their interpretation*, *Astrophys.J.* **559** (2001) 296–303.
- [207] S. Barwick, J. Beatty, C. Bower, C. Chaput, S. Coutu, et al., *The high-energy antimatter telescope (HEAT): An instrument for the study of cosmic ray positrons*, *Nucl.Instrum.Meth.* **A400** (1997) 34–52.
- [208] M. Casolino, P. Picozza, F. Altamura, A. Basili, N. De Simone, et al., *Launch of the Space experiment PAMELA*, *Adv.Space Res.* **42** (2008) 455–466, [[arXiv:0708.1808](https://arxiv.org/abs/0708.1808)].
- [209] “Pamela mission official website.” <http://pamela.roma2.infn.it/index.php>. Accessed: 2015-06-01.
- [210] **PAMELA** Collaboration, O. Adriani et al., *Cosmic-Ray Positron Energy Spectrum Measured by PAMELA*, *Phys.Rev.Lett.* **111** (2013) 081102, [[arXiv:1308.0133](https://arxiv.org/abs/1308.0133)].
- [211] **AMS** Collaboration, A. Kounine, *AMS Experiment on the International Space Station*, .
- [212] S. S. for the AMS Collaboration, *Precision measurements of the electron spectrum and the positron spectrum with AMS*, *Proceedings of the 33rd International Cosmic Ray Conference, Rio de Janeiro, 2-9 July 2013*.
- [213] R. Musenich, R. Becker, K. Bollweg, J. Burger, M. Capell, et al., *Results From the Testing of the AMS Space Superconducting Magnet*, *IEEE Trans.Appl.Supercond.* **22** (2012), no. 3 4500204.
- [214] “Ams-02.” <http://www.ams02.org/>. Accessed: 2015-06-02.
- [215] **AMS** Collaboration, M. Aguilar et al., *Electron and Positron Fluxes in Primary Cosmic Rays Measured with the Alpha Magnetic Spectrometer on the International Space Station*, *Phys.Rev.Lett.* **113** (2014) 121102.
- [216] H.-B. Jin, Y.-L. Wu, and Y.-F. Zhou, *Implications of the first AMS-02 measurement for dark matter annihilation and decay*, *JCAP* **1311** (2013) 026, [[arXiv:1304.1997](https://arxiv.org/abs/1304.1997)].

- [217] L. Bergstrom, T. Bringmann, I. Cholis, D. Hooper, and C. Weniger, *New limits on dark matter annihilation from AMS cosmic ray positron data*, *Phys. Rev. Lett.* **111** (2013) 171101, [[arXiv:1306.3983](#)].
- [218] **Fermi-LAT** Collaboration, M. Ackermann et al., *Fermi LAT Search for Dark Matter in Gamma-ray Lines and the Inclusive Photon Spectrum*, *Phys. Rev.* **D86** (2012) 022002, [[arXiv:1205.2739](#)].
- [219] **Fermi-LAT** Collaboration, M. Ackermann et al., *Dark matter constraints from observations of 25 Milky Way satellite galaxies with the Fermi Large Area Telescope*, *Phys. Rev.* **D89** (2014) 042001, [[arXiv:1310.0828](#)].
- [220] M. Cirelli, E. Moulin, P. Panci, P. D. Serpico, and A. Viana, *Gamma ray constraints on Decaying Dark Matter*, *Phys. Rev.* **D86** (2012) 083506, [[arXiv:1205.5283](#)].
- [221] **Fermi-LAT** Collaboration, M. Ackermann et al., *Searching for Dark Matter Annihilation from Milky Way Dwarf Spheroidal Galaxies with Six Years of Fermi-LAT Data*, [arXiv:1503.02641](#).
- [222] A. Massari, E. Izaguirre, R. Essig, A. Albert, E. Bloom, and G. A. Gómez-Vargas, *Strong Optimized Conservative Fermi-LAT Constraints on Dark Matter Models from the Inclusive Photon Spectrum*, *Phys. Rev.* **D91** (2015), no. 8 083539, [[arXiv:1503.07169](#)].
- [223] S. Ando and K. Ishiwata, *Constraints on decaying dark matter from the extragalactic gamma-ray background*, *JCAP* **1505** (2015), no. 05 024, [[arXiv:1502.02007](#)].
- [224] G. Giesen, M. Boudaud, Y. Genolini, V. Poulin, M. Cirelli, P. Salati, and P. D. Serpico, *AMS-02 antiprotons, at last! Secondary astrophysical component and immediate implications for Dark Matter*, [arXiv:1504.04276](#).
- [225] N. Fornengo, L. Maccione, and A. Vittino, *Constraints on particle dark matter from cosmic-ray antiprotons*, *JCAP* **1404** (2014), no. 04 003, [[arXiv:1312.3579](#)].
- [226] M. Boudaud, M. Cirelli, G. Giesen, and P. Salati, *A fussy revisit of antiprotons as a tool for Dark Matter searches*, *JCAP* **1505** (2015), no. 05 013, [[arXiv:1412.5696](#)].
- [227] **IceCube** Collaboration, M. G. Aartsen et al., *Multipole analysis of IceCube data to search for dark matter accumulated in the Galactic halo*, *Eur. Phys. J.* **C75** (2015), no. 1 20, [[arXiv:1406.6868](#)].
- [228] **IceCube** Collaboration, M. G. Aartsen et al., *Search for Dark Matter Annihilation in the Galactic Center with IceCube-79*, [arXiv:1505.07259](#).
- [229] **ANTARES** Collaboration, S. Adrian-Martinez et al., *Search of Dark Matter Annihilation in the Galactic Centre using the ANTARES Neutrino Telescope*, [arXiv:1505.04866](#).

- [230] **EGRET** Collaboration, R. C. Hartman et al., *The Third EGRET catalog of high-energy gamma-ray sources*, *Astrophys. J. Suppl.* **123** (1999) 79.
- [231] **Fermi-LAT** Collaboration, W. Atwood et al., *The Large Area Telescope on the Fermi Gamma-ray Space Telescope Mission*, *Astrophys.J.* **697** (2009) 1071–1102, [[arXiv:0902.1089](#)].
- [232] **Fermi-LAT** Collaboration, *Fermi Large Area Telescope Second Source Catalog*, *Astrophys. J. Suppl.* **199** (2012) 31, [[arXiv:1108.1435](#)].
- [233] **Fermi-LAT** Collaboration, *Fermi Large Area Telescope Third Source Catalog*, [arXiv:1501.02003](#).
- [234] D. Thompson, *The Gamma-ray Sky with Fermi*, *Nucl.Phys.Proc.Suppl.* **243-244** (2013) 58–63, [[arXiv:1308.1870](#)].
- [235] **Fermi-LAT** Collaboration, *Fermi-LAT Observations of the Diffuse Gamma-Ray Emission: Implications for Cosmic Rays and the Interstellar Medium*, *Astrophys. J.* **750** (2012) 3, [[arXiv:1202.4039](#)].
- [236] F. Calore, I. Cholis, and C. Weniger, *Background model systematics for the Fermi GeV excess*, *JCAP* **1503** (2015) 038, [[arXiv:1409.0042](#)].
- [237] B. Zhou, Y.-F. Liang, X. Huang, X. Li, Y.-Z. Fan, L. Feng, and J. Chang, *GeV excess in the Milky Way: The role of diffuse galactic gamma-ray emission templates*, *Phys. Rev. D* **91** (2015), no. 12 123010, [[arXiv:1406.6948](#)].
- [238] M. Su, T. R. Slatyer, and D. P. Finkbeiner, *Giant Gamma-ray Bubbles from Fermi-LAT: AGN Activity or Bipolar Galactic Wind?*, *Astrophys. J.* **724** (2010) 1044–1082, [[arXiv:1005.5480](#)].
- [239] **Fermi-LAT** Collaboration, M. Ackermann et al., *The Spectrum and Morphology of the Fermi Bubbles*, *Astrophys. J.* **793** (2014), no. 1 64, [[arXiv:1407.7905](#)].
- [240] **Fermi-LAT** Collaboration, J.-M. Casandjian, *The Fermi-LAT model of interstellar emission for standard point source analysis*, 2015. [arXiv:1502.07210](#).
- [241] R. M. Crocker, *Non-Thermal Radiation from the Inner Galaxy*, *PoS CRISM2014* (2014) 040, [[arXiv:1411.7453](#)].
- [242] L. Bergstrom and H. Snellman, *Observable Monochromatic Photons From Cosmic Photino Annihilation*, *Phys. Rev. D* **37** (1988) 3737–3741.
- [243] L. Bergstrom and P. Ullio, *Full one loop calculation of neutralino annihilation into two photons*, *Nucl. Phys.* **B504** (1997) 27–44, [[hep-ph/9706232](#)].

- [244] Z. Bern, P. Gondolo, and M. Perelstein, *Neutralino annihilation into two photons*, *Phys. Lett.* **B411** (1997) 86–96, [[hep-ph/9706538](#)].
- [245] L. Bergstrom, *Radiative Processes in Dark Matter Photino Annihilation*, *Phys. Lett.* **B225** (1989) 372.
- [246] R. Flores, K. A. Olive, and S. Rudaz, *Radiative Processes in Lsp Annihilation*, *Phys. Lett.* **B232** (1989) 377–382.
- [247] L. Bergstrom, T. Bringmann, M. Eriksson, and M. Gustafsson, *Gamma rays from Kaluza-Klein dark matter*, *Phys. Rev. Lett.* **94** (2005) 131301, [[astro-ph/0410359](#)].
- [248] J. F. Beacom, N. F. Bell, and G. Bertone, *Gamma-ray constraint on Galactic positron production by MeV dark matter*, *Phys. Rev. Lett.* **94** (2005) 171301, [[astro-ph/0409403](#)].
- [249] A. Birkedal, K. T. Matchev, M. Perelstein, and A. Spray, *Robust gamma ray signature of WIMP dark matter*, [hep-ph/0507194](#).
- [250] T. Bringmann, L. Bergstrom, and J. Edsjo, *New Gamma-Ray Contributions to Supersymmetric Dark Matter Annihilation*, *JHEP* **01** (2008) 049, [[arXiv:0710.3169](#)].
- [251] L. Bergstrom, P. Ullio, and J. H. Buckley, *Observability of gamma-rays from dark matter neutralino annihilations in the Milky Way halo*, *Astropart. Phys.* **9** (1998) 137–162, [[astro-ph/9712318](#)].
- [252] J. A. R. Cembranos, A. de la Cruz-Dombriz, A. Dobado, R. A. Lineros, and A. L. Maroto, *Photon spectra from WIMP annihilation*, *Phys. Rev.* **D83** (2011) 083507, [[arXiv:1009.4936](#)].
- [253] J. Conrad, *Searches for Particle Dark Matter with gamma-rays*, *AIP Conf. Proc.* **1505** (2012) 166–176, [[arXiv:1210.4392](#)].
- [254] B. Bertoni, D. Hooper, and T. Linden, *Examining The Fermi-LAT Third Source Catalog In Search Of Dark Matter Subhalos*, [arXiv:1504.02087](#).
- [255] N. Fornengo, L. Pieri, and S. Scopel, *Neutralino annihilation into gamma-rays in the Milky Way and in external galaxies*, *Phys. Rev.* **D70** (2004) 103529, [[hep-ph/0407342](#)].
- [256] X. Huang, G. Vertongen, and C. Weniger, *Probing Dark Matter Decay and Annihilation with Fermi LAT Observations of Nearby Galaxy Clusters*, *JCAP* **1201** (2012) 042, [[arXiv:1110.1529](#)].
- [257] H. Silverwood, C. Weniger, P. Scott, and G. Bertone, *A realistic assessment of the CTA sensitivity to dark matter annihilation*, *JCAP* **1503** (2015), no. 03 055, [[arXiv:1408.4131](#)].

- [258] **HESS** Collaboration, A. Abramowski et al., *Search for Photon-Linelike Signatures from Dark Matter Annihilations with H.E.S.S.*, *Phys.Rev.Lett.* **110** (2013) 041301, [[arXiv:1301.1173](#)].
- [259] **Fermi-LAT** Collaboration, *Updated Search for Spectral Lines from Galactic Dark Matter Interactions with Pass 8 Data from the Fermi Large Area Telescope*, *Phys. Rev.* **D91** (2015) 122002, [[arXiv:1506.00013](#)].
- [260] T. Bringmann, X. Huang, A. Ibarra, S. Vogl, and C. Weniger, *Fermi LAT Search for Internal Bremsstrahlung Signatures from Dark Matter Annihilation*, *JCAP* **1207** (2012) 054, [[arXiv:1203.1312](#)].
- [261] T. Bringmann, F. Calore, G. Vertongen, and C. Weniger, *On the Relevance of Sharp Gamma-Ray Features for Indirect Dark Matter Searches*, *Phys.Rev.* **D84** (2011) 103525, [[arXiv:1106.1874](#)].
- [262] **Fermi-LAT** Collaboration, M. Ackermann et al., *Search for gamma-ray spectral lines with the Fermi large area telescope and dark matter implications*, *Phys.Rev.* **D88** (2013) 082002, [[arXiv:1305.5597](#)].
- [263] **CTA** Collaboration, M. Doro et al., *Dark Matter and Fundamental Physics with the Cherenkov Telescope Array*, *Astropart. Phys.* **43** (2013) 189–214, [[arXiv:1208.5356](#)].
- [264] T. Bringmann and C. Weniger, *Gamma Ray Signals from Dark Matter: Concepts, Status and Prospects*, *Phys. Dark Univ.* **1** (2012) 194–217, [[arXiv:1208.5481](#)].
- [265] R. Gould and G. Schréder, *Opacity of the Universe to High-Energy Photons*, *Phys. Rev. Lett.* **16** (1966), no. 6 252–254.
- [266] J. V. Jelley, *High-energy  $\gamma$ -ray absorption in space by a  $3.5^{\circ}K$  microwave field*, *Phys. Rev. Lett.* **16** (Mar, 1966) 479–481.
- [267] A. A. Penzias and R. W. Wilson, *A Measurement of excess antenna temperature at 4080-Mc/s*, *Astrophys. J.* **142** (1965) 419–421.
- [268] R. C. Gilmore, P. Madau, J. R. Primack, R. S. Somerville, and F. Haardt, *GeV Gamma-Ray Attenuation and the High-Redshift UV Background*, [arXiv:0905.1144](#).
- [269] J.-L. Zhang, X.-J. Bi, and H.-B. Hu, *VHE gamma-ray absorption by galactic interstellar radiation field*, *Astron. Astrophys.* **449** (2006) 641, [[astro-ph/0508236](#)].
- [270] K. Bernlöhr, A. Barnacka, Y. Becherini, O. Blanch Bigas, E. Carmona, et al., *Monte Carlo design studies for the Cherenkov Telescope Array*, *Astropart.Phys.* **43** (2013) 171–188, [[arXiv:1210.3503](#)].

- [271] **HERD** Collaboration, S. Zhang, *The High Energy cosmic-Radiation Detection (HERD) Facility onboard China's Future Space Station*, arXiv:1407.4866.
- [272] **HESS** Collaboration, F. Aharonian et al., *Observations of the Crab Nebula with H.E.S.S*, *Astron. Astrophys.* **457** (2006) 899–915, [astro-ph/0607333].
- [273] **HESS** Collaboration, A. Abramowski et al., *Search for a Dark Matter annihilation signal from the Galactic Center halo with H.E.S.S*, *Phys.Rev.Lett.* **106** (2011) 161301, [arXiv:1103.3266].
- [274] **HESS** Collaboration, B. Giebels, *Status and recent results from H.E.S.S*, in *4th International Fermi Symposium Monterey, California, USA, October 28-November 2, 2012*, 2013. arXiv:1303.2850.
- [275] “Cta news.” [https://portal.cta-observatory.org/SiteAssets/Pages/News/SiteNegotiationsStarted\\_10042014.pdf](https://portal.cta-observatory.org/SiteAssets/Pages/News/SiteNegotiationsStarted_10042014.pdf). Accessed: 2015-06-04.
- [276] “Cta performance.” <https://portal.cta-observatory.org/Pages/CTA-Performance.aspx>. Accessed: 2015-07-02.
- [277] R. Bock, A. Chilingarian, M. Gaug, F. Hakl, T. Hengstebeck, et al., *Methods for multidimensional event classification: A case study using images from a Cherenkov gamma-ray telescope*, *Nucl.Instrum.Meth.* **A516** (2004) 511–528.
- [278] **CTA Consortium** Collaboration, M. Actis et al., *Design concepts for the Cherenkov Telescope Array CTA: An advanced facility for ground-based high-energy gamma-ray astronomy*, *Exper.Astron.* **32** (2011) 193–316, [arXiv:1008.3703].
- [279] **ATLAS** Collaboration, *Physics at a High-Luminosity LHC with ATLAS*, in *Community Summer Study 2013: Snowmass on the Mississippi (CSS2013)* Minneapolis, MN, USA, July 29-August 6, 2013, 2013. arXiv:1307.7292.
- [280] **CMS** Collaboration, *Projected Performance of an Upgraded CMS Detector at the LHC and HL-LHC: Contribution to the Snowmass Process*, in *Community Summer Study 2013: Snowmass on the Mississippi (CSS2013)* Minneapolis, MN, USA, July 29-August 6, 2013, 2013. arXiv:1307.7135.
- [281] E. Todesco and F. Zimmermann, eds., *Proceedings, EuCARD-AccNet-EuroLumi Workshop: The High-Energy Large Hadron Collider (HE-LHC10)*, (Geneva), CERN, CERN, 2011.
- [282] A. Zalewska, *Roadmap(s) for Particle Physics*, *Acta Phys. Polon.* **B46** (2015), no. 7 1439–1447.

- [283] **LUX** Collaboration, D. S. Akerib et al., *First results from the LUX dark matter experiment at the Sanford Underground Research Facility*, *Phys. Rev. Lett.* **112** (2014) 091303, [[arXiv:1310.8214](https://arxiv.org/abs/1310.8214)].
- [284] **XENON100** Collaboration, E. Aprile et al., *Dark Matter Results from 225 Live Days of XENON100 Data*, *Phys. Rev. Lett.* **109** (2012) 181301, [[arXiv:1207.5988](https://arxiv.org/abs/1207.5988)].
- [285] W. A. Rolke, A. M. Lopez, and J. Conrad, *Limits and confidence intervals in the presence of nuisance parameters*, *Nucl.Instrum.Meth.* **A551** (2005) 493–503, [[physics/0403059](https://arxiv.org/abs/physics/0403059)].
- [286] C. Weniger, *A Tentative Gamma-Ray Line from Dark Matter Annihilation at the Fermi Large Area Telescope*, *JCAP* **1208** (2012) 007, [[arXiv:1204.2797](https://arxiv.org/abs/1204.2797)].
- [287] A. R. Pullen, R.-R. Chary, and M. Kamionkowski, *Search with EGRET for a Gamma Ray Line from the Galactic Center*, *Phys.Rev.* **D76** (2007) 063006, [[astro-ph/0610295](https://arxiv.org/abs/astro-ph/0610295)].
- [288] A. Abdo, M. Ackermann, M. Ajello, W. Atwood, L. Baldini, et al., *Fermi LAT Search for Photon Lines from 30 to 200 GeV and Dark Matter Implications*, *Phys.Rev.Lett.* **104** (2010) 091302, [[arXiv:1001.4836](https://arxiv.org/abs/1001.4836)].
- [289] R. K. Bock, A. Chilingarian, M. Gaug, F. Hakl, T. Hengstebeck, M. Jiřina, J. Klaschka, E. Kotrč, P. Savický, S. Towers, A. Vaiciulis, and W. Wittek, *Methods for multidimensional event classification: a case study using images from a Cherenkov gamma-ray telescope*, *Nuclear Instruments and Methods in Physics Research A* **516** (Jan., 2004) 511–528.
- [290] J. R. Hoerandel, *On the knee in the energy spectrum of cosmic rays*, *Astropart.Phys.* **19** (2003) 193–220, [[astro-ph/0210453](https://arxiv.org/abs/astro-ph/0210453)].
- [291] D. Maurin, F. Melot, and R. Taillet, *CRDB: a database of charged cosmic rays*, *Astron.Astrophys.* **569** (2014) A32, [[arXiv:1302.5525](https://arxiv.org/abs/1302.5525)].
- [292] D. J. Fegan, *TOPICAL REVIEW:  $\gamma$ /hadron separation at TeV energies*, *Journal of Physics G Nuclear Physics* **23** (Sept., 1997) 1013–1060.
- [293] **H.E.S.S. Collaboration** Collaboration, F. Aharonian et al., *H.E.S.S. observations of the Galactic Center region and their possible dark matter interpretation*, *Phys.Rev.Lett.* **97** (2006) 221102, [[astro-ph/0610509](https://arxiv.org/abs/astro-ph/0610509)].
- [294] **H.E.S.S. Collaboration** Collaboration, F. Aharonian et al., *Discovery of very-high-energy gamma-rays from the galactic centre ridge*, *Nature* **439** (2006) 695–698, [[astro-ph/0603021](https://arxiv.org/abs/astro-ph/0603021)].
- [295] M. Chernyakova, D. Malyshev, F. Aharonian, R. Crocker, and D. Jones, *The high-energy, Arcminute-scale galactic center gamma-ray source*, *Astrophys.J.* **726** (2011) 60, [[arXiv:1009.2630](https://arxiv.org/abs/1009.2630)].

- [296] V. Lefranc, E. Moulin, P. Panci, and J. Silk, *Prospects for Annihilating Dark Matter in the inner Galactic halo by the Cherenkov Telescope Array*, [arXiv:1502.05064](https://arxiv.org/abs/1502.05064).
- [297] AMS-02 collaboration, , in *International Cosmic Ray Conference*, <http://www.ams02.org/2013/07/new-results-from-ams-presented-at-icrc-2013/>, 2013.
- [298] **Fermi-LAT** Collaboration, M. Ackermann et al., *The spectrum of isotropic diffuse gamma-ray emission between 100 MeV and 820 GeV*, *Astrophys.J.* **799** (2015), no. 1 86, [[arXiv:1410.3696](https://arxiv.org/abs/1410.3696)].
- [299] A. Ibarra, S. Lopez Gehler, and M. Pato, *Dark matter constraints from box-shaped gamma-ray features*, *JCAP* **1207** (2012) 043, [[arXiv:1205.0007](https://arxiv.org/abs/1205.0007)].
- [300] A. Ibarra, H. M. Lee, S. López Gehler, W.-I. Park, and M. Pato, *Gamma-ray boxes from axion-mediated dark matter*, *JCAP* **1305** (2013) 016, [[arXiv:1303.6632](https://arxiv.org/abs/1303.6632)].
- [301] H. M. Lee, M. Park, and W.-I. Park, *Fermi Gamma Ray Line at 130 GeV from Axion-Mediated Dark Matter*, *Phys.Rev.* **D86** (2012) 103502, [[arXiv:1205.4675](https://arxiv.org/abs/1205.4675)].
- [302] H. M. Lee, M. Park, and W.-I. Park, *Axion-mediated dark matter and Higgs diphoton signal*, *JHEP* **1212** (2012) 037, [[arXiv:1209.1955](https://arxiv.org/abs/1209.1955)].
- [303] Y. Nomura and J. Thaler, *Dark Matter through the Axion Portal*, *Phys.Rev.* **D79** (2009) 075008, [[arXiv:0810.5397](https://arxiv.org/abs/0810.5397)].
- [304] J. Mardon, Y. Nomura, D. Stolarski, and J. Thaler, *Dark Matter Signals from Cascade Annihilations*, *JCAP* **0905** (2009) 016, [[arXiv:0901.2926](https://arxiv.org/abs/0901.2926)].
- [305] J. Mardon, Y. Nomura, and J. Thaler, *Cosmic Signals from the Hidden Sector*, *Phys.Rev.* **D80** (2009) 035013, [[arXiv:0905.3749](https://arxiv.org/abs/0905.3749)].
- [306] C. Garcia-Cely, A. Ibarra, and E. Molinaro, *Cosmological and astrophysical signatures of dark matter annihilations into pseudo-Goldstone bosons*, *JCAP* **1402** (2014) 032, [[arXiv:1312.3578](https://arxiv.org/abs/1312.3578)].
- [307] D. G. Cerdeno, M. Peiro, and S. Robles, *Fits to the Fermi-LAT GeV excess with RH sneutrino dark matter: implications for direct and indirect dark matter searches and the LHC*, *Phys. Rev.* **D91** (2015), no. 12 123530, [[arXiv:1501.01296](https://arxiv.org/abs/1501.01296)].
- [308] D. G. Cerdeno, M. Peiro, and S. Robles, *Enhanced lines and box-shaped features in the gamma-ray spectrum from annihilating dark matter in the NMSSM*, [arXiv:1507.08974](https://arxiv.org/abs/1507.08974).
- [309] R. D. Peccei and H. R. Quinn, CP, *Phys. Rev. Lett.* **38** (Jun, 1977) 1440–1443.
- [310] J. McDonald, *Thermally generated gauge singlet scalars as selfinteracting dark matter*, *Phys.Rev.Lett.* **88** (2002) 091304, [[hep-ph/0106249](https://arxiv.org/abs/hep-ph/0106249)].

- [311] C. Burgess, M. Pospelov, and T. ter Veldhuis, *The Minimal model of nonbaryonic dark matter: A Singlet scalar*, *Nucl.Phys.* **B619** (2001) 709–728, [[hep-ph/0011335](#)].
- [312] B. Patt and F. Wilczek, *Higgs-field portal into hidden sectors*, [hep-ph/0605188](#).
- [313] N. G. Deshpande and E. Ma, *Pattern of Symmetry Breaking with Two Higgs Doublets*, *Phys.Rev.* **D18** (1978) 2574.
- [314] R. Barbieri, L. J. Hall, and V. S. Rychkov, *Improved naturalness with a heavy Higgs: An Alternative road to LHC physics*, *Phys.Rev.* **D74** (2006) 015007, [[hep-ph/0603188](#)].
- [315] L. Lopez Honorez, E. Nezri, J. F. Oliver, and M. H. Tytgat, *The Inert Doublet Model: An Archetype for Dark Matter*, *JCAP* **0702** (2007) 028, [[hep-ph/0612275](#)].
- [316] M. Cirelli, N. Fornengo, and A. Strumia, *Minimal dark matter*, *Nucl. Phys.* **B753** (2006) 178–194, [[hep-ph/0512090](#)].
- [317] M. Cirelli, A. Strumia, and M. Tamburini, *Cosmology and Astrophysics of Minimal Dark Matter*, *Nucl. Phys.* **B787** (2007) 152–175, [[arXiv:0706.4071](#)].
- [318] M. Cirelli and A. Strumia, *Minimal Dark Matter: Model and results*, *New J. Phys.* **11** (2009) 105005, [[arXiv:0903.3381](#)].
- [319] M. Cirelli, T. Hambye, P. Panci, F. Sala, and M. Taoso, *Gamma ray tests of Minimal Dark Matter*, [arXiv:1507.05519](#).
- [320] E. J. Chun, J.-C. Park, and S. Scopel, *Non-perturbative Effect and PAMELA Limit on Electro-Weak Dark Matter*, *JCAP* **1212** (2012) 022, [[arXiv:1210.6104](#)].
- [321] T. Cohen, M. Lisanti, A. Pierce, and T. R. Slatyer, *Wino Dark Matter Under Siege*, *JCAP* **1310** (2013) 061, [[arXiv:1307.4082](#)].
- [322] M. Baumgart, I. Z. Rothstein, and V. Vaidya, *Calculating the Annihilation Rate of Weakly Interacting Massive Particles*, *Phys.Rev.Lett.* **114** (2015) 211301, [[arXiv:1409.4415](#)].
- [323] L. Di Luzio, R. Grober, J. F. Kamenik, and M. Nardecchia, *Accidental matter at the LHC*, [arXiv:1504.00359](#).
- [324] M. Aoki, T. Toma, and A. Vicente, *Non-thermal Production of Minimal Dark Matter via Right-handed Neutrino Decay*, [arXiv:1507.01591](#).
- [325] A. Sommerfeld, *Über die beugung und bremsung der elektronen*, *Annalen der Physik* **403** (1931), no. 3 257–330.
- [326] L. Bergstrom, G. Bertone, J. Conrad, C. Farnier, and C. Weniger, *Investigating Gamma-Ray Lines from Dark Matter with Future Observatories*, *JCAP* **1211** (2012) 025, [[arXiv:1207.6773](#)].

- [327] A. M. Galper et al., *The GAMMA-400 space observatory: status and perspectives*, [arXiv:1412.4239](https://arxiv.org/abs/1412.4239).
- [328] **ATLAS** Collaboration, G. Aad et al., *Summary of the searches for squarks and gluinos using  $\sqrt{s} = 8$  TeV pp collisions with the ATLAS experiment at the LHC*, [arXiv:1507.05525](https://arxiv.org/abs/1507.05525).
- [329] **CMS** Collaboration, S. Chatrchyan et al., *Search for new physics in the multijet and missing transverse momentum final state in proton-proton collisions at  $\sqrt{s} = 8$  TeV*, *JHEP* **06** (2014) 055, [[arXiv:1402.4770](https://arxiv.org/abs/1402.4770)].
- [330] **Planck** Collaboration, P. Ade et al., *Planck 2013 results. XVI. Cosmological parameters*, *Astron. Astrophys.* **571** (2014) A16, [[arXiv:1303.5076](https://arxiv.org/abs/1303.5076)].
- [331] <http://lepsusy.web.cern.ch/lepsusy/>.
- [332] **ATLAS, CMS** Collaboration, G. Aad et al., *Combined Measurement of the Higgs Boson Mass in pp Collisions at  $\sqrt{s} = 7$  and 8 TeV with the ATLAS and CMS Experiments*, *Phys. Rev. Lett.* **114** (2015) 191803, [[arXiv:1503.07589](https://arxiv.org/abs/1503.07589)].
- [333] **CMS** Collaboration, V. Khachatryan et al., *Precise determination of the mass of the Higgs boson and tests of compatibility of its couplings with the standard model predictions using proton collisions at 7 and 8 TeV*, *Eur. Phys. J.* **C75** (2015), no. 5 212, [[arXiv:1412.8662](https://arxiv.org/abs/1412.8662)].
- [334] <http://www.slac.stanford.edu/xorg/hfag/rare/2012/radll/index.html>.
- [335] **LHCb** Collaboration, R. Aaij et al., *Measurement of the  $B_s^0 \rightarrow \mu^+ \mu^-$  branching fraction and search for  $B^0 \rightarrow \mu^+ \mu^-$  decays at the LHCb experiment*, *Phys. Rev. Lett.* **111** (2013) 101805, [[arXiv:1307.5024](https://arxiv.org/abs/1307.5024)].
- [336] **PICO** Collaboration, C. Amole et al., *Dark Matter Search Results from the PICO-2L C\_3F\_8 Bubble Chamber*, *Phys. Rev. Lett.* **114** (2015), no. 23 231302, [[arXiv:1503.00008](https://arxiv.org/abs/1503.00008)].
- [337] **XENON100** Collaboration, E. Aprile et al., *Limits on spin-dependent WIMP-nucleon cross sections from 225 live days of XENON100 data*, *Phys. Rev. Lett.* **111** (2013), no. 2 021301, [[arXiv:1301.6620](https://arxiv.org/abs/1301.6620)].
- [338] A. Fowlie, K. Kowalska, L. Roszkowski, E. M. Sessolo, and Y.-L. S. Tsai, *Dark matter and collider signatures of the MSSM*, *Phys. Rev.* **D88** (2013) 055012, [[arXiv:1306.1567](https://arxiv.org/abs/1306.1567)].
- [339] A. Djouadi, J. Kalinowski, and M. Spira, *HDECAY: A Program for Higgs boson decays in the standard model and its supersymmetric extension*, *Comput. Phys. Commun.* **108** (1998) 56–74, [[hep-ph/9704448](https://arxiv.org/abs/hep-ph/9704448)].

- [340] H. W. Baer and X. Tata, *Weak scale supersymmetry: from superfields to scattering events.* Cambridge Univ. Press, Cambridge, 2006.
- [341] G. Cowan, *Statistical Data Analysis.* Oxford University Press, Oxford, 1998.
- [342] S. Wilks, *The Large-Sample Distribution of the Likelihood Ratio for Testing Composite Hypotheses,* *Annals Math. Statist.* **9** (1938), no. 1 60–62.
- [343] H. Chernoff, *On the distribution of the likelihood ratio,* *Ann. Math. Statist.* **25** (09, 1954) 573–578.